USAAMRDL-TR-77-10

WIND TUNNEL INVESTIGATION OF THE CONTROLLABLE TWIST ROTOR PERFORMANCE AND DYNAMIC BEHAVIOR

Kaman Aerospace Corporation
Old Windsor Road
Bloomfield, Conn. 06002

June 1977

Final Report for Period June 1972 - March 1976

Prepared for

EUSTIS DIRECTORATE
U. S. ARMY AIR MOBILITY RESEARCH AND DEVELOPMENT LABORATORY
Fort Eustis, Va. 23604

EUSTIS DIRECTORATE POSITION STATEMENT

This report has been reviewed by the Eustis Directorate, U.S. Army Air Mobility Research and Development Laboratory, and is considered to be technically sound. The purpose of this program was to investigate the Controllable Twist Rotor (CTR) through wind tunnel tests conducted in the NASA Ames 40- by 80-foot wind tunnel. Inherent inefficiencies existed in the CTR test model because of the "breadboard" quality of this first test system. These inefficiencies, coupled with the inability to evaluate mission profiles in the wind tunnel environment, did not allow validation of the full projected CTR potential. However, test results did indicate that the dynamic twist distribution was controlled during the wind tunnel tests and that analytically projected blade response characteristics are achievable. Thus, it is reasonable to believe that the CTR potential can be attained in an optimized rotor configuration. This optimization becomes the major problem, and the results of the CTR wind tunnel research clearly point to the need for further research directed at learning to design rotor aeroelastic properties.

Mr. William E. Nettles, Aeromechanics Technical Area, Technology Applications Division, served as the Army Project Engineer for this effort.

UNCLASSIFIED

SECURITY CLASSIFICATION OF THIS PAGE (When Data Entered)

REPORT DOCUMENTATION PAGE

READ INSTRUCTIONS BEFORE COMPLETING FORM

1. REPORT NUMBER: USAAMRDL-TR-77-10
2. GOVT ACCESSION NO.:
3. RECIPIENT'S CATALOG NUMBER:

4. TITLE (and Subtitle): WIND TUNNEL INVESTIGATION OF THE CONTROLLABLE TWIST ROTOR PERFORMANCE AND DYNAMIC BEHAVIOR.

5. TYPE OF REPORT & PERIOD COVERED: Final Report. June 1972 - March 1976.

6. PERFORMING ORG. REPORT NUMBER: R-1487

7. AUTHOR(s): A. Z. Lemnios, H. E. Howes

8. CONTRACT OR GRANT NUMBER(s): DAAJ02-72-C-0092

9. PERFORMING ORGANIZATION NAME AND ADDRESS: Kaman Aerospace Corporation, Old Windsor Road, Bloomfield, Connecticut 06002

10. PROGRAM ELEMENT, PROJECT, TASK AREA & WORK UNIT NUMBERS: 62209A 1F262209AH76 00 008 ER

11. CONTROLLING OFFICE NAME AND ADDRESS: Eustis Directorate, U. S. Army Air Mobility R&D Laboratory, Fort Eustis, Virginia 23604

12. REPORT DATE: June 1977

13. NUMBER OF PAGES: 175

14. MONITORING AGENCY NAME & ADDRESS (if different from Controlling Office): 175p.

15. SECURITY CLASS. (of this report): Unclassified

15a. DECLASSIFICATION/DOWNGRADING SCHEDULE:

16. DISTRIBUTION STATEMENT (of this Report)

Approved for public release; distribution unlimited.

DDC RELEASED AUG 5 1977 C

17. DISTRIBUTION STATEMENT (of the abstract entered in Block 20, if different from Report)

18. SUPPLEMENTARY NOTES

19. KEY WORDS (Continue on reverse side if necessary and identify by block number)

Controllable Twist Rotor
Control Rotors
Rotors, Helicopter
Rotor Aerodynamics
Wind Tunnel Tests
Design, Rotor Systems

20. ABSTRACT (Continue on reverse side if necessary and identify by block number)

The Controllable Twist Rotor (CTR) principle is based on a torsionally flexible helicopter blade, utilizing inboard and outboard collective and cyclic controls to optimize the blade pitch distribution along the radius and around the azimuth. The benefits of this unique rotor system include improved performance, delayed retreating-blade stall, and reduced bending moments and vibration levels.

DD FORM 1 JAN 73 1473 EDITION OF 1 NOV 65 IS OBSOLETE

UNCLASSIFIED

SECURITY CLASSIFICATION OF THIS PAGE (When Data Entered)

H04362

AB

20 (Continued)

The work reported here, sponsored by USAAMRDL, Eustis Directorate, evolved from a feasibility study and covered the design, fabrication and testing of a full-scale wind tunnel model of a CTR. Program objectives were to:

- Demonstrate the CTR principle while making maximum use of proven helicopter components.
- Establish functional relationships between rotor performance, blade vibratory loads, and control settings.
- Provide a firm data base for future tests over an expanded test envelope.
- Correlate test results with predictions.
- Compare the test results with previously tested rotors.

CTR wind tunnel testing, conducted in the 40- x 80-foot wind tunnel at the NASA-Ames Research Center, and the associated test results are described in the text. The model design and qualification testing are described in the appendixes.

Conclusions reached during the wind tunnel testing of the CTR are summarized below.

1. Rotor stall was alleviated at all test conditions, verifying performance characteristics predicted by analysis.

2. CTR and H-34 performance comparisons indicate that the CTR can operate to a 20-percent-higher blade loading than the H-34 blade without encountering stall.

3. Both collective and cyclic servo flap controls are required to operate the CTR efficiently.

4. Functional relationships were defined between rotor performance, blade vibratory loads, and combinations of dual-control settings using optimization techniques developed during the program.

5. Rotor performance parameters optimize more compatibly than predicted, thereby broadening the allowable range of controls.

6. Optimization trends for control combinations are similar to predictions.

7. Servo flaps with external support brackets are not suitable for high-performance rotors.

It is recommended that an advanced-technology CTR be designed for flight testing using the information generated during the wind tunnel tests. It is also recommended that further wind tunnel testing be considered for the existing wind tunnel CTR technology demonstrator in order to expand the CTR data base and to evaluate the effects of higher harmonic control on rotor performance and dynamic behavior.

PREFACE

The work performed on this contract was under the technical direction of William E. Nettles, Eustis Directorate, U. S. Army Air Mobility Research and Development Laboratory (USAAMRDL), Fort Eustis, Virginia. The success of the program was enhanced by the efforts of the NASA-Ames 40- x 80-foot wind tunnel staff and through the cooperative effort of Sikorsky Aircraft. Acknowledgment is also given to the 40- x 80-foot tunnel for photographs supplied of the CTR in the wind tunnel.

The authors also wish to acknowledge the technical assistance provided by the Research, Design, and Test Departments of Kaman Aerospace Corporation.

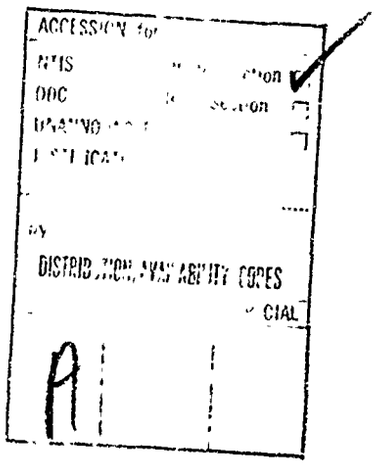

TABLE OF CONTENTS

TABLE OF CONTENTS (Continued)

LIST OF ILLUSTRATIONS

LIST OF ILLUSTRATIONS (Continued)

LIST OF ILLUSTRATIONS (Continued)

INTRODUCTION

The Controllable Twist Rotor (CTR), shown in Figure 1, was conceived as a lifting system in which blade twist distribution could be controlled cyclically and collectively in order to increase its aerodynamic efficiency. The CTR consists of a torsionally flexible blade that is controlled by a conventional pitch horn at its root and an aerodynamic control flap at its tip. The pitch horn is considered the primary trim control system for vectoring rotor thrust, whereas the flap generates the necessary external moments for elastically twisting the blade about its mean trim position in order to provide an efficient distribution of blade airloads. By programming inputs to the dual controls, the blade aeroelastic response is controlled to delay retreating blade stall, improve rotor performance, and reduce blade bending moments.

Figure 1 illustrates the dual-control system, which features two, independently actuated swashplates. Both the primary and secondary control systems can be varied collectively and cyclically. Each can also be scheduled to vary with forward speed.

The initial CTR research consisted of a parametric analysis and preliminary design of the system. The results of this work, reported in Reference 1, indicated that the CTR had a broad potential for improving vehicle performance and reducing dynamic loading. For instance, it was predicted that a helicopter could have, for a given solidity and tip speed, up to a 30-knot-higher stall limit, an improved blade and rotor component life, or a reduced rotor size, with mission effectiveness improvements of up to 30%.

Based on these positive results, the present experimental investigation was initiated in 1972. The general objectives of this program are to demonstrate the accuracy of the predicted CTR potential, to validate the computer techniques required to analyze the system, and to establish a reservoir of measured data upon which design of practical CTR hardware can be based.

The approach used to satisfy these objectives was to design and fabricate a full-scale model of a CTR system, followed by testing in the NASA-Ames 40- x 80-foot wind tunnel. The reason for going directly to a full-scale system is to simultaneously model Reynolds Number, Mach Number, Froude Number, and tip-speed ratio. The full-scale CTR model has the same chord, diameter, and solidity as the H-34 rotor, which was selected as

---

[1] A. Z. Lemnios and A. F. Smith, AN ANALYTICAL EVALUATION OF THE CONTROLLABLE TWIST ROTOR PERFORMANCE AND DYNAMIC BEHAVIOR, USAAMRDL Technical Report 72-16, U. S. Army Air Mobility Research and Development Laboratory, Fort Eustis, Virginia, May 1972, AD 747808.

the standard. The H-34 rotor system was selected as the standard because it had wind tunnel and flight testing and because its planform can be easily replicated with existing hardware and tooling to fabricate the CTR system. This design approach was taken to minimize costs. However, it does not yield a CTR configuration that can be considered aerodynamically optimum. Thus, the full-scale CTR model fabricated and tested in the current program is a technology demonstrator and not a prototype design.

TEST PROGRAM

ROTOR SYSTEM DESCRIPTION

The CTR system, as configured for wind tunnel tests, included rotor blades, rotor head, and associated controls, all fabricated or modified by Kaman, and interfaced with a test module supplied by Army/NASA at the Ames Research Center. A detailed description of the system is given in Appendix A.

Summarizing the main features of the rotor, the blade itself is a modification of the H-43 helicopter blade. The H-43 blade was extended by approximately three feet, and the standard servo flap was moved outboard and shortened to half its original size. Other changes included additional mass balance in the blade, an extended leading-edge guard, and a new blade grip to mate with a standard H-34 pitch barrel.

Outboard control was supplied by the servo flap, whereas inboard control was through a conventional pitch-horn system. The hub was a standard H-34 hub modified to add control cranks for the servo flap and to route the flap controls through the rotor shaft to a rotating swashplate located below the module gearbox. All controls were operated by actuators, commanded through appropriate switching from the main tunnel control room.

WHIRL TOWER TEST

The whirl tower test, performed at Kaman, was the major qualifying test for the CTR prior to wind tunnel tests. Individual component tests were not necessary because all major rotor components were adaptations of production hardware with long service histories. Approximately 30 hours of whirl testing were performed under calm and gusty wind conditions. The tests were performed to substantiate the structure through overspeed, verify stability, and obtain preliminary data concerning rotor dynamics and performance. A detailed description of the test and the results is presented in Appendix B. All tests were concluded successfully. During these tests, no structural limitations, no mechanical problems, and no instabilities were encountered.

WIND TUNNEL SHAKE TESTS

Wind tunnel tests were performed at the Ames Research Center's 40- x 80-foot full-scale tunnel during the Summer of 1975. A photograph of the wind tunnel installation is shown in Figure 2. Two types of tests were conducted during this test period in order to insure stable operating conditions for the rotor, the test pod, the test-pod support struts, and the balance frame configuaration, and to evaluate rotor performance and blade dynamic behavior.

System stability tests of the rotor test module and associated apparatus were made with and without the rotor to determine the system transfer function and the system damping associated with each mode. The test procedure without the rotor uses a hydraulic shaker mounted between the rotor hub and a suspended reaction mass weighing 11,600 pounds. The hub is excited at random by the shaker over a preselected range of frequencies in the lateral or longitudinal directions. A load cell between the shaker and the hub measures the applied force, and accelerometers in the rotor test apparatus (RTA) module measure system response. The applied force and system accelerations are analyzed via Fast Fourier Transform (FFT) techniques to determine the system's dynamic characteristics. Details of the test procedure, the data analysis, and the test results for the rotor hub alone are presented in References 2 and 3.

System stability tests for the hub with the rotor installed were conducted by shaking the pitch-horn swashplate at pseudorandom broad-band input frequencies and amplitudes with a maximum amplitude of 1 degree and a maximum frequency of 3.5 Hz. The frequency range was selected to span the fundamental response modes of the floating frame. The shake system was supplied with the rotor-test module and was operated by NASA. These stability tests were conducted at a rotor tip speed of 585 fps and at wind tunnel speeds from hover to 60 knots. Testing to higher wind speeds was terminated because of malfunctions in the control system. Approximately 6000 pounds of thrust was generated by the rotor during the random frequency shaking. FFT techniques were used to analyze the module accelerometer responses. Data taken during the random shake tests with the rotor installed confirmed the mechanical stability of the test configuration. Sufficient damping was available to preclude mechanical rig resonance of the balance frame, the RTA module, and the CTR.

WIND TUNNEL PERFORMANCE TESTS

Prior to the installation of the CTR blades on the rotor test apparatus module, aerodynamic force and moment tares were obtained of the module and rotor head without blade grips. These tares were incorporated mathematically into the NASA-Ames data reduction computer algorithm for rotor performance. The reduced rotor performance data thus reflect only the forces generated by the CTR blades.

---

[2] W. Johnson and J. C. Biggers, SHAKE TEST OF ROTOR TEST APPARATUS IN THE 40- BY 80-FOOT WIND TUNNEL, NASA Technical Memorandum TM X-62,418, Ames Research Center, Moffett Field, California, February 1975.

[3] W. Johnson and J. C. Biggers, SHAKE TEST OF ROTOR TEST APPARATUS WITH BALANCE DAMPERS IN THE 40- BY 80-FOOT WIND TUNNEL, NASA Technical Memorandum TM X-62,470, Ames Research Center, Moffett Field, California, July 1975.

Steady-state tests to evaluate rotor performance, blade dynamic behavior, and control sensitivity were conducted at wind tunnel speeds of 80, 120, and 135 knots and at a rotor tip speed of 585 fps. Limited test data were also obtained at 155 knots. At each test speed, shaft angles were chosen so that the CTR propulsive force would be sufficient to overcome fuselage drag flat-plate areas of 20-25 square feet at high thrust levels. Longitudinal and lateral cyclic pitches at the blade root were varied to maintain zero ($\pm$0.2 degrees) longitudinal and lateral cyclic flapping. Root collective pitch angle and servo flap collective and cyclic pitch angles were independently controlled.

A limitation was imposed on the test program because of the use of existing flightworthy hardware. The standard H-34 lag dampers that were installed on the rotor head have an internal relief valve that opens above 1750 pounds. Consequently, when the lag damper load exceeds 1750 pounds, the lag damper force is constant and does not vary with lag velocity; i.e., the damper is not a viscous damper above this load level. Although this characteristic is satisfactory for rotors on unconstrained helicopters in flight, it restricts the lag velocities and corresponding amplitudes that can be experienced by rotors on the rotor test apparatus to those below the load limiter setting. The reduction in damping above this point causes the test module to approach its mechanical instability boundary. To avoid mechanical instability for the CTR, blade lag amplitudes were continuously monitored and were maintained at less than $\pm$0.5 degrees of 1/rev motion.

As mentioned above, the independently controlled test variables include wind tunnel speed, rotor tip speed, shaft angle, root collective pitch, servo flap collective pitch, servo flap longitudinal cyclic pitch, and servo flap lateral cyclic pitch. If three levels of each independent variable are tested to define deterministically the dependence of other test parameters on the controlled variables, 2187 (3^7) combinations of the controlled variables are necessary to exhaust all permutations. Obviously, this number of test points is prohibitive. Experimental design techniques were used to reduce the number of test points to approximately 350. Values of the independently controlled variables were selected to provide sufficient information to establish a mathematical model of the main effects, nonlinearities, and principal interactions of the controlled variables. Ranges for the controlled variables were selected from previously obtained analytical data and from test experience with these variables. Because rotor performance characteristics are nondimensionalized on tip speed, only one level of tip speed (585 fps) was selected for the test program. Test ranges for the remaining six independent variables are summarized in Table 1.

The dependent variables that were measured during the test included the rotor aerodynamic force and moment characteristics, blade stresses, blade root motions, servo flap stresses, control loads, control motion, and support module accelerations. Rotor aerodynamic characteristics were measured directly on the main balance in the Ames 40- x 80-foot wind tunnel. The raw performance data were automatically corrected for tare values by the NASA-Ames data-reduction computer program, and the corrected data were reduced to standard wind-axis aerodynamic force and moment coefficients by the same program. Rotor power and torque were independently measured by strain gages on the main driveshaft and by yawing and rolling moments on the main balance. Two blades were fully instrumented with strain gages for stress measurements and angulators at the blade root for blade motions. Data were recorded generally from only one instrumented blade. Strain gage locations and strain gage measurements on the blades and the servo flap are shown in Figure 3. The blade angulators measured flapping, feathering, and lagging angles. Longitudinal, lateral, and vertical accelerations were measured in the module by accelerometers. More details on the instrumentation and the control system are given in Appendix C.

DATA ACQUISITION AND REDUCTION

Several systems were used during the wind tunnel test to acquire test data. Those systems and their functions are synopsized below.

Datex I - Used primarily for tunnel balance data. Also interfaced other selected inputs to the computer.

Peak-to-Peak Display - Used as a test monitor for critical parameters. Provided a permanent record of peak-to-peak levels.

Dynamic Analysis System - Used for on-line analysis during rig resonance tests and for control optimization.

High Speed Data Acquisition System - Digitized and recorded all test parameters on digital tape.

Dynamic Recording System - Recorded all test parameters on analog tape. Operated continuously during test as a backup for safety considerations.

Oscillograph - Recorded all critical parameters for test monitoring and to check the validity of the data on the other systems.

All of the above systems are described in more detail in Appendix C, along with a listing of all parameters recorded. Difficulties experienced with some of the primary data systems made it necessary to base the results presented in this report on data obtained from the Datex I system and the oscillograph.

Because of the large number of man-hours that would have been required to reduce data on all parameters recorded on the oscillograph, a priority listing of parameters was established. In addition to restricting the number of parameters, the type of reduction (steady values, peak-to-peak, harmonic analysis) was also restricted to essential data.

The priority parameter listing was established on the basis of data that was essential for comparison to analytical predictions. The listing is as follows:

	Reduction	
Parameter	Peak-Peak	Harmonic
Servo Flap Control Position	X	X
Servo Flap Control Load	X	
Pitch-Horn Control Load	X	
Flatwise Bending Station 280	X	X
Edgewise Bending Station 168	X	X
Torsion Station 201, 252	X	X
Flap Centerline Bending	X	
Blade Flapping	X	X
Blade Pitch	X	X

ANALYTICAL METHODS

AEROELASTIC AND TRIM ANALYSES

In the course of evaluating the CTR to design the test model and to develop a systematic test plan, it was necessary to perform a comprehensive series of aeroelastic analyses.

The analysis used to evaluate the CTR is called the 6F and is developed in detail in Reference 1, where the method of solution and the coupled aeroelastic equations of motion are derived for six response modes and two control modes for a fully articulated rotor system. The response modes can be considered normal modes and are described as follows:

- Blade Pitching
- Blade Lagging
- Blade Flapping
- Blade Flapwise Bending (First Elastic Bending Mode)
- Blade Twisting (First Elastic Twisting Mode)
- Servo Flap Pitching

The input control functions drive the blade and servo flap pitch angles from separate swashplates via control springs.

The modal approach is used to evaluate the airloads on a fully articulated rotor by mathematically describing blade motions with the six listed degrees of freedom. The complete inertial and centrifugal terms for the equations of motion are derived through the use of matrix transformations. Potential strain energy and dissipative energy terms are included in the equations of motion by assuming concentrated springs and viscous dampers for the four rigid body modes, and by evaluating the fundamental bending and torsional frequencies of the rotating blade for the flapwise bending and torsion modes.

Generalized aerodynamic forces for each of the six modes are obtained from strip theory by calculating an instantaneous local airfoil section angle of attack and using this angle of attack to evaluate aerodynamic force and moment coefficients from available wind tunnel data. In their present form, the aeroelastic equations of motion include all nonlinear inertial coupling effects and nonlinear aerodynamic effects, such as reverse flow, stall, Mach number variations and large induced flow angles. Additional features of the analysis are the inclusion of feedback mechanical coupling among the servo flap, blade feathering, blade flapping, and blade lagging motions, and the inclusion of arbitrary spring rates and dampers for each mode. Any one or combination of these parameters can be eliminated easily from the analysis. Furthermore, spring rates for the two types of control systems are also included in

[1] Lemnios and Smith

order that accurate control loads can be calculated. The present analysis describes the behavior of articulated rotors with pitch control input, with servo flap control input, or with dual-control input.

The CTR aeroelastic loads analysis produces a set of forces, blade responses, and rotor performance data for a specific set of control inputs. However, the forces produced are not necessarily the forces required for trim at the particular flight condition. The method for achieving the proper control inputs to obtain the necessary trim forces is called the trim program. Several initial cases are run, producing a set of forces for each initial case. These forces are compared to the control inputs in the trim program, and a new control prediction is made based on these comparisons. Iteration proceeds to trim convergence.

Blade bending moments are calculated by an associated computer program, BLBEND, which generates the influence coefficients of the rotating blade for each harmonic number of rotor speed. Harmonics of airloads generated by the 6F aeroelastic analysis are combined with the harmonic influence coefficients of BLBEND to yield the harmonics of the blade bending moments and shears, which, in turn, are combined to synthesize the total vibratory internal blade loads and the resultant blade root shears.

OPTIMIZATION TECHNIQUES

As mentioned previously, the CTR has dual controls that can be varied independently to improve rotor performance by redistributing blade airloads radially and azimuthally. In general, the servo flap control will disturb trim, altering the primary pitch-horn control settings required for any specified force trim condition. In contrast to a conventional rotor, with a single, unique, pitch-horn control setting required for a particular trim condition, the CTR can be trimmed with an infinite number of control settings, some of which will be better than others. Trim control, therefore, becomes an optimization problem, with the objective of selecting input primary and secondary control settings to achieve a specified trim point at the most favorable trade-off of performance parameters.

Computer analyses, such as 6F, capable of accounting for the sophisticated response of a dual-control rotor system are large, requiring considerable computer time for each case. Therefore, it is not economic to run the vast number of cases required for "trial and error" multiple-parameter optimization. Further, in order to obtain statistically significant relationships between measured parameters and controlled multiple parameters from test data, analytical techniques must be used that separate the main effects and interactions of these multiple parameters. These techniques are well known and have been used successfully for years in designing experiments for industrial research.

A stepwise approach was developed, based on a statistical response surface analysis, as described, for example, in Section 12.4 of Reference 4. In this approach, simple mathematical models are derived for the several performance parameters of interest from the results of a limited number of rotor aeroelastic analysis cases. Optimization and trade-off studies are performed by manipulating the mathematical models, allowing a large number of combinations of control inputs to be evaluated very quickly and economically. A limited number of promising solutions can then be examined by the complete rotor analysis program to confirm their validity. Alternatively, the optimization and trade-off studies can be used in conjunction with test data to predict the best mix of controls for optimizing the overall rotor performance.

The model to be developed and optimized for each flight condition of interest consists of a set of equations - one for each response variable to be considered. Each equation will contain some function of each of the independent variables. The model, therefore, describes how each response varies as the independent variables are manipulated.

The simplest model, for n independent variables and m responses, is linear:

$$\underset{j=1 \text{ to } m}{Y_j} = a_{oj} + a_{ij}x_i \cdots a_{nj}x_n \qquad (1)$$

Many aerodynamic and dynamic effects are more or less linear, at least over a limited range. The coefficients for a linear model of this form can be defined easily from a number of observations of the Y_j at various input values of the x_i by standard multiple linear regression techniques, available in most computer system libraries. Models of this form can be optimized by linear programming methods, also available in most system libraries.

Some rotor responses of interest, horsepower for example, would not be expected to respond linearly to any single input variable. One would expect a positive minimum value of power at some optimum input, with power increasing as the input is changed in either direction. A second degree polynomial might give a reasonable fit.

Although the secondary control inputs were selected to be mathematically independent, their effects on the rotor may interact. That is, the effect of one parameter may depend on the value of another parameter.

[4] Irwin Miller and John E. Freund, PROBABILITY AND STATISTICS FOR ENGINEERS, Prentice-Hall, Inc., Englewood Cliffs, N.J., 1965.

The same basic model form can be extended to account for these nonlinear effects provided that the equations remain linear in the coefficients. For example, for four independent variables, their second degree terms and mutual interactions:

$$Y_j = a_{oj} + a_{1j}x_1 + a_{2j}x_2 + a_{3j}x_3 + a_{4j}x_4 + a_{11j}x_1^2 + a_{22j}x_2^2$$

$$+ a_{33j}x_3^2 + a_{44j}x_4^2 + a_{12j}x_1x_2 + a_{13j}x_1x_3 + a_{14j}x_1x_4$$

$$+ a_{23j}x_2x_3 + a_{24j}x_2x_4 + a_{34j}x_3x_4 + a_{123j}x_1x_2x_3$$

$$+ a_{134j}x_1x_3x_4 + a_{234j}x_2x_3x_4 \qquad (2)$$

The full model will give a better fit over a larger domain than the simple linear model when nonlinear effects are present but requires much more data to develop coefficients. At least one complete rotor analysis case or one test data point per term on the right-hand side of the equation is needed to define the coefficients. Additional cases or test points will be required to evaluate the degree of fit.

There will usually be several response parameters that, taken together, define the performance of the rotor being evaluated. These will be the dependent variables of the optimization model. Horsepower, maximum retreating-blade angle-of-attack, maximum blade bending moment, and vibratory shears are examples. For "good" performance, each response parameter should be as small or as large as possible, or at least remain within certain limits. It may not be possible to find a secondary control setting that will cause all parameters to be optimum at the same time. Trade-offs will then have to be accepted. The number of response parameters to be included in the optimization study is itself a trade-off. All parameters that are critically important for the rotor and flight condition under consideration should be included.

Independent variables for the model will be the control inputs that are manipulated to cause the desired changes in the response parameters, while the desired trim point is being maintained. The primary helicopter controls are dependent variables because particular values of each will be required for any given combination of secondary control inputs to maintain the rotor in trim at the desired flight condition. The secondary control inputs become the independent variables of the optimization model.

The number of independent variables and the use of these variables in the model will govern the optimization procedure. If there is only one variable, it is convenient to plot each response against the variable to determine by visual inspection the optimum control setting for the selected strategy, as in Figure 4a. The acceptable range of x_1 is seen to be bounded at the lower value by the maximum allowable α, and at the upper value by the maximum allowable horsepower. Within this range either α or horsepower can be absolutely minimized, but not both. Bending moment and vibration level must be traded off.

Two variables also can be optimized graphically by plotting contours of various levels of each response on the x_1, x_2 plane and selecting the intersection of each response's acceptable area, as in Figure 4b. The acceptable area is shown cross-hatched. The optimum within that area depends upon the strategy being followed.

Graphical methods become difficult for larger numbers of variables. For three or more variables, several x_1 versus x_2 contour plots at various levels of x_3, x_4, and x_n can be drawn, and all corners of all acceptable areas can be evaluated against the optimization strategy. For more than three variables, graphic presentations are not useful. Computer mapping of acceptable areas is generally applicable for any number of variables and is simple to apply and interpret.

Three computer programs were prepared to perform regression analyses of data and to graphically present the results of the regression analyses for final optimization. The first of these programs, called SURGEN, generates the response surface using Equation 2 as a general model and tests the surface for fit to the data. The two remaining programs, PLOPT3 and PLOPT4, use the model generated by SURGEN to define optimum operating conditions. PLOPT3 plots contours with an automatic x-y plotter; PLOPT4 maps acceptable operating areas on the computer terminal. These programs were used extensively during the CTR design phase and during the test data analysis phase; specific applications in each phase are discussed in Appendix C and in the next section of this report, respectively.

DISCUSSION OF TEST DATA

BLADE DYNAMIC BEHAVIOR

Blade dynamic tuning and frequency placement was verified during the early portion of the wind tunnel tests. Strain gage responses were continuously recorded and analyzed at many rotor speeds up to values just beyond the test speed (200 rpm). Different strain gages responded vigorously over the rotor speed range, thereby identifying the particular blade modes that were excited. Results of these resonant responses are plotted in Figure 5 and are compared to predicted values on the same figure. Three flatwise elastic modes were identified from the test data, and they are labeled F2, F3, and F4 in Figure 5; the rigid-body flapping mode is labeled F1. Comparisons of these data points with the corresponding predicted frequencies show excellent correlations. One edgewise elastic mode was identified and is labeled E2; the rigid-body lagging mode is labeled E1. Comparisons of the measured E2 frequencies with the predicted E2 frequencies reveal a constant difference between the two data sets. This difference may occur because the predicted values were calculated using pin-end boundary conditions at the blade root, which ignore the effects of the lag damper. Lag dampers normally exhibit significant spring effects at the higher frequencies. Calibration data for the H-34 dampers used on the CTR were available only at 1/2. The first blade torsion mode, labeled T1, was not easily excited during the rotor speed sweeps. One data point was obtained at the lower end of the test range. Two curves of T1 predicted frequencies are shown in Figure 5. The lower curve was calculated by ignoring the aerodynamic stiffening effects due to the chordwise offset of aerodynamic center in the servo flap region of the blade. The upper T1 curve includes these aerodynamic stiffening effects by assuming a hovering rotor with axisymmetric flow. The observed T1 test point falls between the two predicted curves. Overall, the comparisons between test and predictions in Figure 5 show good agreement and satisfactory placement of the various frequencies to avoid resonance at the rotor test speed.

During the rotor performance tests, blade torsion strain gage signals at stations 201.6 and 252.2 were converted to equivalent twist angles at these stations. Twist angles at the tip were obtained by extrapolating the measured twist angles at the two inboard stations by means of the calculated torsion mode shape. The signals were harmonically analyzed for five harmonics and were compared to net servo flap deflections in order to evaluate servo flap control effectiveness. Data are available at all test speeds and for various phase angle differences between control input and twist response. Figure 6 illustrates typical variations of the blade cyclic twist response at the tip to servo flap cyclic inputs for wind speeds of 135 knots. The upper curves were obtained at root collective pitch settings of 12° and the lower curves at root collective pitch settings of 14°. In both figures, the servo flap collective was maintained at the preselected values indicated. The phase angle between

input and response was selected from the measured data to be nominally 170° ±10°. Cyclic twist response for 135 knots at other phase angles has the same sensitivities as those of Figure 6. Cyclic servo flap effectiveness is linear over the range tested. Cyclic control effectiveness, as measured from Figure 6, is 1.0 degree cyclic twist per degree servo flap cyclic regardless of root collective pitch or servo flap collective. Other cyclic twist responses that can be obtained from Figure 6 are cyclic twist responses due to servo flap collective and due to root collective. The following values summarize these sensitivities:

$$\frac{\partial|\phi_1|}{\partial\theta_0} = -0.3, \quad \frac{\partial|\phi_1|}{\partial\delta_0} = 0.5, \quad \frac{\partial|\phi_1|}{\partial|\delta_1|} = 1.0 \tag{3}$$

Servo flap effectiveness on coning and cyclic flapping at zero airspeed was evaluated during the whirl tests reported in Appendix B; these test results are summarized below:

$$\frac{\partial\beta_0}{\partial\theta_0} = 0.4, \quad \frac{\partial\beta_0}{\partial\delta_0} = -0.3, \quad \frac{\partial|\beta_1|}{\partial|\delta_1|} = 0.9 \tag{4}$$

ROTOR PERFORMANCE

Rotor performance for the CTR, as described in the previous section and in Reference 4, is more than just a measure of the power required to generate a specified rotor thrust and propulsive force. More broadly, rotor performance of a dual-control system involves concurrent measures of multiple parameters that characterize the efficiency and effectiveness of the total rotor system when the secondary control inputs have been optimized. For the CTR, the ratio of the profile power coefficient to the solidity was selected as one of the parameters because it characterizes the aerodynamic efficiency of the rotor and defines the onset of rotor stall. The second parameter selected to measure rotor performance was the maximum vibratory flatwise bending moment on the blade. The blade bending moment was selected because it is a measure of blade life. A third measure of rotor performance was the pitch-link load at the blade root. This load was chosen as a measure of vibratory excitation and as another indicator of stall flutter. Module vibration levels were also considered, but were not included in the final evaluation because the accelerometer signal traces were illegible on the oscillograph.

[4] Miller and Freund

The total rotor power was measured independently with two separate systems - the main balance frame in the wind tunnel and the torque strain gages on the rotor shaft. The balance frame data proved to be more reliable and was used in the final evaluation. All force and moment data from the balance were reduced to dimensionless coefficients by the standard NASA-Ames data-reduction computer program. Because the test procedure resulted in variations in lift force and propulsive force in contrast to the theoretical work, a profile power coefficient was calculated at each test point from these coefficients. The total power coefficient was modified to yield the profile power coefficient to solidity ratio by means of the following equation.

$$\left(\frac{C_{Q_o}}{\sigma}\right) = \left(\frac{C_Q}{\sigma}\right) - \left(\frac{C_{L_R}}{\sigma}\right)^2 \frac{\sigma}{2\mu} - \left(\frac{C_{X_R}}{\sigma}\right)\mu \qquad (5)$$

Throughout the test program, bending moments were measured at the various spanwise stations shown in Figure 3. The maximum flatwise bending moments were obtained at station 283.64 on the blade. Total vibratory moments were recorded and the peak-to-peak values are reported here because they are used to calculate blade fatigue life. The endurance limit at station 283.64 on the tested CTR blade is $\pm$7730 lb-in. or 15.46 kip-in. peak to peak.

The signals used to measure the pitch-link load were obtained from strain gages on the rotating-star portion of the control swashplate. Total vibratory pitch-link (rotating star) loads were measured at all test conditions and are reported here as peak-to-peak values.

Multiple regression analyses were made of all test data at the various test points. Four independent parameters were selected to represent the control variables in the regression model described by Equation 2. These parameters are the servo flap net collective (δ_o), the servo flap net longitudinal cyclic (δ_{1s}), the servo flap net lateral cyclic (δ_{1c}), and the rotor lift coefficient to solidity ratio (C_{L_R}/σ). The resultant servo flap motions differ from the command inputs because of kinematic coupling at the blade-root end between the blade root motions (feathering and lagging) and the servo flap control commands. Net servo flap angles were measured directly at the flap by a potentiometer; these angles were harmonically analyzed to yield the net values of flap collective and flap cyclic. The rotor lift coefficient to solidity ratio was selected as a parameter of the overall blade lift, representing the influence of blade pitch collective and shaft angles.

Because the propulsive force coefficient to solidity ratio (C_{L_R}/σ) varies with the rotor disc load distribution, it is implicitly included in the regression model through use of the preceding four parameters. The multiple regression equation that was finally chosen as the best model to fit the test data is given in Equation 6. The servo flap deflections used in Equation 6 are the net values measured at the flap.

$$\begin{Bmatrix} \text{BF 283} \\ \text{ROT STAR} \\ C_{Q_0}/\sigma \end{Bmatrix} = \{a_0\} + \{a_1\}\delta_0 + \{a_2\}\delta_{1s} + \{a_3\}\delta_{1c} + \{a_4\}(C_{L_R}/\sigma)$$

$$+ \{a_{11}\}\delta_0^2 + \{a_{22}\}\delta_{1s}^2 + \{a_{33}\}\delta_{1c}^2 + \{a_{44}\}(C_{L_R}/\sigma)^2$$

$$+ \{a_{12}\}\delta_0\delta_{1s} + \{a_{13}\}\delta_0\delta_{1c} + \{a_{23}\}\delta_{1s}\delta_{1c}$$

$$+ \{a_{123}\}\delta_0\delta_{1s}\delta_{1c} \qquad (6)$$

The "a" coefficients enclosed by the braces were obtained through the use of the SURGEN computer code; they vary for each parameter and for each test combination of wind speed and rotor shaft angle. Equation 6 differs from Equation 2 in that all of the interaction terms are not included because the correlation between the regression model and the test data was not significantly improved by carrying the extra interactive terms.

Table 2 summarizes the values of the "a" coefficients at each test condition for the three performance parameters previously discussed. The number of test points and the multiple correlation coefficients for each parameter at each test condition are included in Table 2. Multiple correlation coefficients indicate the degree to which test data points can be predicted by the generated response surface. The correlation coefficients indicate that the twelve regression models can predict the probable values of the dependent variables over the range of test conditions.

Topographic response surfaces are obtained for each parameter by selecting values of the independent variables and exercising each of the twelve regression models. The response surfaces represent the variation of the dependent parameters (horsepower, blade bending moment, pitch-link load) with combinations of servo flap controls. Values of each particular dependent parameter are constant on its respective response surface.

Typical isometric views of the three response surfaces are illustrated in Figure 7. This figure is simplified to show one response surface for each parameter. Multiple response surfaces for each parameter are concentric to those typified in Figure 7 and constitute related quadratic families.

In order to visualize the relationships among the dependent and independent variables, response contours in the $\delta_{1s} - \delta_{1c}$ plane were generated through the use of the PLOPT3 program for profile power coefficient, pitch-link load, and blade flatwise bending moment. The contours were generated from the multiple response surfaces by preselecting values of blade lift coefficient and servo flap collective and varying servo flap cyclic; they represent the intersections of the response surfaces with planes normal to the δ_0 axis. These contours were generated at each test condition for values of blade lift coefficient (C_{L_R}/σ) varying from 0.06 to 0.12 and for values of servo flap collective (δ_0) varying from -2° to +2°. The ranges of the blade lift coefficient and the servo flap collective were chosen to span the test values. Individual response surface contours and superposed surface contours are presented in Figures 8 through 11. Figure 8 shows the variations in the response contours at 80 knots and -5° shaft tilt, Figure 9 shows variations at 120 knots and -5°, Figure 10 shows variations at 120 knots and -8°, and Figure 11 shows variations at 135 knots and -8°.

Because of the assumed quadratic form of the regression model in Equation 6, the response surfaces are conic (spheres, ellipsoids, paraboloids, hyperboloids). Consequently, the response contours of Figures 8 through 11, generated by PLOPT3, are conic. The shape of the contours in these figures are elliptic for the pitch-link load and hyperbolic for the flatwise bending moment at all test conditions, loading conditions, and servo flap collective settings. Contour shapes for the profile power coefficient are elliptic in all figures except for the maximum servo flap collective settings ($\delta_0 = +2°$) in Figure 8. At these collective settings, the character of the response contours changes from elliptic to hyperbolic. The combinations of longitudinal-cyclic and lateral-cyclic servo flap control settings that minimize the elliptical contours in Figures 8 through 11 are obtained from the intersection of their major and minor axes. The orientations of the major axes for the contours of the profile power coefficient are approximately -45° for servo flap collective settings of -2°, and they consistently change to approximately +45° as the servo flap collective is increased to +2°. This orientation change holds at all test conditions. Thus, for negative servo flap collective settings, profile power can be minimized by a mix of right lateral servo flap cyclic angle and aft longitudinal servo flap cyclic angle. For positive servo flap collective settings, minimum profile power is obtained by changing the servo flap cyclic control mix to left lateral cyclic and aft longitudinal cyclic or to right lateral cyclic

and forward longitudinal cyclic. The appropriate servo flap cyclic control mix for positive servo flap collective angles depends on the advance ratio.

The major axes for the pitch-link load (rotating star) elliptic contours remain fixed at approximately -45°. Thus, pitch link loads can be minimized at all servo flap collective angles by a mix of right lateral servo flap cyclic and aft longitudinal servo flap cyclic. The appropriate servo flap cyclic control mix to minimize pitch link load depends on the advance ratio.

In order to minimize the hyperbolic contours which represent the blade flatwise bending moments, the servo flap cyclic controls, as predicted by the response surfaces, would have to be extrapolated to large flap angles, beyond the range of valid test data. Consequently, it was decided to optimize each of the hyperbolic contours by selecting the servo flap cyclic controls obtained from the intersections of the hyperbolic asymptotes. These intersections are the saddle points of the hyperbolic response surfaces and fall within the range of valid test data. The saddle points for the hyperbolic response surfaces occur at right lateral servo flap cyclic control angles in combination with small amounts of forward or aft longitudinal servo flap cyclic control angles depending on the advance ratio and blade lift.

An examination of the response contours shows that for a given combination of advance ratio, shaft angle, blade lift, and servo-flap collective, each parameter minimizes at different combinations of servo flap cyclic controls. Consequently, a procedure was established to optimize the individual parameters by overlapping their response contours and defining a region of acceptable operation. The acceptable operating regions for the combined contours are shaded in Figures 8 through 11. The objectives arbitrarily selected for this optimization procedure were to simultaneously minimize profile power and rotating star load while maintaining blade stress levels, which would assure no cumulative fatigue damage to the blade. A survey of the optimum areas in Figures 8 through 11 shows that during the tests the vibratory bending moments never exceeded the endurance limit of 15.46 kip-in. established for this blade. Consequently, the minimum profile power and the minimum pitch-link load defined the optimum combinations for the net servo flap position.

At each combination of velocity and shaft angle, the shaded optimization areas can be compared at each level of blade loading to determine the absolute values of servo flap collective that will yield the largest allowable combination of operational cyclic flap controls, i.e., the largest optimization areas. An in-depth review of Figures 8 through 11 shows that, at blade loading coefficients of 0.06, the largest optimum area occurs at -2° servo flap collective. As blade loading is increased to 0.12, the servo flap collective setting for optimum operation increases to +1°. This trend holds at all tested advance ratios and shaft angles.

The approximate centers of the shaded areas define the appropriate mixes of longitudinal cyclic and lateral cyclic servo flap controls for optimizing the selected rotor parameters. Figures 8 through 11 show that these cyclic control combinations vary with each combination of test condition, blade loading, and servo flap collective. The centers of the shaded optimization areas for Figure 8 shift from a forward-longitudinal cyclic ($+\delta_{1s}$) and right-lateral cyclic ($+\delta_{1c}$) at $\delta_0 = -2°$ to aft-longitudinal cyclic and left-lateral cyclic at $\delta_0 = +2°$. This cyclic-control phase shift holds at all blade loadings for an advance ratio of 0.22 and a shaft angle of -5°. Figures 9 and 10 show the phase shift in servo flap cyclic at advance ratio 0.33 for two different shaft angles, -5° and -8°. In Figures 9 and 10, the centers of the shaded areas indicate that the longitudinal cyclic control shifts from forward to aft as servo flap collective is increased from -2° to +2°. Lateral control at this advance ratio remains at a constant level of right-lateral cyclic. The shift in cyclic phasing with collective at advance ratio 0.33 repeats consistently at all tested levels of blade loading. Figure 11 defines the cyclic control combinations required at an advance ratio of 0.366 and a shaft angle of -8°. At this test condition, the optimization area centers vary from forward-longitudinal cyclic and right-lateral cyclic at -2° servo flap collective to approximately zero cyclic at +2° collective. This trend holds at all blade loading values. Generally, less cyclic amplitude is required at all advance ratios with increasing collective because the increased collective twists the blade negatively. Thus, the periodic aerodynamic forces acting on a highly twisted, torsionally soft blade twist the blade cyclically, thereby relieving the cyclic duty of the servo flap. However, the absolute values of the parameters selected for optimization are not always at their minimum levels for positive servo flap collective. Thus, it can be concluded that both collective and cyclic servo flap controls are required to operate the CTR efficiently at various test conditions.

Figures 8 and 9 can be compared with Figures 10 and 11 to show the influence of advance ratio at constant levels of shaft angle. Each pair of figures illustrates that the allowable ranges of servo flap cyclic for optimum conditions are reduced as the advance ratio is increased. Although the shaded areas appear to differ when comparing Figures 8 with 9 or Figures 10 with 11, the absolute levels of parameters defining the optimization area boundaries differ between these figures. The advance ratio has little apparent influence on servo flap collective requirements.

The effects of rotor shaft angle on optimization areas and servo flap control settings are obtained by comparing Figures 9 and 10. A detailed comparison of the combined contours in these two figures reveals that the servo flap control combinations for optimum operation are insensitive to the shaft-angle variations tested. However, the absolute levels of the selected optimization parameters vary with increased forward shaft

tilt, i.e., from -5° to -8°. For example, the profile power coefficient decreases with forward shaft tilt whereas the pitch-link load and the blade flatwise bending moment increase with forward tilt.

Overall CTR performance can be reduced to its essence by cross-plotting the levels of data defined by the optimum control areas. Figure 12 summarizes these data, which are plotted against blade loading for the four test conditions. Shown in Figure 12 are the optimized values of profile power coefficient and pitch-link load with the associated values of vibratory blade bending moment. Superposed onto Figure 12 are isoclines of the servo flap collective angle, which illustrate the required variation in the servo flap collective required for operation at optimum conditions. The cyclic control requirements can be obtained by referring to the appropriate optimization contours for each test condition, each blade-loading coefficient, and the indicated servo flap collective setting. An evaluation of Figure 12 shows that no sharp rise is evident in the profile power coefficient or in the pitch-link load, thereby indicating stall avoidance for the test rotor. Furthermore, the variations of the servo flap collective settings affect the optimization parameters at all levels of blade loading and in all test conditions, especially at loading conditions where the rotor would normally be stalled (above $C_{L_R}/\sigma = 0.10$).

Further demonstration of CTR stall avoidance is shown in Figure 13, where profile power coefficients for the CTR are compared to those of the H-34 at similar advance ratios, shaft angles, and advancing-tip Mach numbers. Both rotors have the same diameter and blade chord, and both were tested in the same facility. Results of the H-34 tests are reported in References 5 and 6. Comparisons between CTR data and H-34 data at other test conditions could not be made because there are no other directly comparable test conditions.

As seen in Figure 13, the CTR test data are reported for an advance ratio that is 10 percent higher than the data on the H-34 (0.33 vs 0.30), whereas the advancing tip Mach number is 8 percent lower (0.68 vs 0.74). The airfoil used for the CTR is a modified NACA 23012 and, for the H-34, is a NACA 0012. In order to eliminate any bias in the data due to these differences, their influences on rotor stall characteristics were

---

[5] V. M. Paglino and A. H. Logan, AN EXPERIMENTAL STUDY OF THE PERFORMANCE AND STRUCTURAL LOADS OF A FULL-SCALE ROTOR AT EXTREME OPERATING CONDITIONS, USAAVLABS Technical Report 68-3, U. S. Army Aviation Materiel Laboratories, Fort Eustis, Virginia, July 1968, AD 674187.

[6] J. L. McCloud, III, J. C. Biggers, and R. H. Stroub, AN INVESTIGATION OF FULL-SCALE HELICOPTER ROTORS AT HIGH ADVANCE RATIOS AND ADVANCING TIP MACH NUMBERS, NASA Technical Note D-4632, NASA-Ames Research Center, Moffett Field, California, July 1968.

estimated. Because the retreating-blade stall characteristics are insensitive to advancing-tip Mach number, it was assumed that the retreating blade stall boundary would be influenced only by advance ratio differences and airfoil contour differences. The higher advance ratio for the CTR was estimated to decrease the level of C_{L_R}/σ at stall by 0.004. This reduction was estimated from a stall boundary that was experimentally determined by full-scale rotor tests in the Ames 40- x 80-foot wind tunnel, as reported in Reference 7. The camber differences in airfoil contour were estimated to increase the level of C_{L_R}/σ at stall by 0.014. This increase was also estimated from a stall boundary that was experimentally determined by full-scale rotor tests in the same facility and is reported in Reference 8. Thus, the CTR could be expected to operate at a C_{L_R}/σ that is 0.010 higher than that of an H-34 rotor due to the differences in camber and advance ratio. The CTR built-in twist distribution is equivalent to -6.6° over the outboard half of the blade span compared to built-in twist distributions of 0° and -8° for the experimental H-34 rotors. No attempt was made to estimate the variation of blade loading at stall due to these twist differences because the data for all three configurations are compared directly in Figure 13.

As seen in Figure 13, the CTR test demonstrator was able to reach blade-lift coefficients that are 20 percent higher than those of either H-34 rotor with no discontinuity in the power curve. Higher blade-lift coefficients can be achieved for the CTR if the operating limits on the lag dampers are expanded. The comparison of the profile power coefficients in Figure 13 verifies the anticipated performance improvements due to stall relief. Although part of this stall relief is due to camber and advance-ratio effects as discussed previously, the remaining performance improvement increment can only be attributed to controlling the twist and, subsequently, the airload distributions of the CTR blades.

---

[7] J. L. McCloud, III and G. B. McCullough, COMPARISON OF CALCULATED AND MEASURED STALL BOUNDARIES OF A HELICOPTER ROTOR AT ADVANCE RATIOS FROM 0.3 TO 0.4, NASA Technical Note D-73, NASA-Ames Research Center, Moffett Field, California, September 1959.

[8] J. L. McCloud, III and G. B. McCullough, WIND-TUNNEL TESTS OF A FULL-SCALE HELICOPTER ROTOR WITH SYMMETRICAL AND WITH CAMBERED BLADE SECTIONS AT ADVANCE RATIOS FROM 0.3 TO 0.4, NACA Technical Note 4367, NASA-Ames Research Center, Moffett Field, California, September 1958.

At low values of blade loading, the CTR test demonstrator required more profile power than the H-34 rotor. The difference in power was caused by two separate effects, both of which are the direct results of using existing hardware on the test rotor. One of these effects results from the use of external support brackets and trailing servo flaps in the outboard blade region. The second effect is caused by the thick, blunt-edge shank sections in the blade root region. The decision to use this existing hardware was made in order to provide a valid technology demonstrator at minimum overall program cost.

One series of wind-tunnel tests on the CTR was run to quantify the power that can be attributed directly to the external support brackets and the trailing servo flaps. The servo flaps and the support brackets were removed from the CTR, and the outboard airfoil sections at the support bracket stations were faired to be aerodynamically clean. The resulting configuration was tested, and its profile power coefficient is plotted in Figure 13. As seen in this figure, approximately 35 percent of the power difference at 120 knots can be attributed to the trailing servo flaps and the external support brackets.

In order to resolve the remaining difference in profile power, an analysis was performed to determine if the source was the aerodynamically inefficient blade grip and shank region. The area under consideration includes the blade grip section beginning at the point where the grip attaches to the H-34 hub and continues to transition to the spanwise station where a reasonably complete airfoil section is developed. This distance represents blade radii from station 28 to station 105. Representative cross-sections of the blade up to radial station 45.5 are shown in Figure 14. The CTR technology demonstrator blade shanks were unnecessarily thick and blunt because the root-end configuration was a carryover from the HH-43 blade which was designed to take the high bending moments carried by teetering rotors. The HH-43 blade grip was also closer to the shaft centerline than the CTR blade grip so that its aerodynamic penalties were not pronounced. The aerodynamic efficiency of the CTR inboard region can be improved significantly by reducing the blade-spar thickness and by rounding the leading edge to duplicate the H-34 D-spar geometry. Effective lift and drag coefficients for the CTR-blunted region were estimated from References 9-12 and were used in Kaman's 6F airloads program. Power

---

[9] N. K. Delany and N. E. Sorensen, LOW-SPEED DRAG OF CYLINDERS OF VARIOUS SHAPES, NACA Technical Note 3038, Ames Aeronautical Laboratory, Moffett Field, California, November 1953.

[10] L. W. McKinney, EFFECTS OF FINELESS RATIO AND REYNOLDS NUMBER ON THE LOW-SPEED CROSSWIND DRAG CHARACTERISTICS OF CIRCULAR AND MODIFIED SQUARE CYLINDERS, NASA Technical Note D-540, Langley Research Center, Langley Field, Virginia, October 1960.

[11] S. F. Hoerner, FLUID-DYNAMIC DRAG, Published by the Author, 1965.

[12] S. F. Hoerner and H. V. Borst, FLUID-DYNAMIC LIFT, Published by the Authors, 1975.

calculations were made of the CTR using these data at wind speeds of 80 knots and 120 knots. These calculated power coefficients were compared to the power coefficients calculated at the same control settings from previous 6F analyses on the CTR, which had used lift and drag coefficient data from D-spar wind-tunnel tests. The D-spar data are reported in Reference 13 and represent data obtained on the H-34 blade spar.

Calculated differences in the C_{Q_o}/σ of the CTR test rotor due to the blunt-edge shank region are .00049 at 80 knots and .00108 at 120 knots. These differences are direct results of a greater H-force than originally anticipated and do not accrue from a larger rotational drag of the blade shanks. Supplementary tests conducted on the CTR and the H-34 blade shanks, subsequent to the currently reported wind-tunnel tests, verify that at least half the remaining profile power coefficient increment results from the aerodynamic inefficiencies of the CTR inboard profiles.

The calculated profile power difference at 120 knots was subtracted from the CTR test data obtained without external servo flaps. The resultant CTR power curve, shown in Figure 13, compares favorably with the H-34 profile power curve. Thus, the differences observed between the CTR and the H-34 profile power coefficients can be attributed completely to the aerodynamic inefficiencies of the test hardware and are not related to the operational principles of the CTR.

For an advanced CTR design, the aerodynamic efficiency of the servo flap region can be improved by fairing the servo flap within the airfoil contour, thereby eliminating external protuberances. Greater leverage to twist the blade can be obtained from the faired flap by designing a swept-tip configuration with an aileron-type flap to provide chordwise offset. The benefits to be gained by using a thin, swept-tip, faired servo flap include reduced noise and the ability to operate at increased advancing tip Mach numbers. An equivalent profile power coefficient for an advanced CTR design can be estimated from the data shown in Figure 13. The equivalent profile power coefficient for a CTR with faired servo flaps and a low profile shank is compared in Figure 15 to the H-34 power curve. The advantages of aerodynamic improvements such as those described above are immediately obvious. Equally obvious are the significant improvements in CTR performance over conventional rotor performance.

---

[13] W. H. Tanner, CHARTS FOR ESTIMATING ROTARY WING PERFORMANCE IN HOVER AND AT HIGH FORWARD SPEEDS, NASA Contractor Report CR-114, NASA Hq, Washington, D. C., November 1964.

COMPARISONS OF TEST WITH THEORY

An in-depth analysis that was performed to evaluate rotor performance and blade dynamic behavior of an early CTR configuration was reported in Reference 1. The configuration and the operating conditions reported in that reference differ significantly from the CTR technology demonstrator reported herein so that a direct comparison cannot be made between the results of that initial study and the results of the current test program.

During the design phase of the technology demonstrator, aeroelastic analyses were conducted to substantiate the design and to define the ranges of servo flap controls required for optimum operation. The aeroelastic analyses were made at wind speeds of 80, 120, 150, and 170 knots, and at a tip speed of 614 fps. The CTR was analyzed at these wind speeds for two levels of vertical force, 11,500 lbs and 13,500 lbs, and sufficient propulsive force at each wind speed to fly a helicopter with an equivalent flat-plate drag area (20 square feet). As noted previously, the wind-tunnel tests were conducted at wind speeds of 80, 120, 135, and 155 knots, and at a tip speed of 585 fps. Because of the nature of wind-tunnel testing, the CTR was tested at many levels of vertical force and propulsive force, none of which are exactly comparable to the substantiating aeroelastic analyses previously conducted. Consequently, only general comparisons can be made at this time between test data and theoretical predictions.

The optimization procedures developed during the design phase of the program provided valuable insights into the definitions of the ranges of control variables to be investigated. The analyses indicate that servo flap control settings for optimum performance occur at the low collective values combined with forward-longitudinal cyclic and right-lateral cyclic at the flap. Changing the servo flap from negative collective (trailing edge up) to positive collective (trailing edge down) reduces the amount of longitudinal and lateral cyclic required. Positive servo flap collective ($+\delta_0$) twists each blade negatively (blade leading edge down) and negative servo flap collective twists each blade positively (blade leading edge up). Right-lateral cyclic ($+\delta_{1c}$) on the servo flap twists the trailing blade negatively and the forward blade positively. (The trailing blade is at zero azimuth.) Forward longitudinal cyclic ($+\delta_{1s}$) on the servo flap twists the advancing blade negatively and the retreating blade positively. At fixed values of root collective and servo flap collective, more servo flap cyclic is required with increased advance ratio. The optimization trends predicted by analysis are supported by test results, as seen in Figures 8 to 11. A comparison of the predicted absolute levels of the controls with the measured control values for optimum performance at 120 knots indicates that the servo flap collective

[1] Lemnios and Smith

and the cyclic controls agree to within one degree of the predicted values. Thus, the CTR theory can predict control levels accurately.

Predictions of rotor performance indicated that contours of rotor power, maximum blade section angle of attack, and maximum blade vibratory bending moments optimized at servo flap control settings that were not always compatible. For example, minimum power was predicted to occur at servo flap cyclic control settings that resulted in increased angles of attack and increased blade bending moments. In contrast to the predicted optimization trends, the test results optimize more compatibly. As seen in Figures 8 through 11, response contours of the rotor profile power and the pitch-link load (an indirect measure of the angle of attack) are more concentric with each other than were the predicted contours. Further, maximum blade bending moment contours have shallow gradients and do not influence the optimization area defined by the profile power and the pitch-link loads. Because the combined parametric response contours are concentric, the controls necessary to optimize the individual responses are compatible with each other and thereby provide a broader range of allowable control settings. Thus, the servo flap control settings required to minimize power also tend to minimize pitch-link load and do not significantly increase blade vibratory bending moments.

VALIDATION OF PREVIOUSLY PREDICTED CRITERIA

The analytical investigation reported in Reference 1 established the benefits to be expected from a near-optimum configuration of a CTR. The primary benefit was derived by redistributing blade airloads radially and azimuthally through blade twist control so that the CTR can carry a 30-percent-higher blade loading than an equivalent conventional rotor without stalling. This allows lower solidity, smaller diameter rotors, reduced installed power, and smaller helicopters to perform the missions now performed with helicopters with conventional rotor systems. Conversely, CTR designs that are geometrically sized to be equivalent to conventional rotors have 30-percent greater load capacities than their conventional counterpart. An additional benefit derived from the blade load redistribution was an increased CTR blade life which resulted from the 20 to 30 percent reduction in the blade vibratory bending moments.

[1] Lemnios and Smith

The present work utilized a CTR configuration that was less than optimum because of the necessity for making the maximum use of proven rotor components to keep program costs at a reasonable level. Analysis of the demonstrator configuration established new predictions of performance improvements using the H-34 rotor as a baseline for comparison. These predictions, which establish the criteria for the wind-tunnel demonstrator, reconfirmed the Reference 1 analysis with regard to rotor performance improvements and blade vibratory bending moments from blade load redistributions.

Results of the wind-tunnel test program further substantiate the predicted criteria by demonstrating that the CTR achieved blade loadings 20 percent higher than the H-34 rotor. The vibratory blade bending moments and pitch-horn loads of these two rotor systems were not compared because the appropriate data were not available.

[1] Lemnios and Smith

CONCLUDING REMARKS

The objectives of the full-scale controllable twist rotor wind-tunnel test program were to generate information that would relate to predictions and to provide a data base for advancing the state of the art. Defined goals were specified at the outset and were used as a checklist to measure the success of the test results. The goals are reviewed below:

- Demonstrate the CTR principle through the use of existing hardware.
- Establish functional relationships between rotor performance, blade vibratory loads, and control settings.
- Provide a firm data base for future tests over an expanded test envelope.
- Correlate test results with predictions.
- Compare the test results with previously tested rotors.

Conclusions reached during the CTR wind-tunnel test program are summarized below.

1. Rotor stall was alleviated at all test conditions. Stall alleviation demonstrates the CTR principle of improved rotor performance by redistributing the airloads to reduce local angles of attack. This result verifies the performance characteristics predicted by Kaman's 6F aeroelastic analysis.

2. Comparisons of the CTR and the H-34 performances indicate that the CTR can operate to blade loadings that are 20 percent higher than the H-34 without encountering stall.

3. Both collective and cyclic servo flap controls are required to operate the CTR efficiently at the various test conditions.

4. The existing test hardware represents a satisfactory configuration for demonstrating CTR technology and defining a data base for additional wind-tunnel testing. However, the existing configuration is not suitable for flight testing.

5. Trailing servo flaps with external support brackets are not suitable for high-performance rotors.

6. Functional relationships were defined between rotor performance, blade vibratory loads, and combinations of dual-control settings using optimization procedures that were developed during the program.

7. Optimization trends for control combinations are similar to those predicted by analysis.

8. Rotor performance parameters optimize more compatibility than predicted by analysis so that the allowable range of control settings is broader than predicted for optimized performance.

9. Torsional response of the CTR configuration tested is stable at all tested conditions and can be effectively controlled by the pitch-horn and servo flap systems at all conditions to improve rotor performance.

10. Servo flap collective and cyclic controls for optimum CTR performance have been verified by test results to within one degree of their predicted levels.

The following recommendation is made:

Design an advanced technology CTR for flight test using data resulting from the wind-tunnel demonstrator test program. Analysis of the flight test blade will use the same techniques validated by the wind-tunnel program. As discussed in the text, performance penalties resulting from the trailing servo flap and inefficient blade grip dictate that the flight-test blade design should feature a swept tip with an aileron-type flap and aerodynamically suitable blade retentions.

TABLE 1 . RANGES OF TEST CONTROL VARIABLES.

ΩR = 585 ft/sec

V	α_s	θ_o	δ_o / δ_{1s} / δ_{1c}
80 kts	-5°	+ 8°	-4° → 0°/ -3° → + 3°/ -2° → + 4°
		+10°	-3° → 0°/ -3° → + 3°/ -2° → + 4°
		+11°	-3° → 0°/ 0° → + 6°/ 0° → + 6°
120 kts	-5°	+ 8°	-4° → +2°/ -3° → + 6°/ 0° → + 6°
		+10°	-4° → 0°/ +2° → + 6°/ +2° → + 6°
		+12°	-4° → 2°/ -3° → + 6°/ 0° → + 6°
120 kts	-8°	+10°	-4° → 0°/ 0° → + 6°/ 0° → + 6°
		+12°	-4° → 0°/ 0° → + 6°/ 0° → + 6°
		+14°	-2° → +1°/ 0° → + 6°/ 0° → + 6°
135 kts	-8°	+10°	-2° → 0°/ 0° → + 6°/ 0° → + 6°
		+12°	-2° → +1°/ 0° → + 6°/ 0° → + 6°
		+14°	-2° → +1°/ 0° → + 6°/ 0° → + 6°
155 kts	-5°	+10°	-6° → -2°/ +4° → + 8°/ +2° → + 5°
		+12°	-2°/ + 4° / + 2°
155 kts	-8°	+13°	0°/ 0° → +2°/ 0° → + 6°

TABLE 2 . REGRESSION MODEL USED TO GENERATE CONTOUR PLOTS.

EQUATION FORM:

$$Y = a_0 + a_1 \delta_0 + a_2 \delta_{1s} + a_3 \delta_{1c} + a_4 (C_{L_R}/\sigma) \times 10.0$$
$$+ a_{11} \delta_0^2 + a_{22} \delta_{1s}^2 + a_{33} \delta_{1c}^2 + a_{44} (C_{L_R}/\sigma)^2 \times 100.0$$
$$+ a_{12} \delta_0 \delta_{1s} + a_{1s} \delta_0 \delta_{1c} + a_{23} \delta_{1s} \delta_{1c} + a_{123} \delta_0 \delta_{1s} \delta_{1c}$$

TEST PARAMETER	REGRESSION COEFFICIENTS	TEST CONDITIONS V = 80 kts α_s = - 5°	V = 120 kts α_s = -5°	V = 120 kts α_s = -8°	V = 135 kts α_s = -8°
Blade	a_0	3.2397	1.0778	3.2770	2.1739
Flatwise	a_1	-0.0627	-0.1014	-0.2572	-0.4409
Bending	a_2	-0.0700	-0.1966	-0.1430	-0.2872
Moment	a_3	-0.0387	0.0911	0.1436	0.2319
Sta. 283	a_4	-4.6079	2.0942	-3.2284	0.1072
(BF 283)	a_{11}	0.0097	0.0334	0.0106	0.0196
kip-in	a_{22}	0.0036	0.0170	0.0071	0.0238
	a_{33}	0.0003	-0.0108	-0.0089	-0.0101
	a_{44}	4.1484	0.7631	3.8383	2.7790
	a_{12}	0.0184	0.0344	0.0332	0.0684
	a_{13}	0.0068	-0.0278	0.0157	0.0200
	a_{23}	0.0043	-0.0064	-0.0145	-0.0293
	a_{123}	-0.0007	0.0013	-0.0050	-0.0076
MULTIPLE CORRELATION COEFFICIENTS		0.975	0.965	0.970	0.959
NO. OF TEST POINTS USED		59	84	60	131

TABLE 2. (Continued)

TEST PARAMETER	REGRESSION COEFFICIENTS	TEST CONDITIONS V = 80 kts α_s = -5°	V = 120 kts α_s = -5°	V = 120 kts α_s = -8°	V = 135 kts α_s = -8°
Rotating Star Loads (Rot Star) lbs x 10^{-2}	a_0	7.6281	1.8650	5.0761	2.2314
	a_1	-0.4094	-0.1597	-0.1346	-0.4671
	a_2	0.0477	-0.1817	-0.1152	-0.1422
	a_3	-0.0436	-0.2138	-0.2385	-0.0568
	a_4	18.4338	-0.7791	-7.7401	-1.3467
	a_{11}	-0.0300	0.0566	0.0586	-0.0018
	a_{22}	0.0221	0.0538	0.0387	0.0397
	a_{33}	0.0221	0.0447	0.0529	0.0406
	a_{44}	11.0156	1.2808	5.2445	2.4259
	a_{12}	0.0688	0.0929	0.0882	0.1076
	a_{13}	0.0367	-0.0500	-0.0374	-0.0002
	a_{23}	-0.0202	-0.0322	-0.0342	-0.0556
	a_{123}	-0.0017	0.0035	-0.0025	-0.0073
MULTIPLE CORRELATION COEFFICIENTS		0.893	0.893	0.854	0.882
NO. OF TEST POINTS USED		59	84	60	131

TABLE 2. (Concluded)

TEST PARAMETER	REGRESSION COEFFICIENTS	TEST CONDITIONS V = 80 kts α_s = -5°	V = 120 kts α_s = -5°	V = 120 kts α_s = -8°	V = 135 kts α_s = -8°
Blade Profile Power Coefficient ($C_{Q_{o/\sigma}} \times 10^2$)	a_o	0.4594	0.3821	0.3168	0.5380
	a_1	-0.0013	0.0010	-0.0060	-0.0020
	a_2	-0.0008	-0.0017	-0.0071	-0.0041
	a_3	-0.0006	-0.0030	-0.0072	0.0008
	a_4	-0.6005	-0.3880	-0.2242	-0.6479
	a_{11}	0.0013	0.0022	-0.0002	0.0059
	a_{22}	0.0009	0.0011	0.0013	0.0014
	a_{33}	0.0006	0.0008	0.0012	0.0008
	a_{44}	0.3261	0.3937	0.3034	0.6221
	a_{12}	0.0012	0.0020	0.0005	0.0029
	a_{13}	0.0009	-0.0005	-0.0010	-0.0009
	a_{23}	0.0006	0.0004	0.0010	-0.0003
	a_{123}	0.0005	0.0006	0.0007	0.0006
MULTIPLE CORRELATION COEFFICIENTS		0.808	0.956	0.890	0.908
NO. OF TEST POINTS USED		59	84	60	131

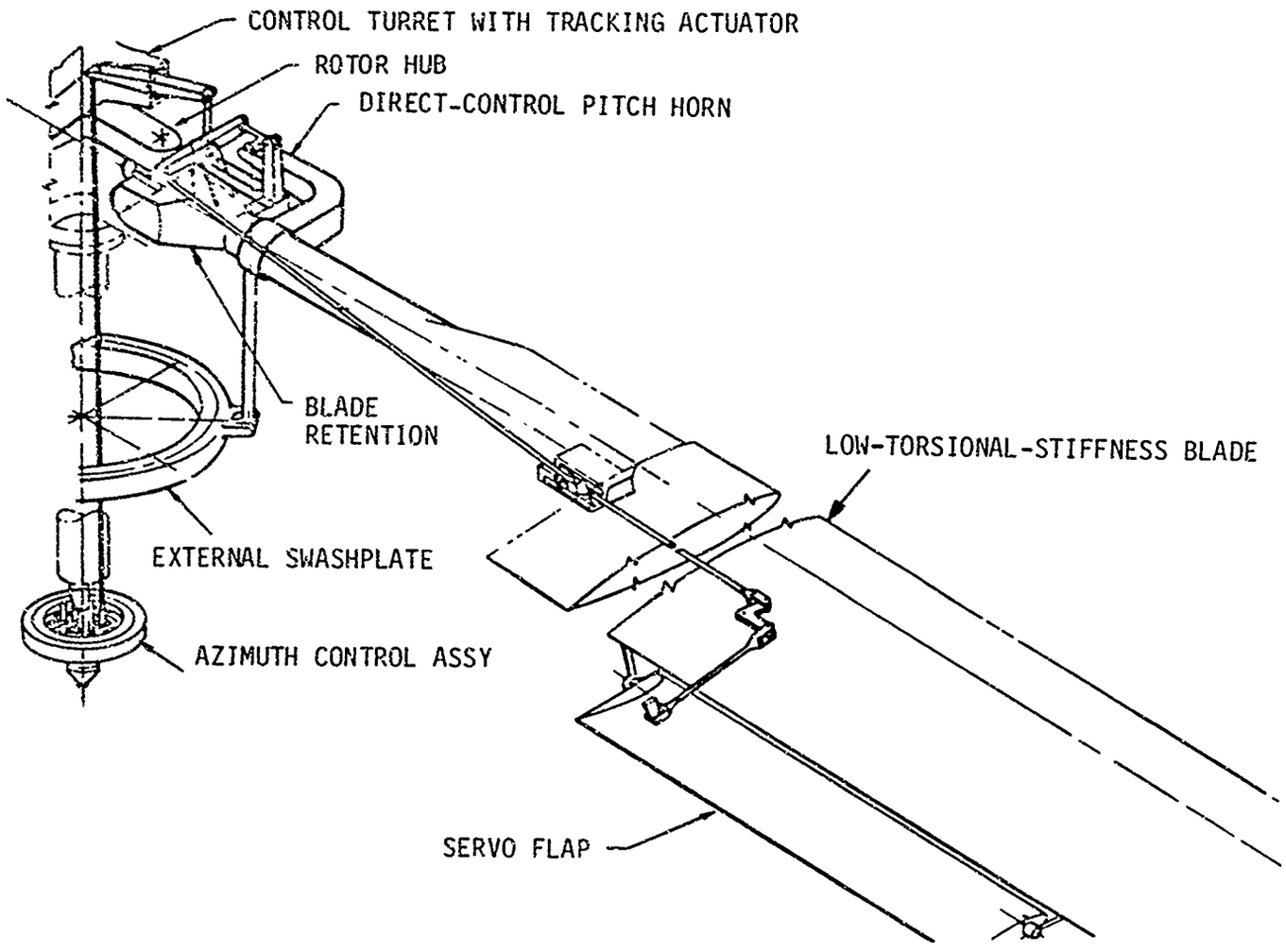

Figure 1. Control Arrangements for the Controllable Twist Rotor

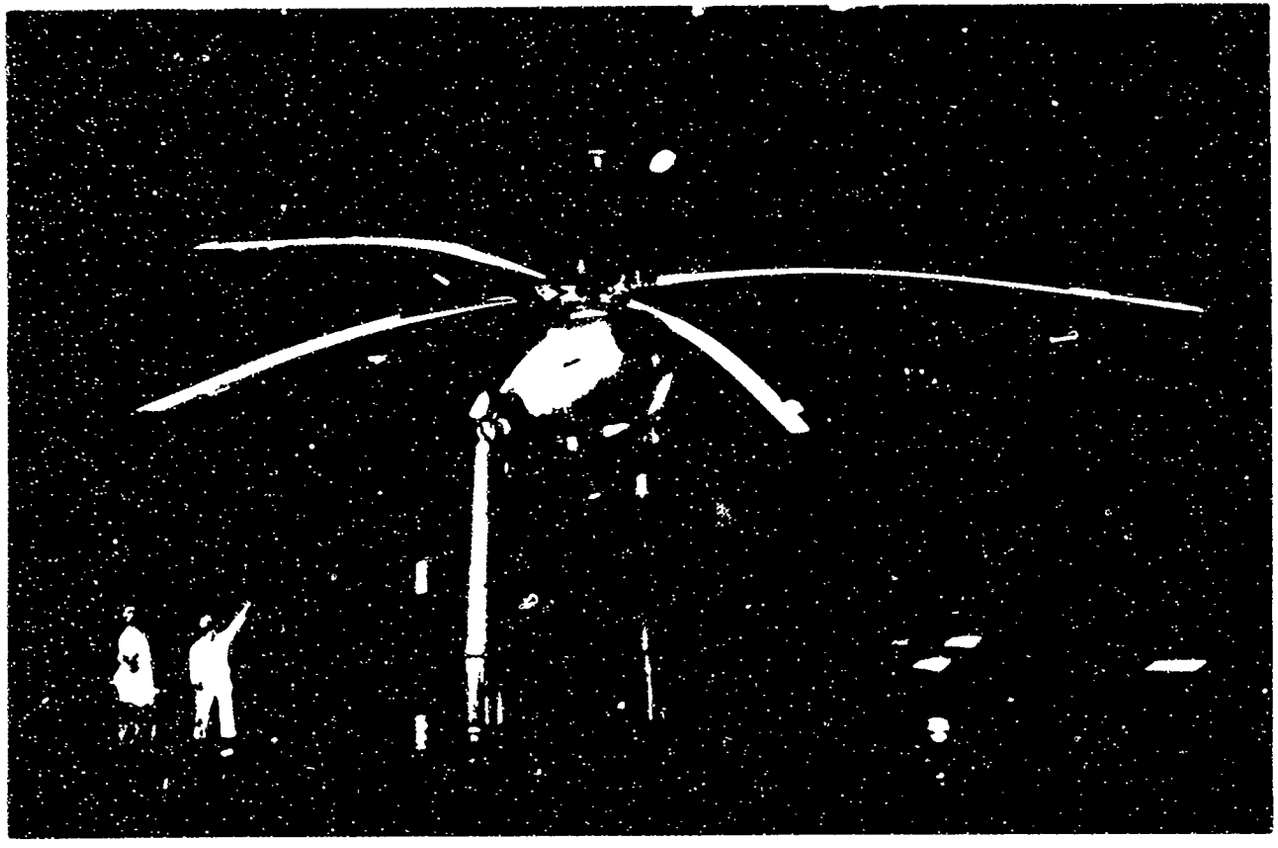

Figure 2. Controllable Twist Rotor Installed in 40- x 80-Foot Wind Tunnel

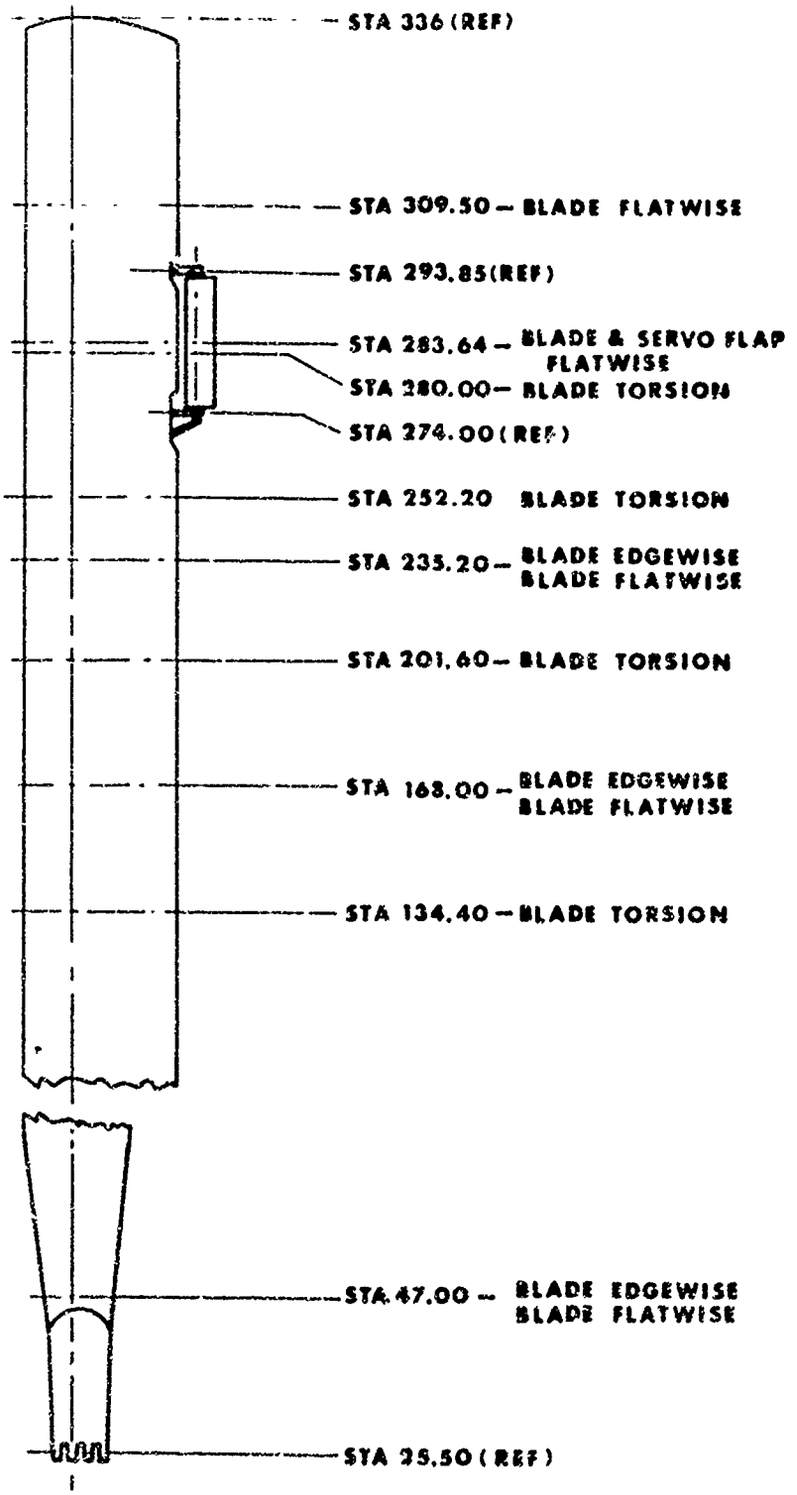

Figure 3. CTR Blade Strain-Gage Locations

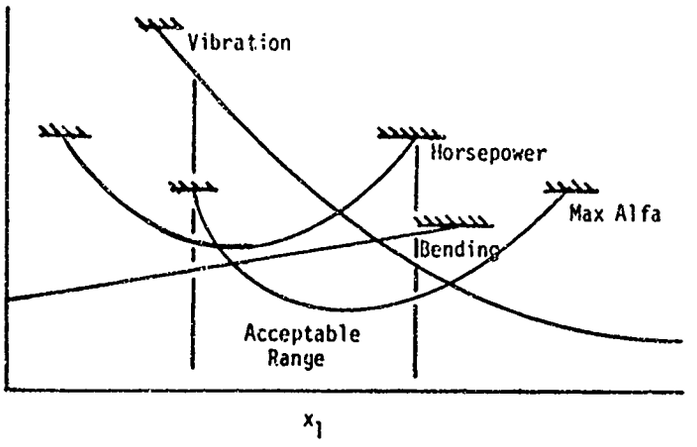

a. Single Variable

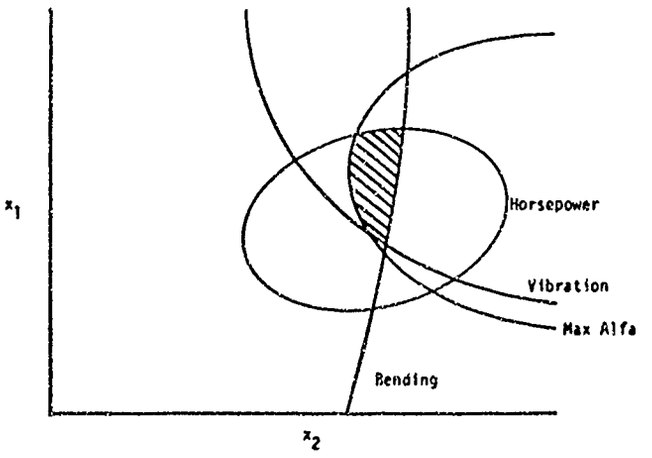

b. Two Variables

Figure 4. Response Surface Presentation

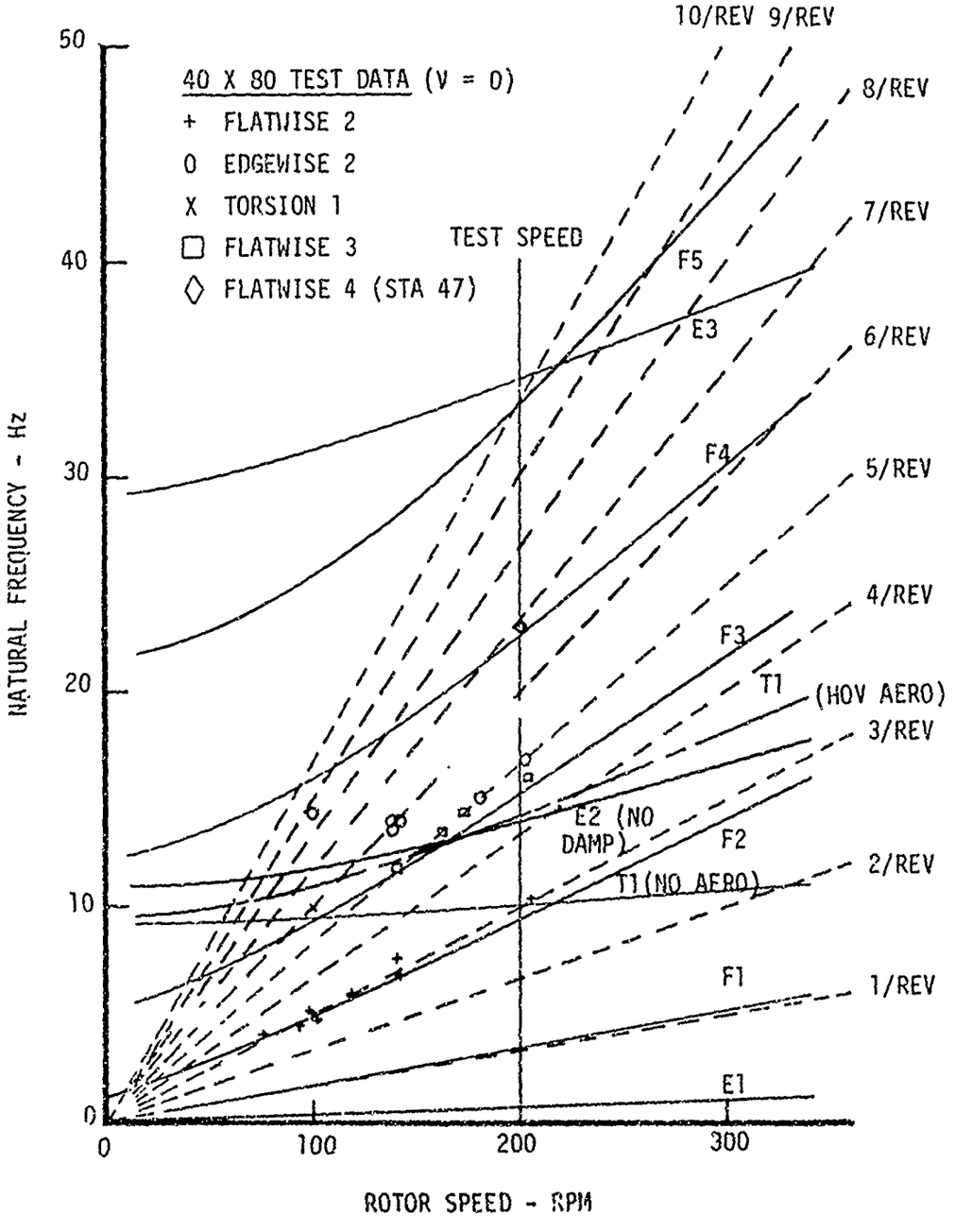

Figure 5 . CTR Uncoupled Natural Frequencies

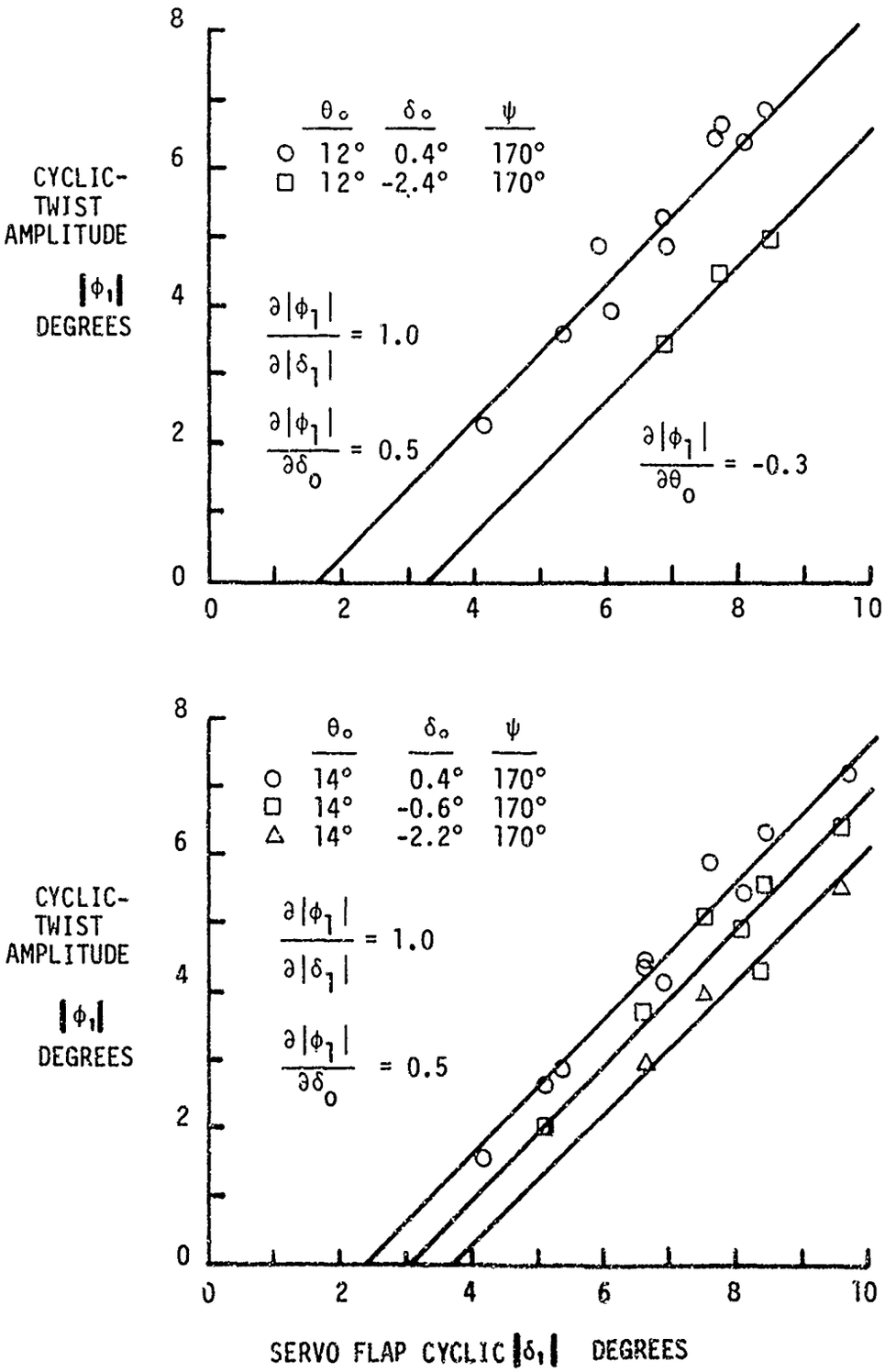

Figure 6. Cyclic-Twisting Responses ($V/\Omega R = 0.366$, $\alpha_s = -8°$)

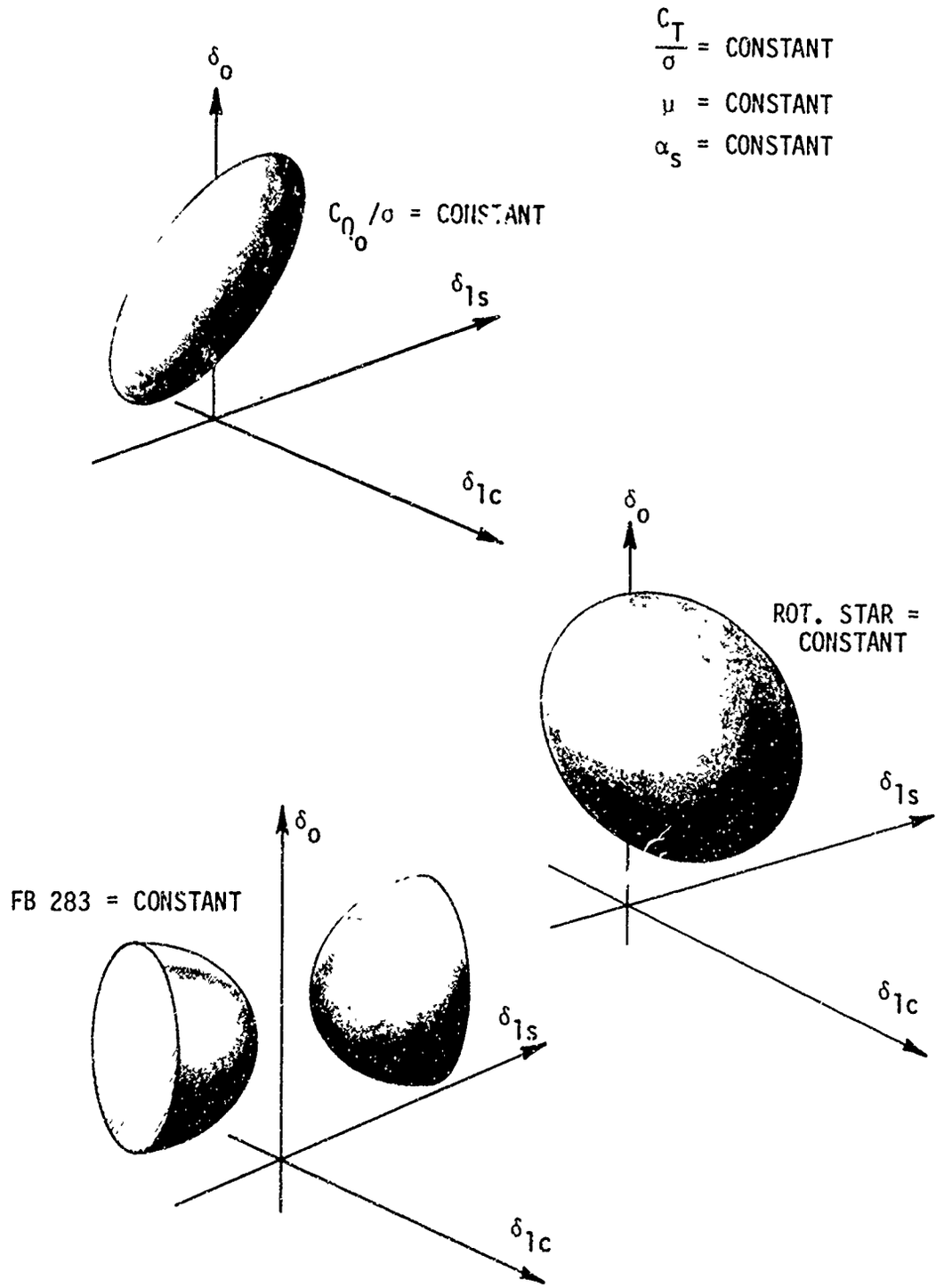

Figure 7. Typical Response Surfaces of CTR Test Data

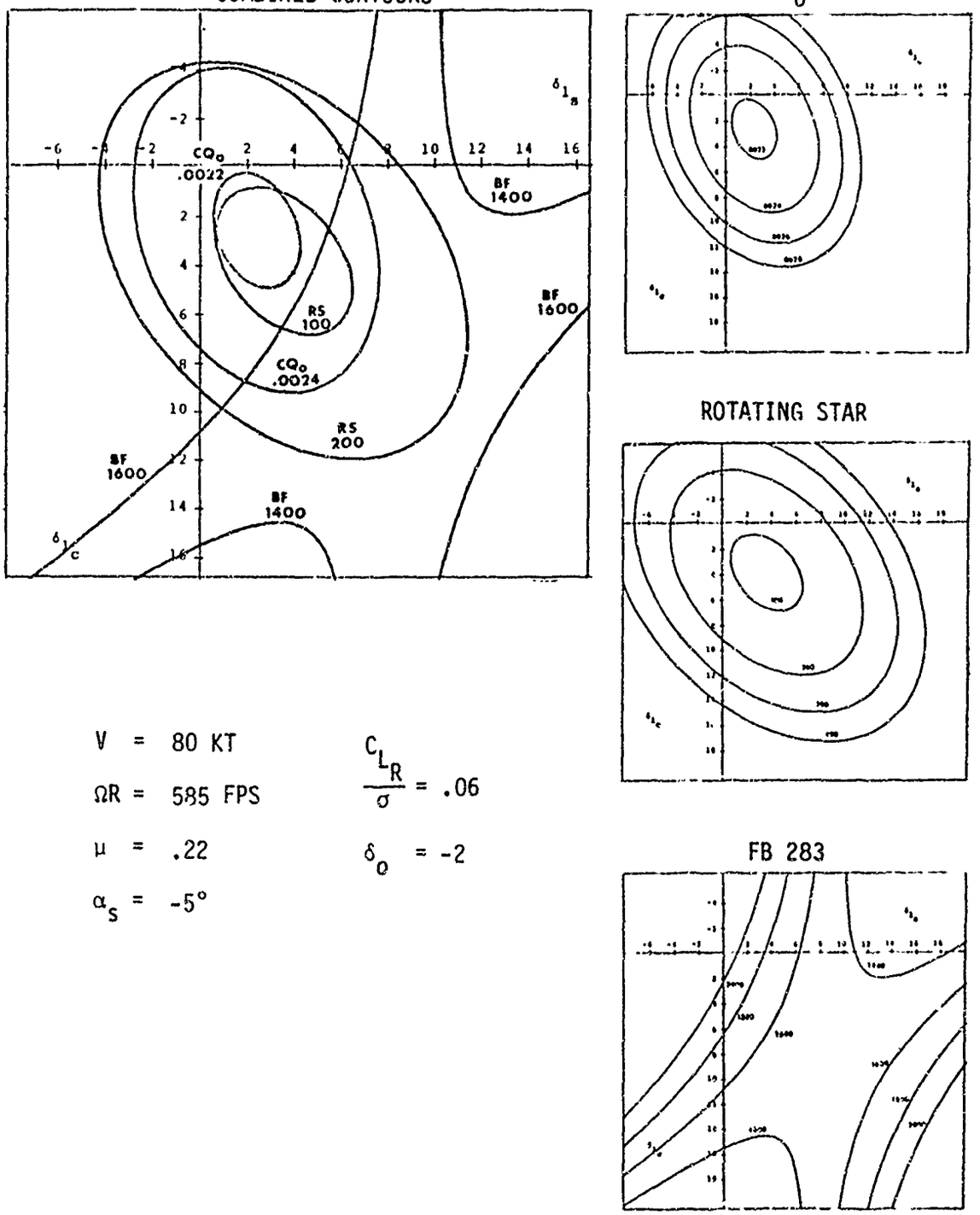

Figure 8. Optimization Response Contours at 80 Knots and -5° Shaft Tilt

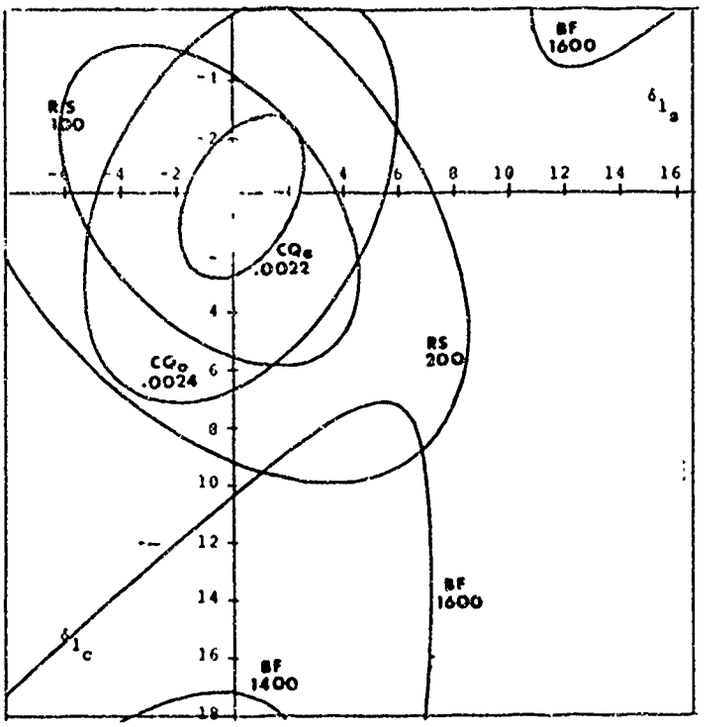

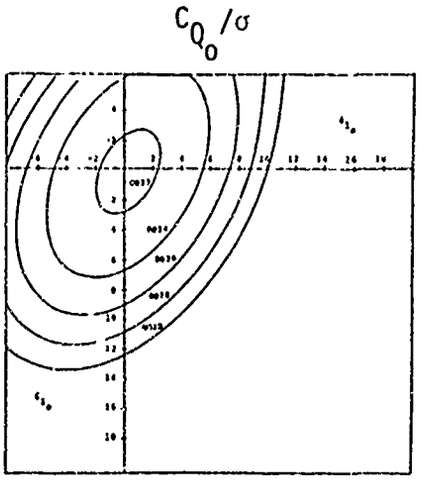

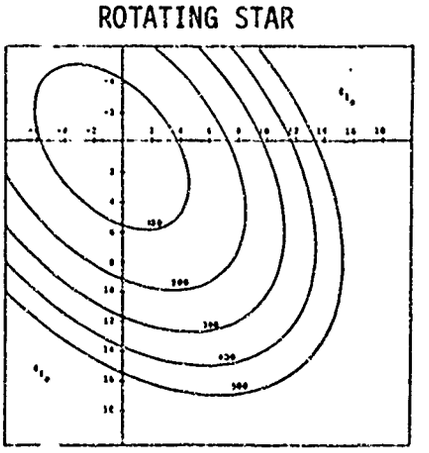

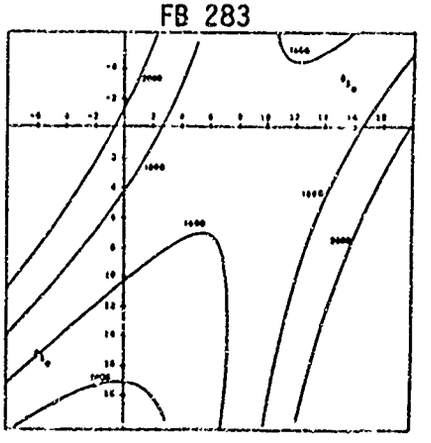

V = 80 KT

ΩR = 585 FPS

μ = .22

α_s = -5°

$\frac{C_{L_R}}{\sigma}$ = .06

δ_0 = 0

Figure 8 (Continued)

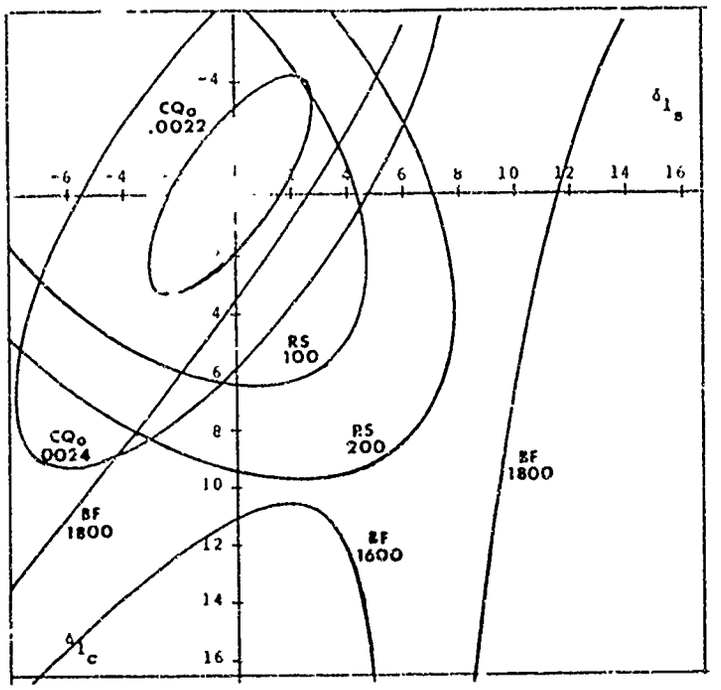

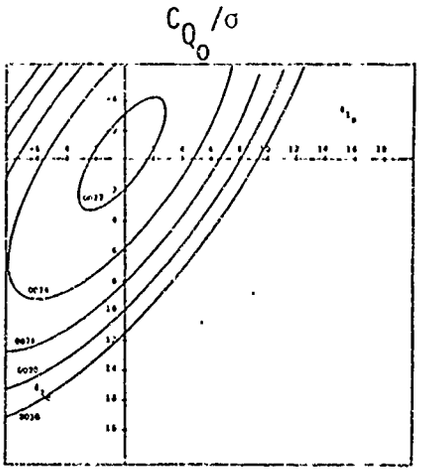

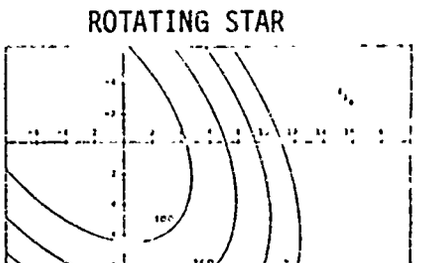

V = 80 KT

ΩR = 585 FPS

μ = .22

α_s = -5°

$\frac{C_{L_R}}{\sigma}$ = .06

δ_0 = 1

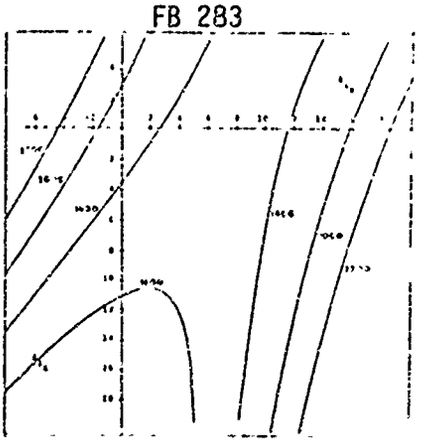

Figure 8 (Continued)

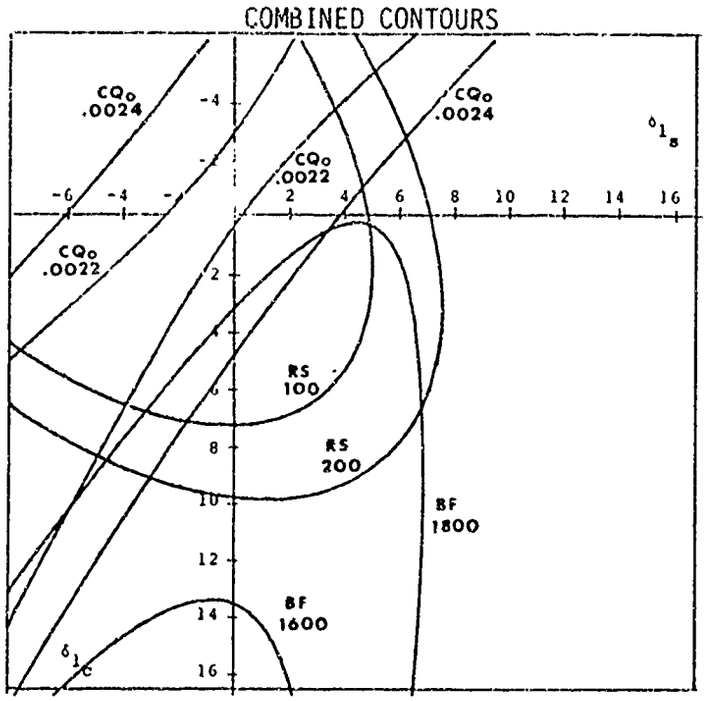

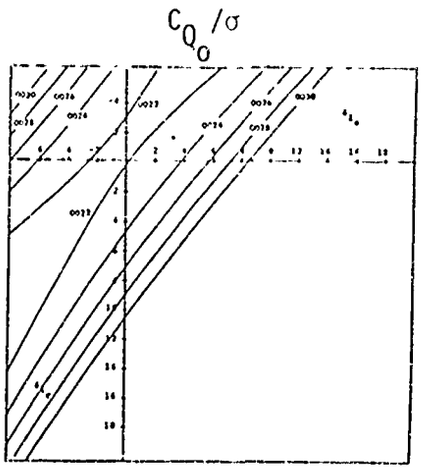

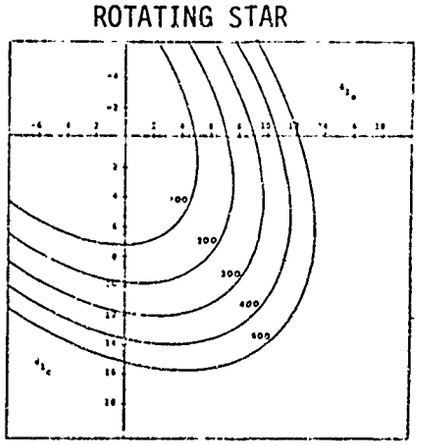

V = 80 KT

ΩR = 585 FPS

μ = .22

α_s = -5°

$\frac{C_{L_R}}{\sigma}$ = .06

δ_o = 2

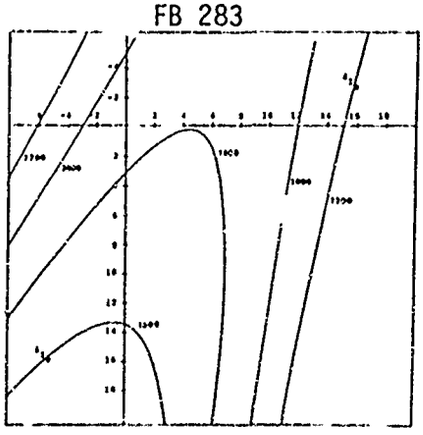

Figure 8 (Continued)

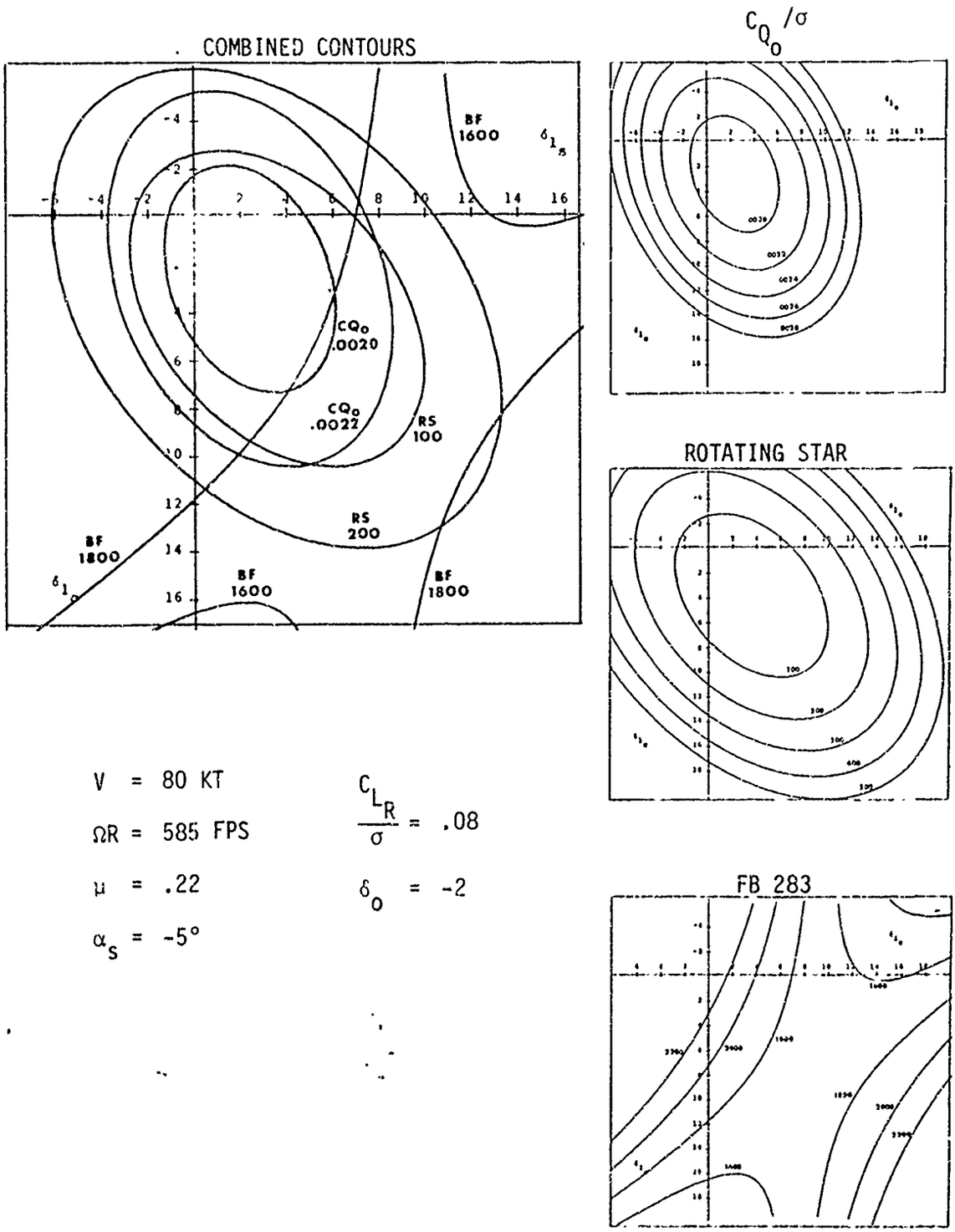

Figure 8 (Continued)

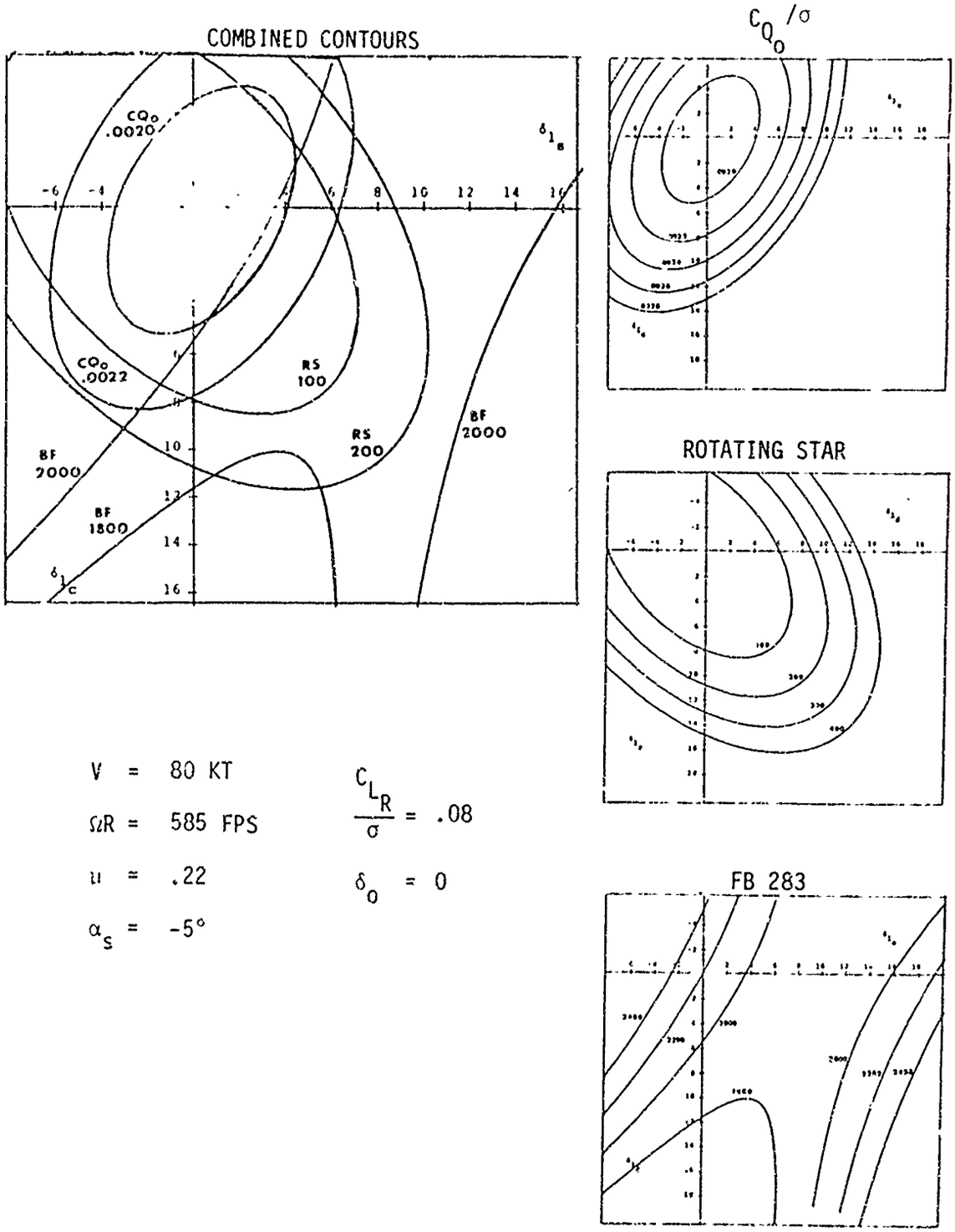

$V = 80$ KT

$\Omega R = 585$ FPS

$\mu = .22$

$\alpha_s = -5°$

$\frac{C_{L_R}}{\sigma} = .08$

$\delta_0 = 0$

Figure 8 (Continued)

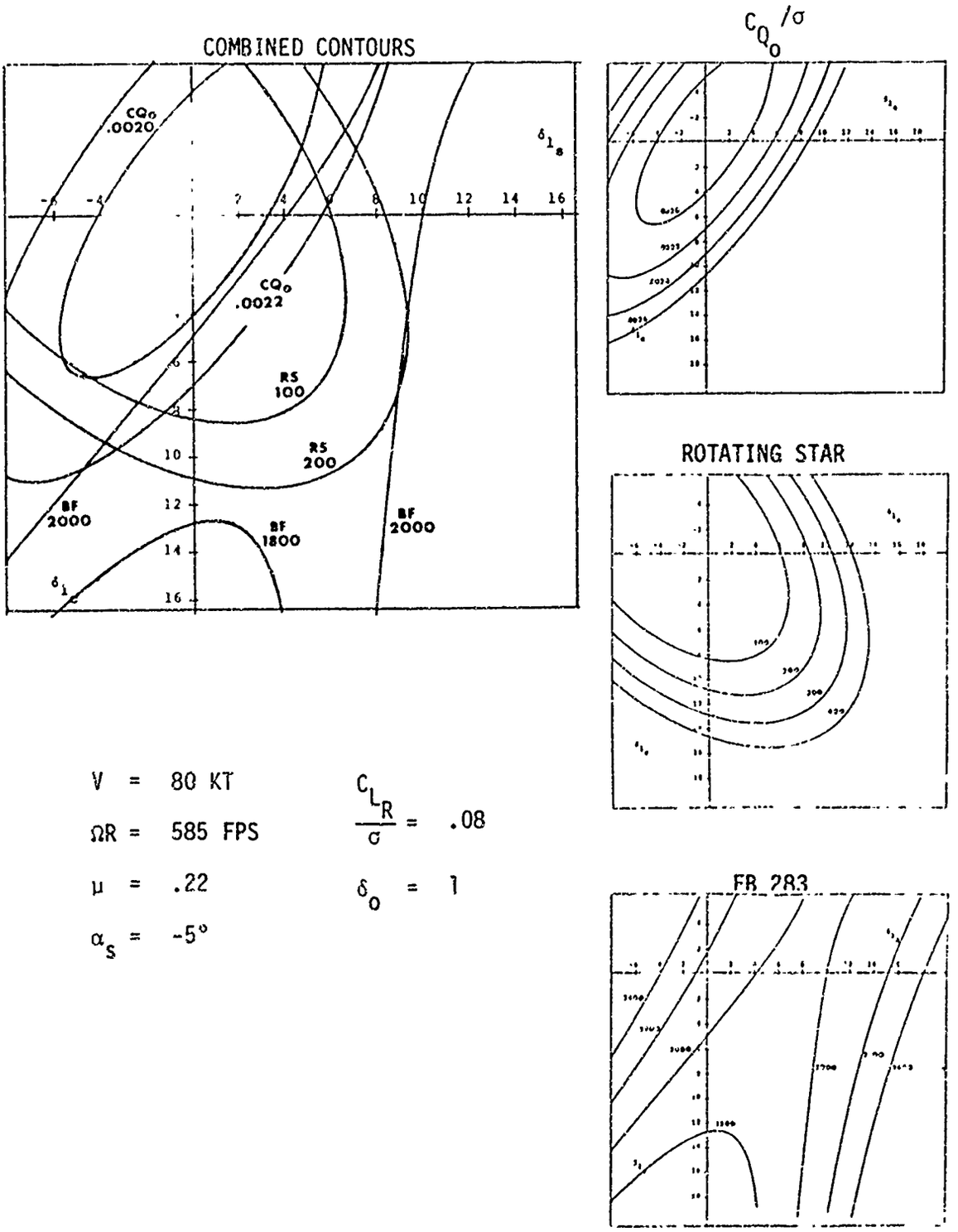

Figure 8 (Continued)

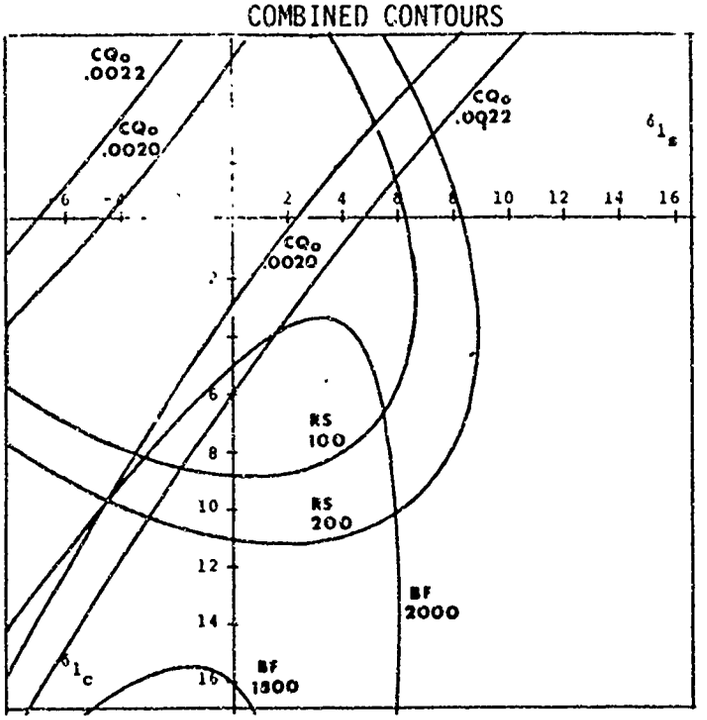

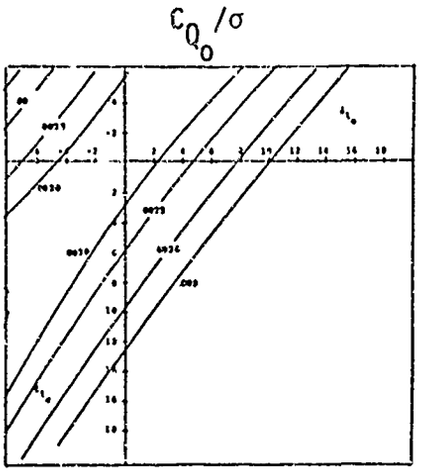

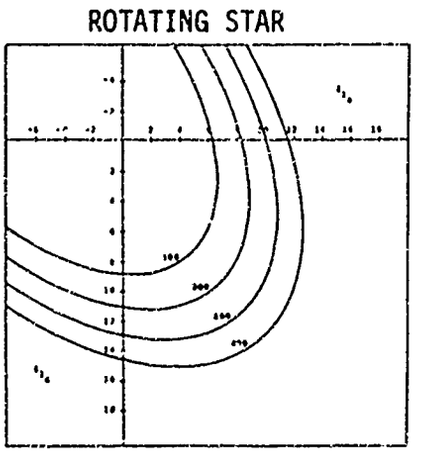

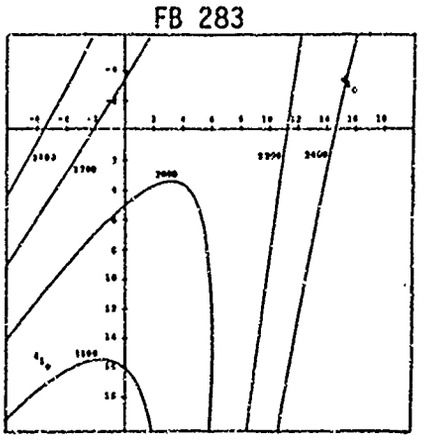

V = 80 KT

ΩR = 585 FPS

μ = .22

α_s = -5°

$\frac{C_{L_R}}{\sigma}$ = .08

δ_o = 2

Figure 8 (Continued)

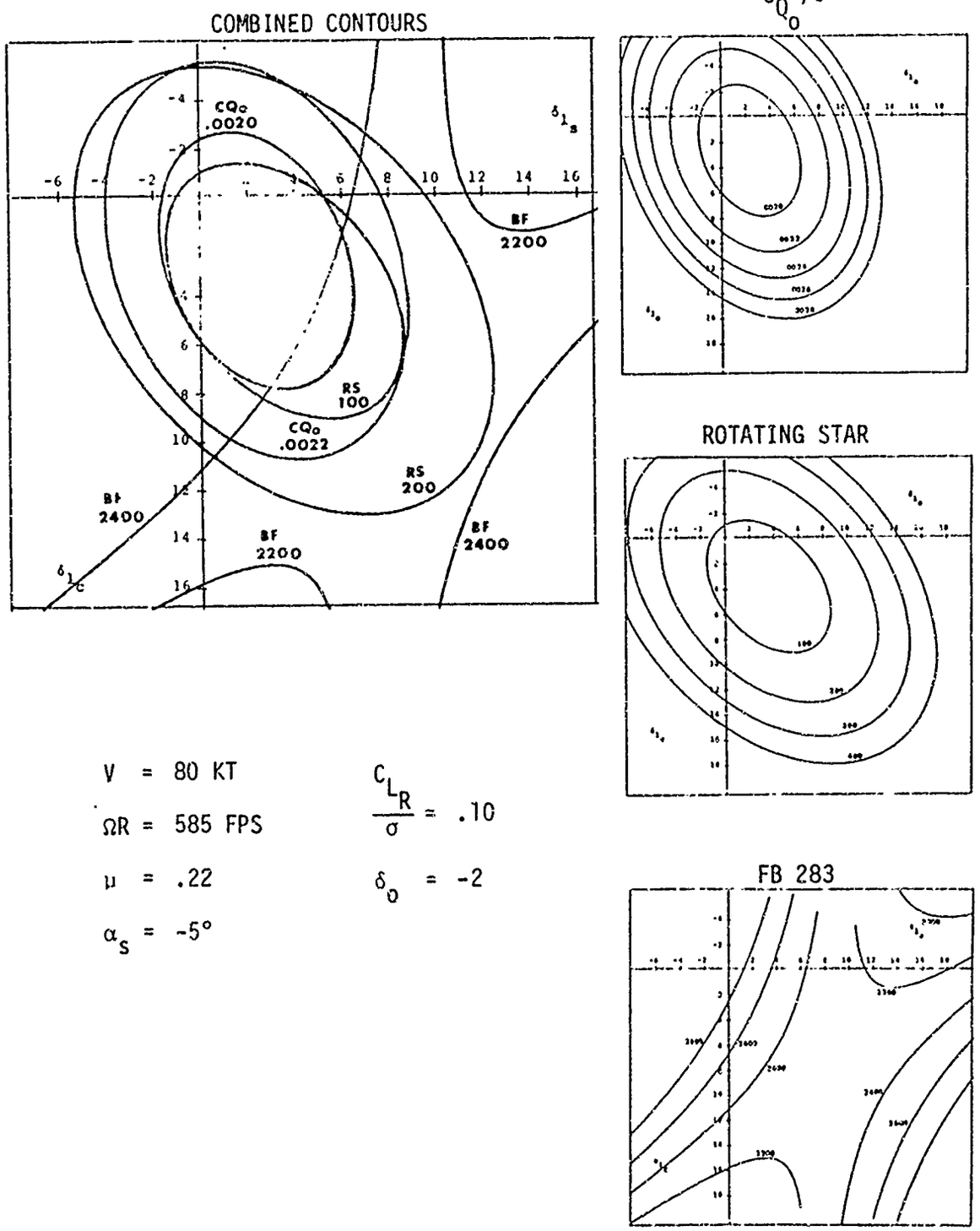

Figure 8 (Continued).

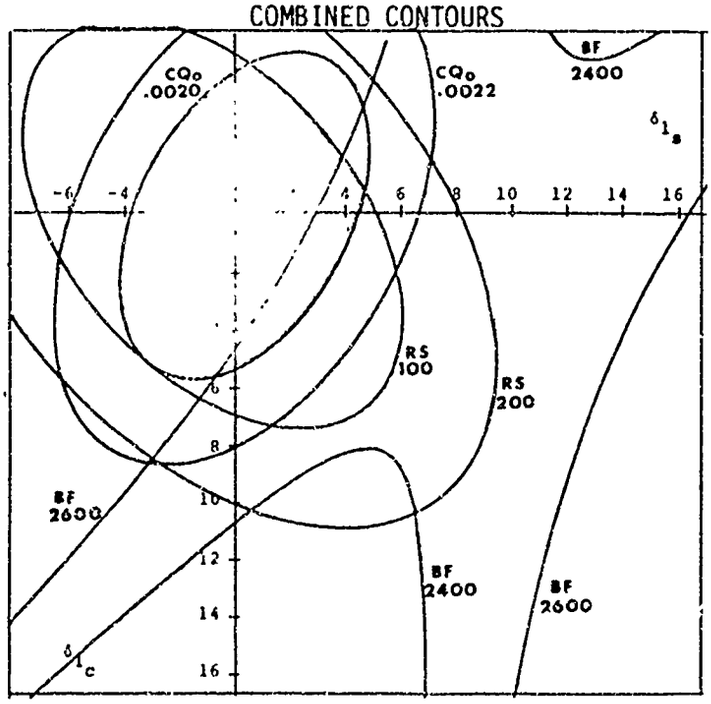

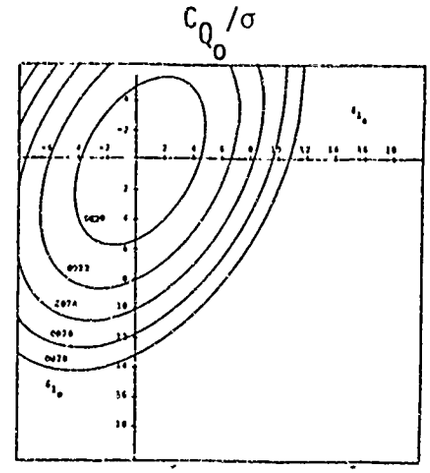

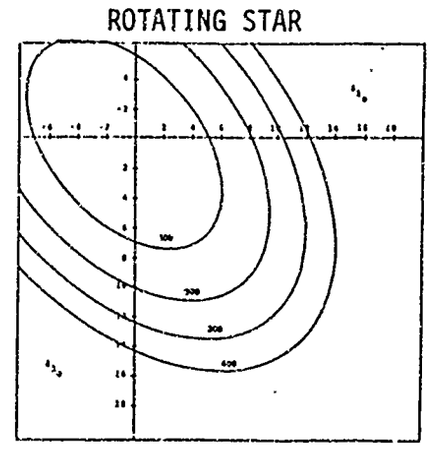

V = 80 KT

ΩR = 585 FPS

μ = .22

α_s = -5°

$\frac{C_{L_R}}{\sigma}$ = .10

δ_0 = 0

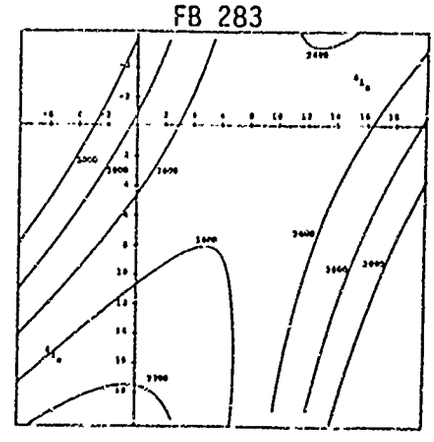

Figure 8 (Continued)

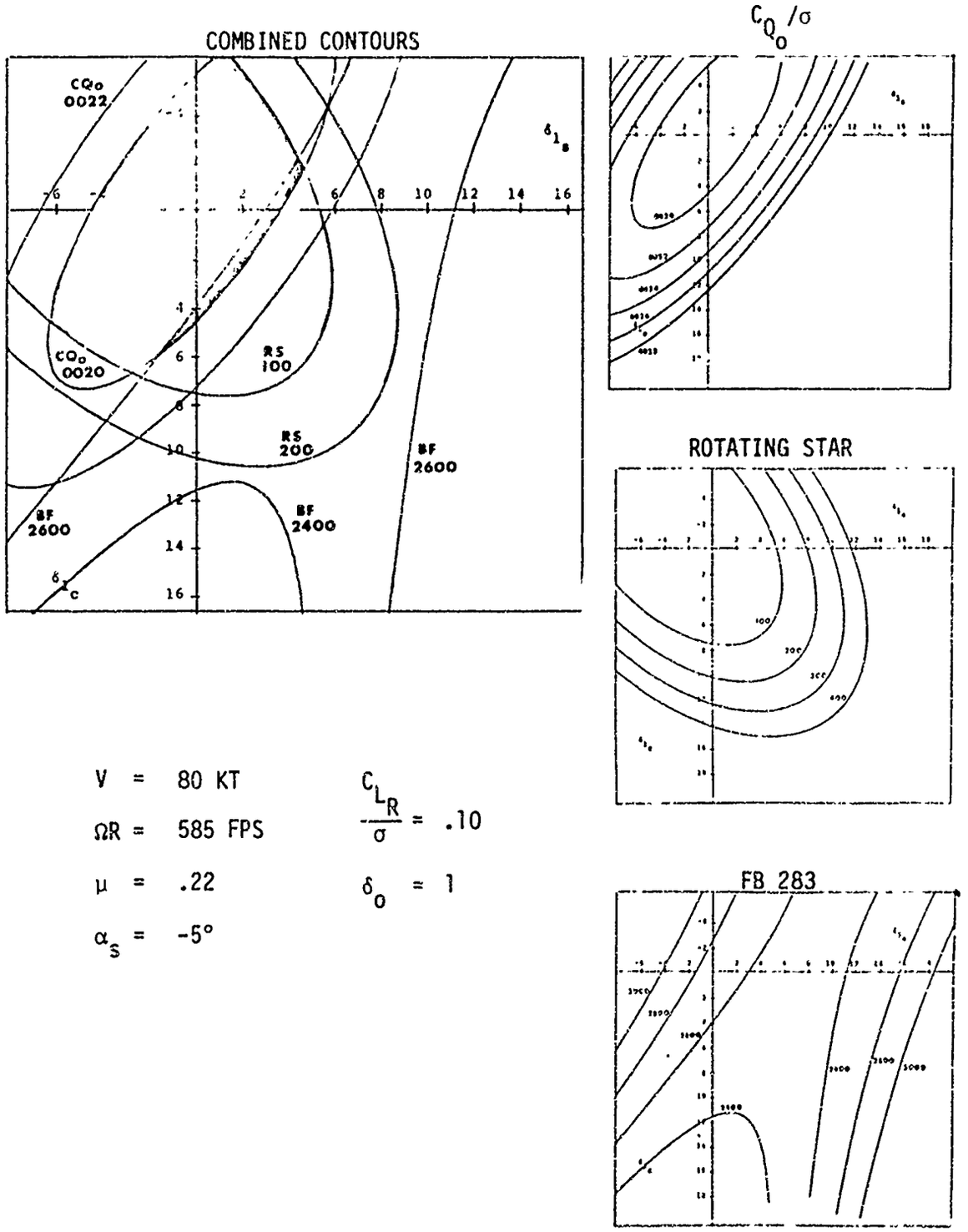

V = 80 KT

ΩR = 585 FPS

μ = .22

α_s = -5°

$\frac{C_{L_R}}{\sigma}$ = .10

δ_o = 1

Figure 8 (Continued)

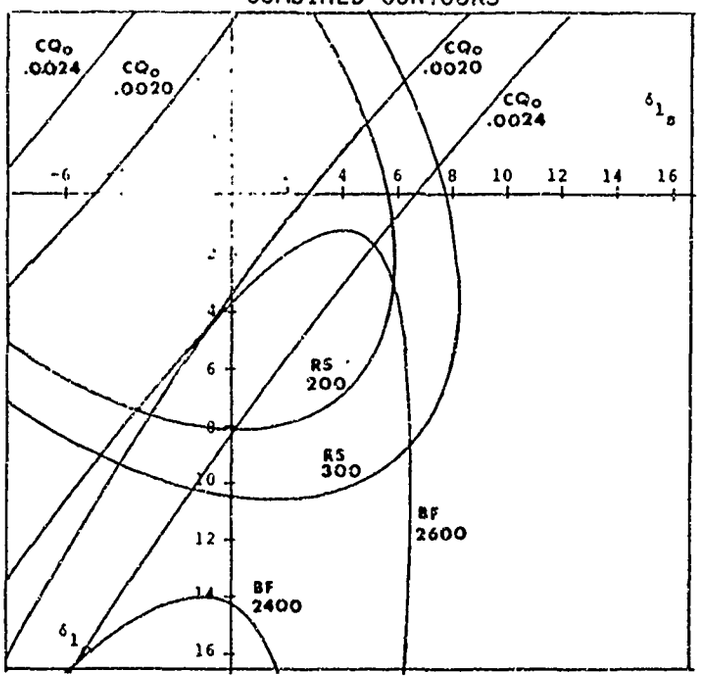

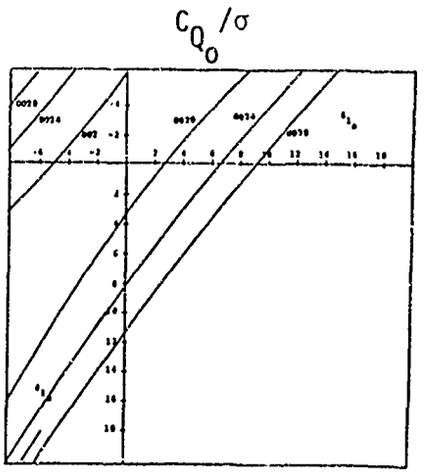

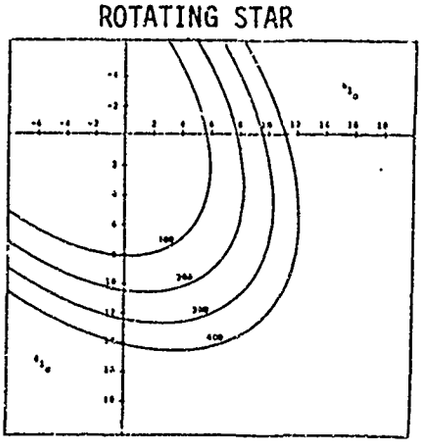

V = 80 KT

ΩR = 585 FPS

μ = .22

α_s = -5°

$\frac{C_{L_R}}{\sigma}$ = .10

δ_0 = 2

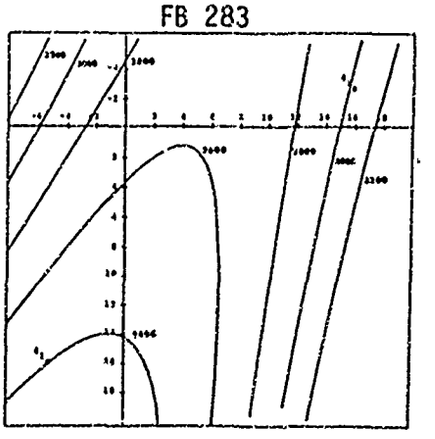

Figure 8 (Continued)

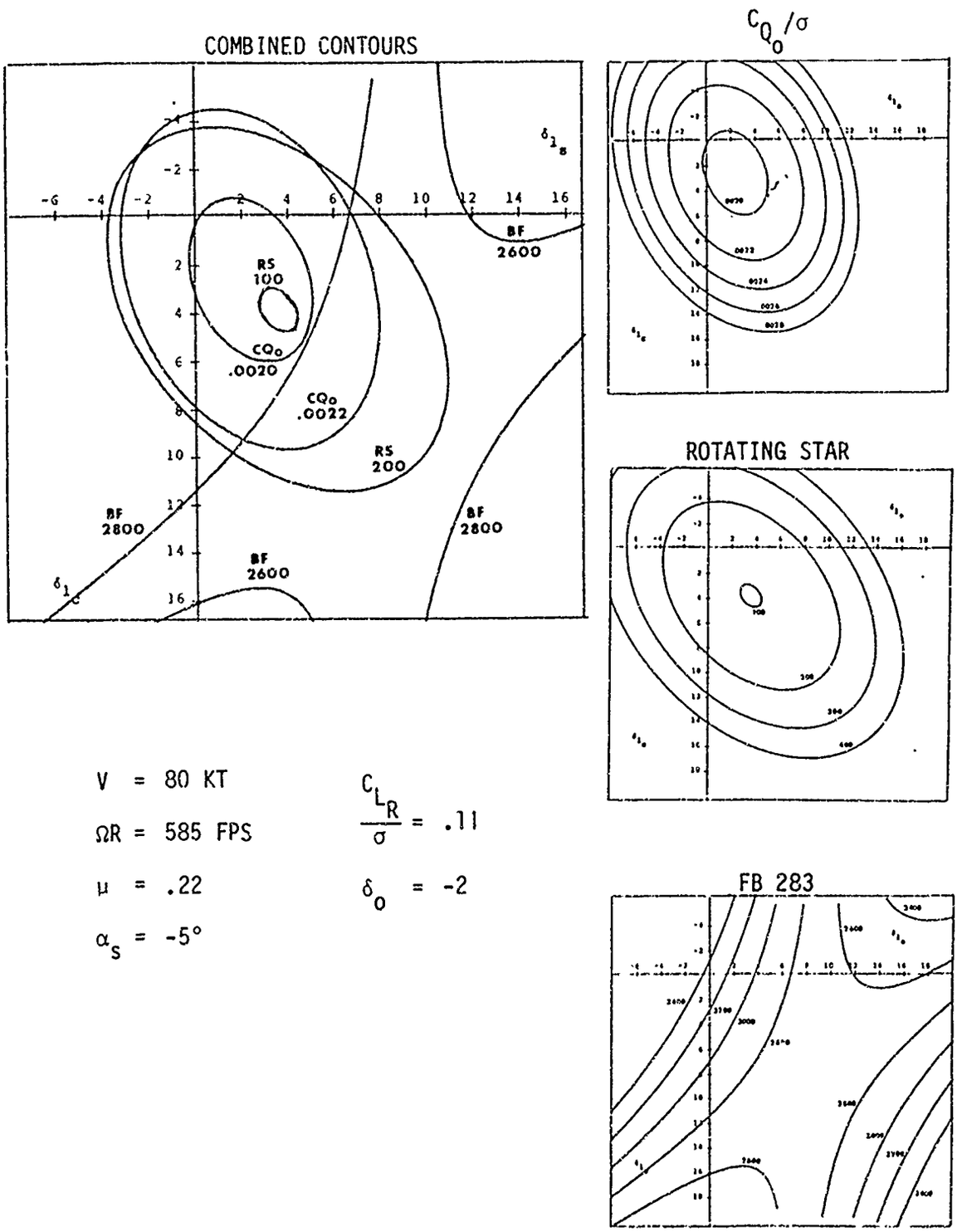

$V = 80$ KT

$\Omega R = 585$ FPS

$\mu = .22$

$\alpha_s = -5°$

$\frac{C_{L_R}}{\sigma} = .11$

$\delta_o = -2$

Figure 8 (Continued)

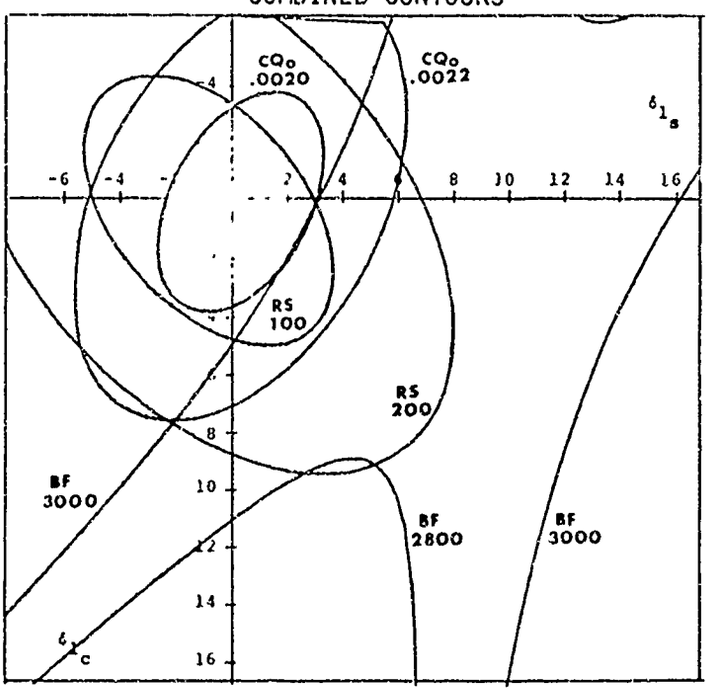

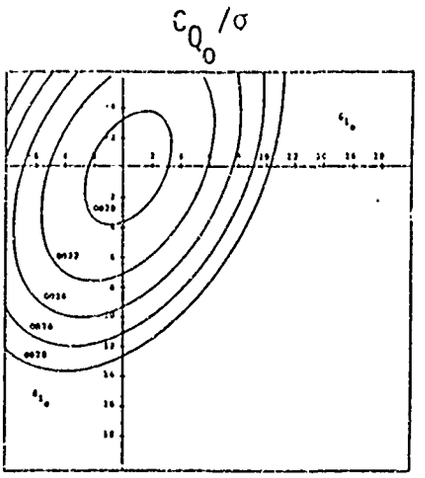

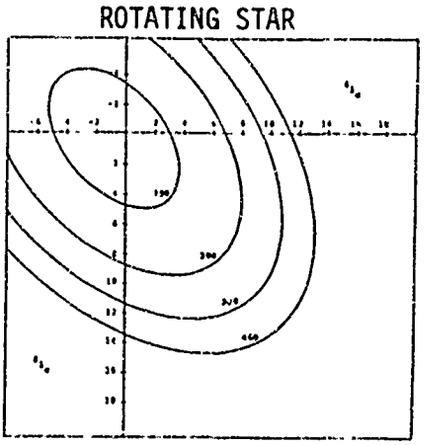

V = 80 KT

ΩR = 585 FPS

μ = .22

α_s = -5°

$\frac{C_{L_R}}{\sigma}$ = .11

δ_o = 0

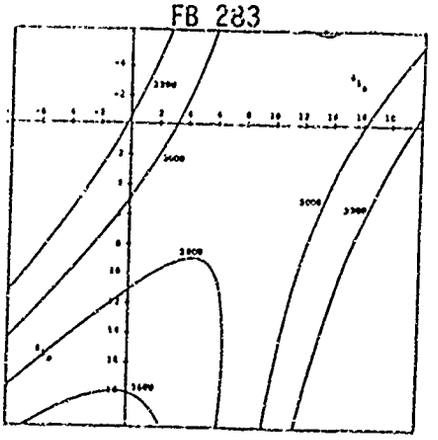

Figure 8 (Continued)

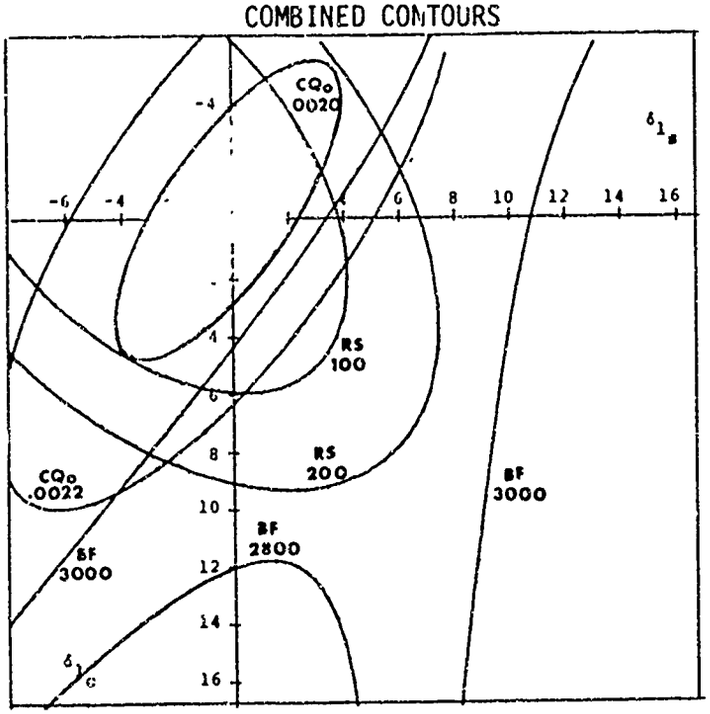

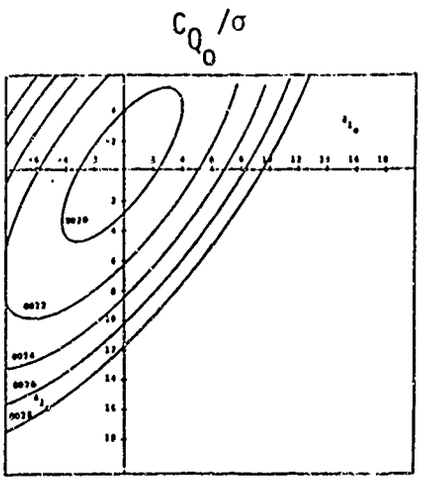

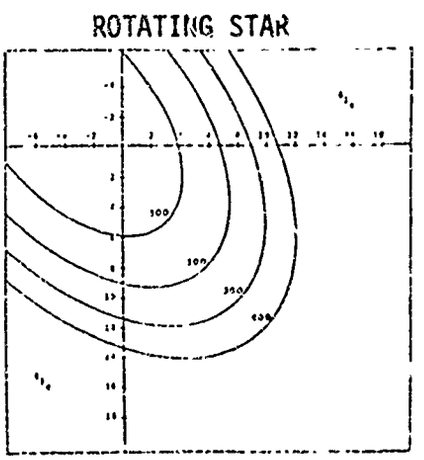

V = 80 KT

ΩR = 585 FPS

μ = .22

α_s = -5°

$\frac{C_{L_R}}{\sigma}$ = .11

δ_o = 1

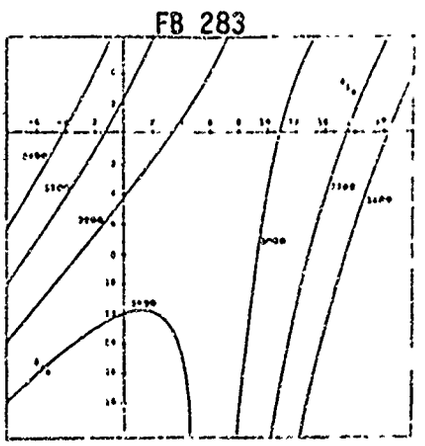

Figure 8 (Continued)

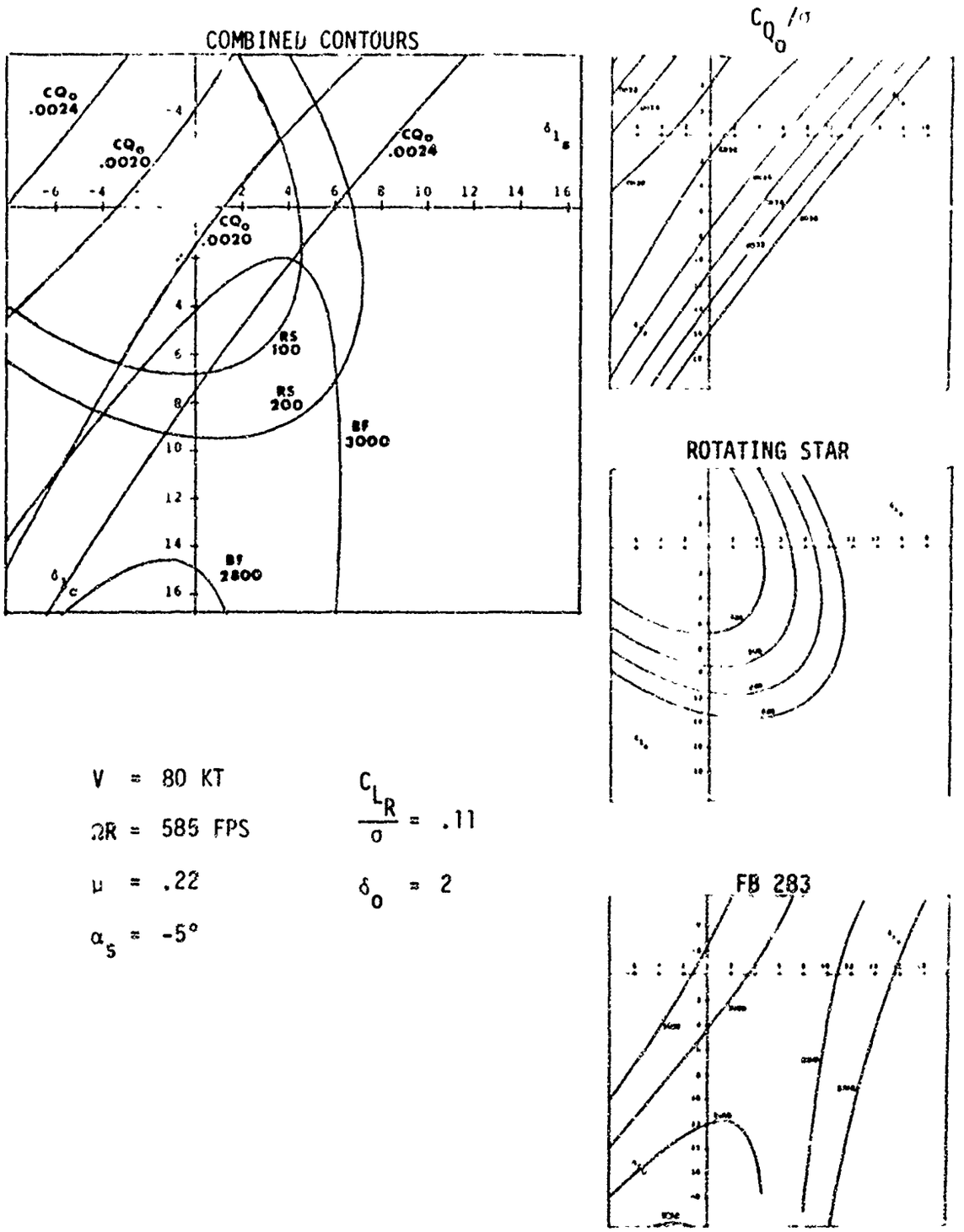

$V = 80$ KT

$\Omega R = 585$ FPS

$\mu = .22$

$\alpha_s = -5°$

$\frac{C_{L_R}}{\sigma} = .11$

$\delta_o = 2$

Figure 8 (Continued)

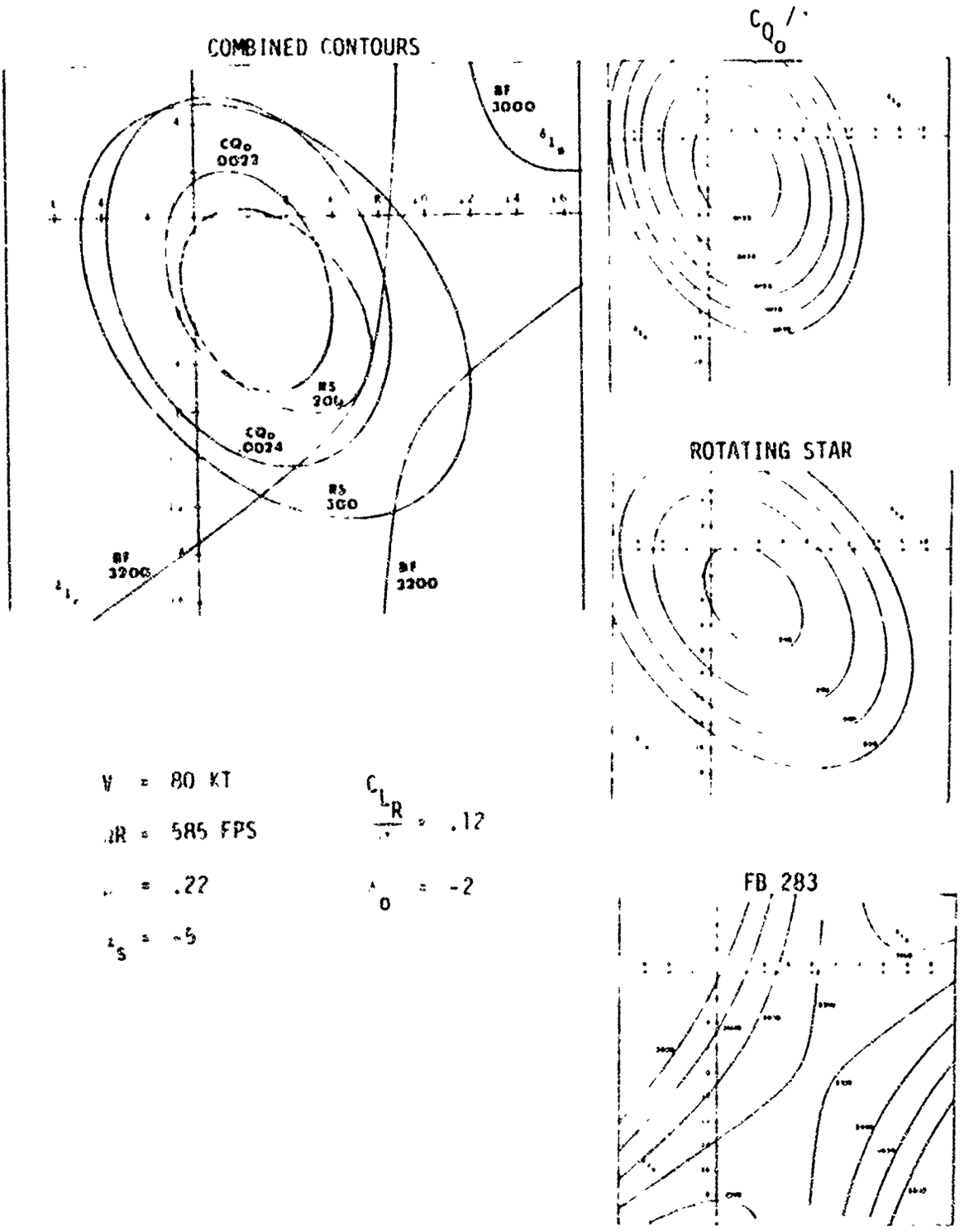

Figure 8 (Continued)

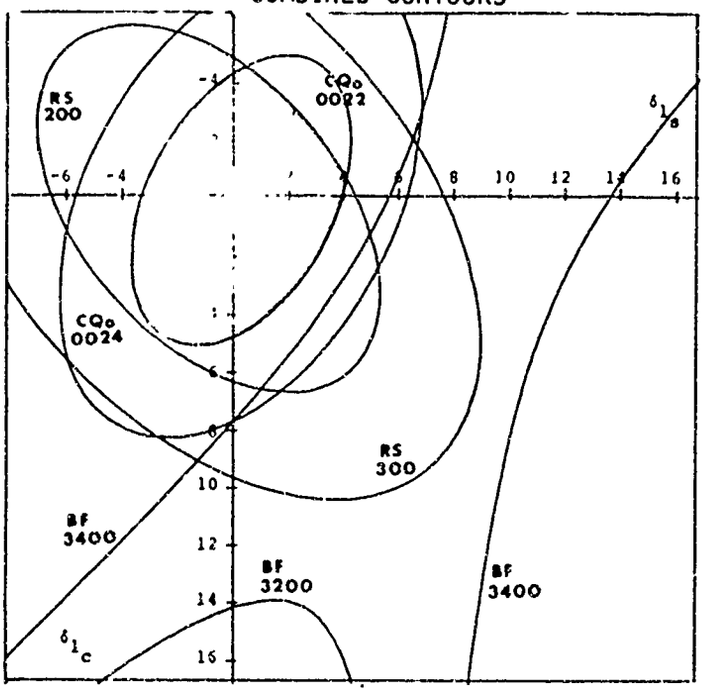

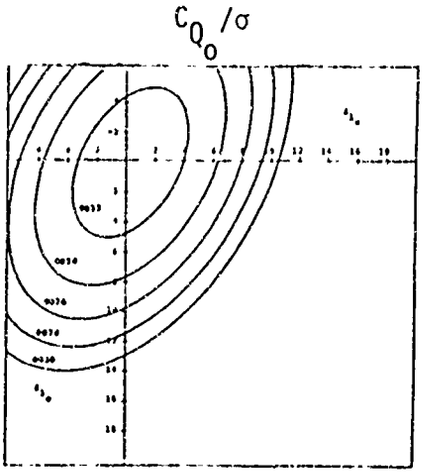

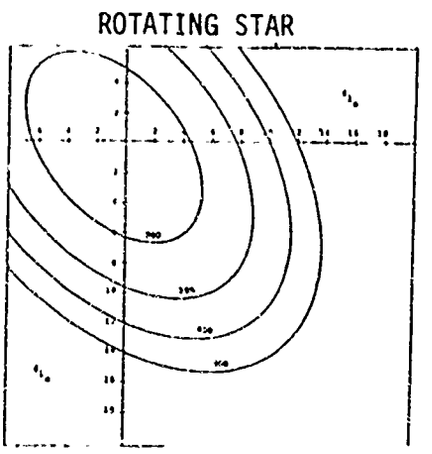

V = 80 KT

ΩR = 585 FPS

μ = .22

α_s = -5°

$\frac{C_{L_R}}{\sigma}$ = .12

δ_o = 0

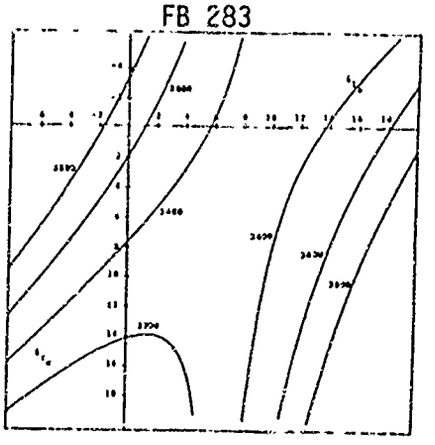

Figure 8 (Continued)

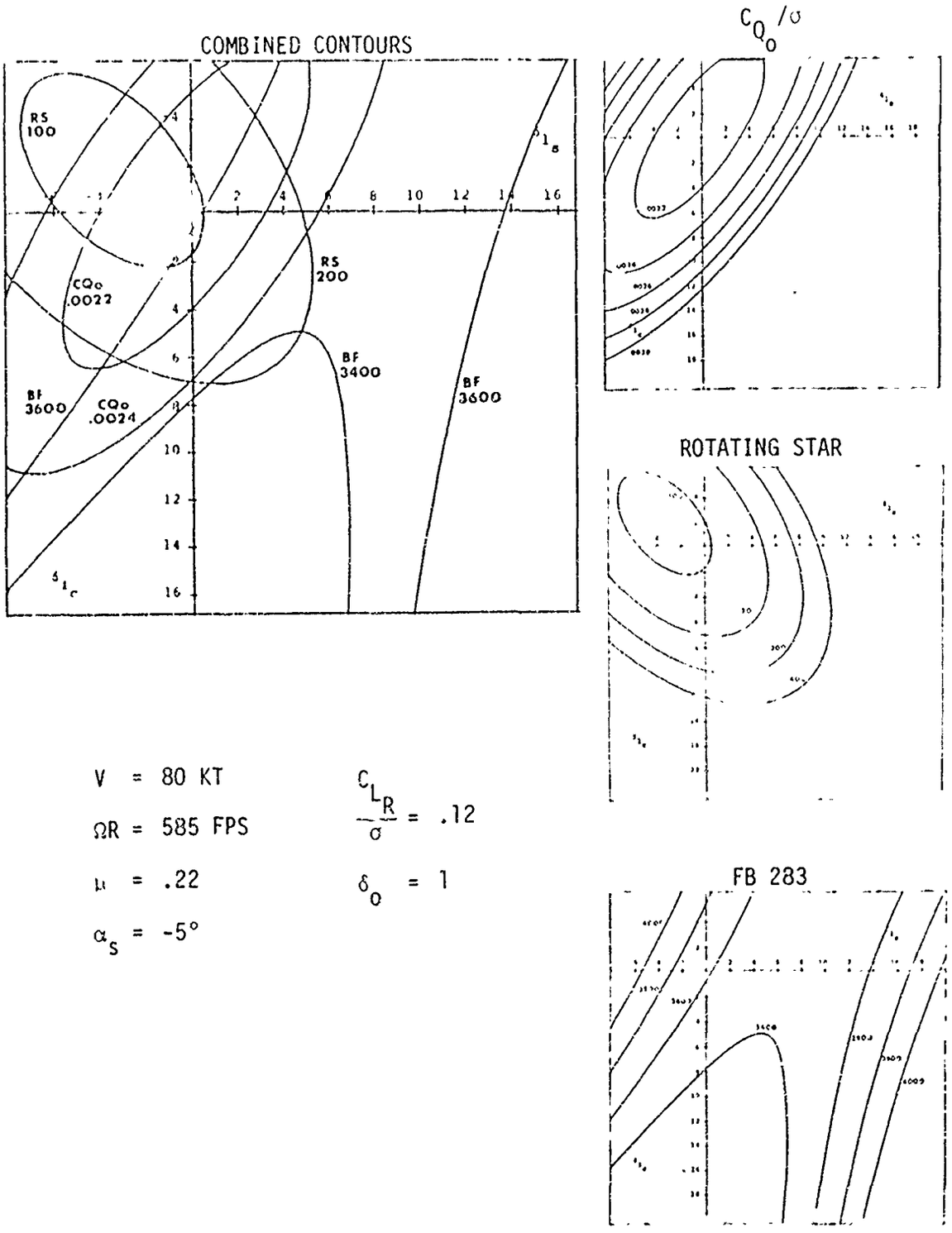

V = 80 KT

ΩR = 585 FPS

μ = .22

α_s = -5°

$\frac{C_{L_R}}{\sigma}$ = .12

δ_o = 1

Figure 8 (Continued)

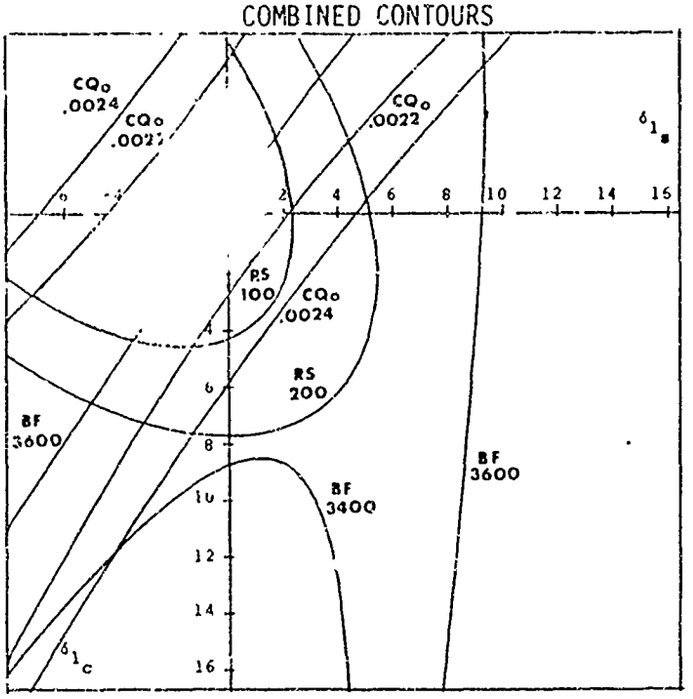

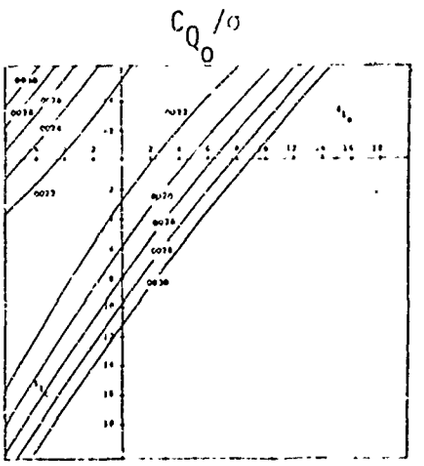

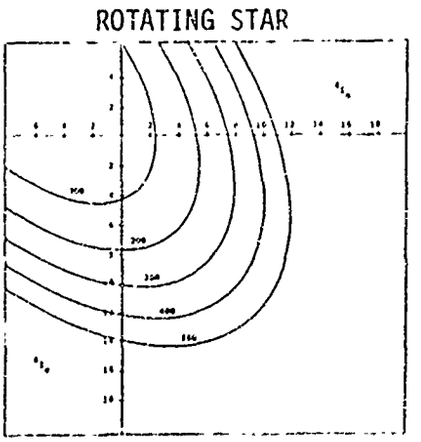

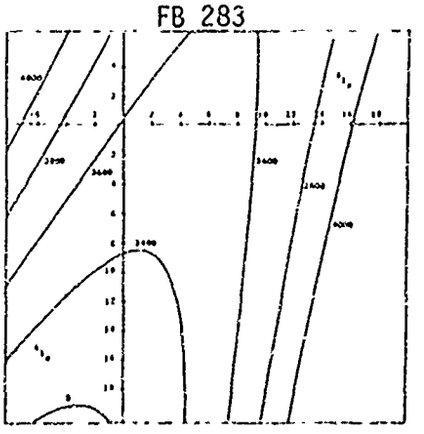

V = 80 KT

ΩR = 585 FPS

μ = .22

α_s = -5°

$\frac{C_{L_R}}{\sigma}$ = .12

δ_o = 2

Figure 8 (Concluded)

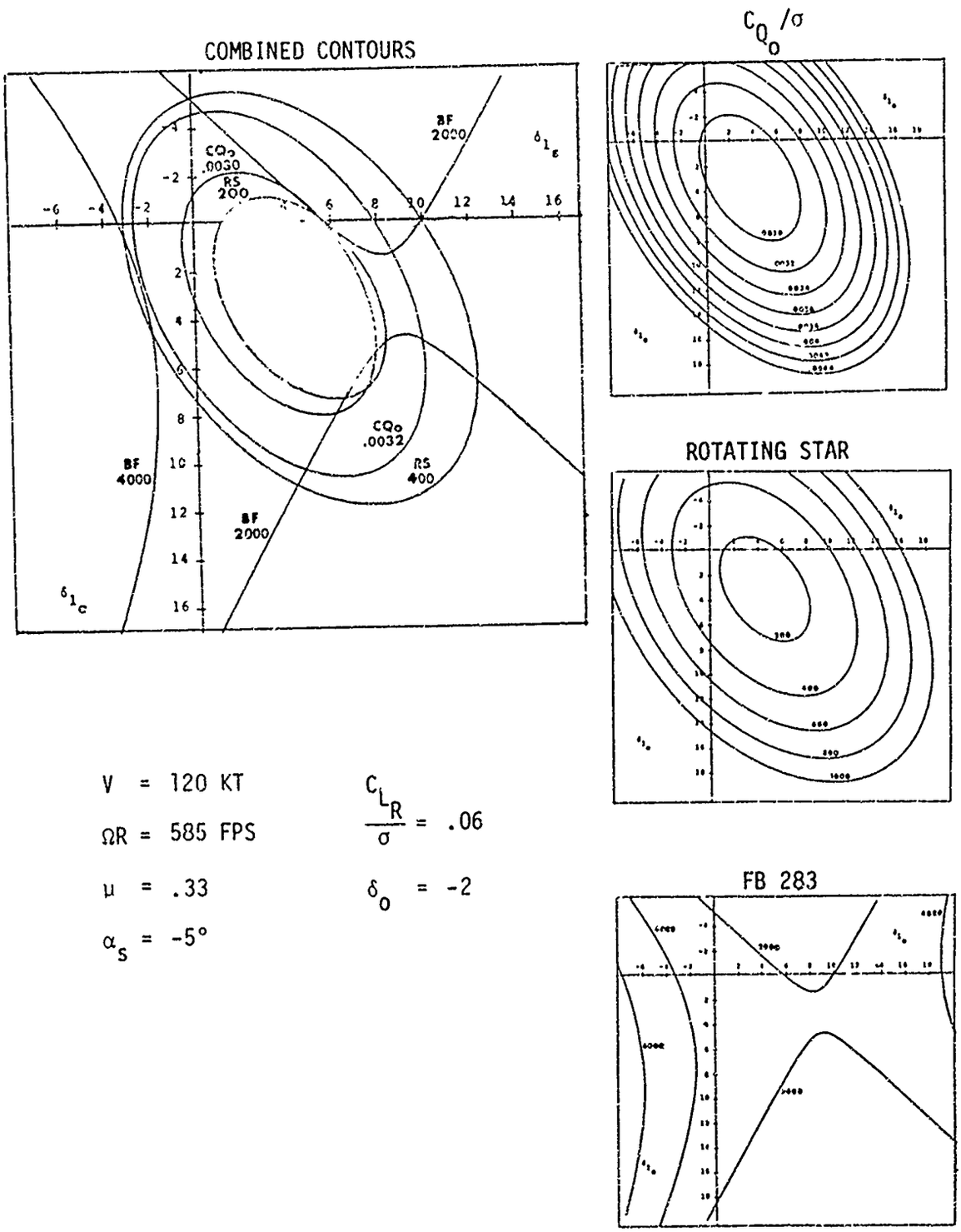

$V = 120$ KT

$\Omega R = 585$ FPS

$\mu = .33$

$\alpha_s = -5°$

$\frac{C_{L_R}}{\sigma} = .06$

$\delta_o = -2$

Figure 9. Optimization Response Contours at 120 Knots and -5° Shaft Tilt

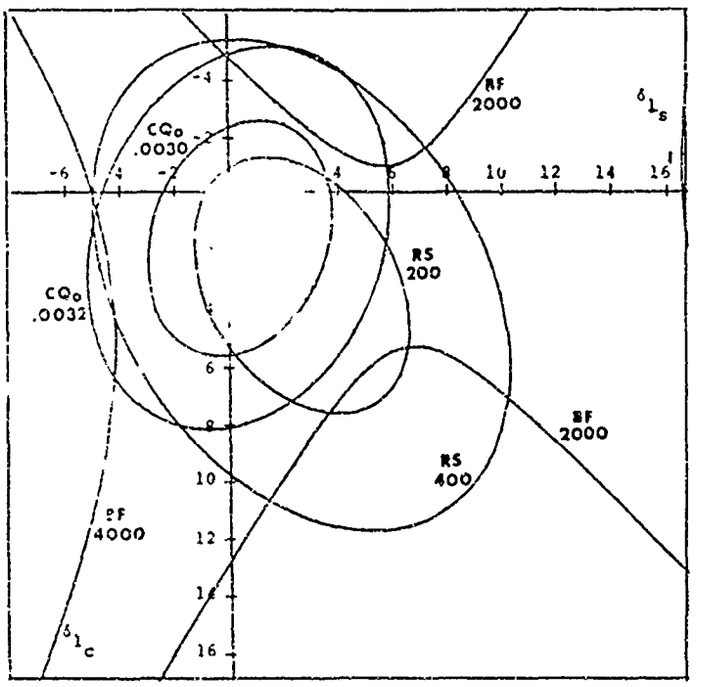

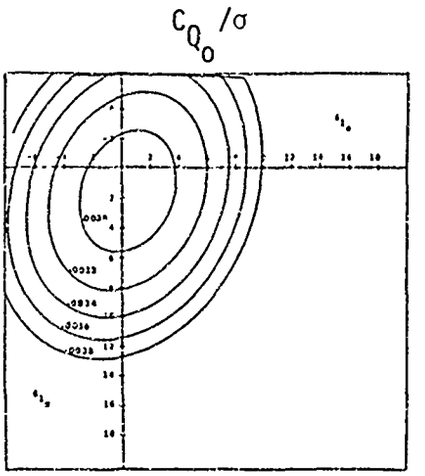

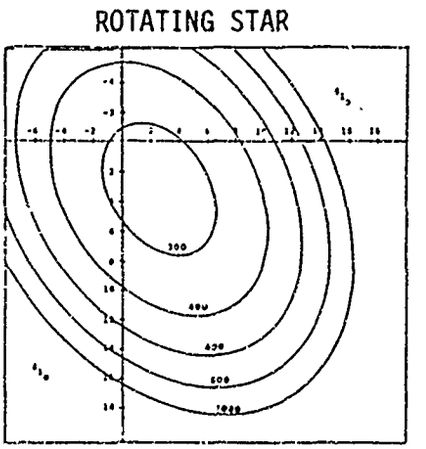

V = 120 KT

ΩR = 585 FPS

μ = .33

α_s = -5°

$\frac{C_{L_R}}{\sigma}$ = .06

δ_0 = 0

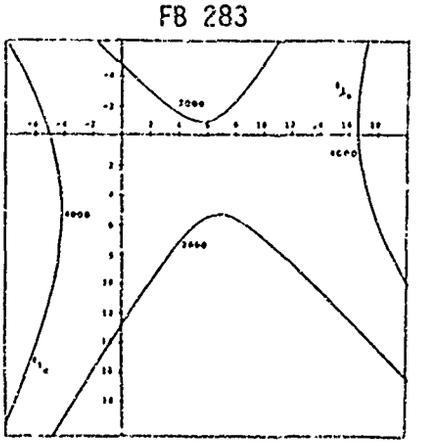

Figure 9 (Continued)

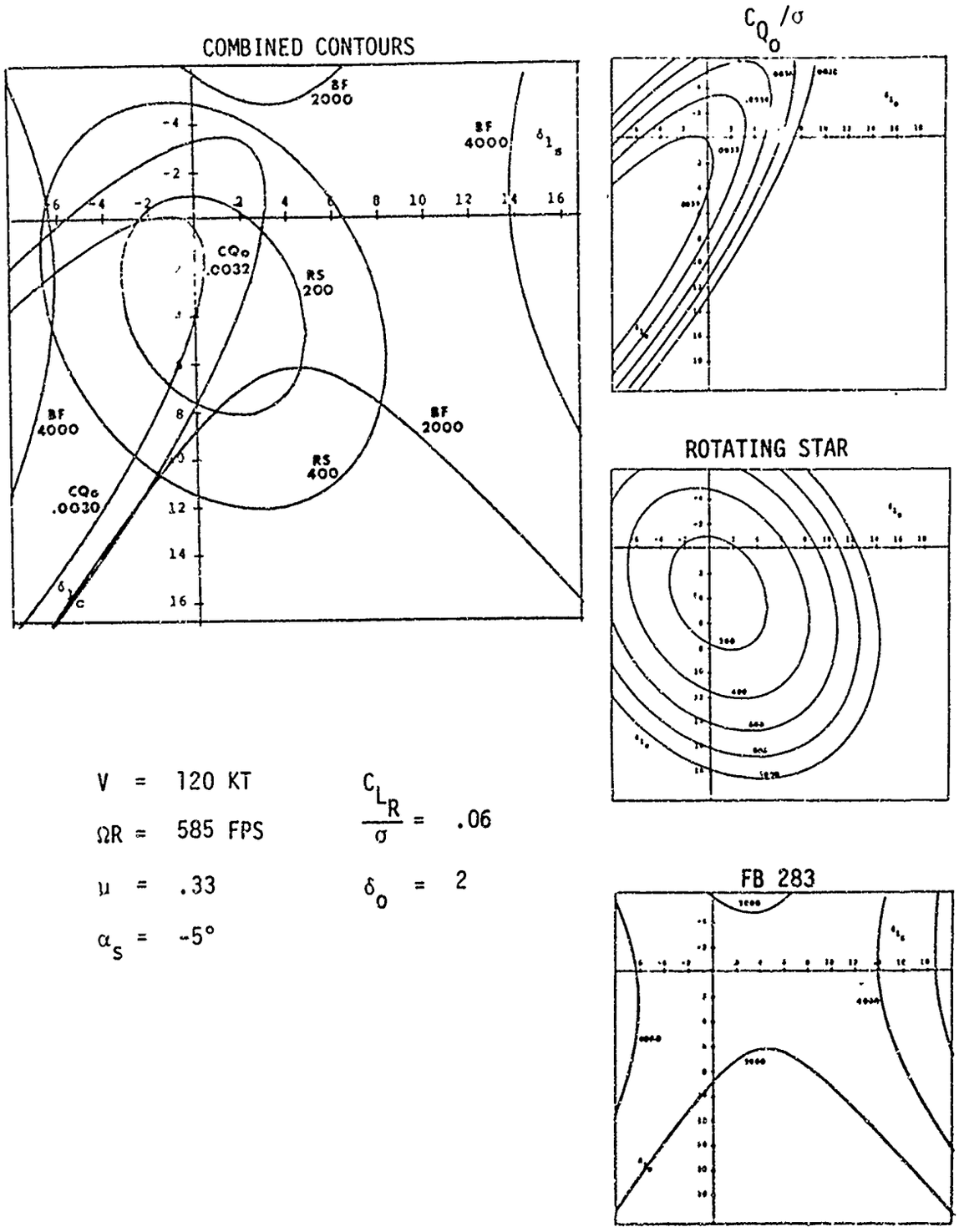

V = 120 KT

ΩR = 585 FPS

μ = .33

α_s = -5°

$\frac{C_{L_R}}{\sigma}$ = .06

δ_0 = 2

Figure 9 (Continued)

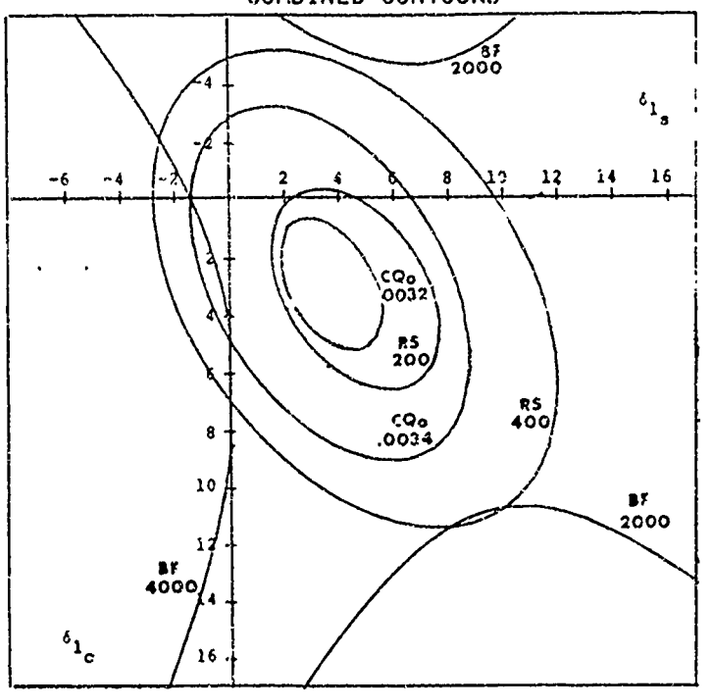

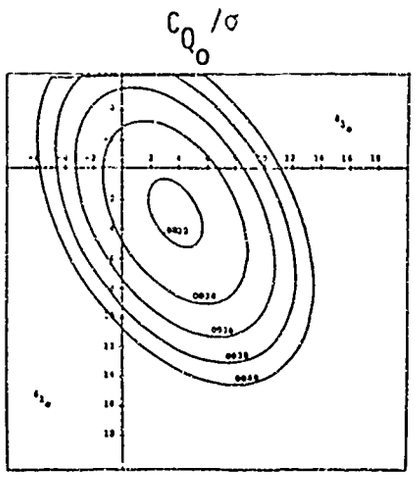

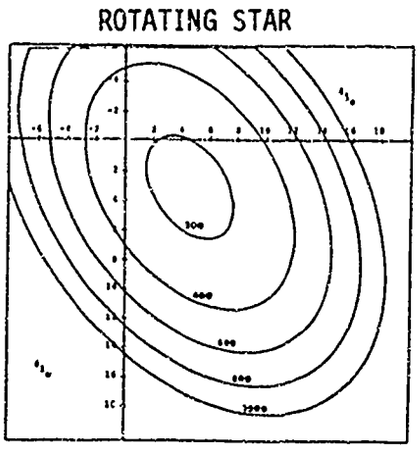

V = 120 KT

ΩR = 585 FPS

μ = .33

α_s = -5°

$\frac{C_{L_R}}{\sigma}$ = .08

δ_0 = -2

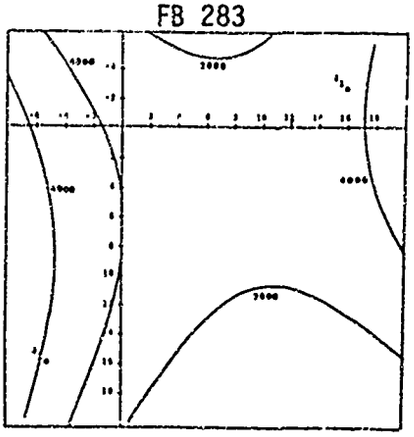

Figure 9 (Continued)

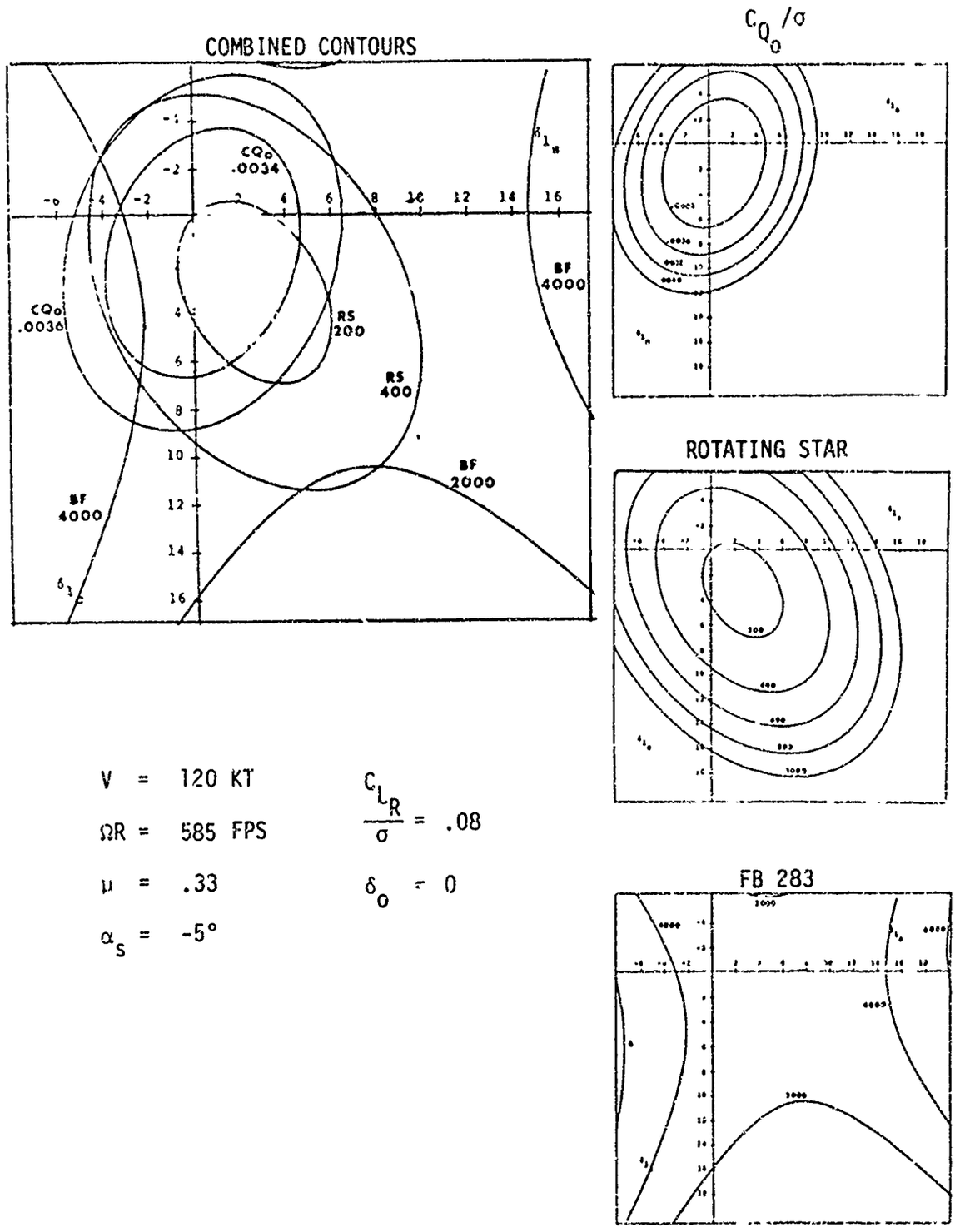

$V = 120$ KT

$\Omega R = 585$ FPS

$\mu = .33$

$\alpha_s = -5°$

$\frac{C_{L_R}}{\sigma} = .08$

$\delta_o = 0$

Figure 9 (Continued)

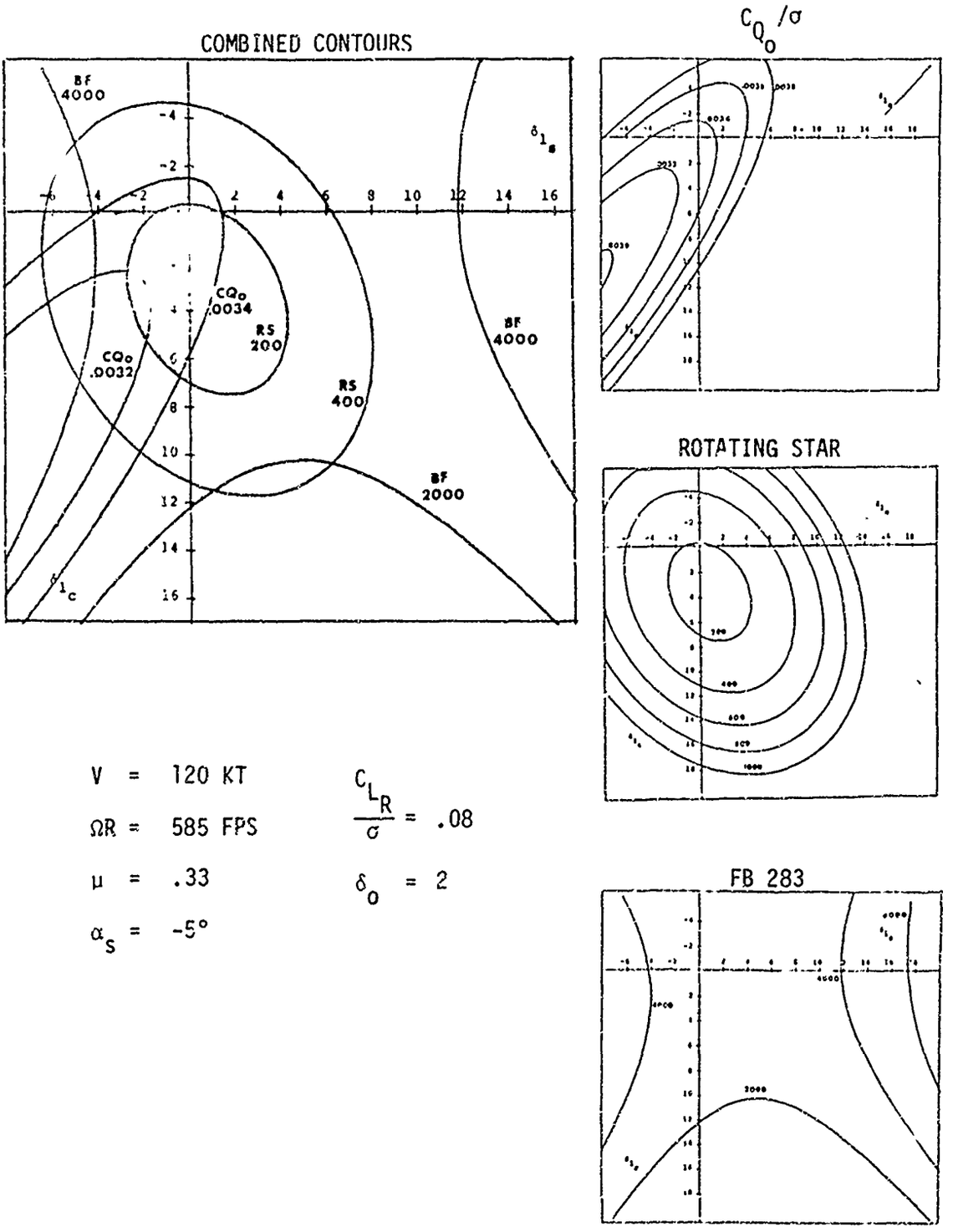

V = 120 KT

ΩR = 585 FPS

μ = .33

α_s = -5°

$\frac{C_{L_R}}{\sigma}$ = .08

δ_o = 2

Figure 9 (Continued)

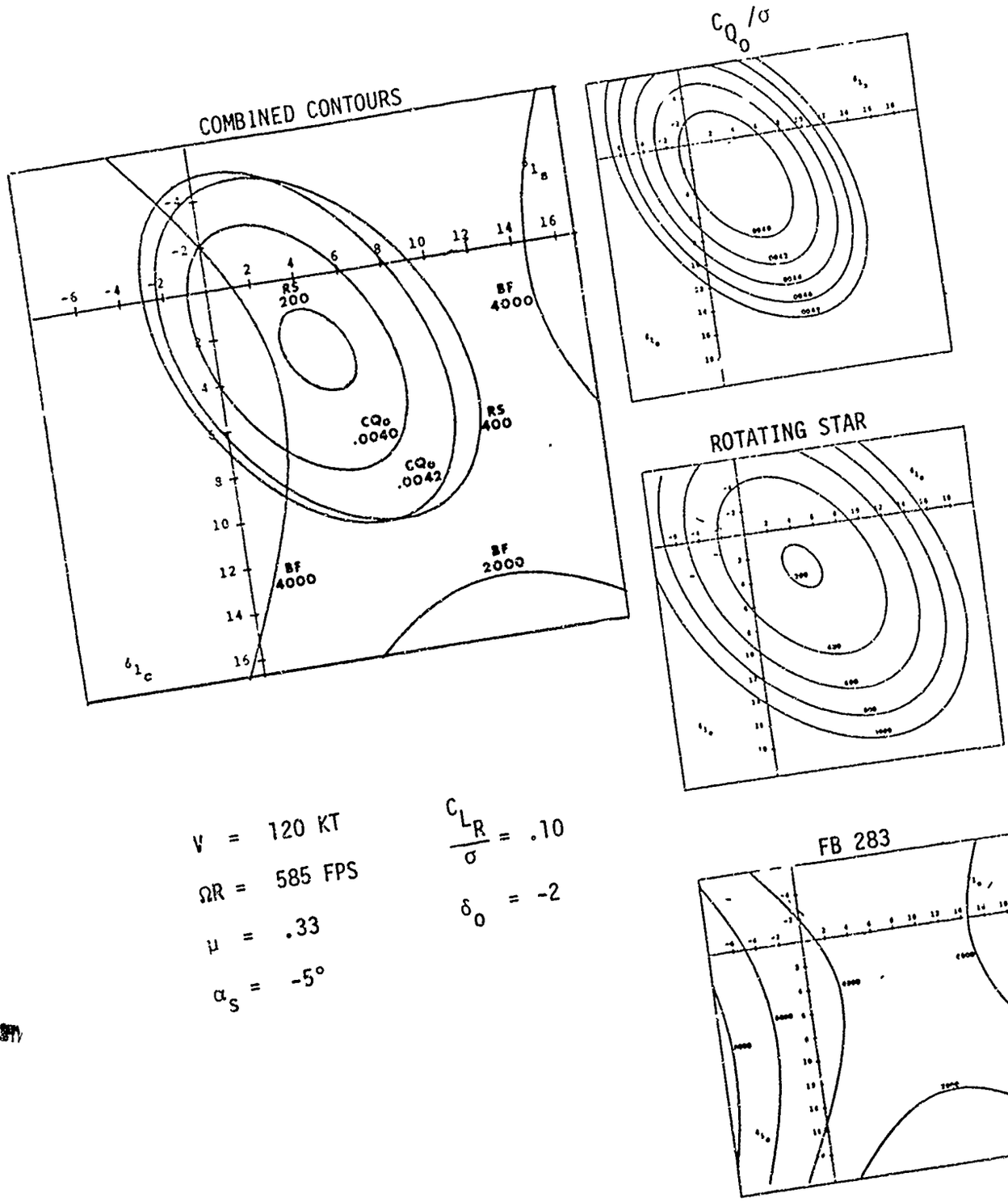

V = 120 KT

ΩR = 585 FPS

μ = .33

α_s = -5°

$\frac{C_{L_R}}{\sigma}$ = .10

θ_0 = -2

Figure 9 (Continued)

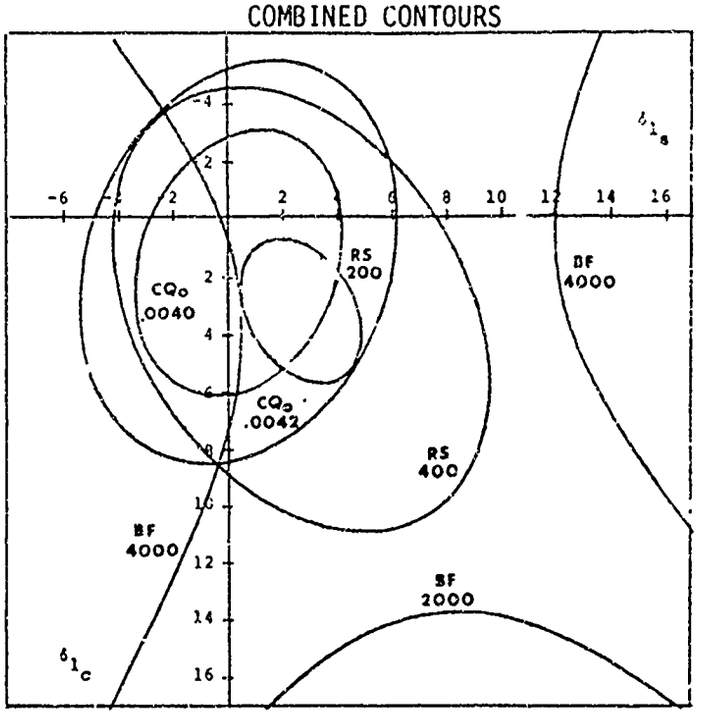

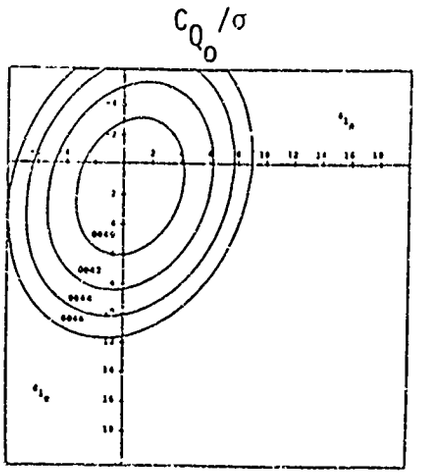

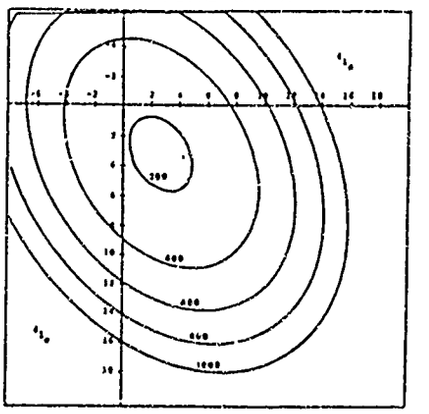

V = 120 KT

ΩR = 585 FPS

μ = .33

α_s = -5°

$\frac{C_{L_R}}{\sigma}$ = .10

δ_o = 0

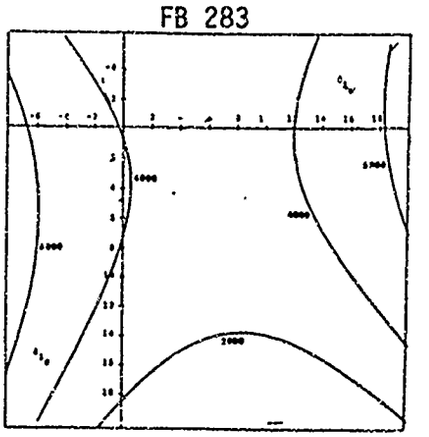

Figure 9 (Continued)

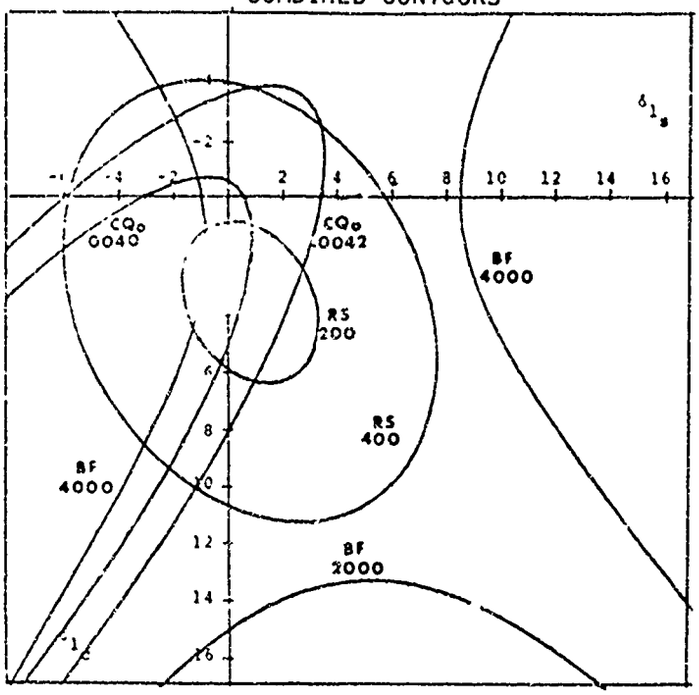

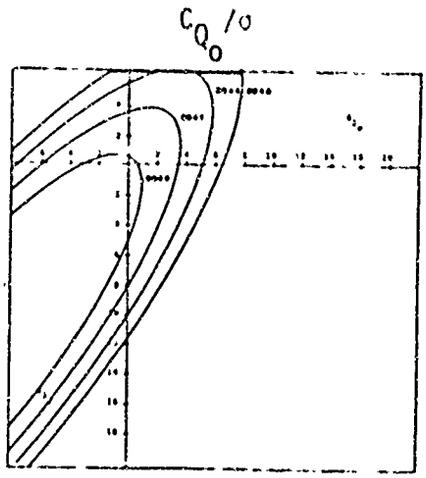

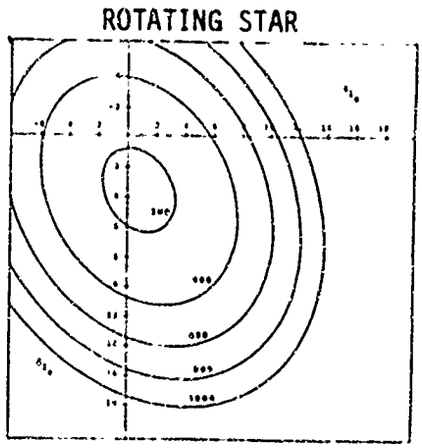

V = 120 KT

ΩR = 585 FPS

μ = .33

α_s = -5°

$\frac{C_{L_R}}{\sigma}$ = .10

δ_0 = 2

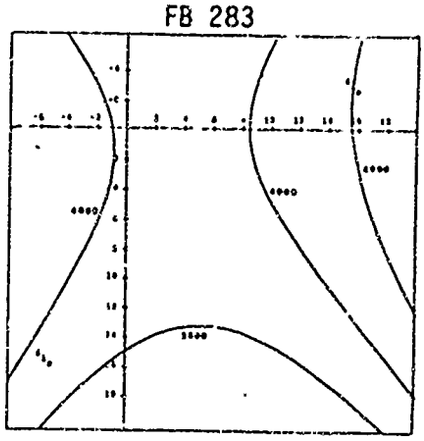

Figure 9 (Continued)

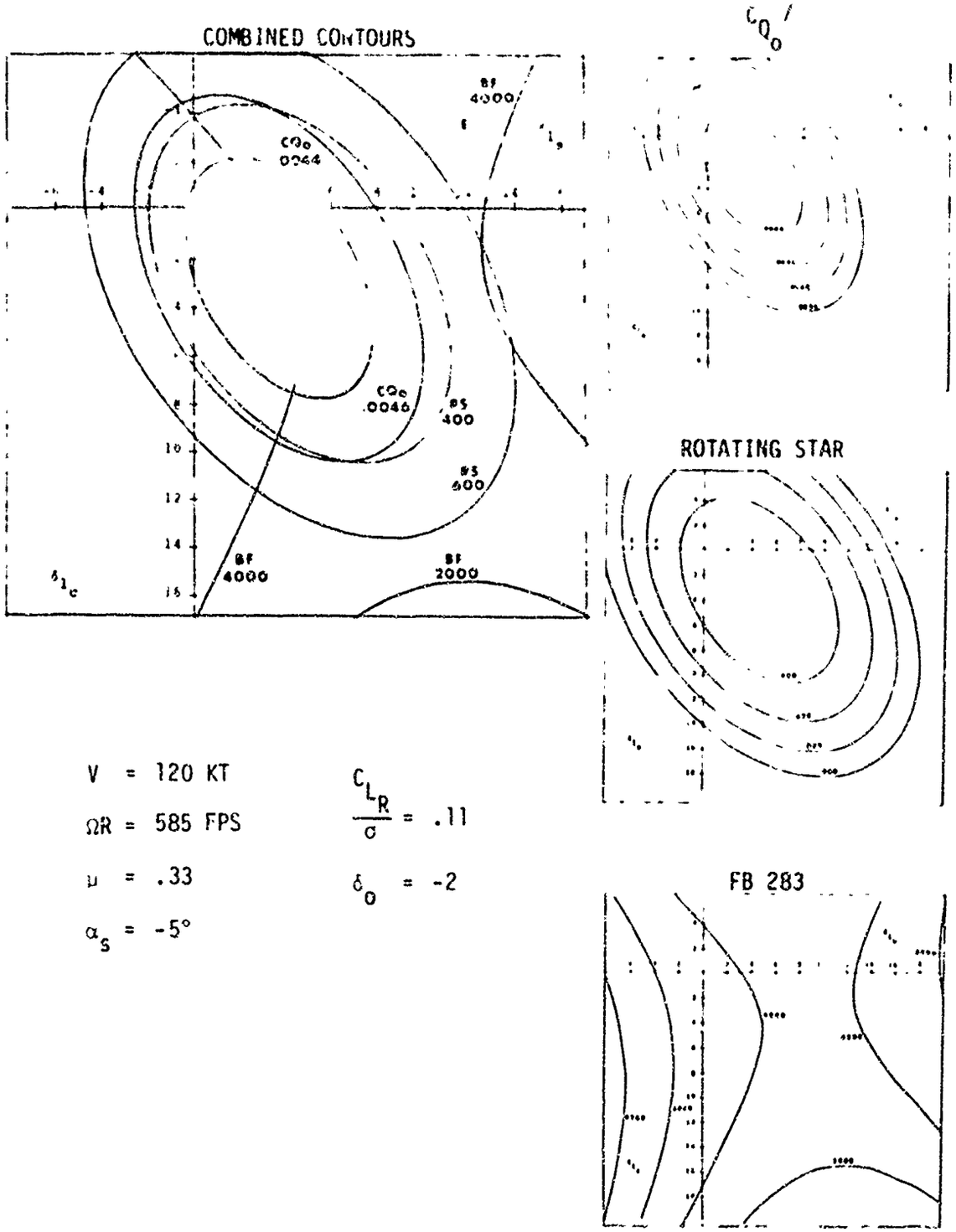

$V = 120$ KT

$\Omega R = 585$ FPS

$\mu = .33$

$\alpha_s = -5°$

$\frac{C_{L_R}}{\sigma} = .11$

$\delta_0 = -2$

Figure 9 (Continued)

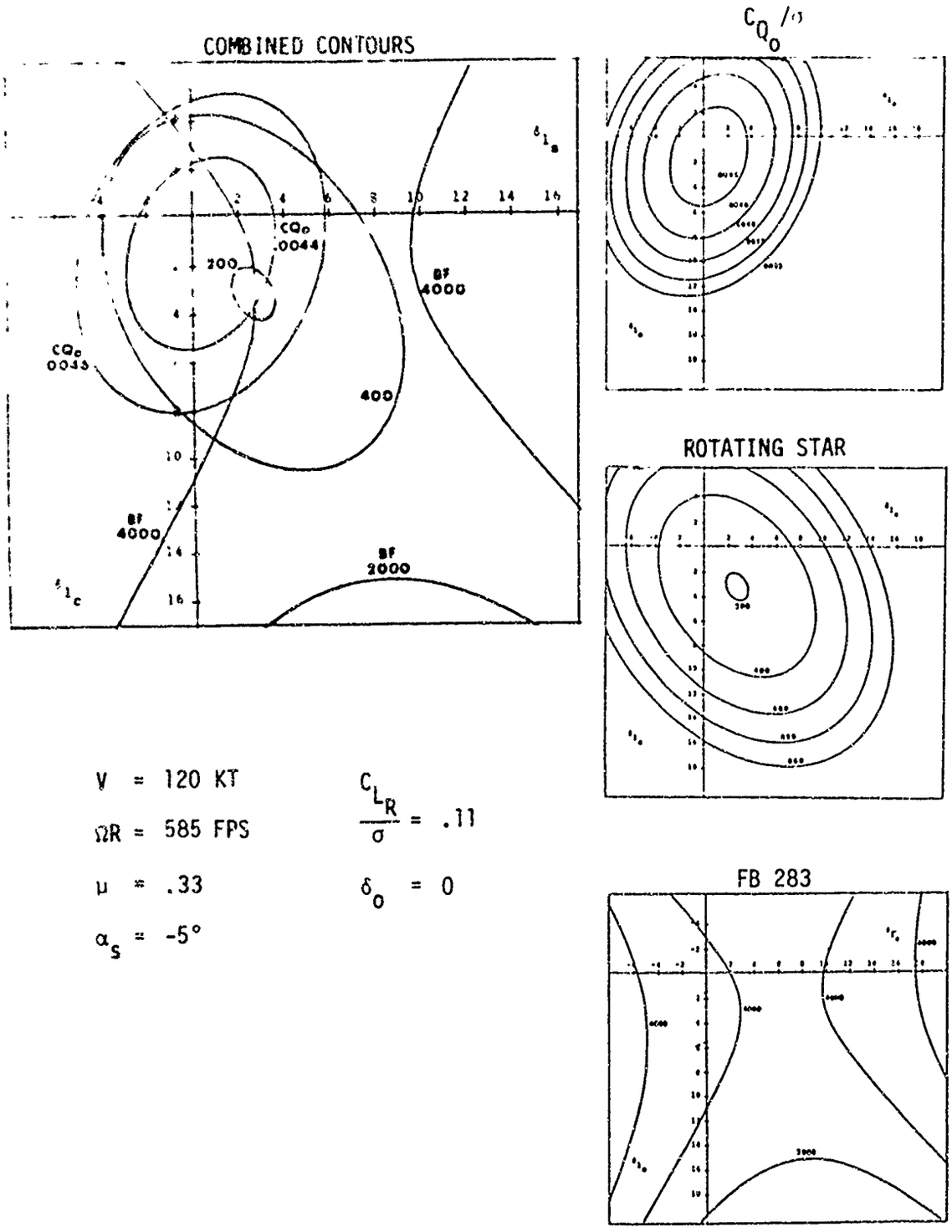

V = 120 KT

ΩR = 585 FPS

μ = .33

α_s = -5°

$\frac{C_{L_R}}{\sigma}$ = .11

δ_o = 0

Figure 9 (Continued)

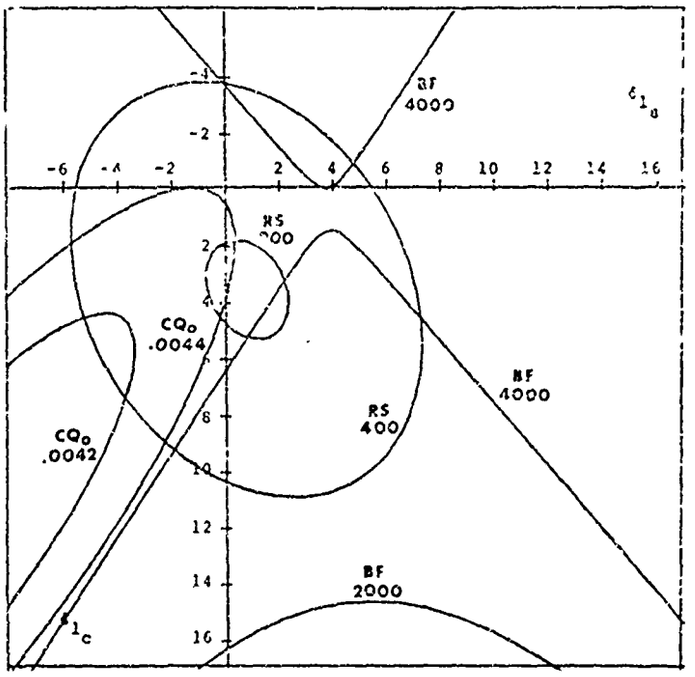

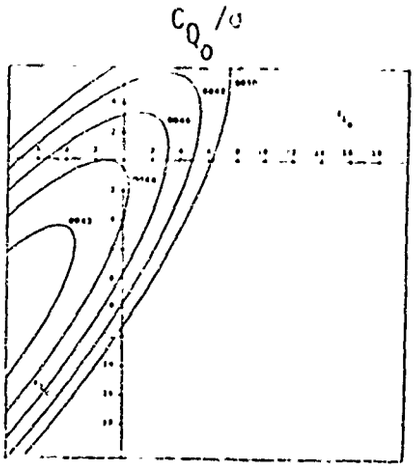

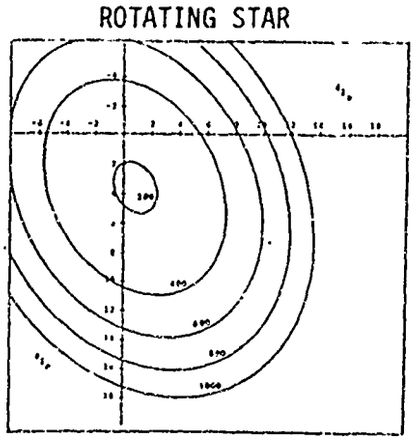

V = 120 KT

ΩR = 585 FPS

μ = .33

α_s = -5°

$\frac{C_{L_R}}{\sigma}$ = .11

δ_0 = 2

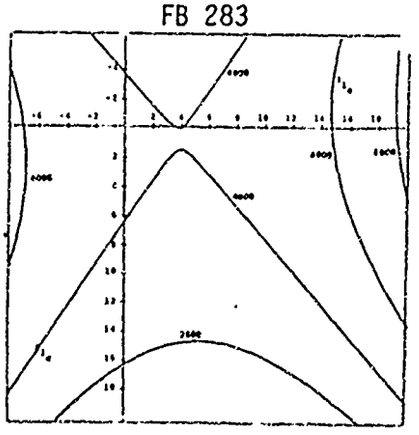

Figure 9 (Continued)

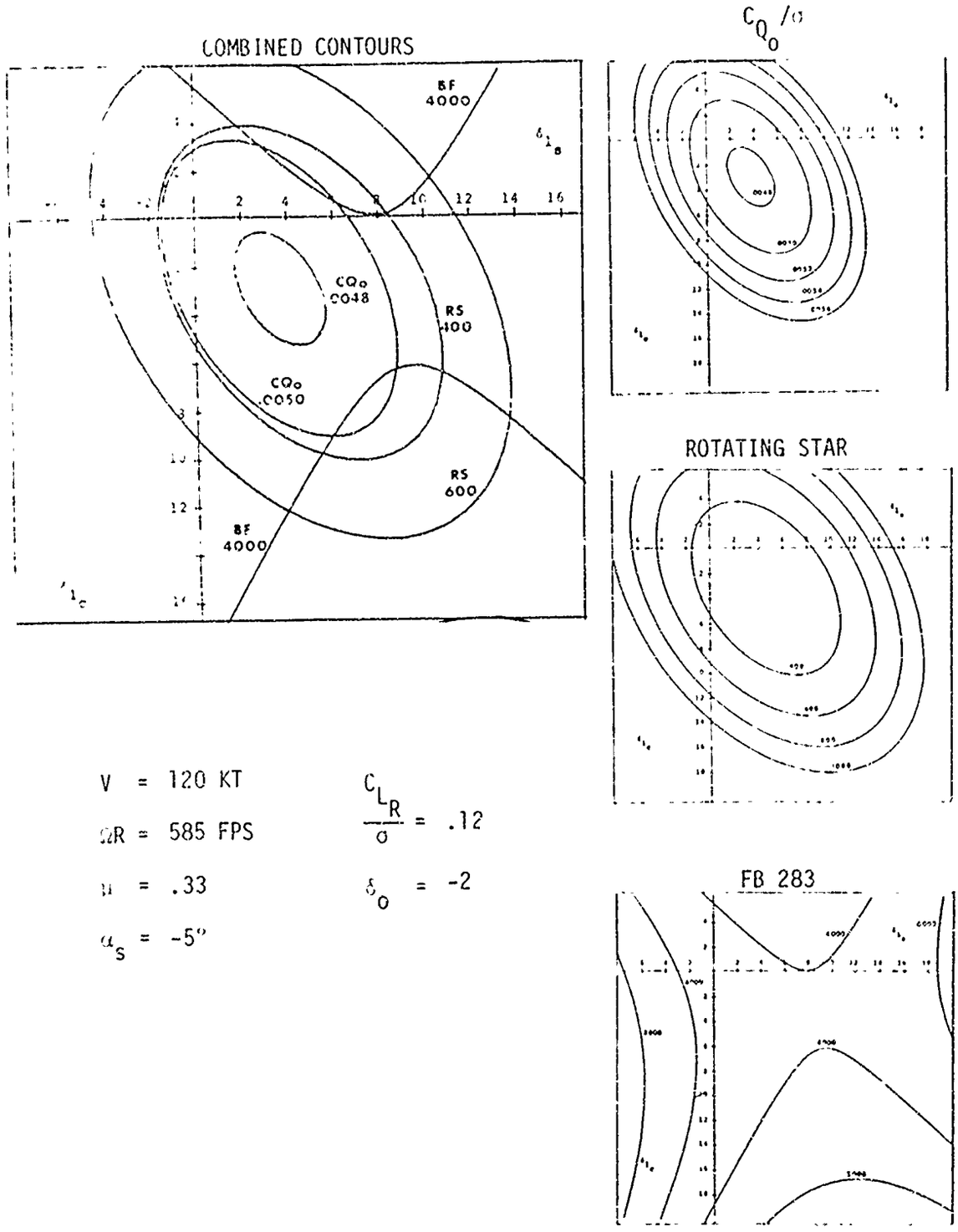

V = 120 KT

ΩR = 585 FPS

μ = .33

α_s = -5°

$\frac{C_{L_R}}{\sigma}$ = .12

δ_0 = -2

Figure 9 (Continued)

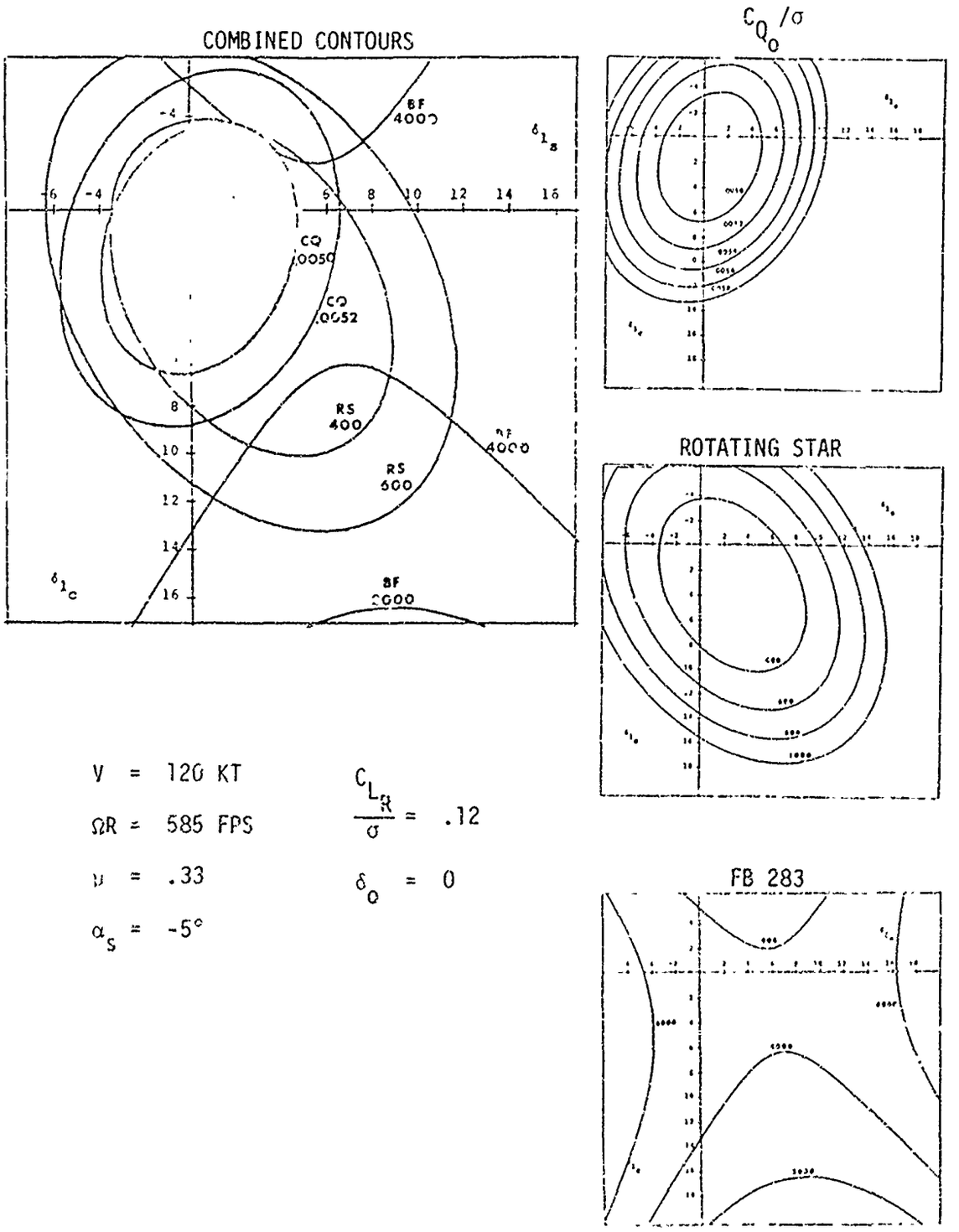

V = 120 KT

ΩR = 585 FPS

μ = .33

α_s = -5°

$\frac{C_{L_R}}{\sigma}$ = .12

δ_o = 0

Figure 9 (Continued)

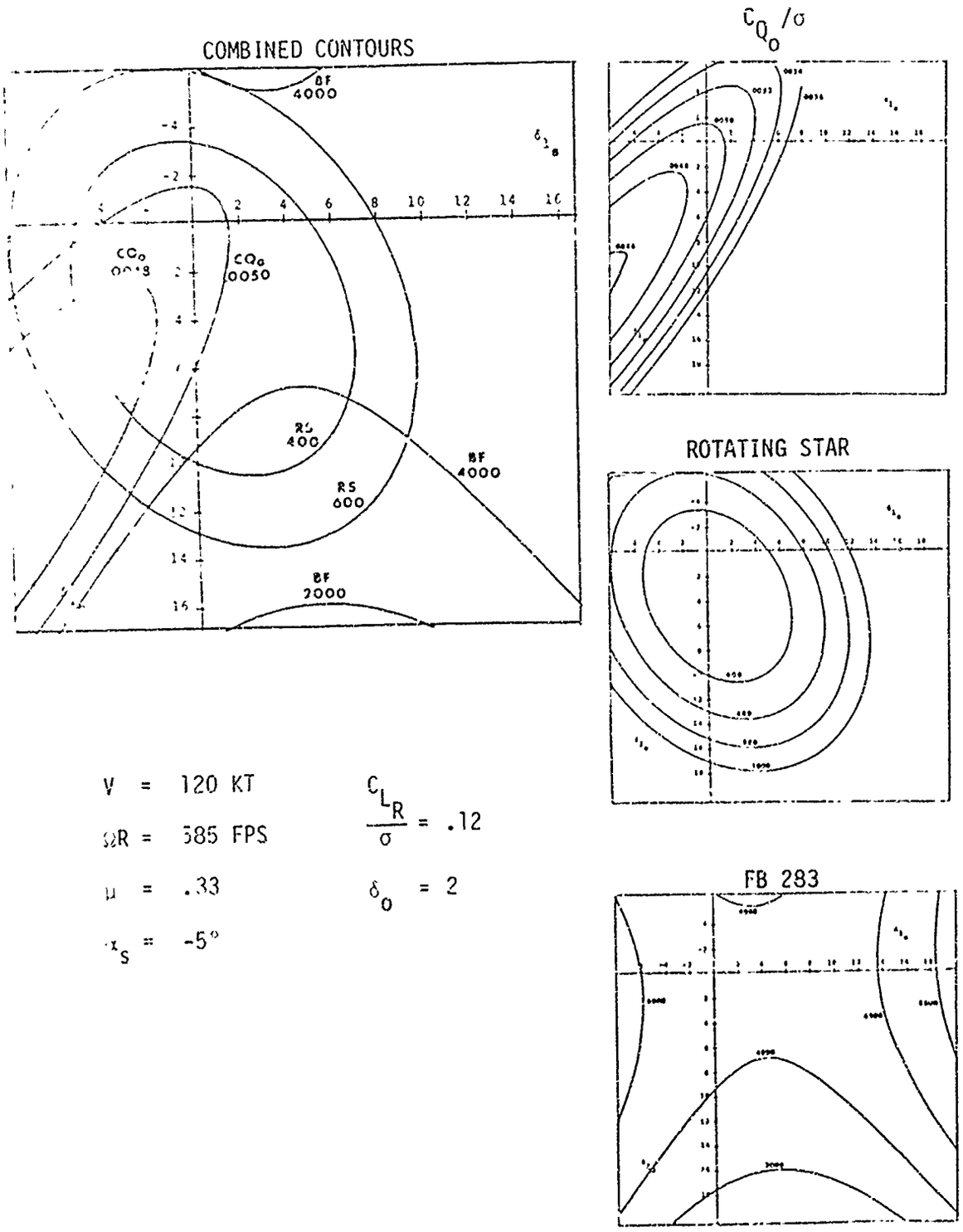

V = 120 KT

ΩR = 385 FPS

μ = .33

α_s = -5°

$\frac{C_{L_R}}{\sigma}$ = .12

δ_o = 2

Figure 9 (Concluded)

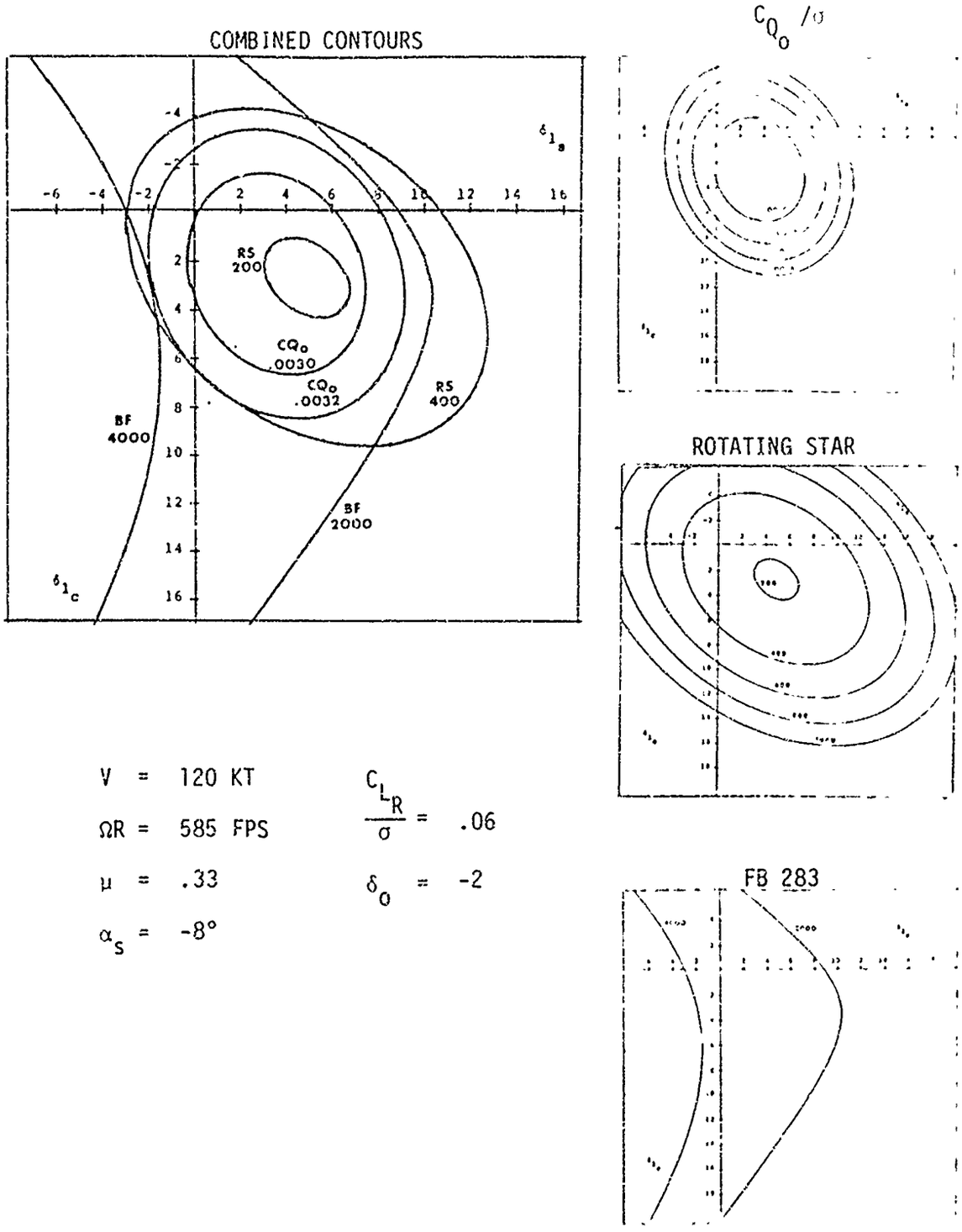

V = 120 KT

ΩR = 585 FPS

μ = .33

α_s = -8°

$\frac{C_{L_R}}{\sigma}$ = .06

δ_0 = -2

Figure 10. Optimization Response Contours at 120 Knots and -8° Shaft Tilt

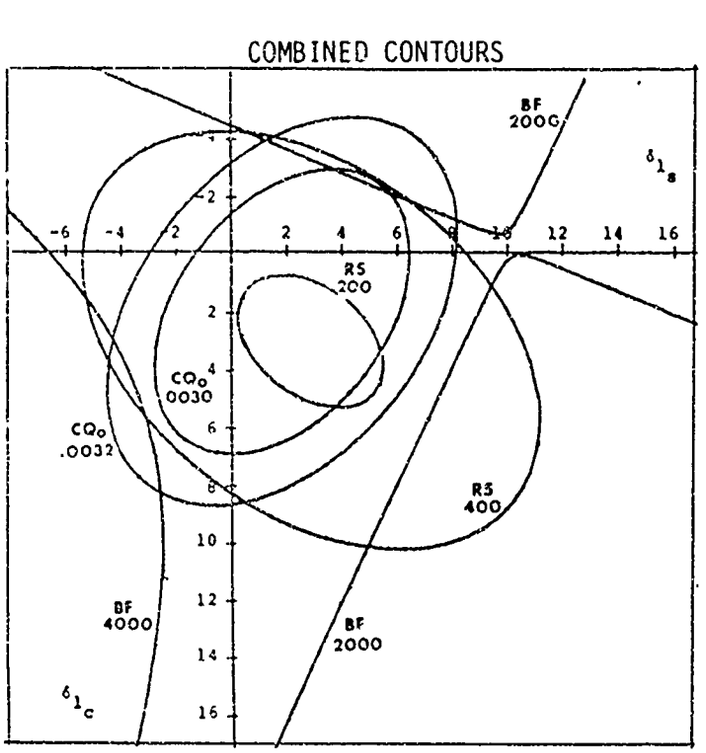

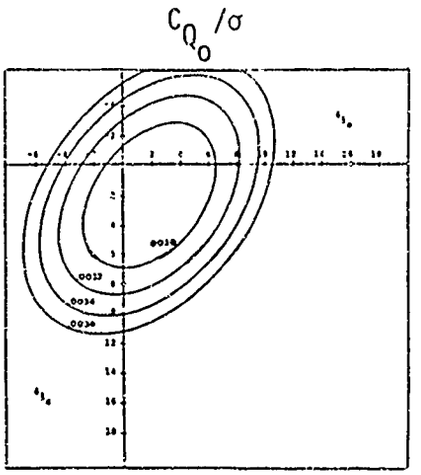

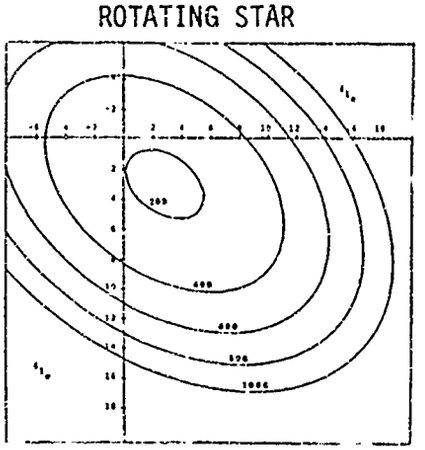

V = 120 KT

ΩR = 585 FPS

μ = .33

α_s = -8°

$\frac{C_{L_R}}{\sigma}$ = .06

δ_o = 0

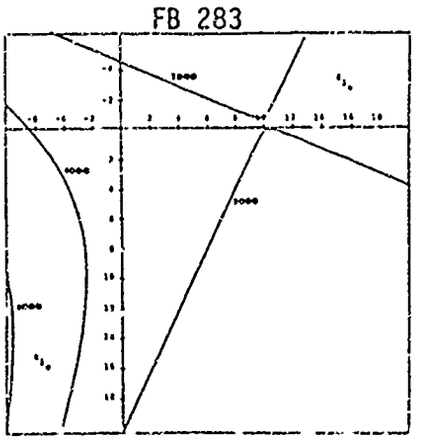

Figure 10 (Continued)

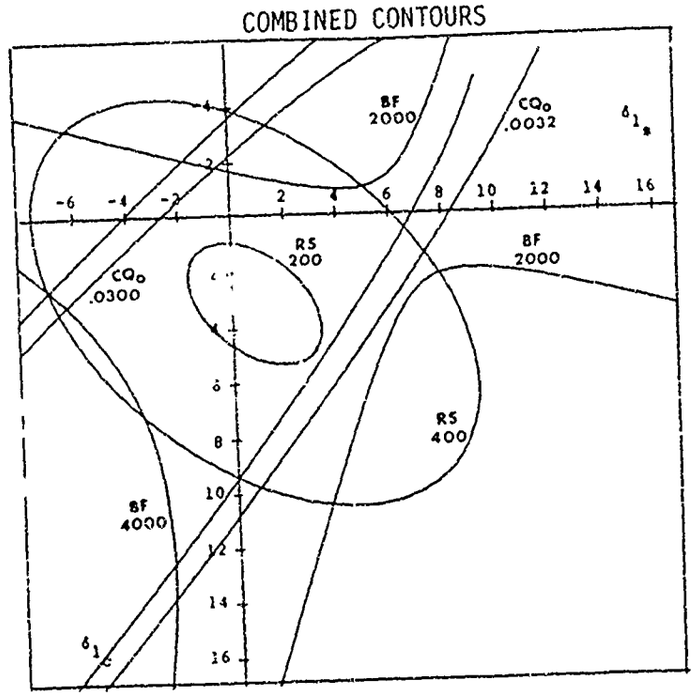

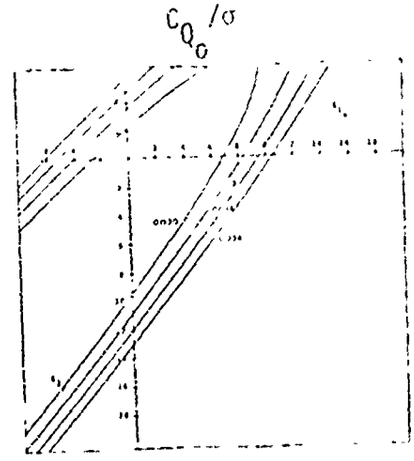

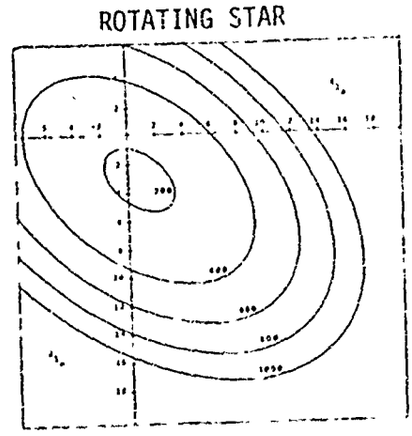

V = 120 KT

ΩR = 585 FPS

μ = .33

α_s = -8°

$\frac{C_{L_R}}{\sigma}$ = .06

δ_0 = 2

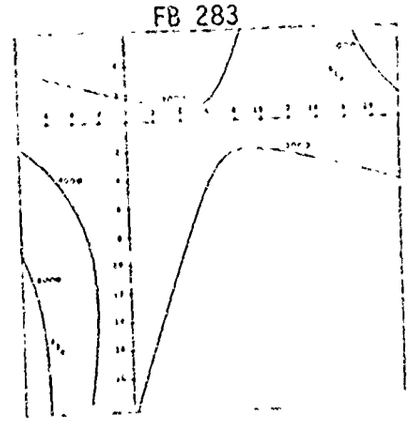

Figure 10 (Continued)

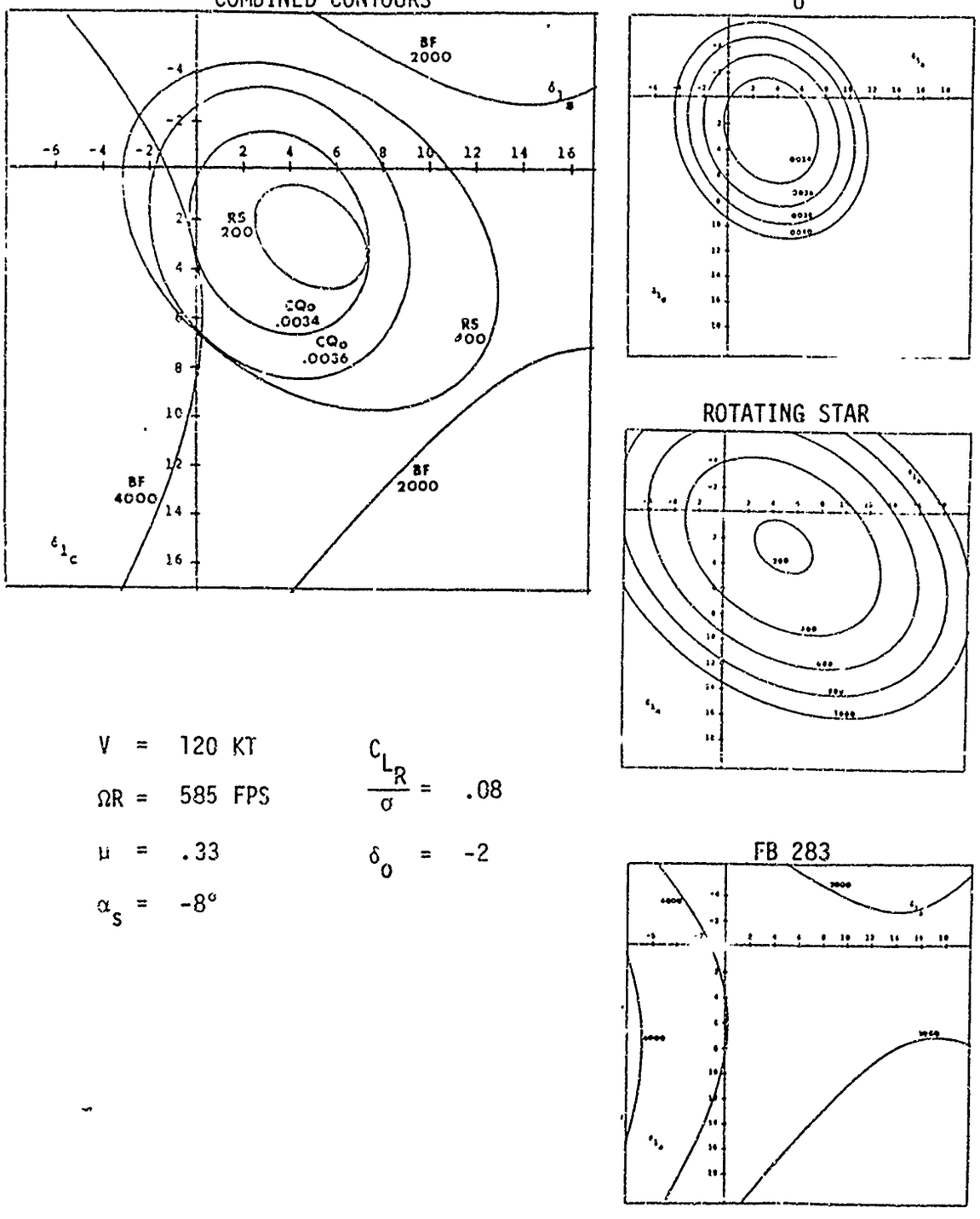

$V = 120$ KT

$\Omega R = 585$ FPS

$\mu = .33$

$\alpha_s = -8°$

$\frac{C_{L_R}}{\sigma} = .08$

$\delta_0 = -2$

Figure 10 (Continued)

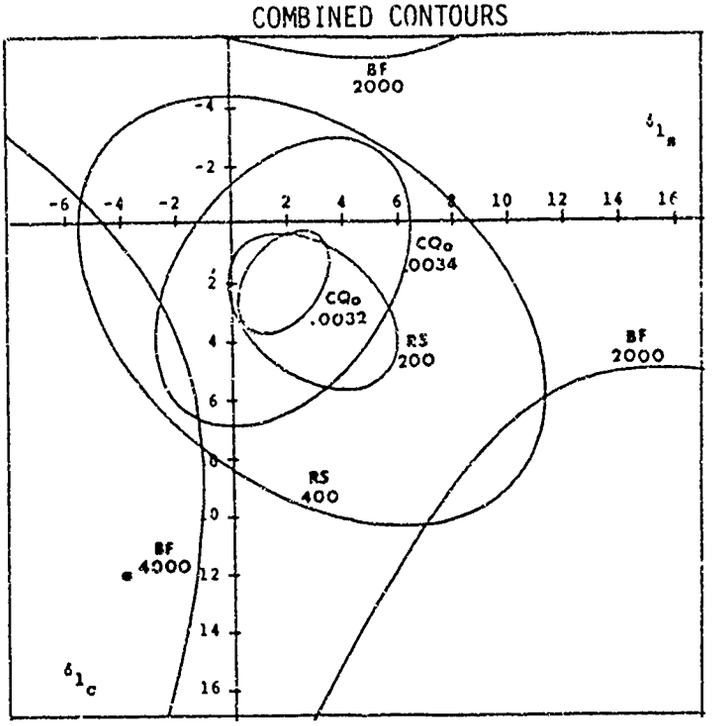

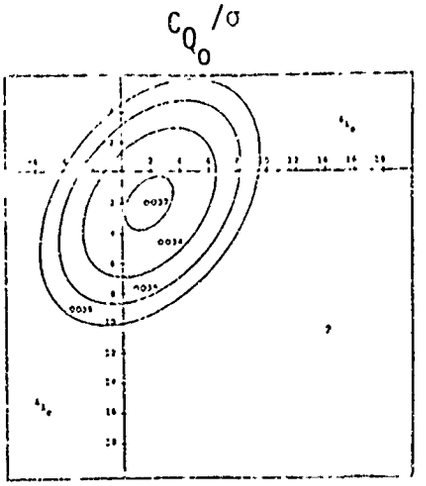

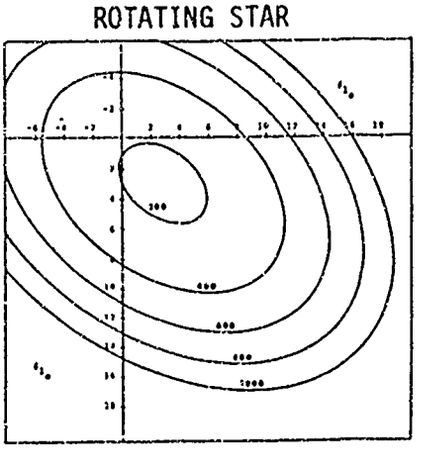

V = 120 KT

ΩR = 585 FPS

μ = .33

α_s = -8°

$\frac{C_{L_R}}{\sigma}$ = .08

δ_o = 0

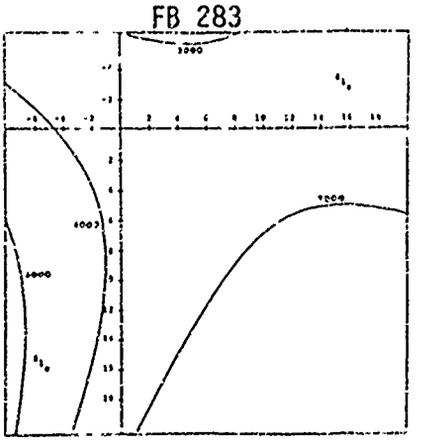

Figure 10 (Continued)

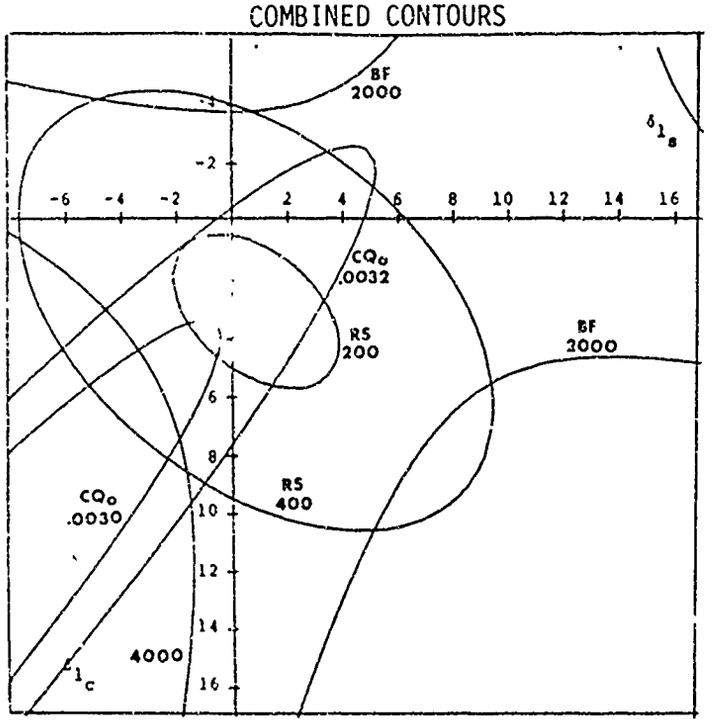

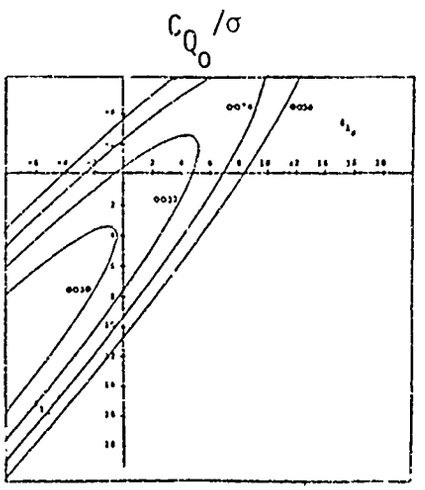

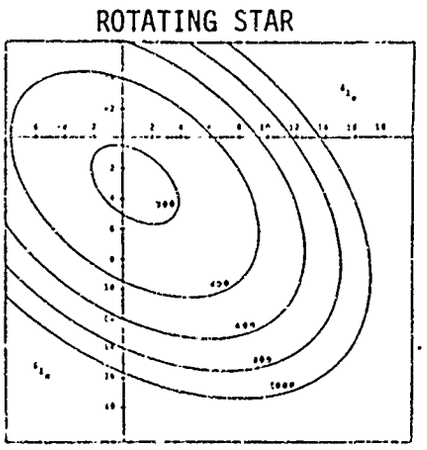

V = 120 KT

ΩR = 585 FPS

μ = .33

α_s = -8°

$\frac{C_{L_R}}{\sigma}$ = .08

δ_0 = 2

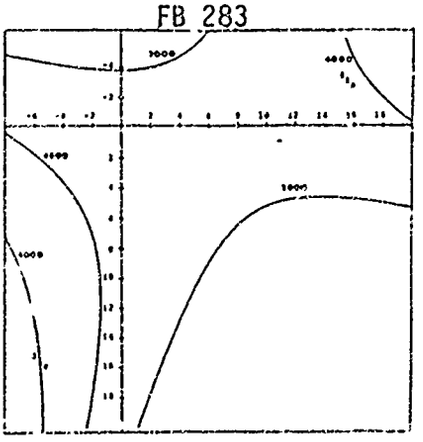

Figure 10 (Continued)

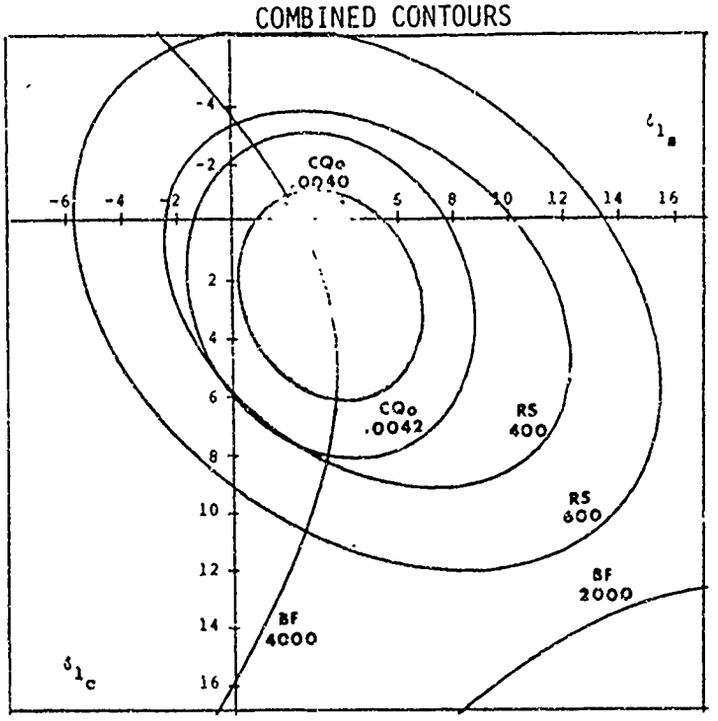

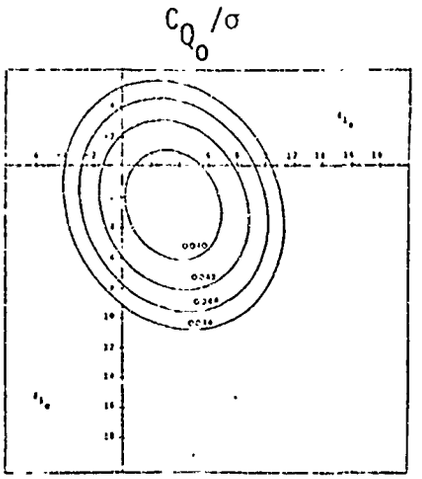

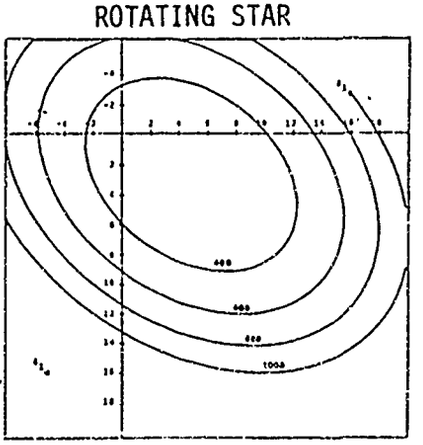

V = 120 KT

ΩR = 585 FPS

μ = .33

α_s = -8°

$\frac{C_{L_R}}{\sigma}$ = .10

δ_o = -2

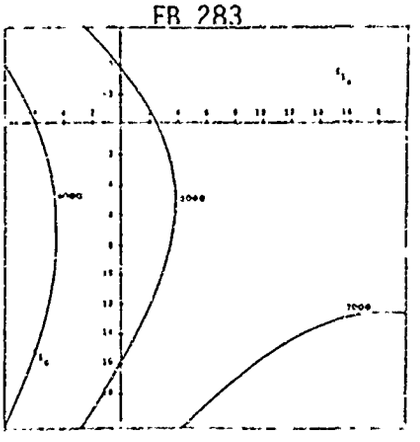

Figure 10 (Continued)

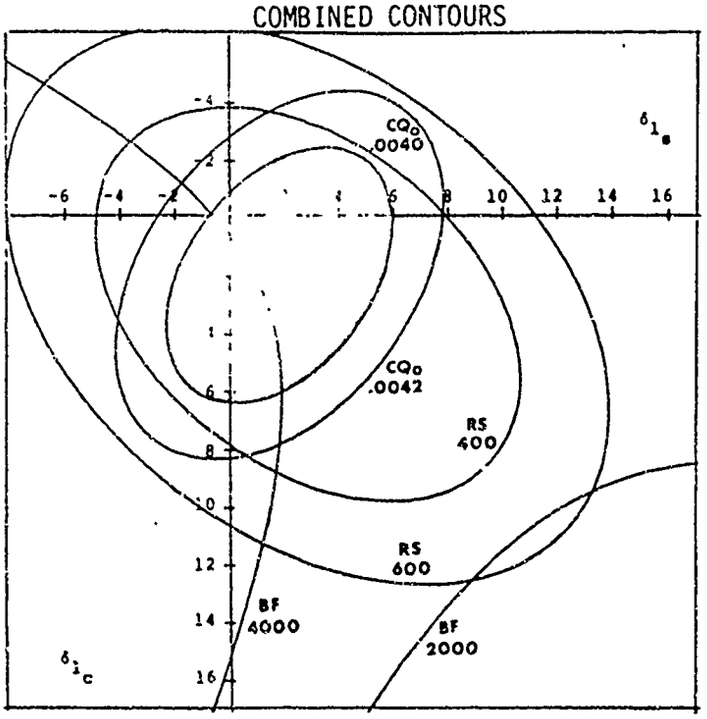

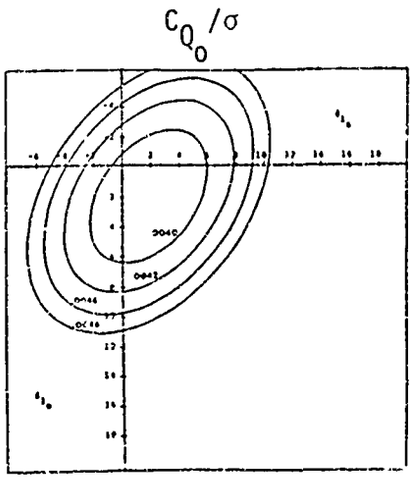

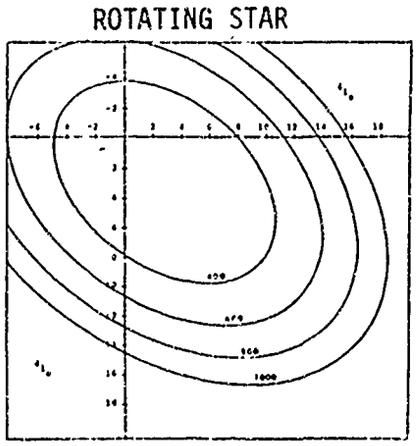

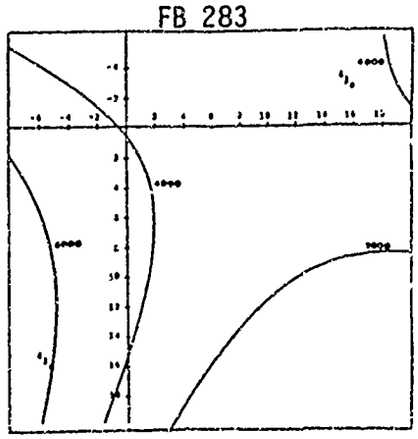

V = 120 KT

ΩR = 585 FPS

μ = .33

α_s = -8°

$\frac{C_{L_R}}{\sigma}$ = .10

δ_0 = 0

Figure 10 (Continued)

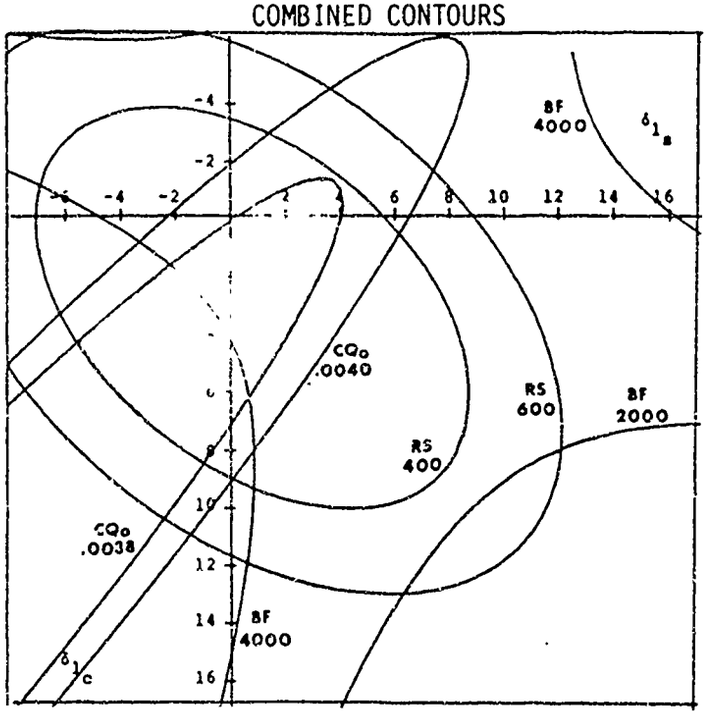

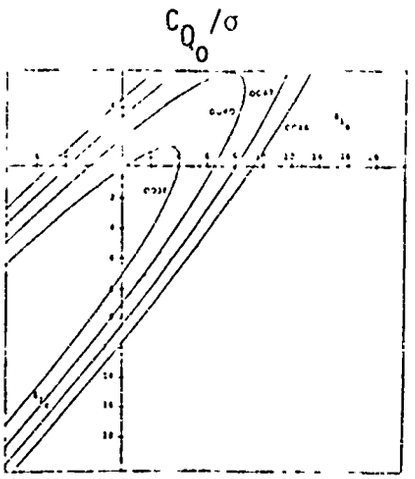

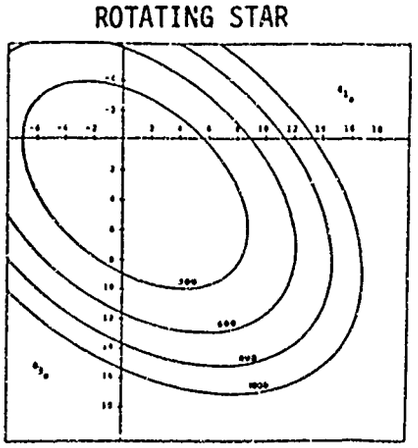

$V = 120$ KT

$\Omega R = 585$ FPS

$\mu = .33$

$\alpha_s = -8°$

$\frac{C_{L_R}}{\sigma} = .10$

$\delta_o = 2$

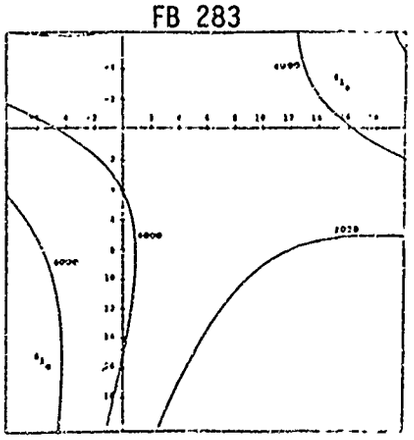

Figure 10 (Continued)

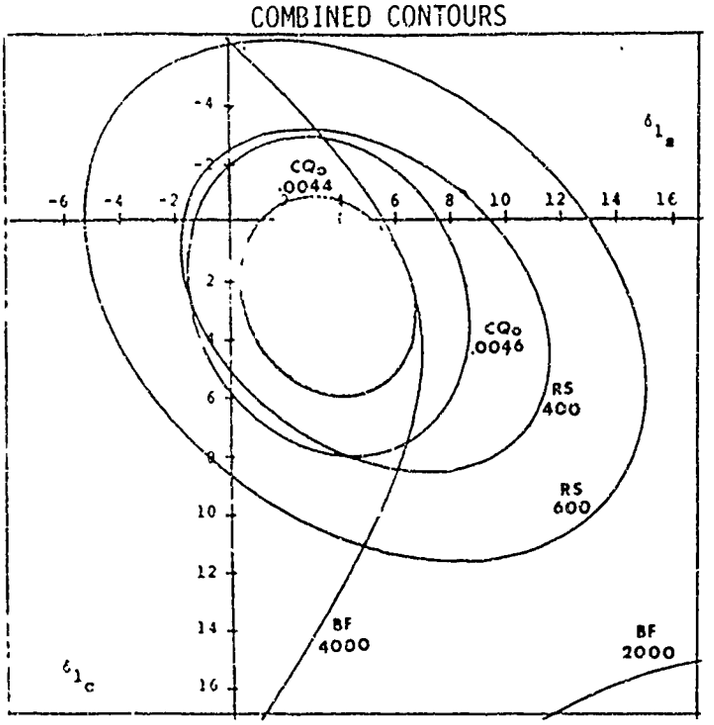

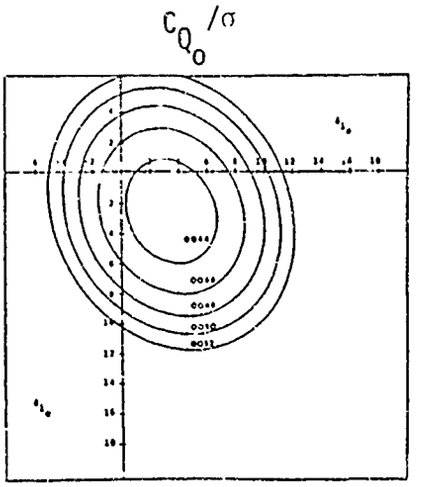

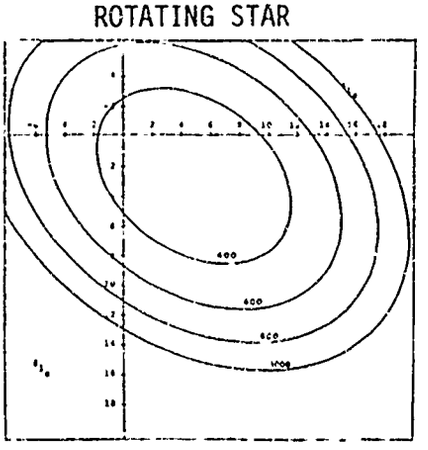

V = 120 KT

ΩR = 585 FPS

μ = .33

α_s = -8°

$\frac{C_{L_R}}{\sigma}$ = .11

δ_0 = -2

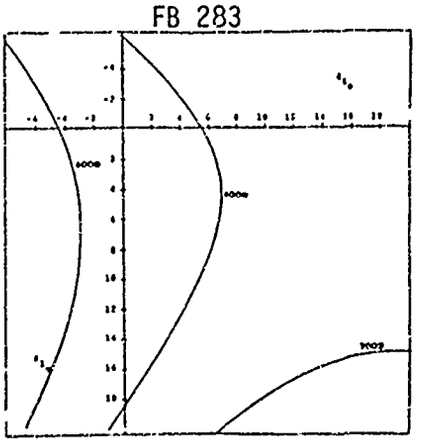

Figure 10 (Continued)

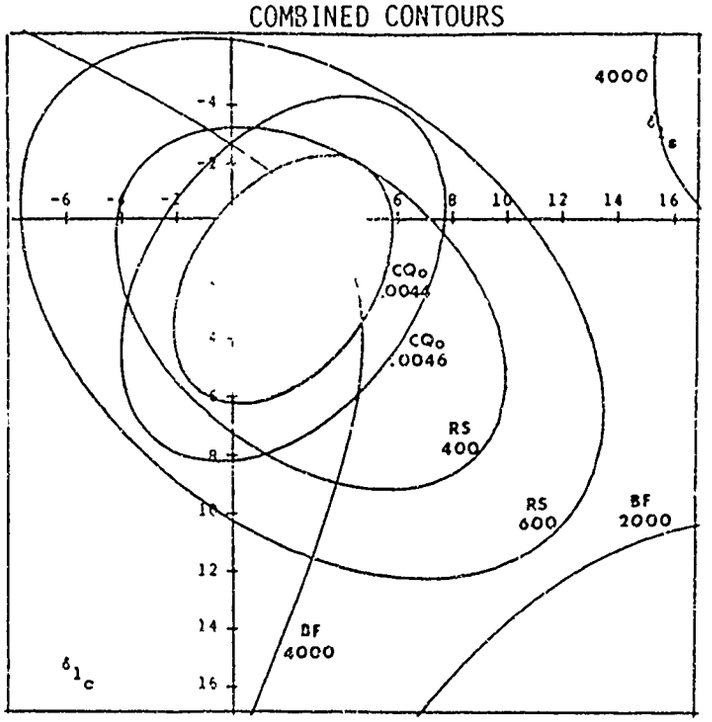

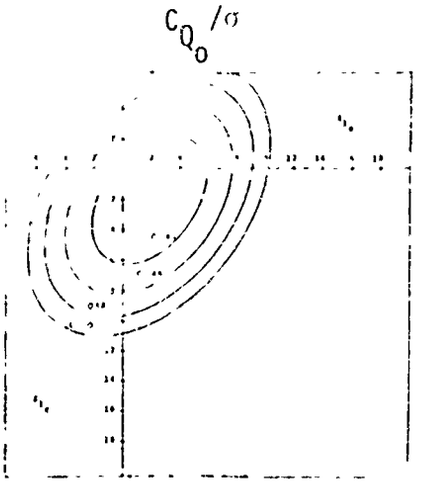

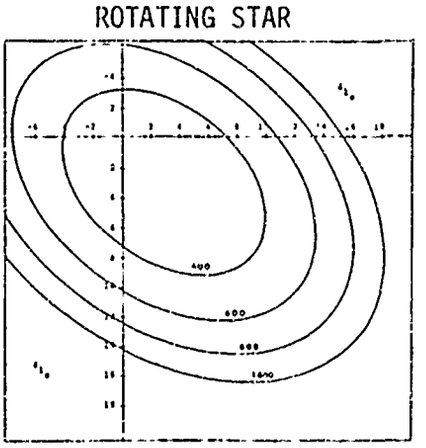

V = 120 KT

ΩR = 585 FPS

μ = .33

α_s = -8°

$\frac{C_{L_R}}{\sigma}$ = .11

δ_o = 0

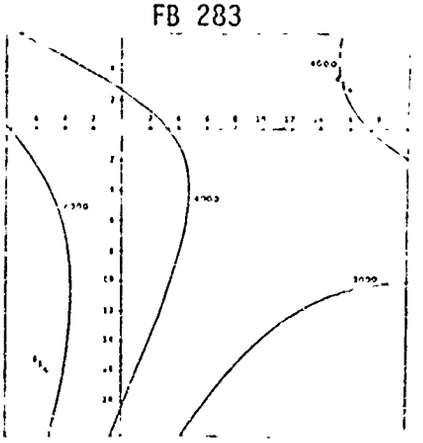

Figure 10 (Continued)

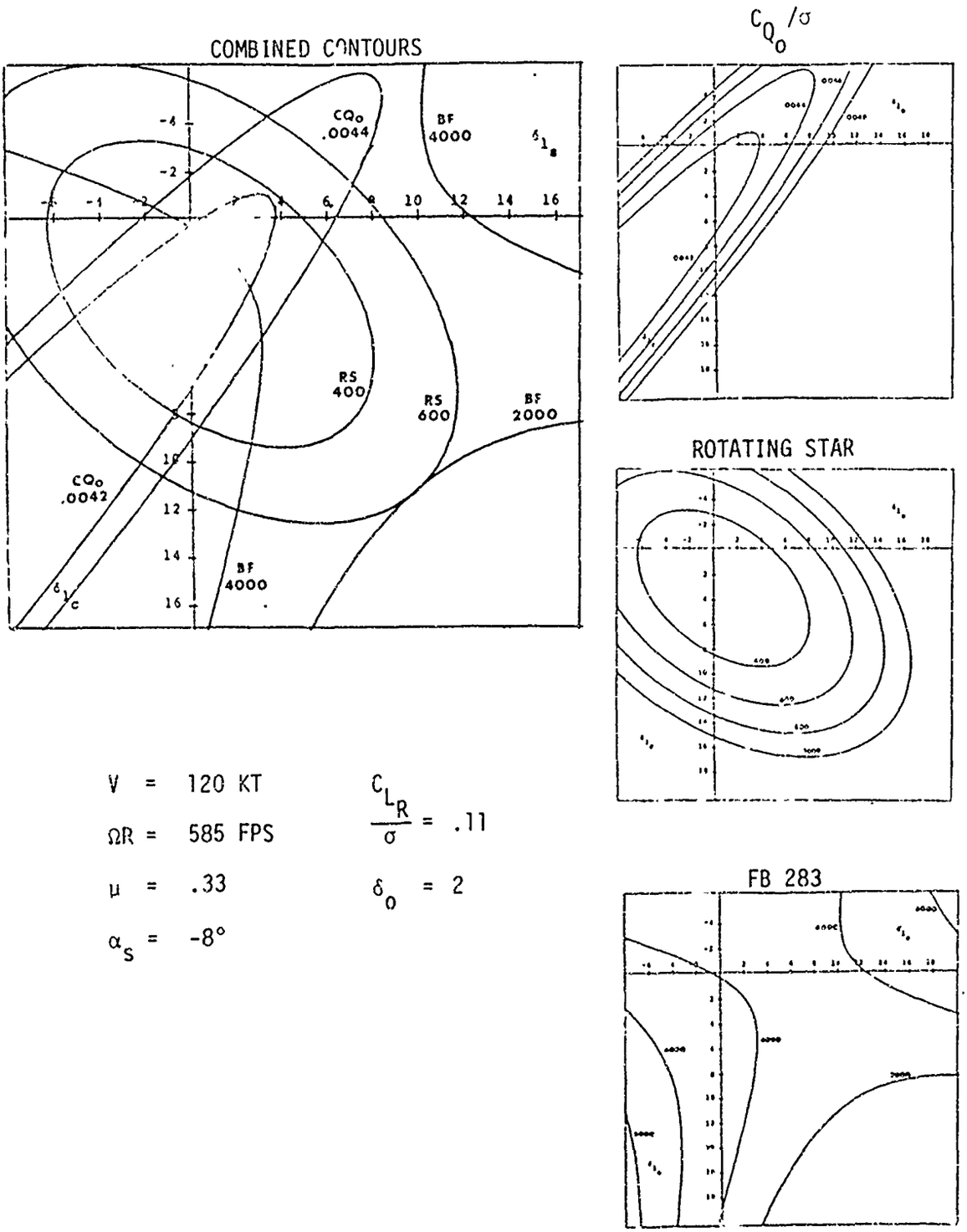

$V = 120$ KT $\qquad \frac{C_{L_R}}{\sigma} = .11$

$\Omega R = 585$ FPS $\qquad \delta_0 = 2$

$\mu = .33$

$\alpha_s = -8°$

Figure 10 (Continued)

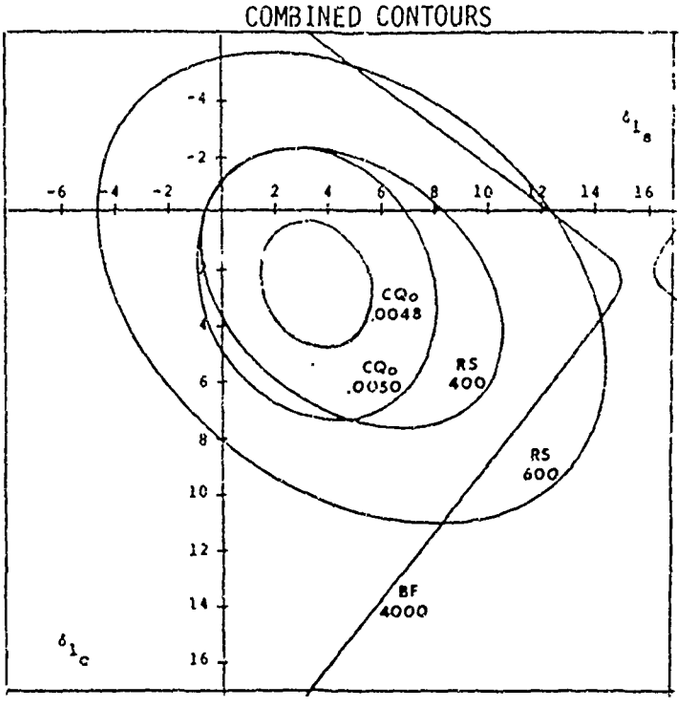

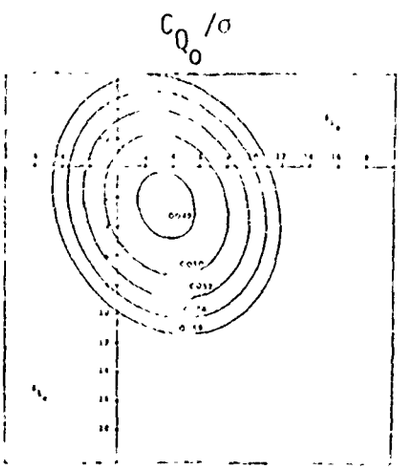

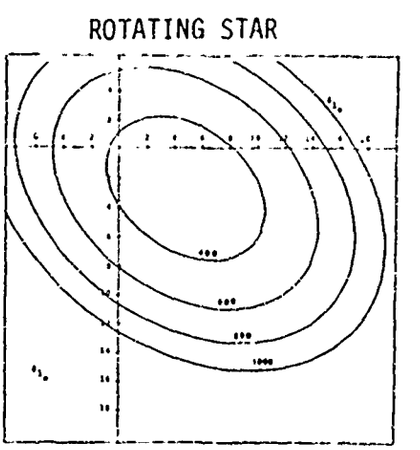

V = 120 KT

ΩR = 585 FPS

μ = .33

α_s = -8°

$\frac{C_{L_R}}{\sigma}$ = .12

δ_o = -2

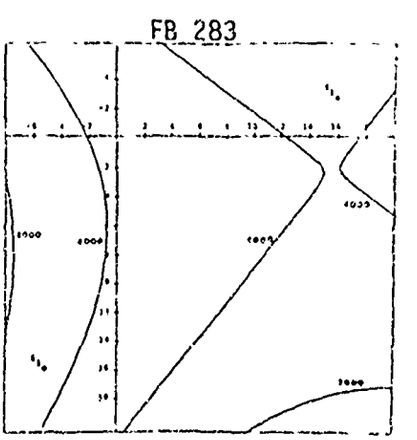

Figure 10 (Continued)

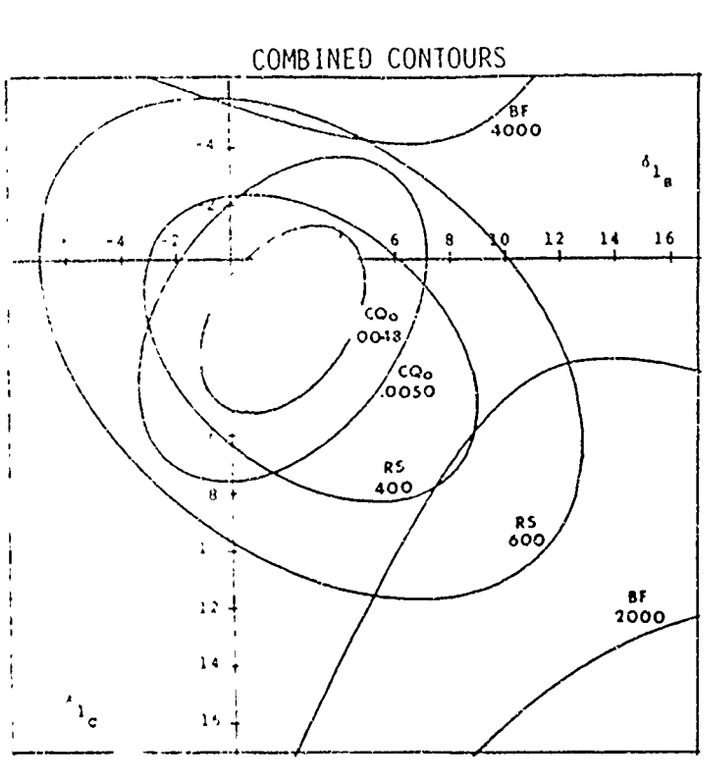

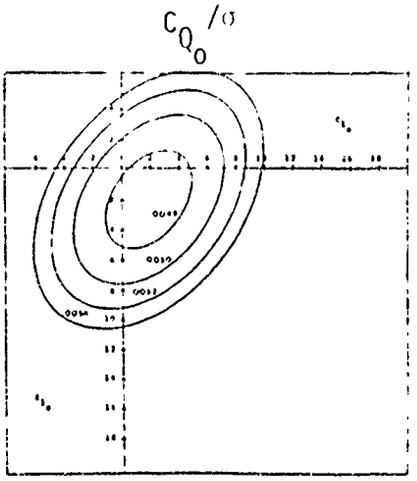

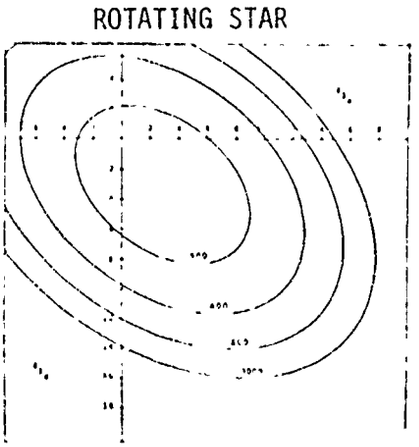

V = 120 KT

C_{L_R}/σ = .12

R = 585 FPS

= .33

δ_o = 0

i_s = -8°

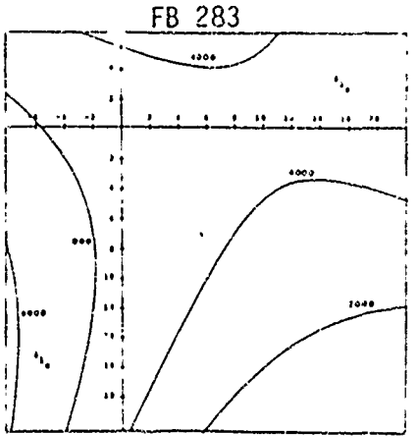

Figure 10 (Continued)

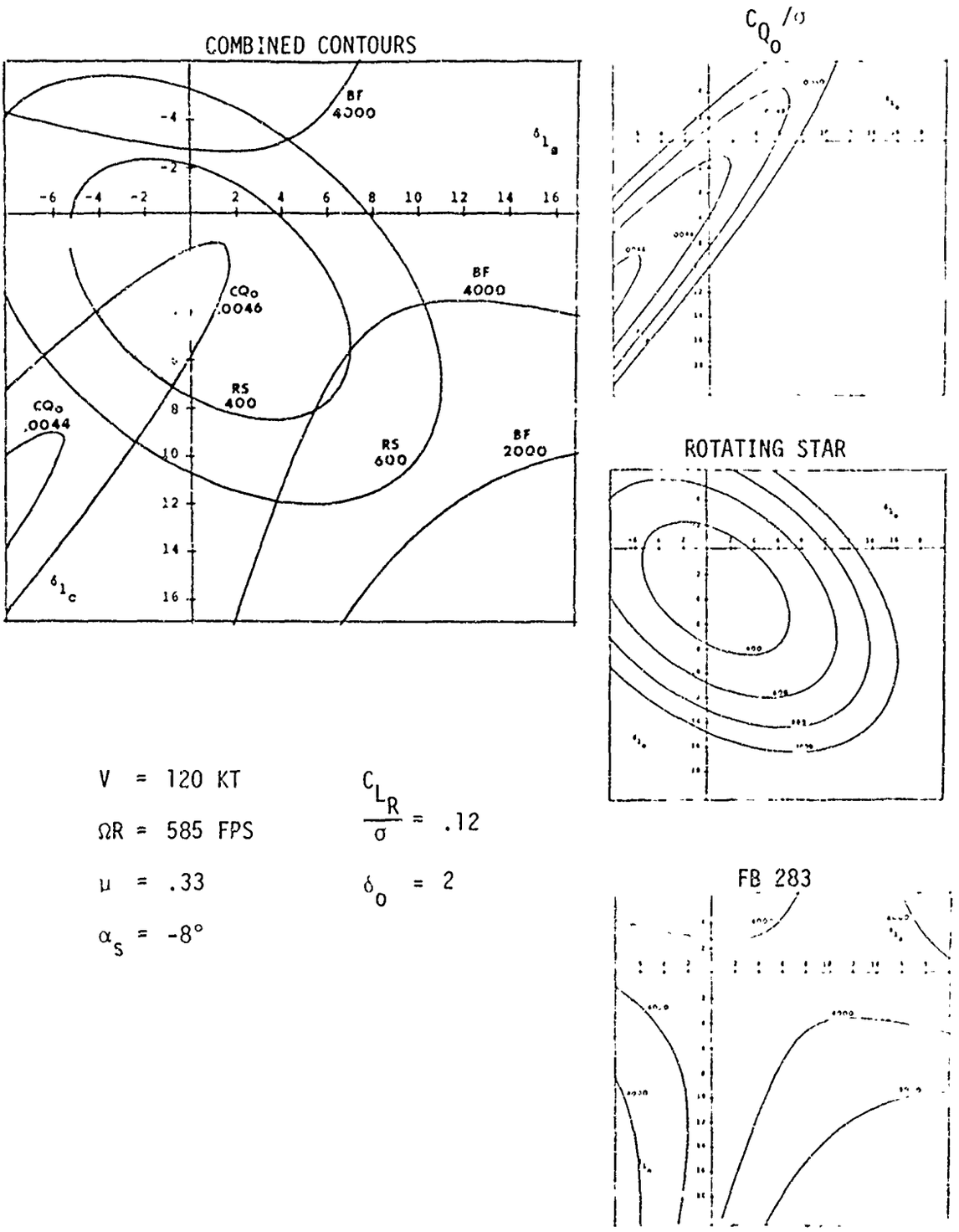

V = 120 KT

ΩR = 585 FPS

μ = .33

α_s = -8°

$\frac{C_{L_R}}{\sigma}$ = .12

δ_0 = 2

Figure 10 (Concluded)

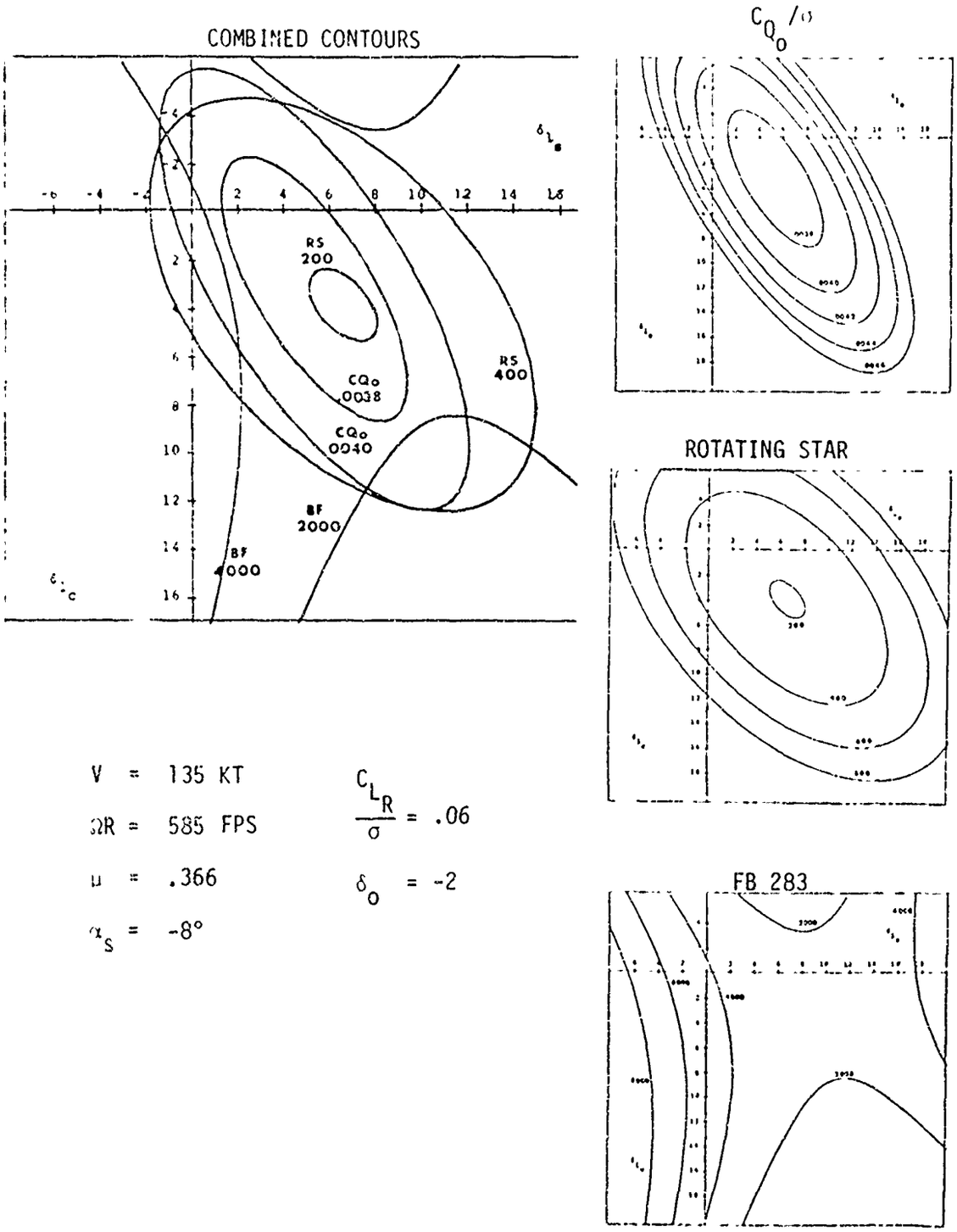

V = 135 KT

ΩR = 585 FPS

μ = .366

α_S = -8°

$\frac{C_{L_R}}{\sigma}$ = .06

δ_o = -2

Figure 11. Optimization Response Contours at 135 Knots and -8° Shaft Tilt

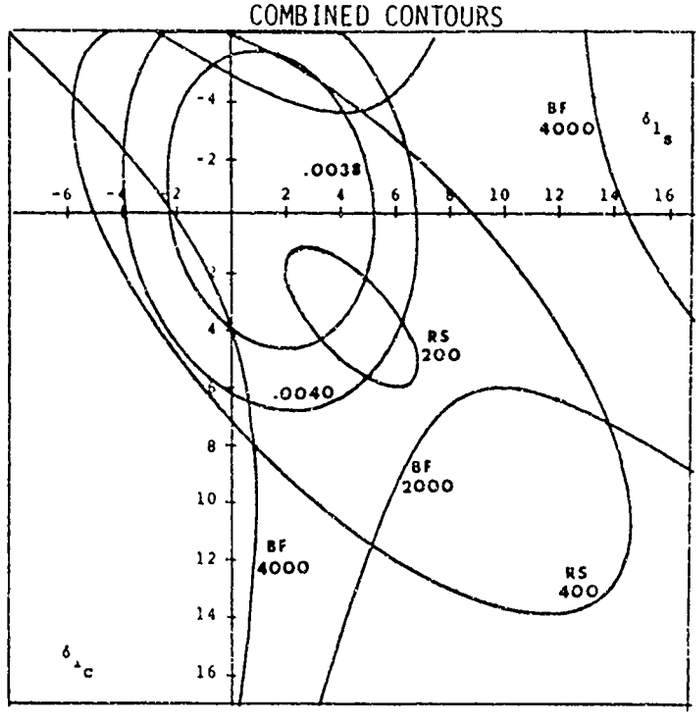

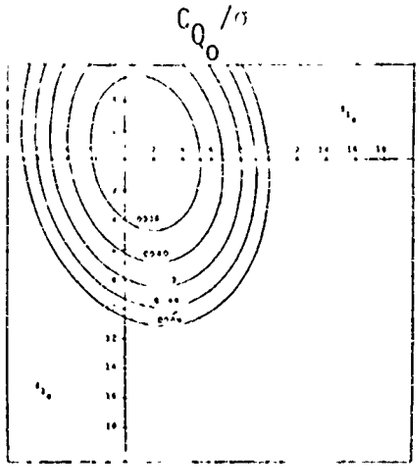

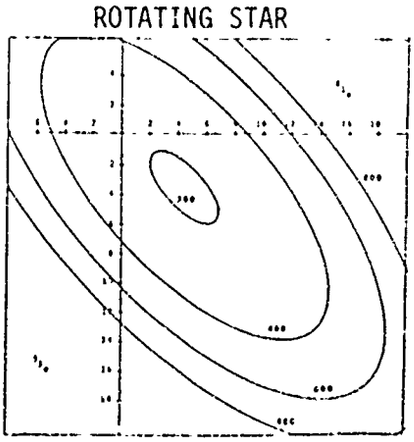

V = 135 KT

ΩR = 585 FPS

μ = .366

α_s = ~8°

$\frac{C_{L_R}}{\sigma}$ = .06

δ_o = 0

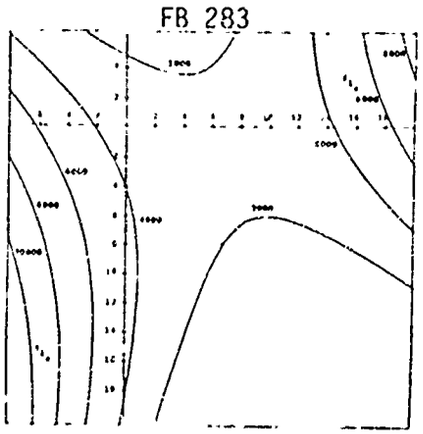

Figure 11 (Continued)

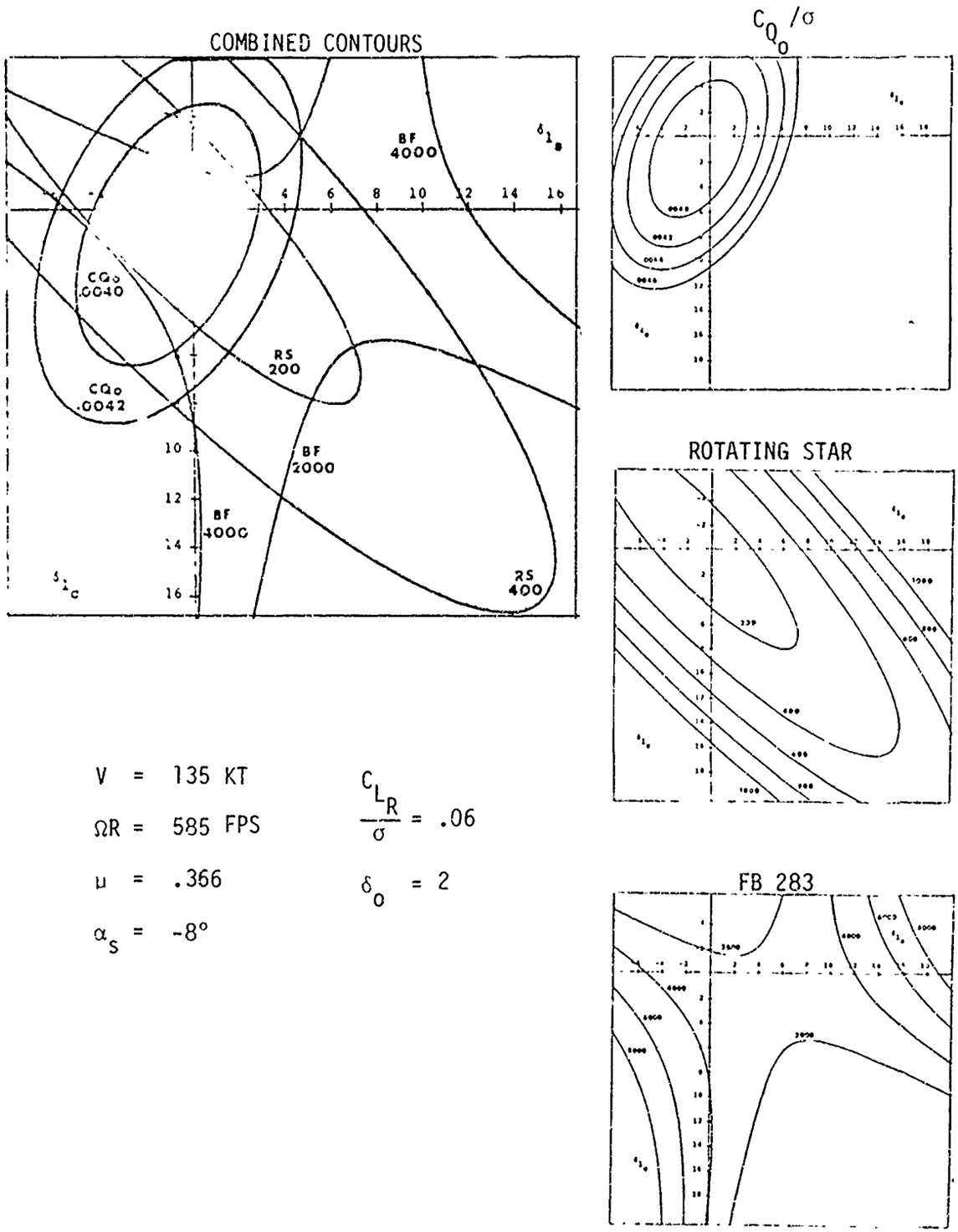

V = 135 KT

ΩR = 585 FPS

μ = .366

α_s = -8°

$\frac{C_{L_R}}{\sigma}$ = .06

δ_o = 2

Figure 11 (Continued)

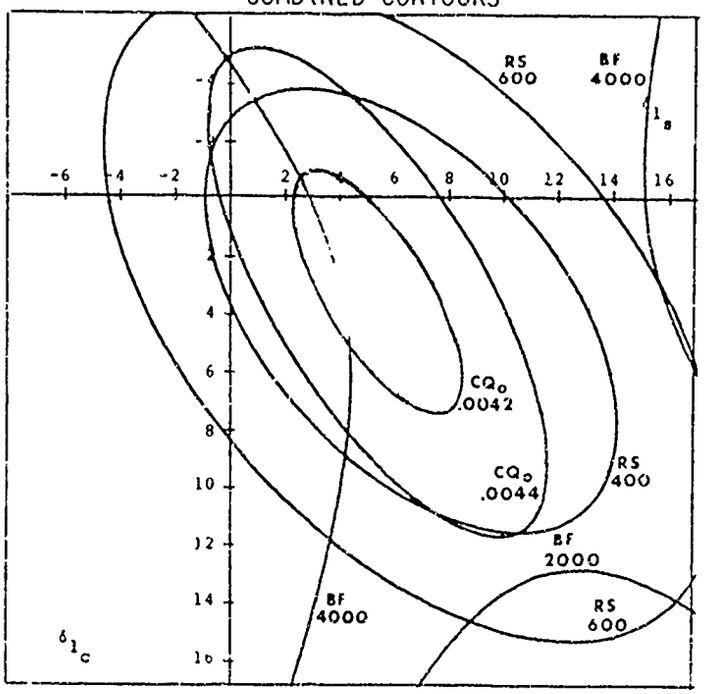

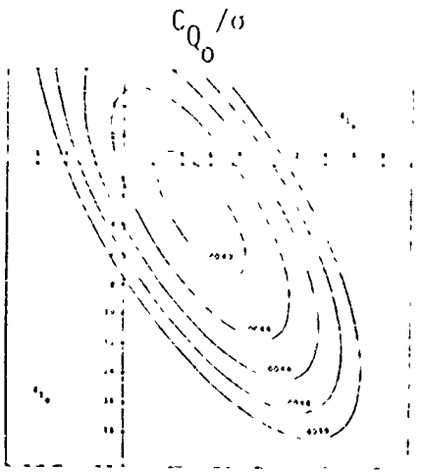

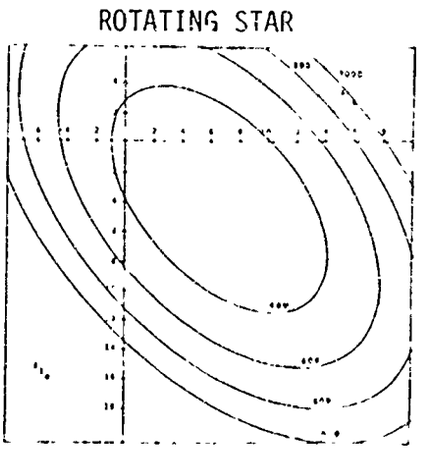

V = 135 KT

ΩR = 585 FPS

μ = .366

α_s = -8°

$\frac{C_{L_R}}{\sigma}$ = .08

δ_0 = -2

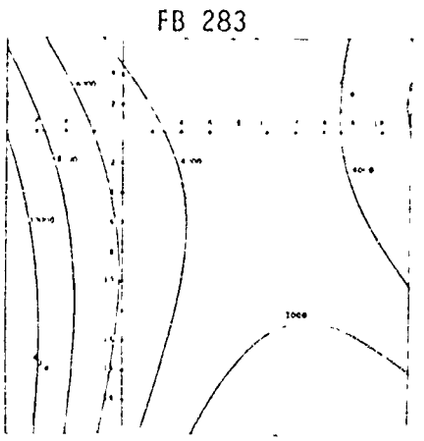

Figure 11 (Continued)

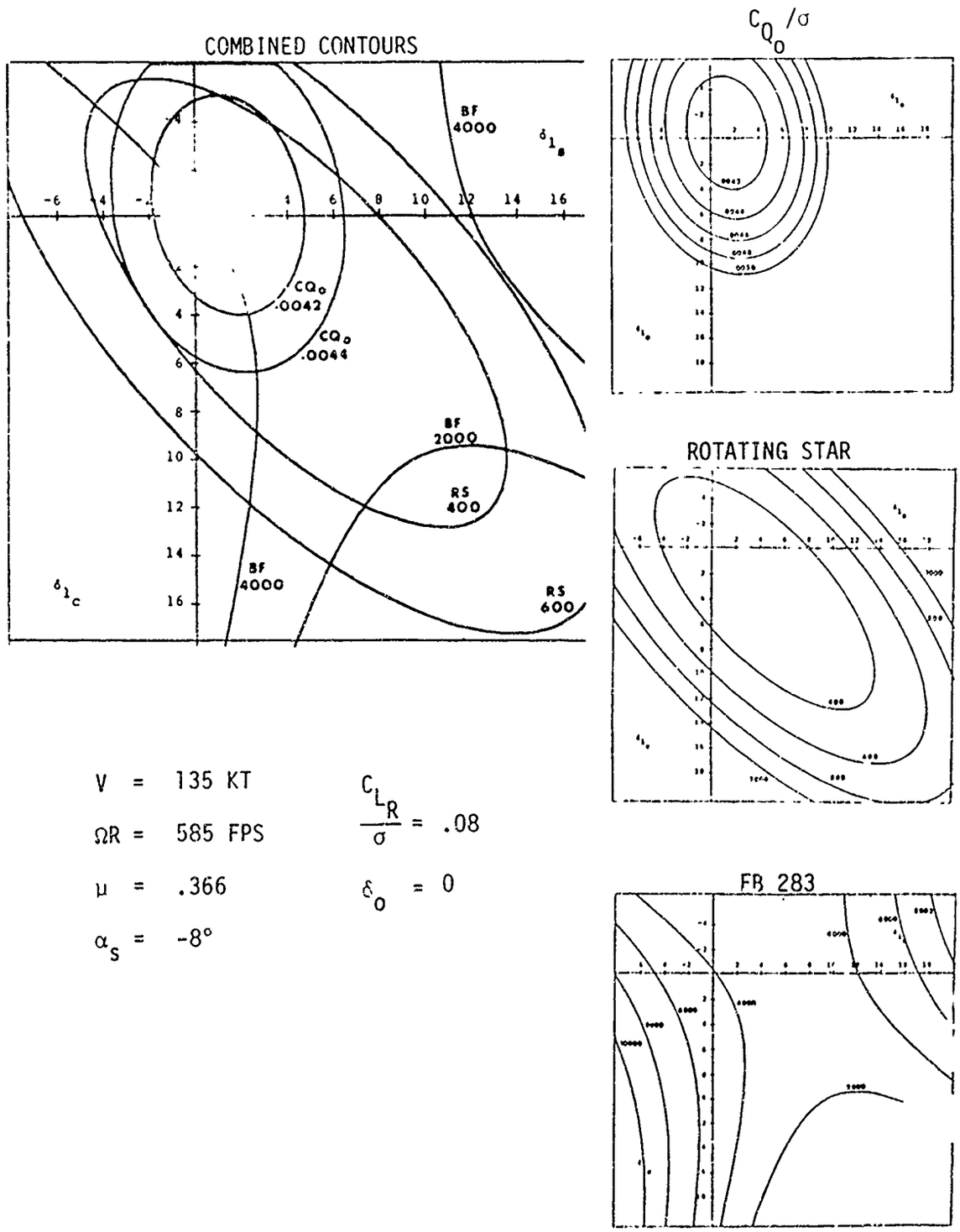

Figure 11 (Continued)

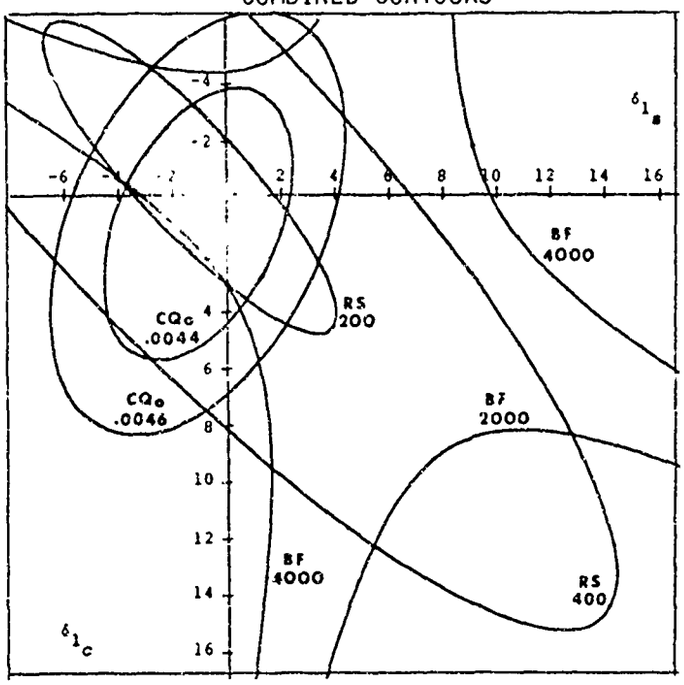

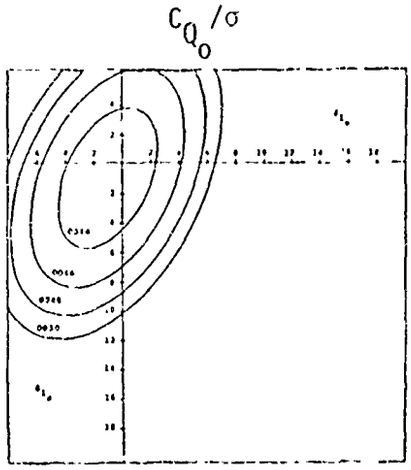

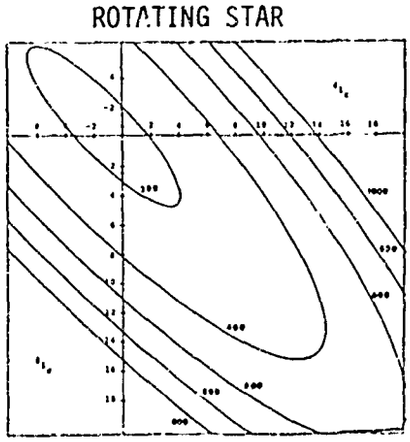

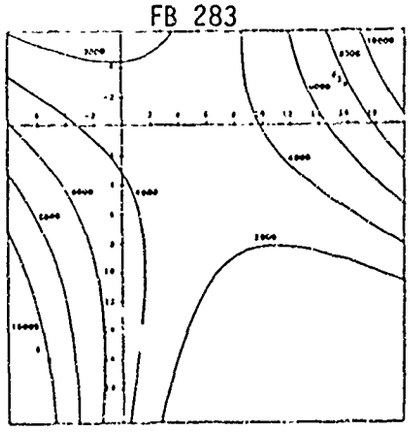

V = 135 KT

ΩR = 585 FPS

μ = .366

α_s = -8°

$\frac{C_{L_R}}{\sigma}$ = .08

δ_o = 2

Figure 11 (Continued)

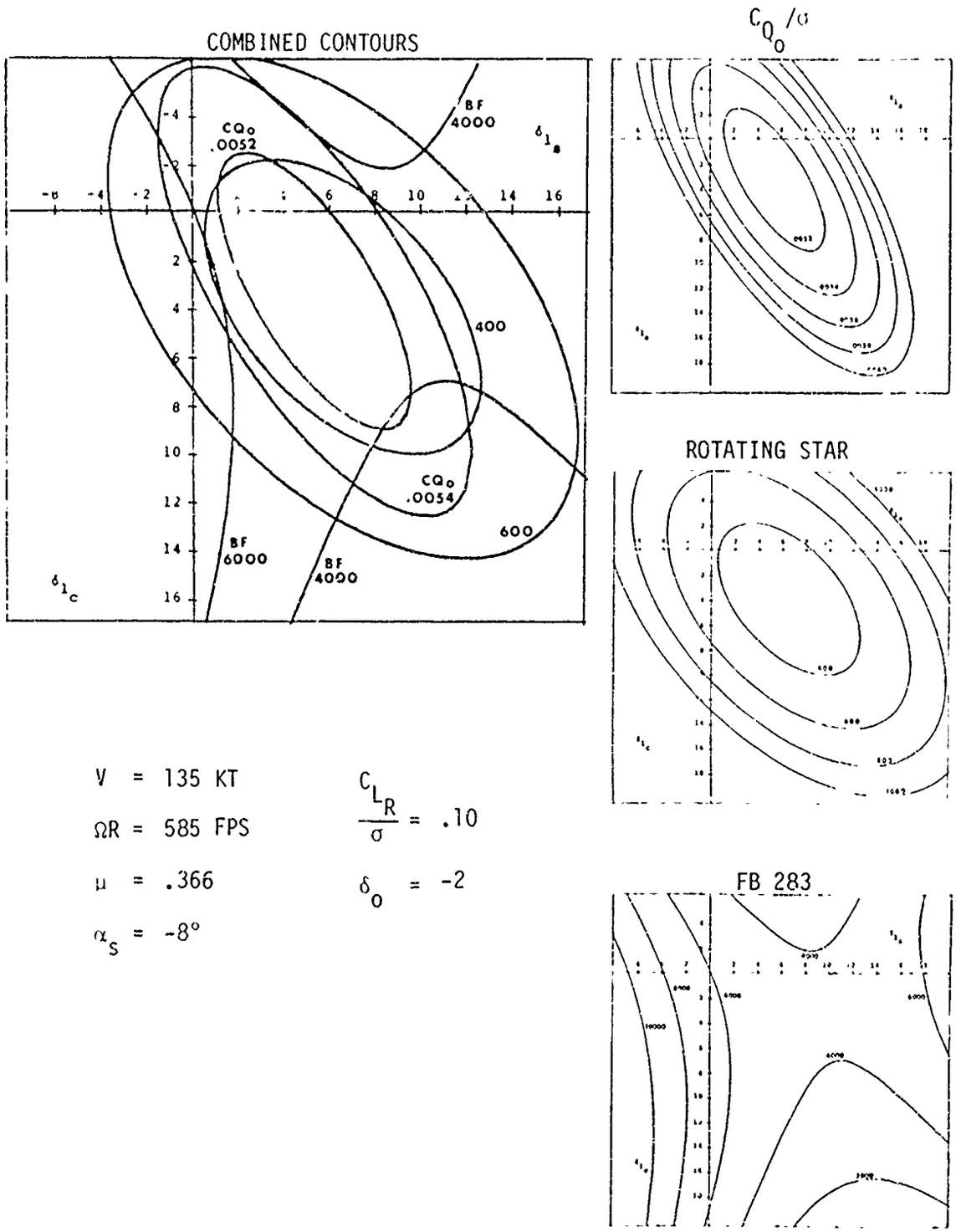

Figure 11 (Continued)

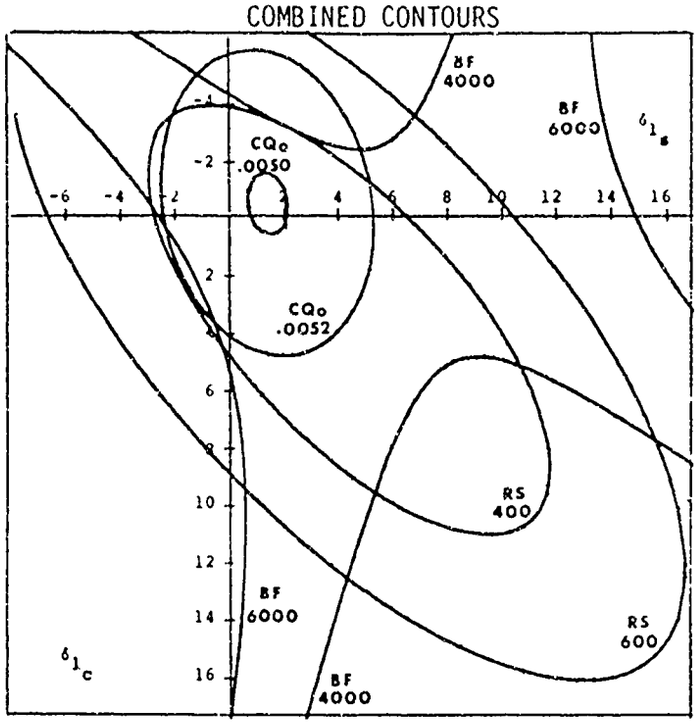

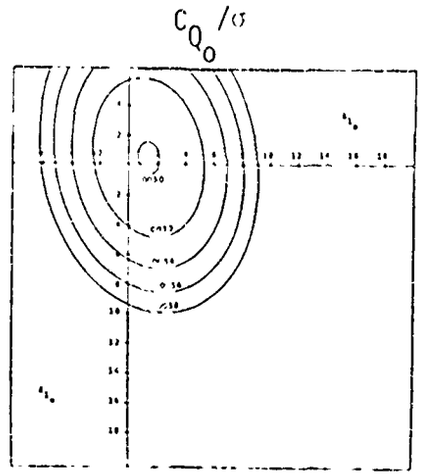

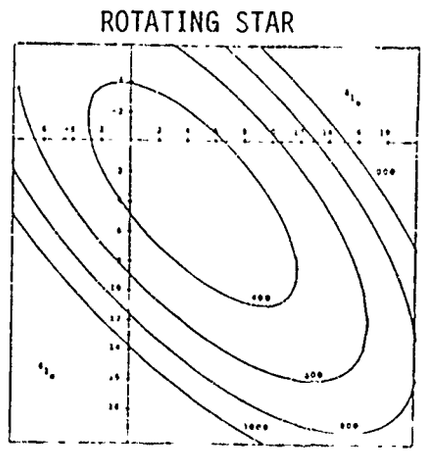

V = 135 KT

ΩR = 685 FPS

μ = .366

α_s = -8°

$\frac{C_{L_R}}{\sigma}$ = .10

δ_o = 0

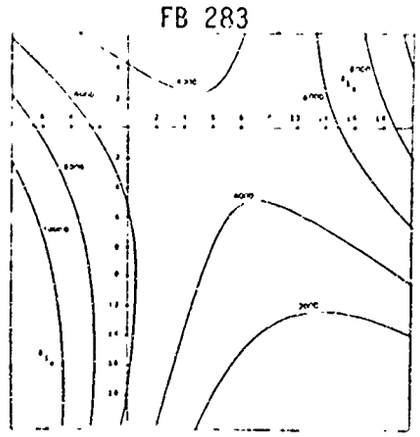

Figure 11 (Continued)

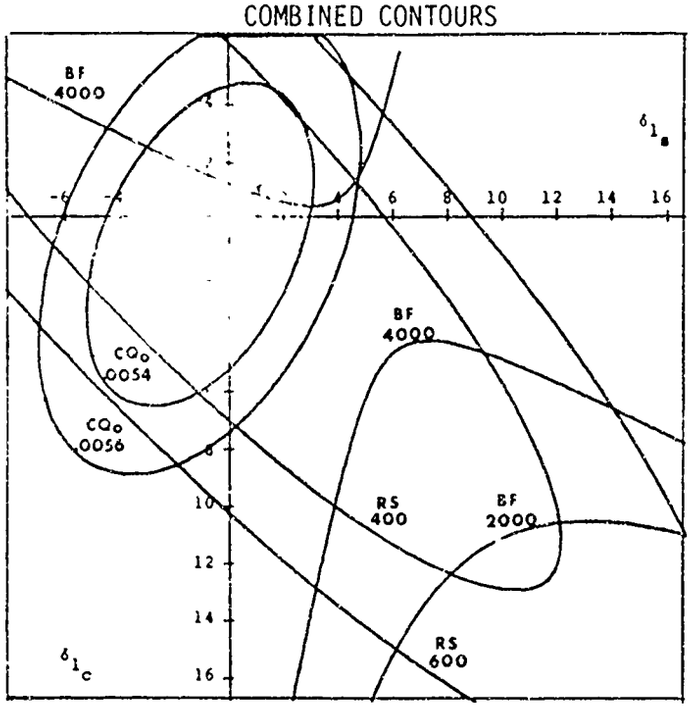

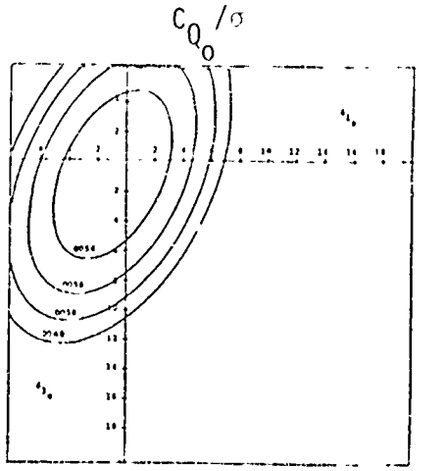

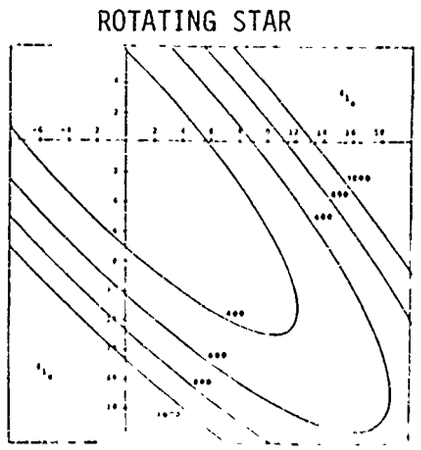

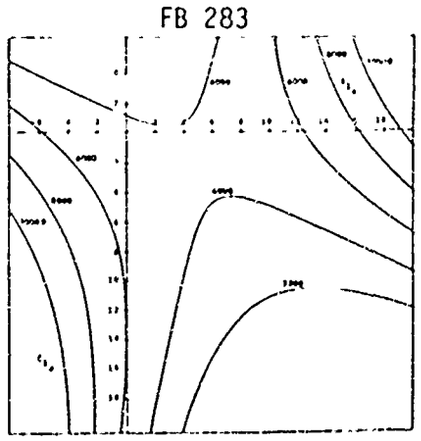

V = 135 KT

ΩR = 585 FPS

μ = .366

α_s = -8°

$\frac{C_{L_R}}{\sigma}$ = .10

δ_o = 2

Figure 11 (Continued)

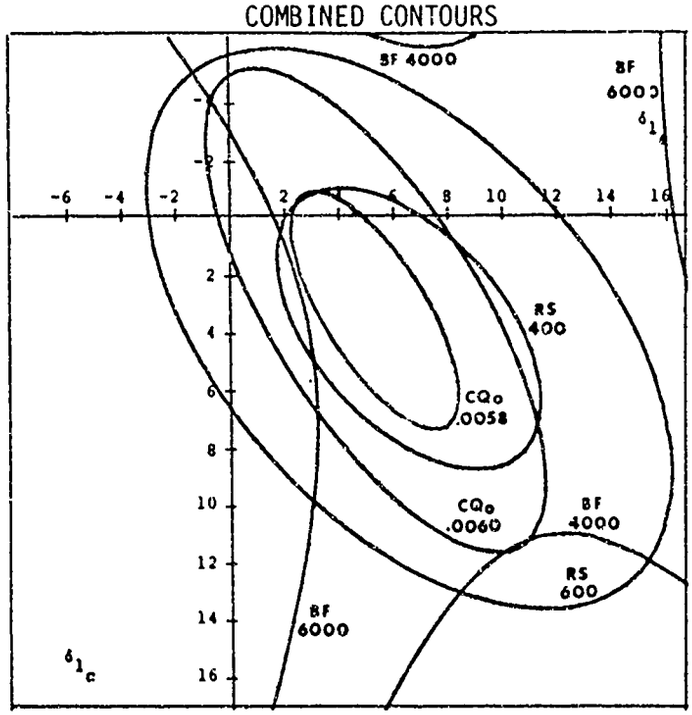

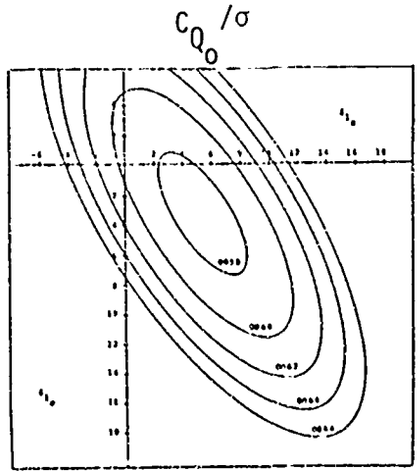

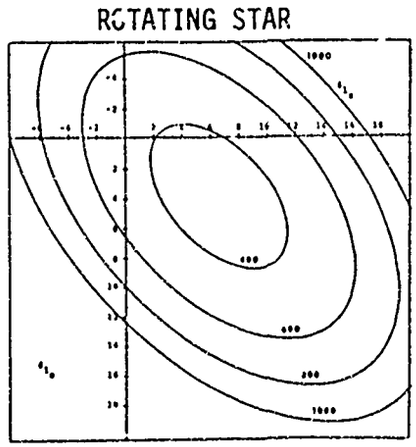

V = 135 KT

ΩR = 585 FPS

μ = .366

α_s = -8°

$\frac{C_{L_R}}{\sigma}$ = .11

δ_0 = -2

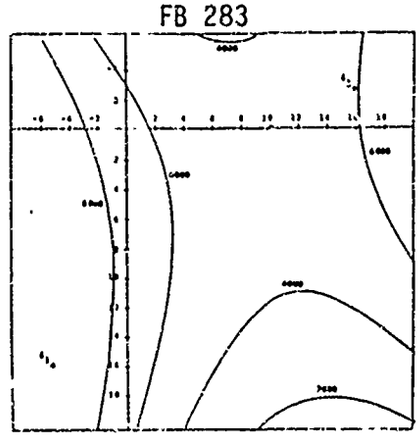

Figure 11 (Continued)

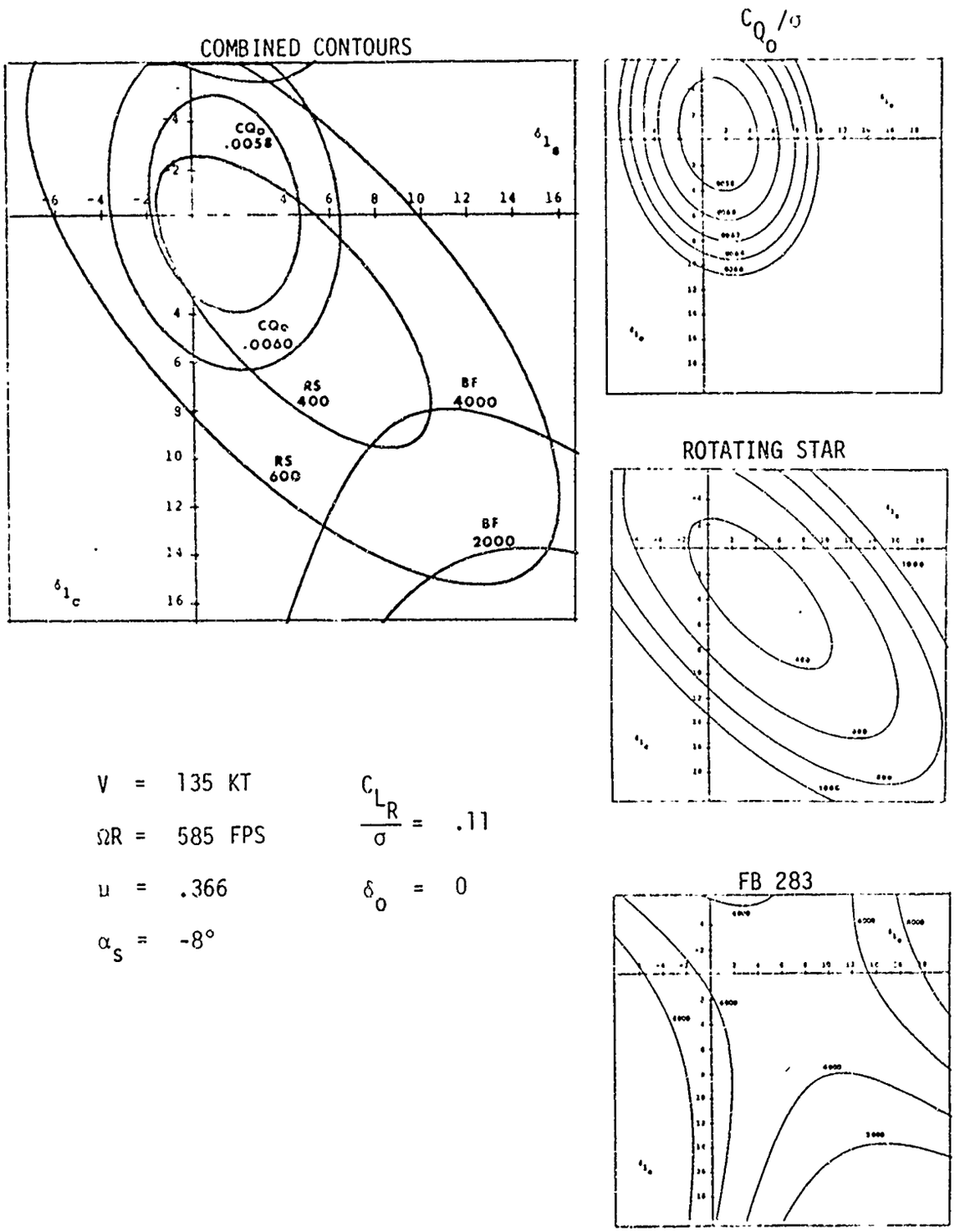

V = 135 KT

ΩR = 585 FPS

μ = .366

α_s = -8°

$\frac{C_{L_R}}{\sigma}$ = .11

δ_o = 0

Figure 11 (Continued).

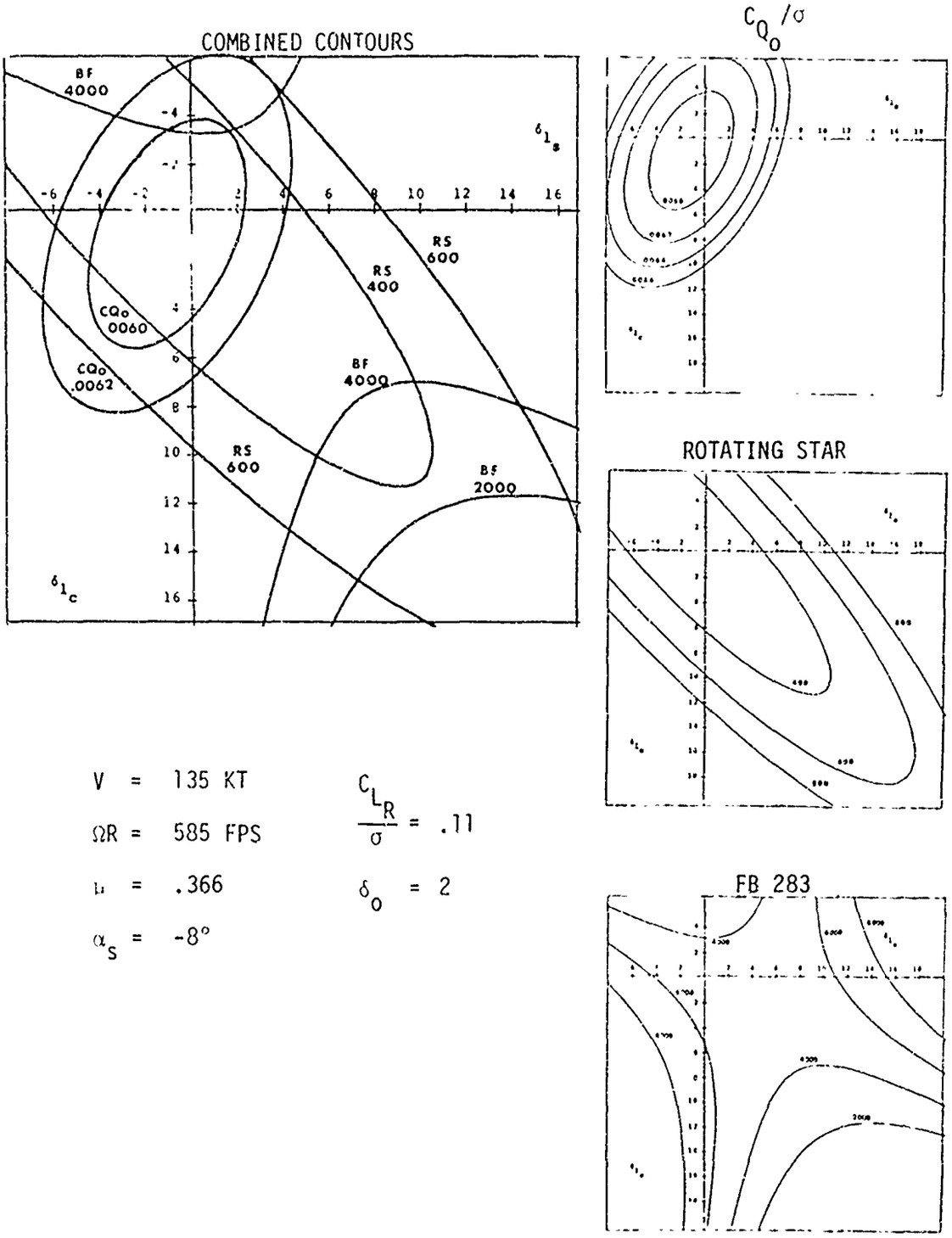

V = 135 KT

ΩR = 585 FPS

μ = .366

α_s = -8°

$\frac{C_{L_R}}{\sigma}$ = .11

δ_o = 2

Figure 11 (Continued)

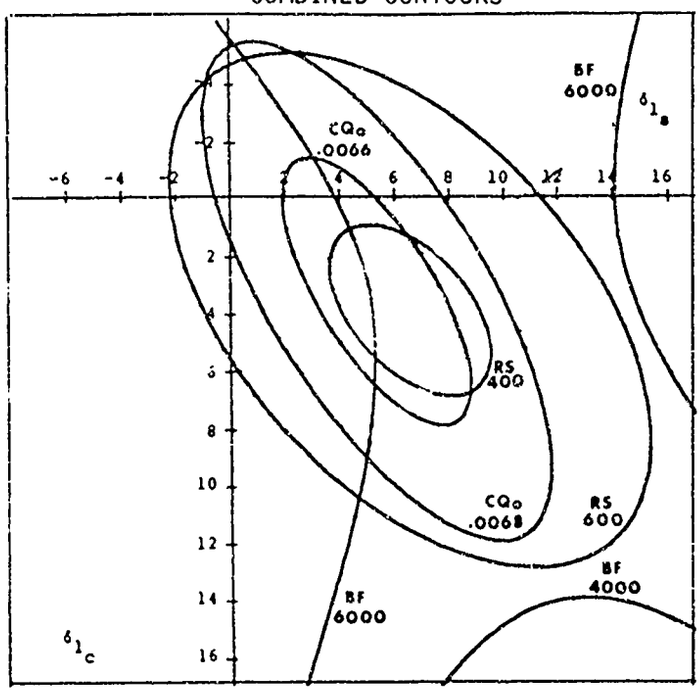

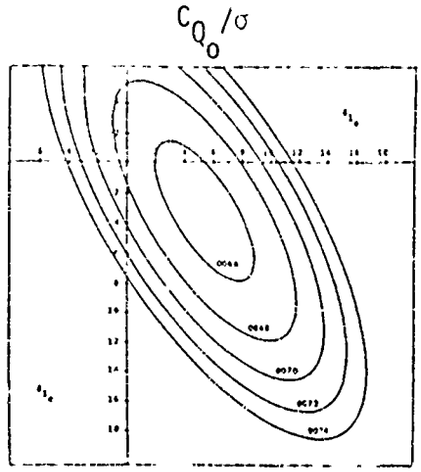

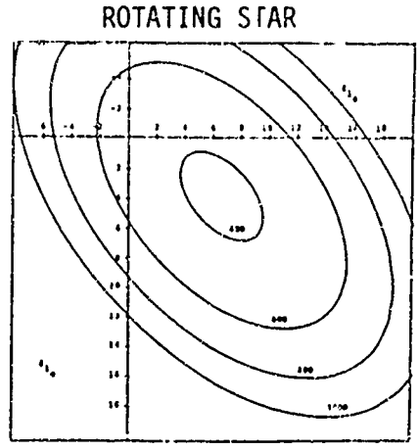

V = 135 KT

ΩR = 585 FPS

μ = .366

α_s = -8°

$\frac{C_{L_R}}{\sigma}$ = .12

δ_o = -2

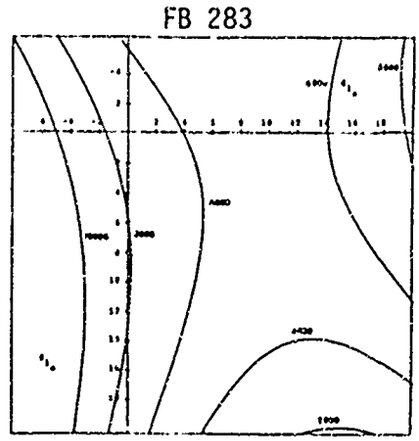

Figure 11 (Continued)

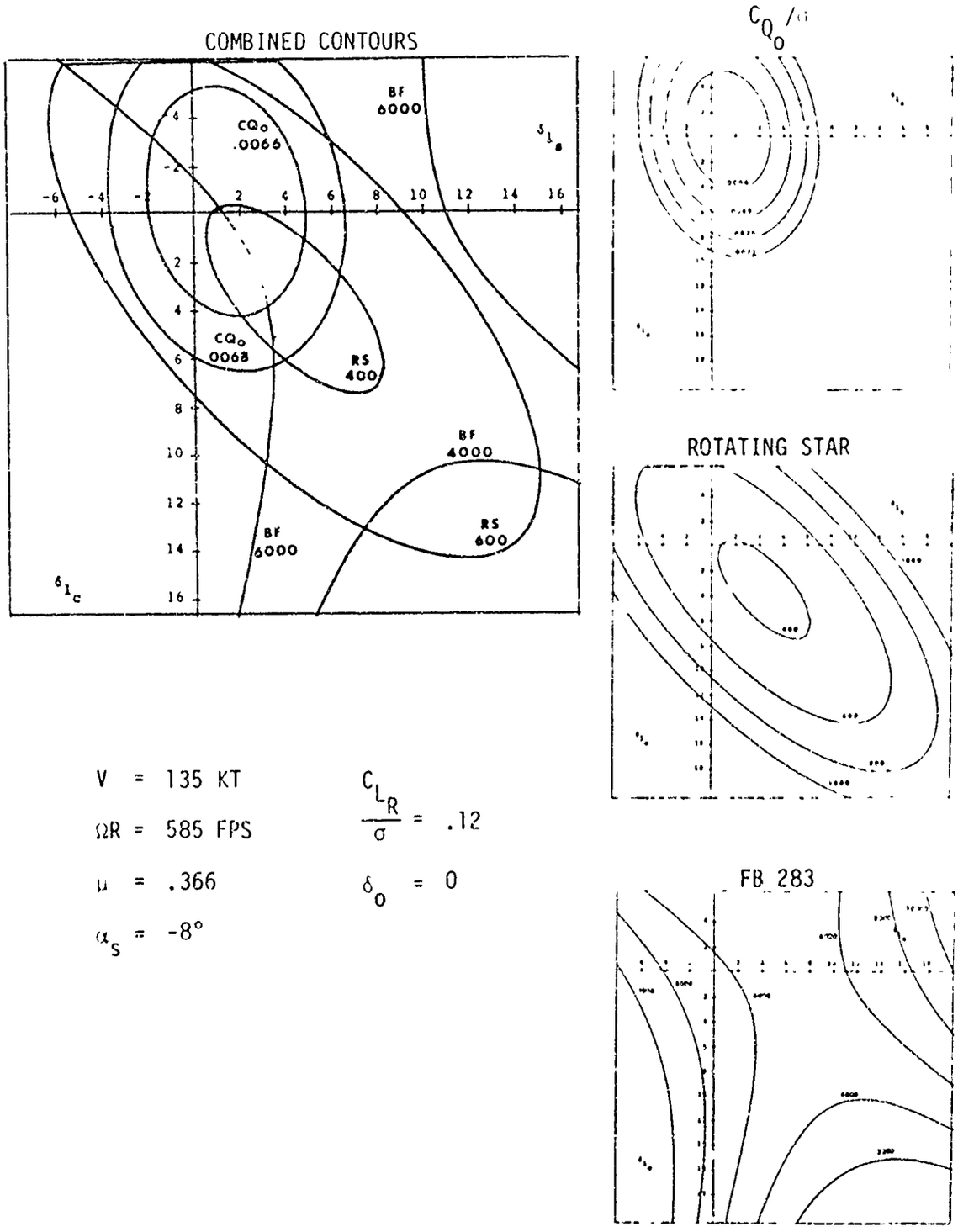

V = 135 KT

ΩR = 585 FPS

μ = .366

α_s = -8°

$\frac{C_{L_R}}{\sigma}$ = .12

δ_0 = 0

Figure 11 (Continued)

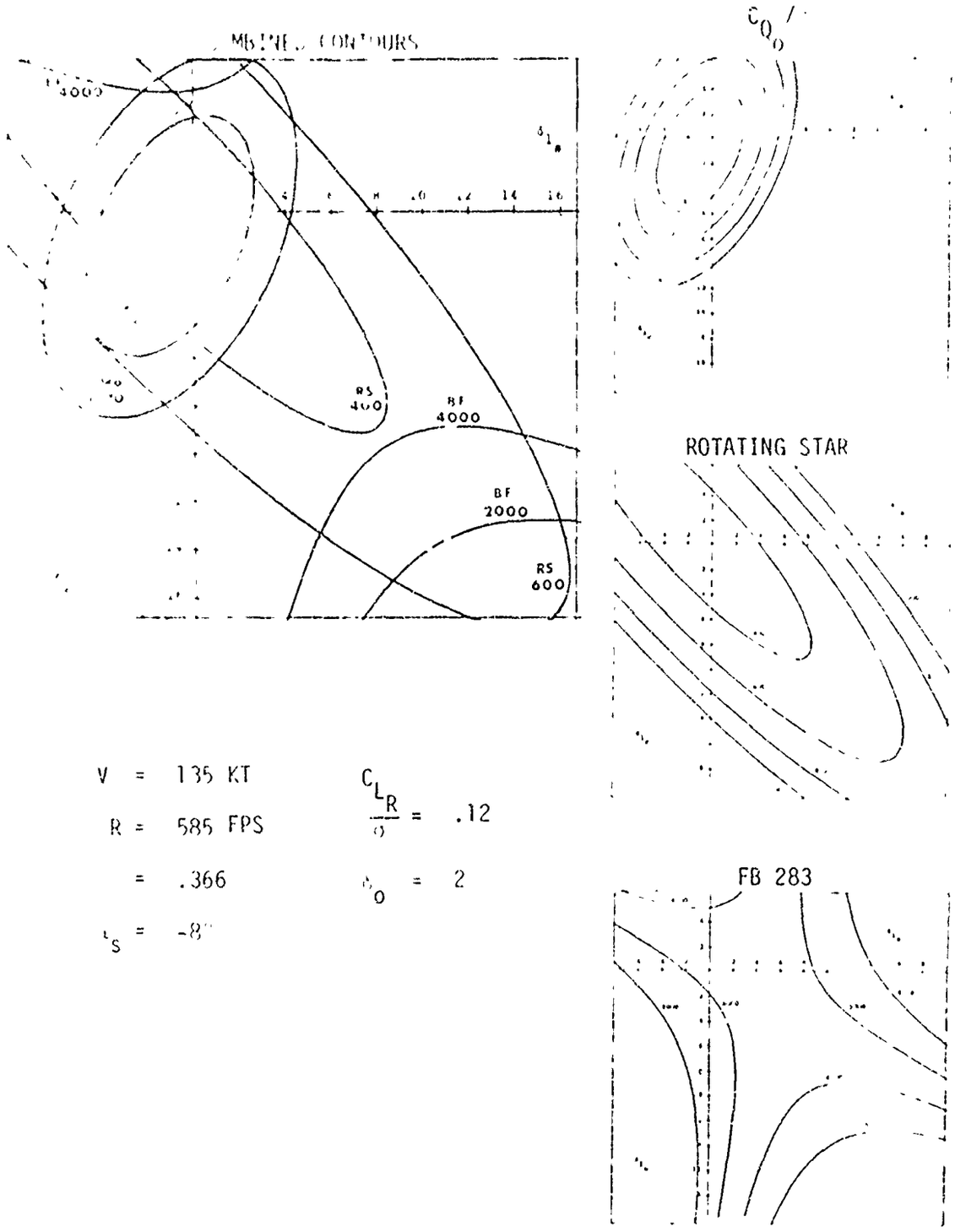

V = 135 KT

R = 585 FPS

= .366

ι_S = -8°

$\frac{C_{L_R}}{O}$ = .12

δ_O = 2

Figure 11 (Concluded)

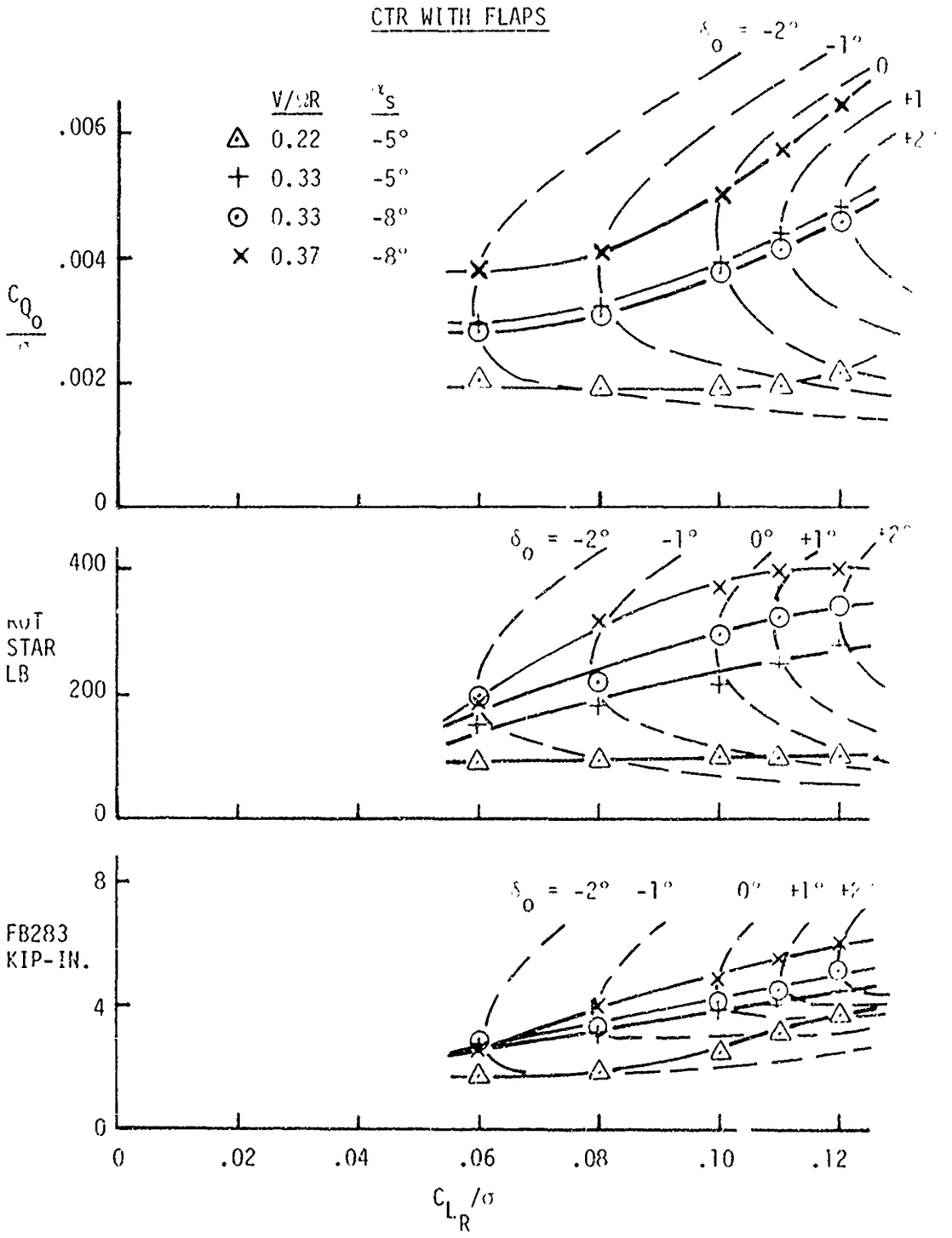

Figure 12. Rotor Performance Versus Blade Loading

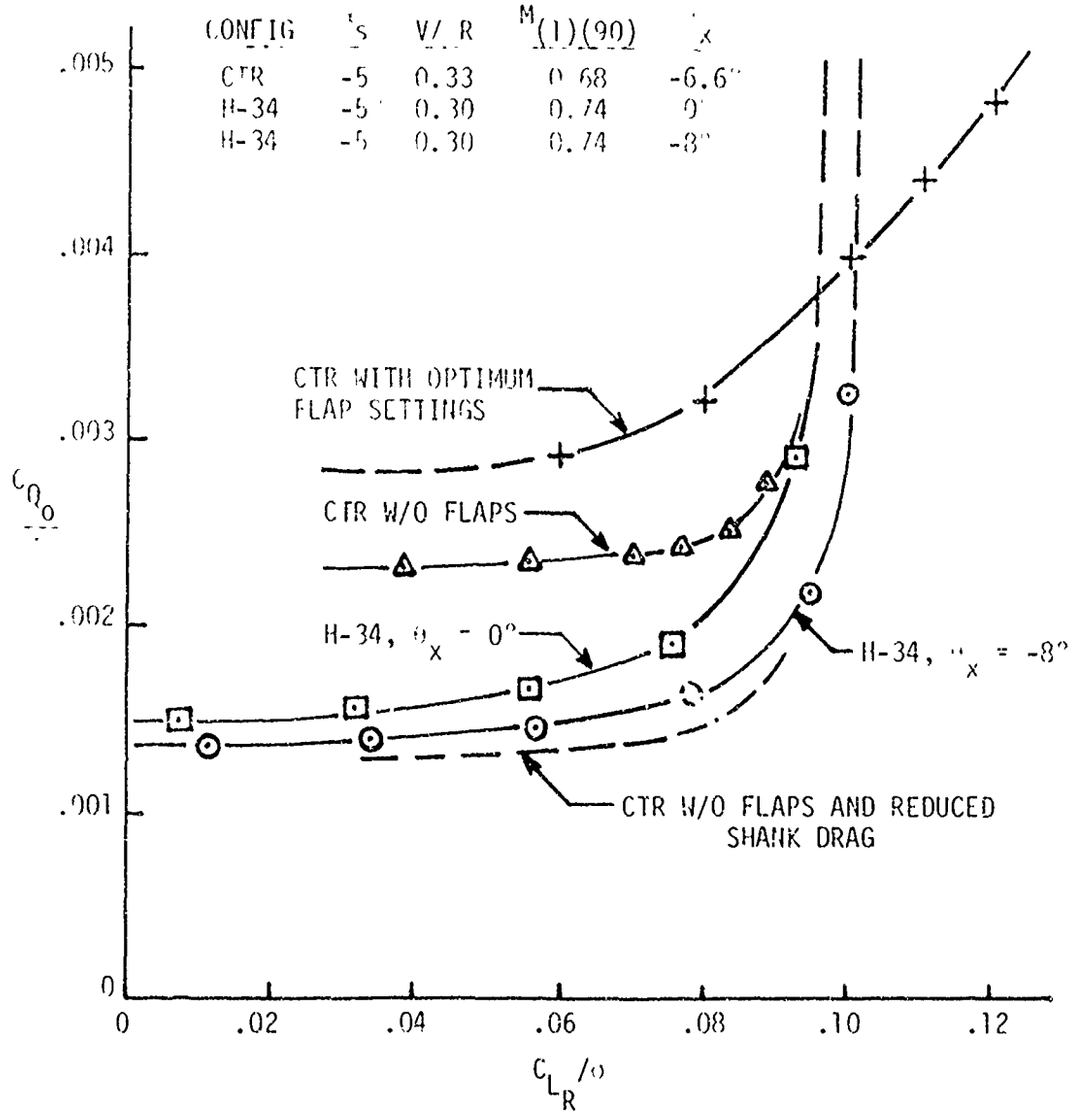

Figure 13. Comparison of Profile Power Coefficients of CTR and Conventional Rotor

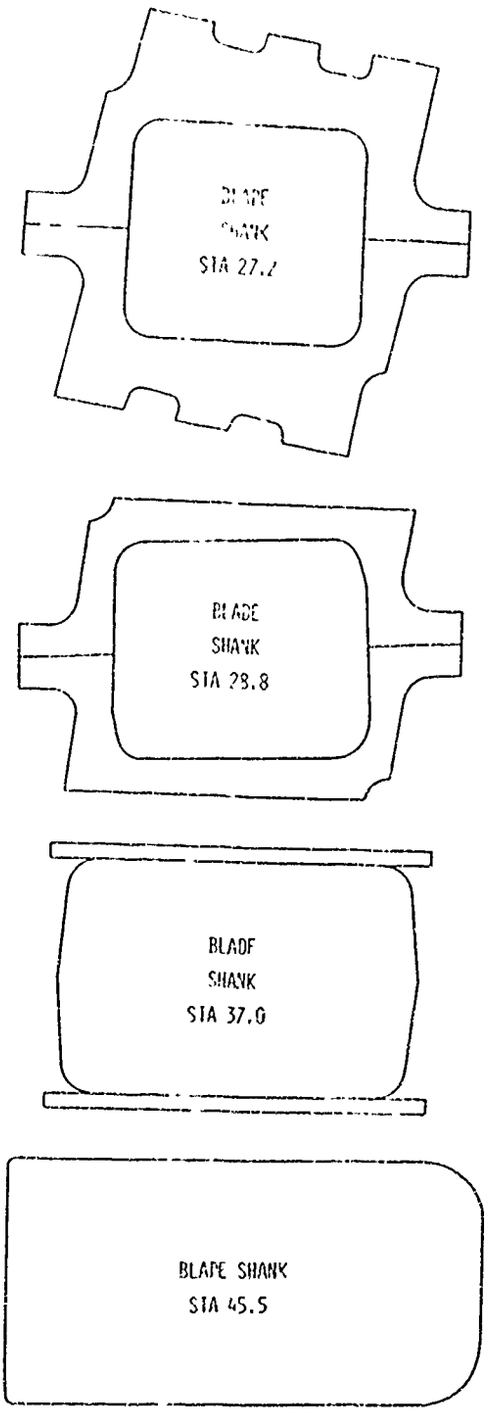

Figure 14. CTR Blade Shank Cross Sections

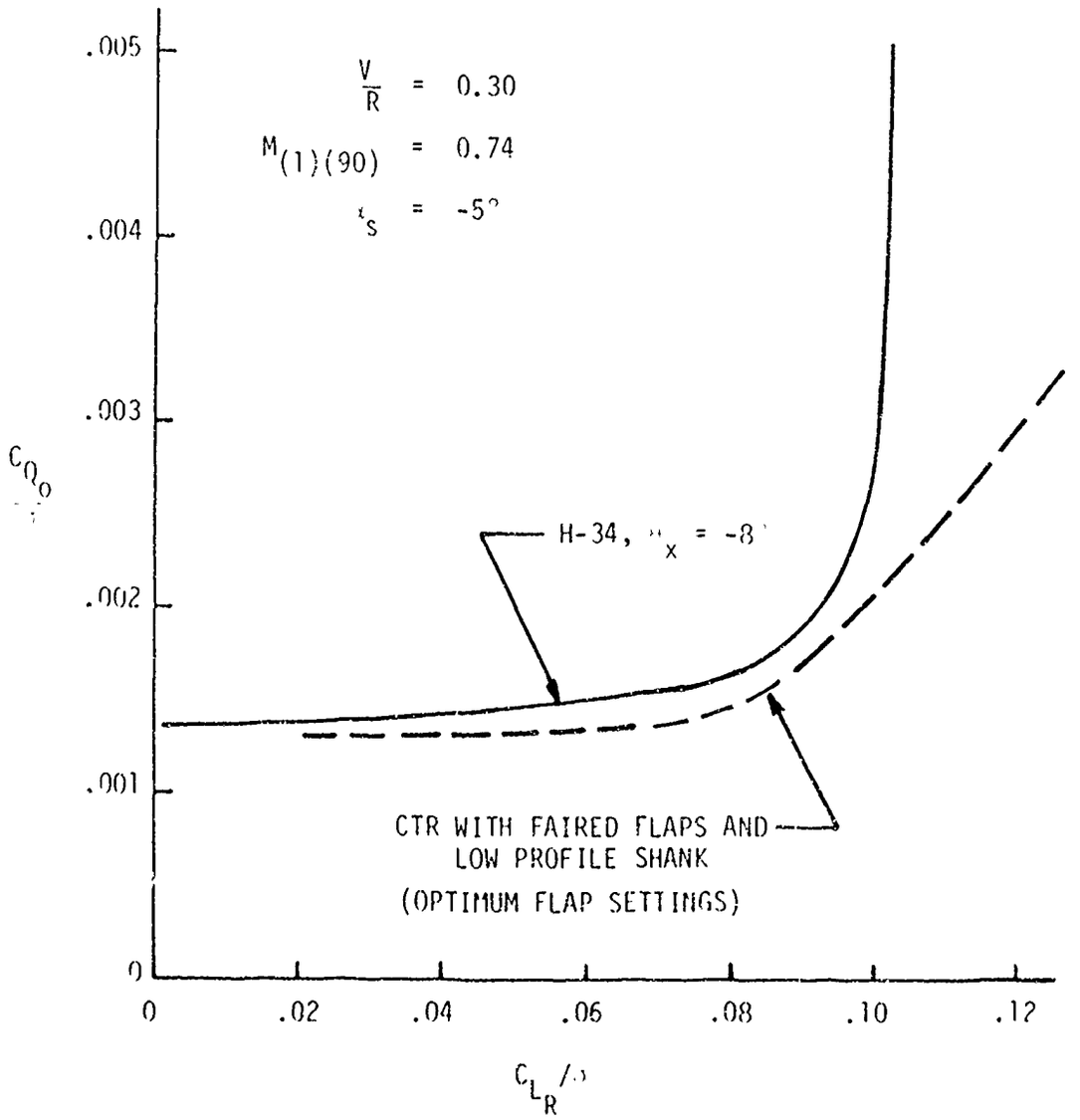

Figure 15. Equivalent Profile Power Coefficients for CTR and Conventional Rotor

REFERENCES

1. Lemnios, A. Z. and Smith, A. F., AN ANALYTICAL [illegible] CONTROLLABLE TWIST ROTOR PERFORMANCE AND DYNAMIC [illegible], USAAVLABS Technical Report 72-16, U. S. Army Air Mobility Research and Development Laboratory, Fort Eustis, Virginia, May [illegible].

2. Johnson, W. and Biggers, J. C., SHAKE TEST OF ROTOR [illegible] IN THE 40- BY 80-FOOT WIND TUNNEL, NASA Technical Memorandum TM X-62,418, Ames Research Center, Moffett Field, California, February 1975.

3. Johnson, W. and Biggers, J. C., SHAKE [illegible] WITH BALANCE DAMPERS IN THE 40- BY 80-FOOT WIND TUNNEL, NASA Technical Memorandum TM X-62,470, Ames Research Center, Moffett Field, California, July 1975.

4. Miller, Irwin and Freund, John E., PROBABILITY AND STATISTICS FOR ENGINEERS, Prentice-Hall, Inc., Englewood Cliffs, N.J., [illegible].

5. Paglino, V. M. and Logan, A. H., AN EXPERIMENTAL EVALUATION OF PERFORMANCE AND STRUCTURAL LOADS OF A FULL-SCALE [illegible] OPERATING CONDITIONS, USAAVLABS Technical Report [illegible], U. S. Army Aviation Materiel Laboratories, Fort Eustis, Virginia, [illegible] AD 674187.

6. McCloud, J. L., III, Biggers, J. C. and [illegible], FULL-SCALE WIND TUNNEL TEST OF AN UNSTALLED HELICOPTER ROTOR AT [illegible] ADVANCING TIP MACH NUMBERS, NASA Technical Note [illegible], Ames Research Center, Moffett Field, California, [illegible].

7. McCloud, J. L., III and McCullough, [illegible], AN EXPERIMENTAL AND MEASURED STALL BOUNDARIES OF A [illegible] RATIOS FROM 0.3 TO 0.4, NASA Technical Note [illegible], Ames Research Center, Moffett Field, California, [illegible].

8. McCloud, J. L., III and McCullough, [illegible], FULL-SCALE HELICOPTER ROTOR WITH SYMMETRICAL AIRFOIL SECTIONS AT ADVANCE RATIOS FROM 0.3 TO 0.4, NASA Technical Note [illegible], NASA-Ames Research Center, Moffett Field, California, [illegible] 1975.

9. Delany, N. K. and Sorensen, N. E., LOW-SPEED DRAG OF CYLINDERS OF VARIOUS SHAPES, NACA Technical Note 3038, Ames Aeronautical Laboratory, Moffett Field, California, November 1953.

REFERENCES (Continued)

10. McKinney, L. W., EFFECTS OF FINELESS RATIO AND REYNOLDS NUMBER ON THE LOW-SPEED CROSSWIND DRAG CHARACTERISTICS OF CIRCULAR AND MODIFIED SQUARE CYLINDERS, NASA Technical Note D-540, Langley Research Center, Langley Field, Virginia, October 1960.

11. Hoerner, S. F., FLUID-DYNAMIC DRAG, Published by the Author, 1965.

12. Hoerner, S. F. and Borst, H. V., FLUID-DYNAMIC LIFT, Published by the Authors, 1975.

13. Tanner, W. H., CHARTS FOR ESTIMATING ROTARY WING PERFORMANCE IN HOVER AND AT HIGH FORWARD SPEEDS, NASA Contractor Report CR-114, NASA Hq, Washington, D. C., November 1964.

14. Robinson, Donald W., Jr., and Dunn, Frank D., TRIMMING DUAL CONTROL ROTORS FOR OPTIMUM PERFORMANCE, American Helicopter Society National Symposium on Helicopter Aerodynamic Efficiency, Hartford, Conn., March 6-7, 1975.

15. Cambra, Joseph M. and Tolari, Geno P., REAL TIME COMPUTER DATA SYSTEMS FOR THE 40- BY 80-FOOT WIND TUNNEL FACILITY AT AMES RESEARCH CENTER, NASA Technical Note TN D-7970, Ames Research Center, Moffett Field, California, May 1975.

APPENDIX A

DESIGN DESCRIPTION - CONTROLLABLE TWIST ROTOR

PRELIMINARY REQUIREMENTS

The design of the Controllable Twist Rotor (CTR) system took into consideration several basic requirements. The factors that determined the design evolved around desired blade characteristics, cost, and the many equipment and facility interfaces. The following were primary considerations that guided the system design:

- The rotor blade had to be torsionally soft.
- Blade twist was to be controlled by independent inboard and outboard control systems.
- Geometric specifications were to nominally match the H-34 blade to the extent that resulting test data could be directly compared with appropriate H-34 baseline data.
- The blade retention had to be designed to mate with standard H-34 components for easy adaptation to a Rotor Test Module which was to be provided by the NASA-Ames Research Center 40- x 80-foot Wind Tunnel.
- The hub and control system had to be designed to allow the maximum use of proven hardware and for easy installation on either Kaman or wind-tunnel test rigs.
- Instrumentation design was to be compatible with either Kaman or wind-tunnel systems.
- The entire rotor and control system design was to allow the maximum use of existing, proven components, and tooling for cost considerations.

DESIGN DESCRIPTION

Rotor Blade/Servo Flap-Selection

The feasibility demonstration model of the CTR was based on the existing design of the H-43 blade. The torsional, edgewise, and flapwise stiffness characteristics of this blade were compatible with CTR requirements. The servo flap control used by the H-43 provided the CTR with the necessary outboard control for twist. The H-43 grip redesign made mating the components with the standard H-34 pitch barrel possible, permitting the use of the conventional H-34 inboard pitch-horn control system.

The H-43 blade is noted for its ease of modification as well as its excellent serviceability. Existing H-43 tooling was adaptable to CTR without affecting H-43 production configurations. By adapting the blade to the H-34 rotor head, compatibility with all test rig requirements was assured.

Rotor Blade/Servo Flap - Construction (H-43)

The H-43 blade, from which the experimental CTR design evolved, is constructed from the highest quality sitka spruce and maple woods, birch plywood, fiberglass, and stainless steel. The laminated spruce main spar block forms the basic structure of the rotor blade from the root end to the tip. Laminated maple blocks with fiberglass and scotchply reinforcements are used at the root end to form the foundation for attaching the blade grip. Laminated maple is also secured to the leading edge face of the main spar to form the blade's leading edge. Spruce ribs, secured to the aft face of the main spar with spruce corner blocks, form the airfoil contour. Laminated maple and birch plywood with a fiberglass covering form the skin panels. Mass balance is obtained with weights imbedded in the leading edge and in the tip of the spar. Tip weights are secured with four inches of wooden dowel bonded horizontally in the spar and then double safetied with two steel pins inserted and bonded vertically through both spar and dowel. The entire blade is protected with an acrylic lacquer finish, and the leading edge is protected with stainless steel against abrasion.

The blade's control-rod assembly consists of a long rod that is routed through a phenolic tube extending from the grip area to the servo flap area. The control rod connects to a bellcrank, which translates spanwise control motion to chordwise motion through a short rod connected to the flap.

The servo flap assembly is constructed of a plywood and spruce main spar, a spruce leading edge, and spruce ribs covered on the upper and lower surfaces with a birch plywood skin. The upper and lower spar caps are constructed from fiberglass. Support fittings, inboard and outboard, secure the flap to support brackets on each rotor blade assembly. The control fitting is located on the inboard support fitting. An armored cable passing through the center of the flap spar carries the centrifugal load of the flap from the outboard flap fitting to the inboard flap bracket, where the cable is secured.

Rotor Blade/Servo Flap - CTR Modifications

Modifications of the H-43 blade for CTR were designed to: (a) closely match the H-34 blade geometry, to facilitate data comparison; (b) move the control servo flap outboard to control blade twist over a longer spanwise portion of the blade; and (c) be adaptable to existing H-43 production blade tooling. To accomplish the modifications, the following design changes were made:

The fiberglass-sheathed wooden spar was lengthened 38 inches to match the 28-foot radius of the H-34. The H-43 blade's after structure was continued over the longer span.

Blade chord was increased 0.71 inch, giving a total chord of 16.4 inches. The overlapping of skins at the trailing edge, normally trimmed in manufacture, was left in an untrimmed state to provide the desired extension. Airfoil section was otherwise identical to the H-43.

The standard H-43 control flap was moved outboard 74.81 inches. The structure immediately inboard of the flap on the H-43 blade forms a torsion-tuning section, and this section was extended outboard with the flap. A scotchply stiffening plank in the underside of the blade spar was also continued outboard to maintain the same termination distance relationship to the flap mounting hardware.

The servo flap was shortened by cutting the original flap in half. The balance weight in the nose was reduced to keep flap chordwise balance at the quarter-chord hinge line.

Mass balance was redistributed by adding weights in the leading edge of the blade, by using a heavier-gage stainless-steel guard over the section of the blade outboard of the inboard-flap support bracket, and by increasing the tuning weights in the blade tips. Blade stiffness was also increased by extending the leading-edge guard inboard through the torsion section of the blades.

The blade grip was redesigned to mate with the H-43 root on the blade side and with the H-34 knuckle joint on the pitch-barrel side.

Figure A-1 shows the completed CTR blades, illustrating the short flap, the extended chord, the extended leading-edge guard, and the redesigned blade grip.

The following is a listing of rotor data, and blade and servo flap characteristics (as fabricated).

Number of blade - 4
Rotor diameter - 56 ft.
Solidity - .062
Lag hinge offset - 1 ft.
Lag damper rate (same as H-34) - 1742 lb. in.-sec/degree
Blade weight (including flap, pitch barrel, and controls affected by pitching - 285.35 lbs
Torsional spring constant - 267.04 in./lb/degree (measured just inboard of the flap)
Blade chord c.g. - 4.514 in.
Blade span c.g. - 110.15 in.
Span moment - 31,431 in.-lbs
Blade moment of inertia (about lag hinge) - 1374.4 slug ft^2

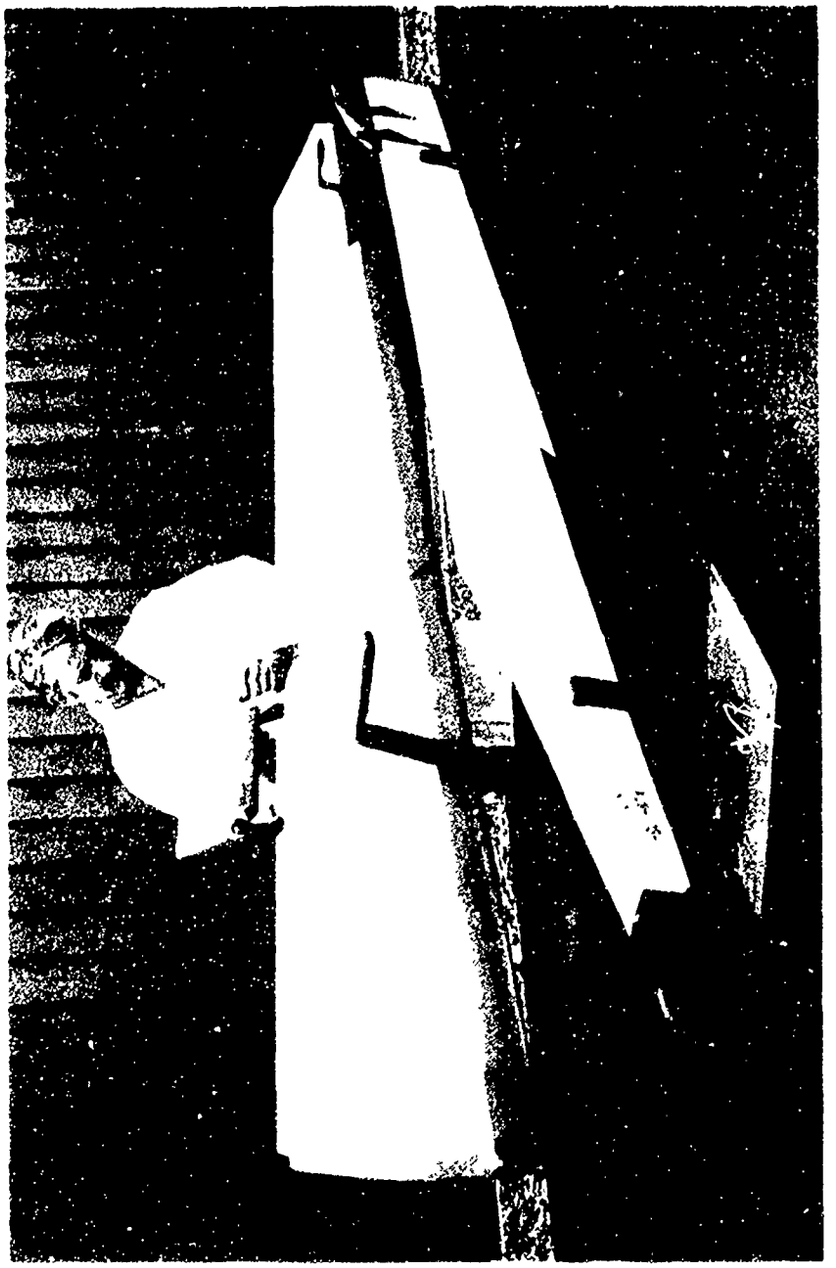

Figure A-1. Controllable Twist Rotor Blades

Flap weight - 1.65 lbs
Flap chord moment - 32.29 in.-lbs
Flap span moment - 463.99 in.-lbs

Controls/Rotor Head

The control system was designed to have independent collective, longitudinal, and lateral cyclic controls for both the pitch horn and the flap. The pitch horn was operated through the hydraulic servo system existing in the test module, from a control panel located in the tunnel control room. The flap control system was a new design but used proven components in all critical areas. The flap was operated from a control panel adjacent to the pitch-horn panel. Displays and switching functions were designed so that meter and switch types were identical, and the directions of meter movement and switch actuation had the same meaning.

The flap control was designed to operate through a system of rods, cranks, rotating swashplates, and linear actuators. The rod and crank routing through the blade was the standard H-43 system with lengthened rods to accommodate the longer blade. The control rod exited from the blade at the root end as shown in Figure A-1 and was routed through a system of cranks and short control rods to a walking beam that translated control motions through control rods in the center of the rotor shaft. The walking beams were mounted to a turret assembly that was added to the top of the hub. Turret height was chosen to decouple servo flap control motion resulting from lag motion. The turret also provided a convenient location for mounting terminal points for rotating instrumentation transducers. Small electric motors were mounted at the walking beams and operated eccentrics, resulting in small control motions to make blade track changes. The motors were operated from the tunnel control room. Figure A-2 illustrates the complete rotor head and upper control installation.

The upper and lower control installations were connected by four long control rods that extended from the walking beams, through the rotor shaft and instrumentation slip ring to an SH-2 swashplate. The swashplate was operated by linear actuators through a system of L-cranks to provide independent control for collective, lateral, and longitudinal cyclic. The actuators were operated from a control panel in the tunnel control room. Figure A-3 shows the complete lower control assembly with the slip ring prior to installation in the test module. Figure A-4 shows the lower controls installed.

DESIGN ANALYSIS

During the total design and fabrication cycle of the CTR, a closed loop was maintained with the on-going analysis. Pertinent results of the preliminary and detail analysis were continuously fed into the preliminary and detail design. Also, factors evolving from design efforts and actual fabrication data were fed back into the analysis, continuously updating the analysis to the point of whirl testing the CTR system. The effort to

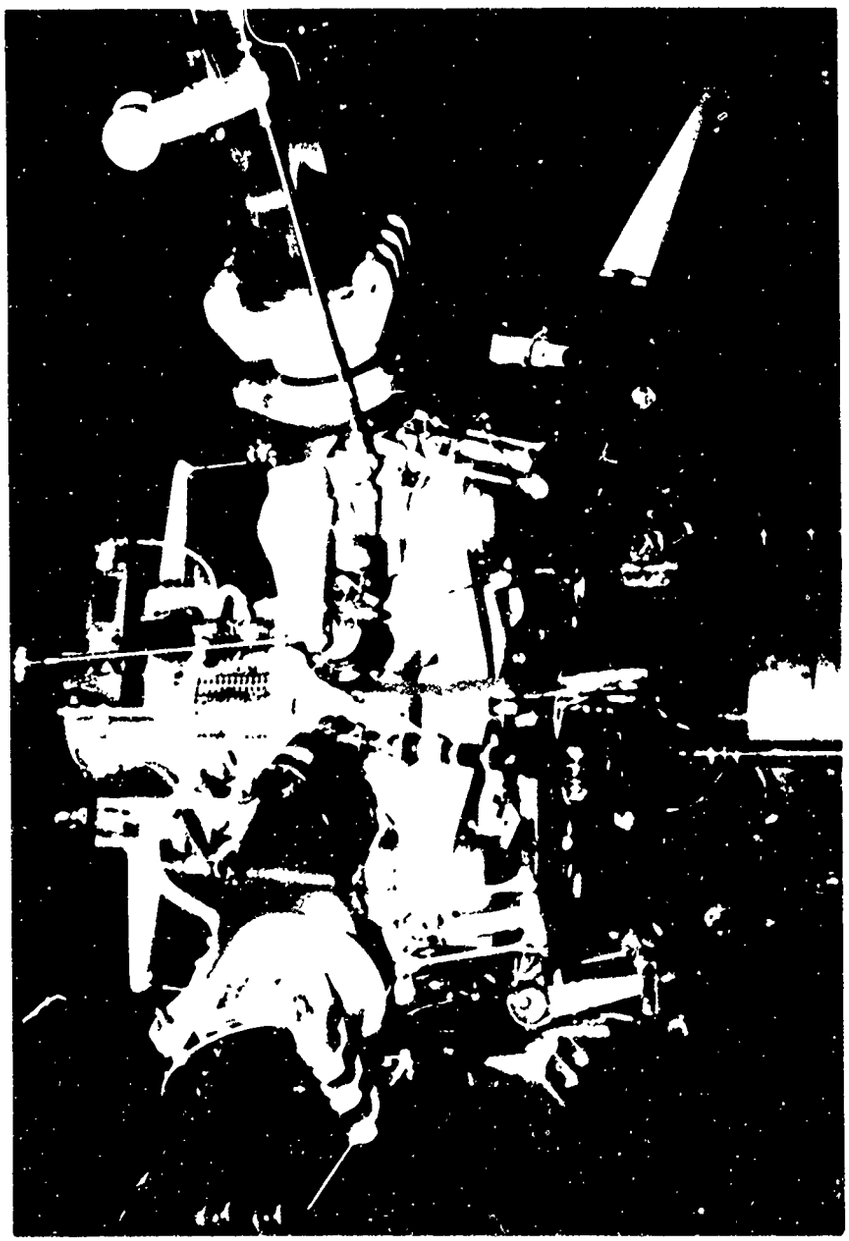

Figure A-2. Controllable Twist Rotor Head

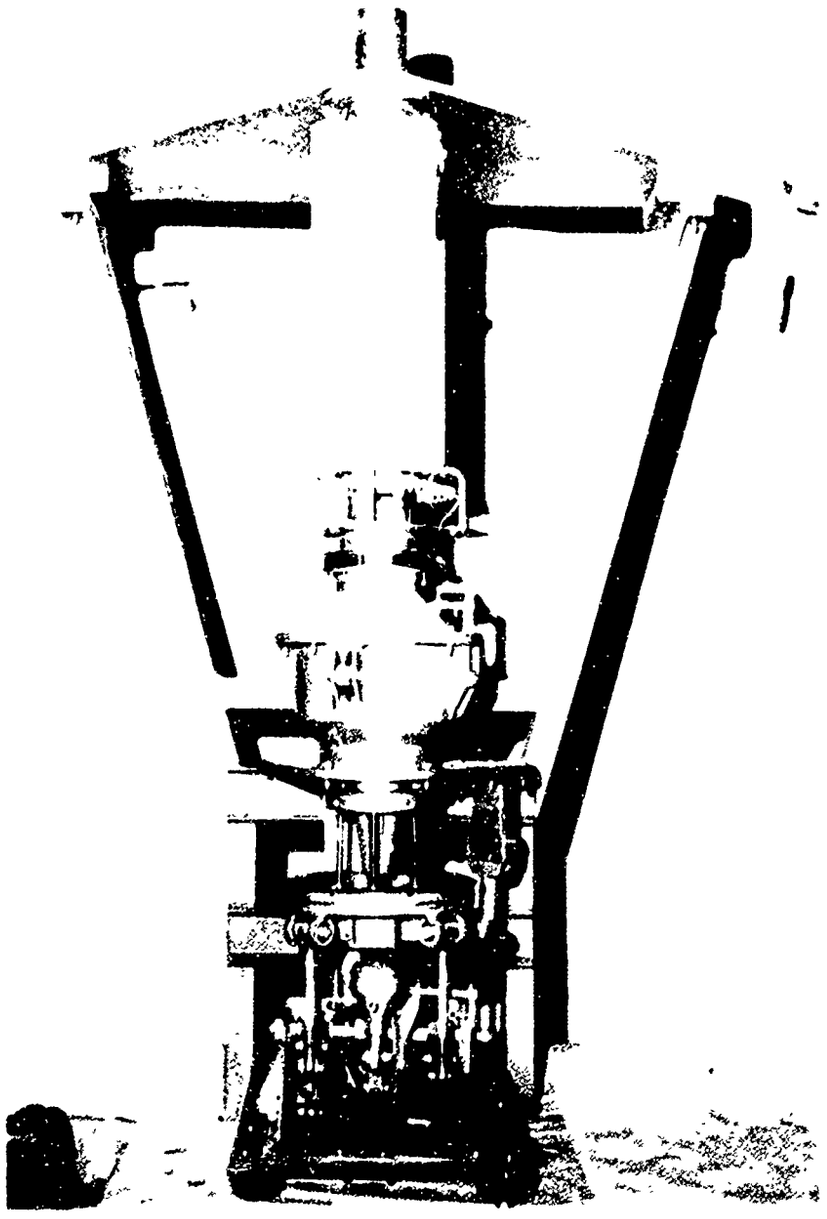

Figure A-3. Lower Servo Flap Controls

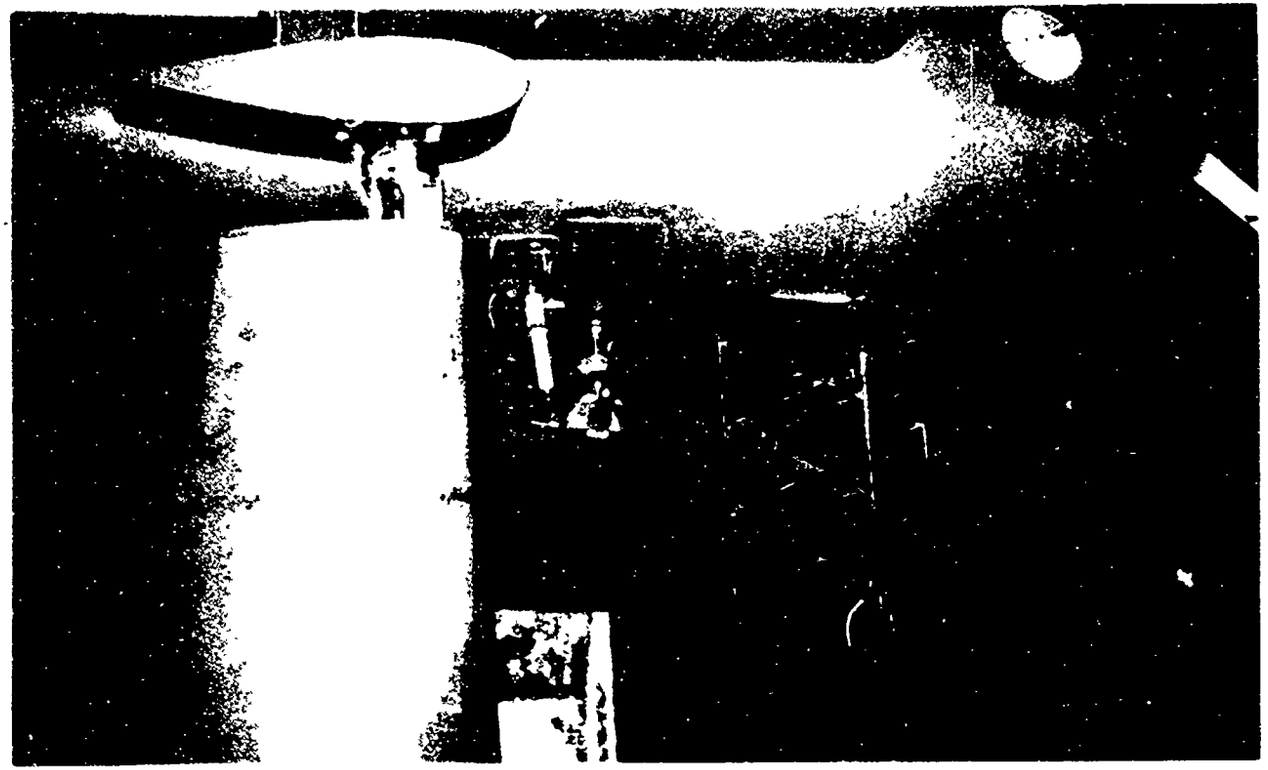

Figure A-4. Lower Servo Flap Controls (Installed)

maintain close coordination between the analysis and other development phases resulted in a rotor system closely represented by the final analysis, as it went into the whirl test phase.

PRELIMINARY ANALYSIS

Natural Frequencies

Preliminary tuning was performed using an uncoupled beam analysis for flatwise and edgewise bending, and for torsion. Stiffness and mass distributions of the structure were estimated from the preliminary design drawings. Preliminary mass balance was added to bring the integrated product of inertia in flapping and feathering close to zero, adjusting the total weight and spanwise distribution to place the flatwise bending frequencies near those of the H-34 blade. Edgewise stiffness was adjusted and fed back to the designers - to place the first in-plane elastic bending mode comfortably above 4 Ω.

Torsional frequency, neglecting aerodynamics, was placed between 2 Ω and 3 Ω to assure adequate twisting response to servo flap deflection. The presence of the flap near 80% radius shifts the effective aerodynamic center aft, introducing static aerodynamic stability, which is in effect an added torsional spring. The effective hovering torsional frequency was thus expected to lie between 3 Ω and 4 Ω.

Blade Stability

The 6F Aeroelastic Blade Loads and Response program, developed earlier in the CTR program and reported in Reference 1, internally couples together six independent modes of response-feathering, flapping, lagging, servo flap deflection, first elastic bending, and torsion. It is run in two parts. The first part is a perturbation analysis in which linear aerodynamic derivatives are used, one or more of the six blade responses are perturbed, and time histories of the blade responses are calculated for several rotor cycles. A Floquet analysis provides a quick stability summary. For a more detailed look, the time histories of the six blade responses are harmonically analyzed with a Fast Fourier Transform (FFT) routine at successive time increments, and log decrement curves fitted to the decay of each harmonic component by a regression analysis. A spectral analysis of response amplitude and damping is provided for each aeroelastically coupled degree of freedom. These analyses give a good picture of classical flutter and other low-angle-of-attack stability modes.

The FFT method assumes that each response is made up of n harmonics, and that each harmonic has its own decay rate. This may be described mathematically as:

---

[1] Lemnios and Smith

$$Y = \sum_{n=0}^{N} A_n e^{\sigma_n n} \qquad (A1)$$

where Y is the response, A_n is the intercept of the n-th harmonic at time t = 0, N is the maximum number of harmonics considered, n is the harmonic number and σ_n is the decay rate for the n-th harmonic. A negative decay rate indicates a stable configuration, a zero decay is a neutrally stable condition, and a positive decay rate is unstable.

Part II of the 6F program introduces cyclic and collective control of blade pitch and servo flap, and applies two-dimensional airfoil data and unsteady aerodynamic derivatives. The inflow distribution is input from external wake calculations or may be assumed to be uniform where that is appropriate. The solution of the nonlinear equations of motion is not a forward integration, but assumes steady-state periodicity. The difference in responses between the beginning and the end of each rotor cycle is taken as a measure of deviation from steady-state conditions, and a cycle-by-cycle iteration brings conditions into equilibrium. The rate of convergence is a measure of high-angle-of-attack stability modes. The converged Part II solution, with associated subroutines, then provides radial and azimuthal distributions of angle-of-attack, Mach number, air loading, deflections, and bending moments. Harmonic analyses of all blade responses are also produced.

Analysis of the first preliminary design of the CTR blades showed oversensitivity to flap cyclic control input and poor Part II convergence, due to the presence of a bending/torsion coupled response. These problems were resolved by halving the span of the flap, increasing torsional stiffness by 20%, and redistributing the mass balance spanwise to alter the torsion/bending coupling. A recheck of natural frequencies showed some shifting of flatwise and torsional modes, but placement still appeared satisfactory.

A number of operating conditions were trimmed with the aeroelastic loads program, and critical design loadings were calculated. These data, with the desired mass, stiffness, and chordwise cg distributions then became the criteria for detailed design of the full-scale CTR system.

ANALYSIS-FINAL BLADE PROPERTIES

Data from bench testing the completed blades provided a better estimate of blade physical properties for dynamic analysis. Torsional and bending deflection tests were used to correct preliminary estimates of spanwise stiffness distributions. Measurements of weight, and spanwise and chordwise cg locations were reconciled with the calculated design mass and inertia distributions by a pseudo-inverse redistribution computer program

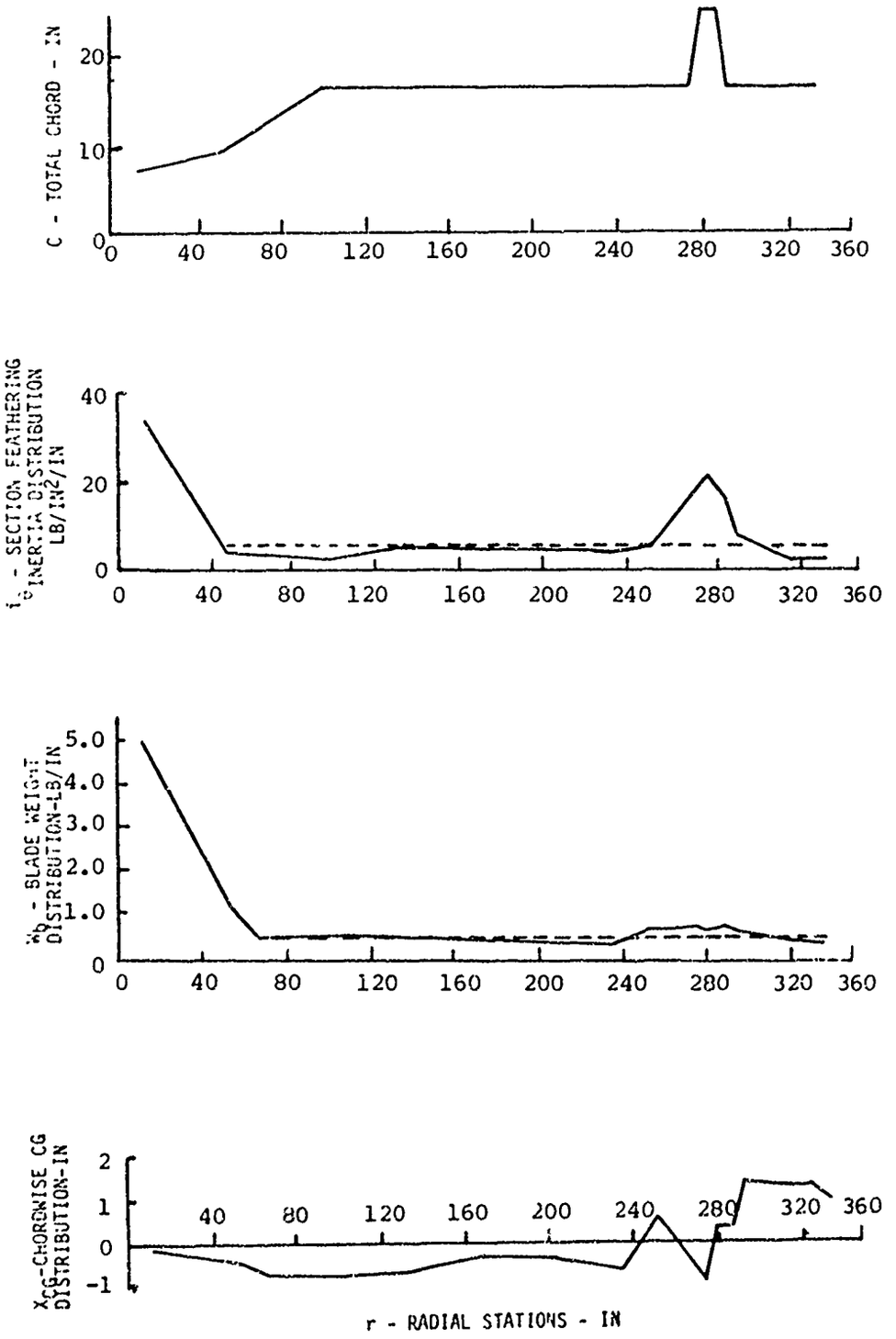

Figure A-5. CTR Physical Properties

that calculates the least-square deviation from the initially estimated distribution that is required to exactly match the measured properties. These improved physical property estimates, shown in Figures A-5 and A-6 were input to the appropriate analyses for a complete recycle of blade performance and aeroelastic responses.

Frequencies and Mode Shapes

An uncoupled beam analysis was used for two reasons. The 6F Aeroelastic Blade Loads and Response Program couples the blade responses internally and requires uncoupled frequencies and mode shapes as input. Proximity of the uncoupled frequencies in the operating range would provide adequate warning of any problem with a coupled normal mode, which then could be studied in more detail with a coupled analysis.

A fan plot for the CTR blade as manufactured is shown on Figure A-7. The design operating speed is shown at 210 rpm.

Flatwise modes are desirably placed between principal rotor harmonics at and near design operating speeds. The lower modes are very close to those of the H-34.

The two elastic edgewise modes reflect actual blade stiffness less than originally intended and are poorly placed - E2 at 4 Ω and E3 at 10 Ω. They were calculated as pin-ended beams with no end restraints, neglecting any lag damper effects. Impedance data over the frequency range of interest were not available for the H-34 damper, so that effective spring rates and damping coefficients at the higher rotor harmonics could not be estimated. Impedance testing of other dampers had shown a significant spring effect at the higher frequencies, which would have the effect of detuning the edgewise modes at operating speed. Further, this issue was not considered critical for the projected whirl tower and wind tunnel testing because a very small rpm reduction would detune these edgewise modes, and would be equally satisfactory for obtaining the desired data. For these reasons, no edgewise tuning changes were made to the blade.

Torsional frequency, neglecting aerodynamic stiffening, was just below 3 Ω near the first elastic flatwise mode. Aerodynamic stiffening at operating tip speed raised this to slight above 4 Ω. In forward flight, however, the stiffness coefficient is periodic, and there would be no well-defined natural frequency. Desirable torsional dynamics, therefore, were determined from a coupled aeroelastic stability analysis, rather than by any particular frequency placement.

Aeroelastic Stability

The physical properties data of Figures A-5 and A-6 were entered into the 6F Aeroelastic Blade Loads and Response Program, and a Part I time-history was run for coupled aeroelastic stability. Response spectra for flapping, bending, and twisting at 170 knots are presented in Figures A-8, A-9 and A-10. Comparable spectra for the H-34 are also shown for

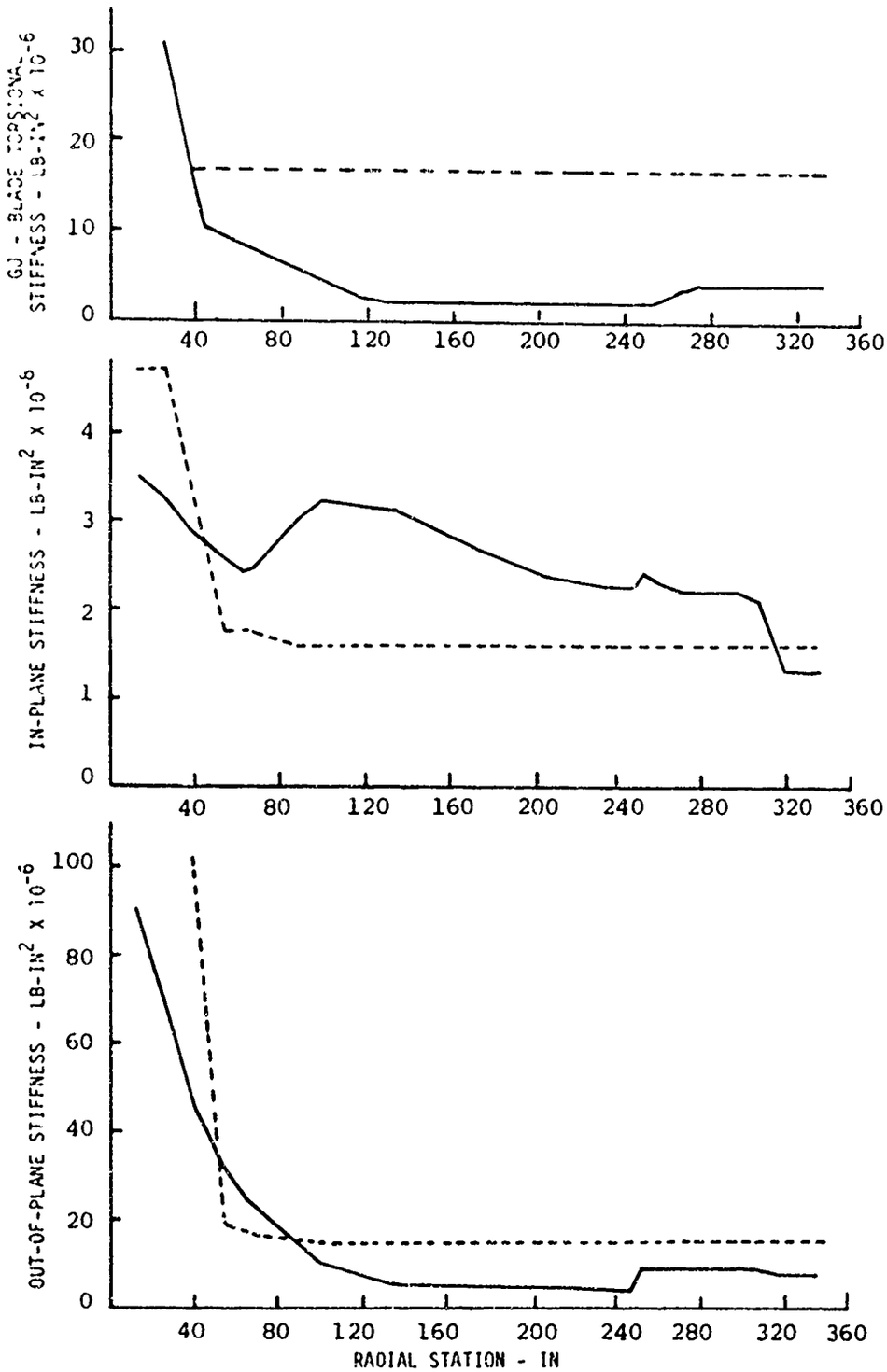

Figure A-6. CTR Physical Properties

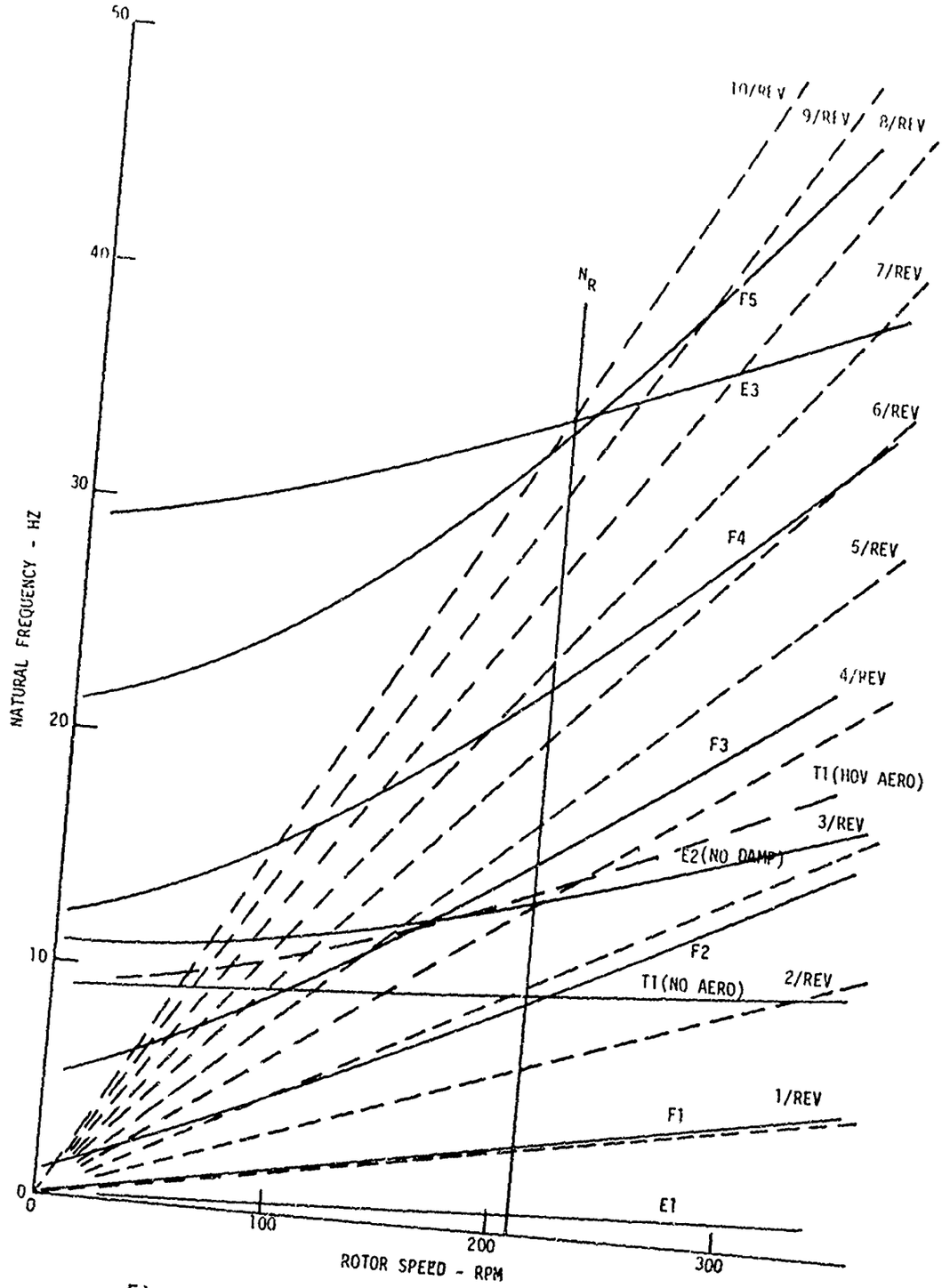

Figure A-7. Uncoupled Natural Frequencies

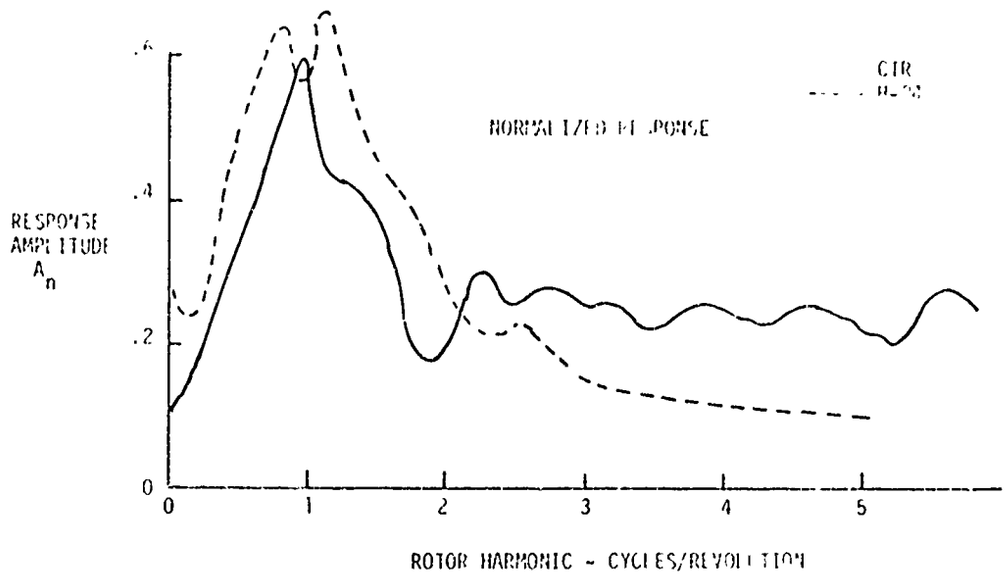

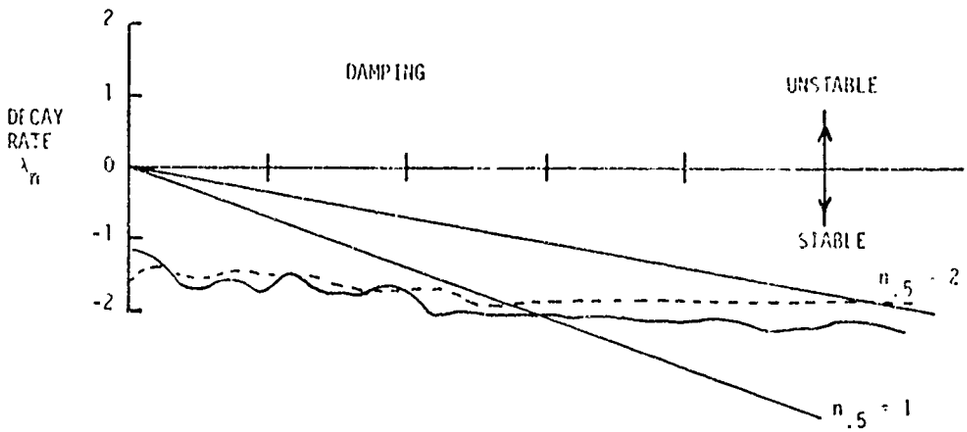

Figure A-8. Flapping Response

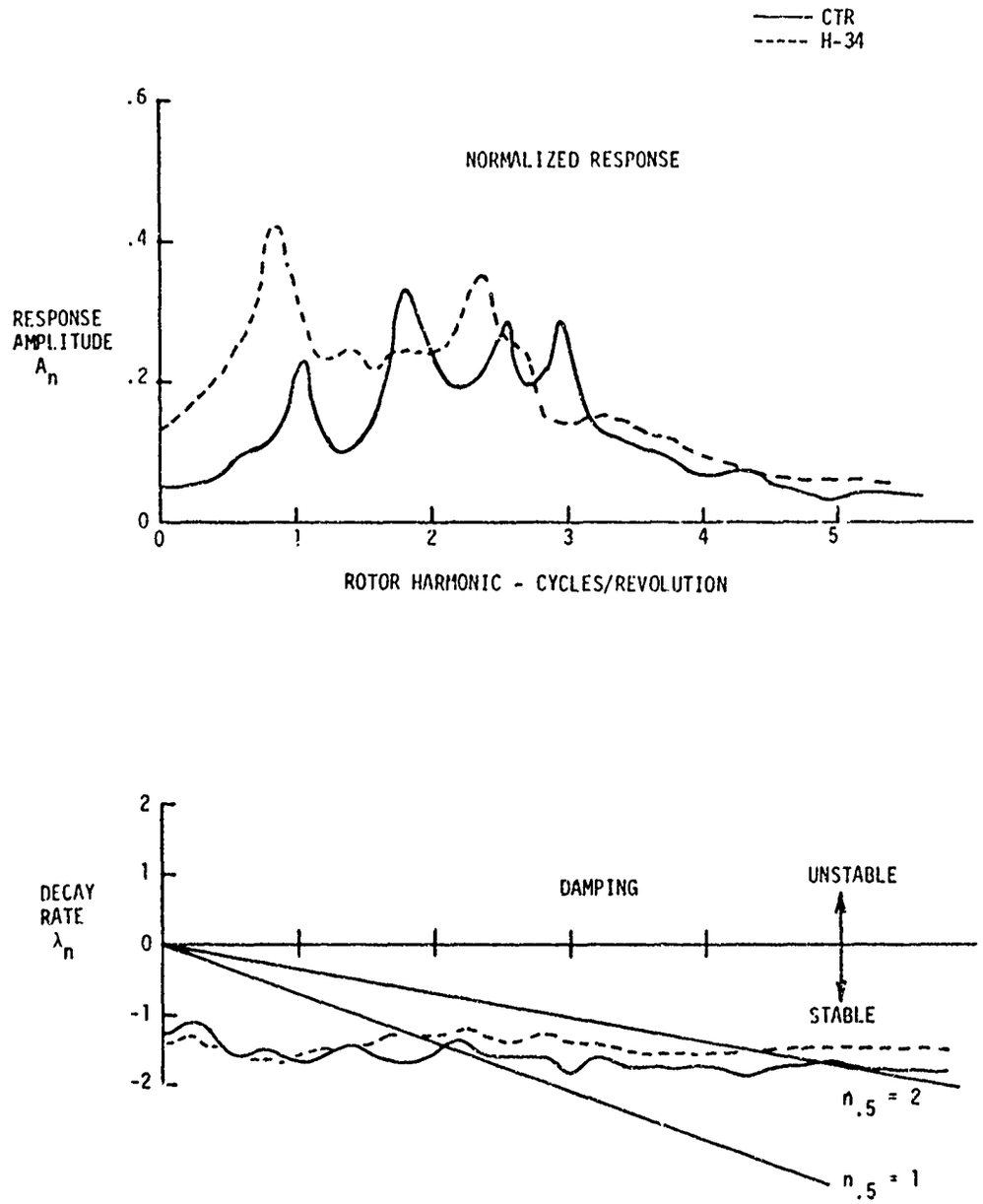

Figure A-9. Bending Response

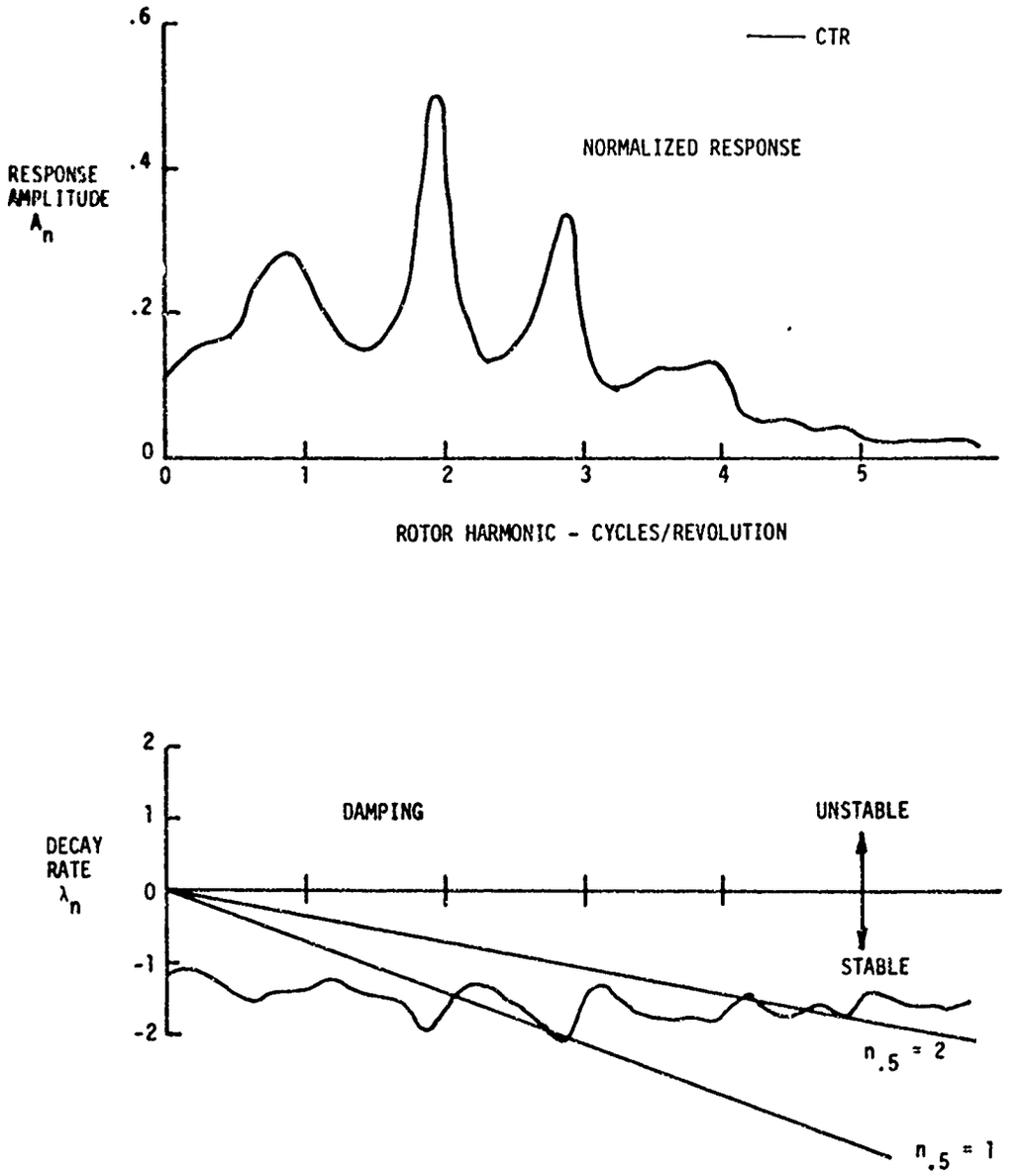

Figure A-10. Twisting Response

reference. The response spectra show the harmonic content of model response immediately following perturbation. The damping spectra show the log decrement damping rate of each harmonic over the next several rotor revolutions. Blade stability of the H-34 and the CTR are evaluated by comparing the time required to reach half amplitude. The number of cycles required to reach half amplitude are shown in Figures A-8, A-9, and A-10 by lines radiating from the origin. These lines are defined by Equation (A2).

$$\frac{\lambda_n}{n} = \frac{\log 0.5}{n_{0.5}} \qquad \text{(A2)}$$

Stable and unstable regions are indicated. All responses are very stable and quite comparable to the H-34 blade.

Aeroelastic Response

A number of steady-state operating conditions were selected at several thrust levels and flight speeds within the envelope of the Ames Research Center's 40- x 80-foot wind tunnel. At each condition, performance, loads, and blade responses were calculated by the 6F program at a series of flap, cyclic and collective control settings, to establish the effect of twist control, to select optimum control settings, and to predict the performance expected during subsequent wind-tunnel testing of the full-scale rotor. At each flap control setting, pitch-horn controls were adjusted to trim the rotor to the lift, propulsive and side forces specified for the particular operating condition. Reference 14 discusses the methods by which the flap control settings were selected, the response data were analyzed, and the optimum flap setting for each operating condition were determined and displayed. The information calculated for the rotor by each 6F case is listed in Table A-1.

[14] Donald W. Robinson, Jr. and Frank K. Dunn, TRIMMING DUAL CONTROL ROTORS FOR OPTIMUM PERFORMANCE, American Helicopter Society National Symposium on Helicopter Aerodynamic Efficiency, Hartford, Connecticut, March 6-7, 1975.

TABLE A-1

Rotor Performance

Horsepower	Propulsive Force
Thrust	Side Force

Azimuthal Distributions and Harmonic Analyses

Flapping	Servo-Flap Deflection
Feathering	Twisting
Lagging	Pitch-Horn Moment
Bending	Flap-Hinge Moment

Radial/Azimuthal Distributions

Angle of Attack	In-Plane Air Loading
Mach Number	In-Plane Bending Moment
Out-of-Plane Air Loading	Incremental Torque
Out-of-Plane Bending Moment	Feathering Moment

Harmonic Analyses of Radial Distributions

Out-of-Plane Bending Moment	In-Plane Bending Moment
Out-of-Plane Slope	In-Plane Slope
Out-of-Plane Deflection	In-Plane Deflection

Harmonic Analyses

Out-of-Plane Root Shear
In-Plane Root Shear

The responses of four of the parameters of one of the operating conditions for the optimum collective-flap setting are shown in Figures A-11 through A-14. Each of these figures presents contours at various levels of the parameter at corresponding combinations of sine and cosine components of cyclic-flap input. The cyclic-flap setting required to minimize each of the four parameters is clearly seen. Equally clear, no single setting will minimize them all at the same time. Superimposing the contours, as in Figure A-15, permits selecting the most desirable trade-off for the particular situation or helicopter mission.

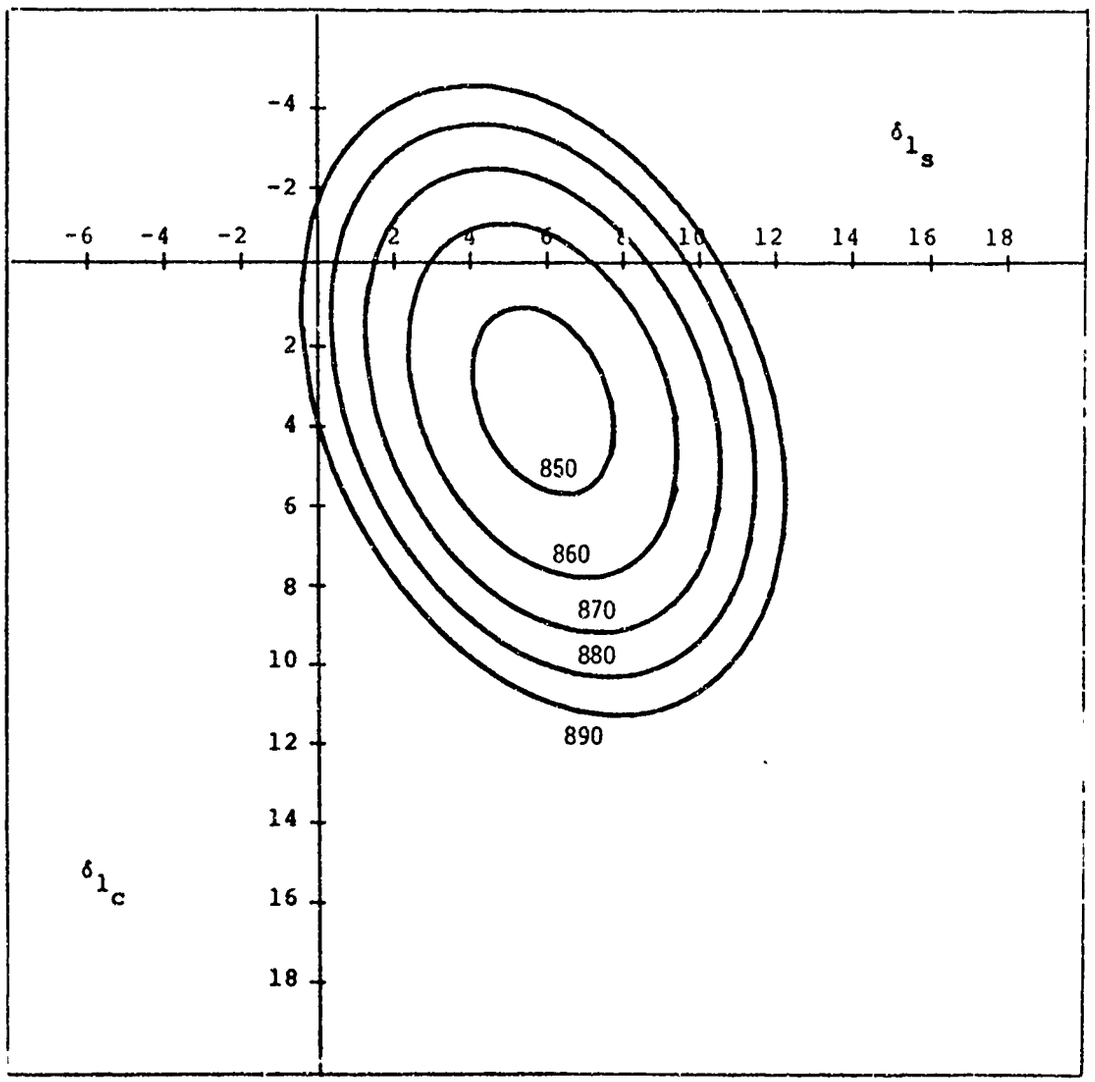

Figure A-11. CTR Control Optimization - Horsepower

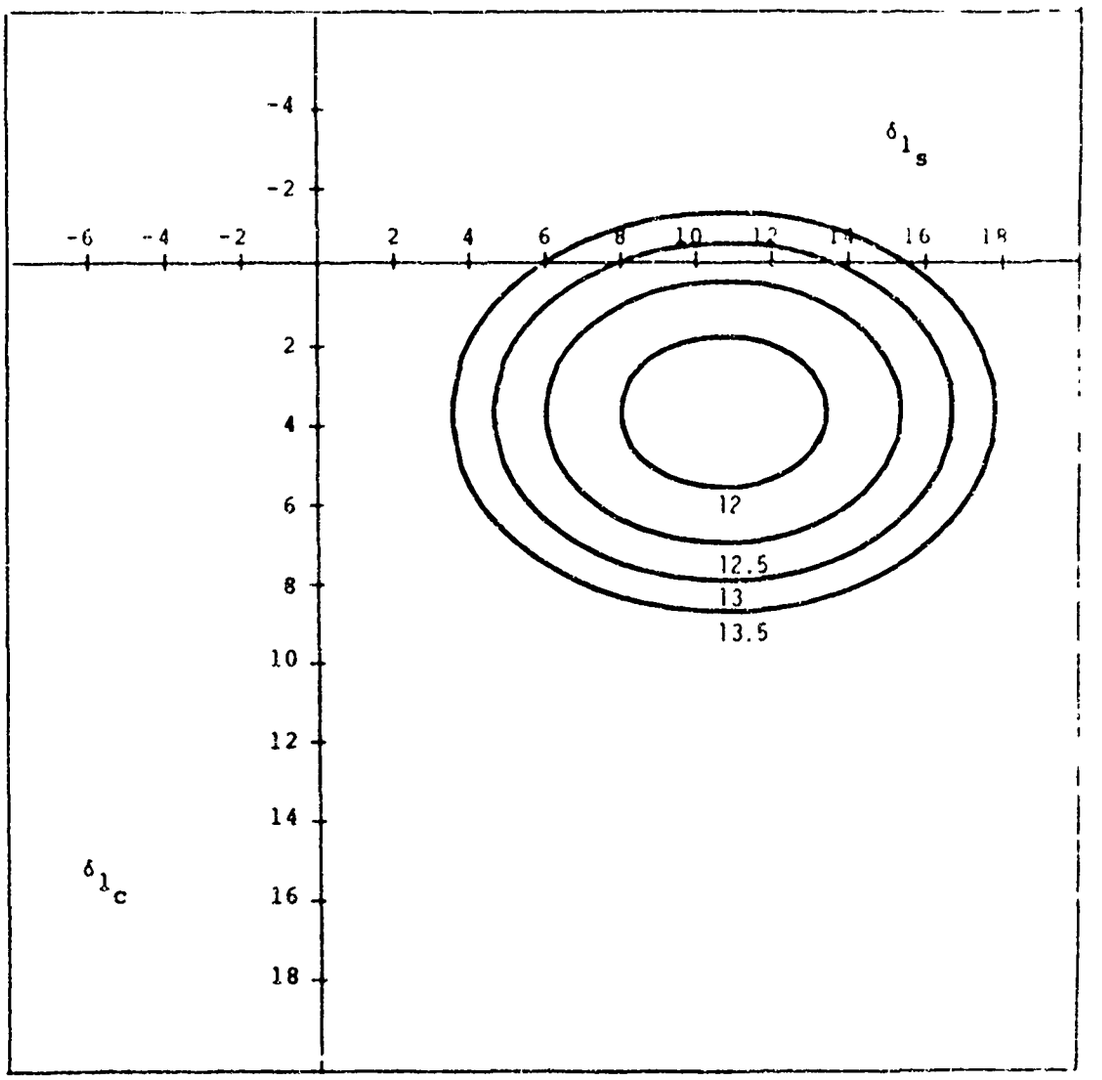

Figure A-12. CTR Control Optimization - Alpha Max - Degrees

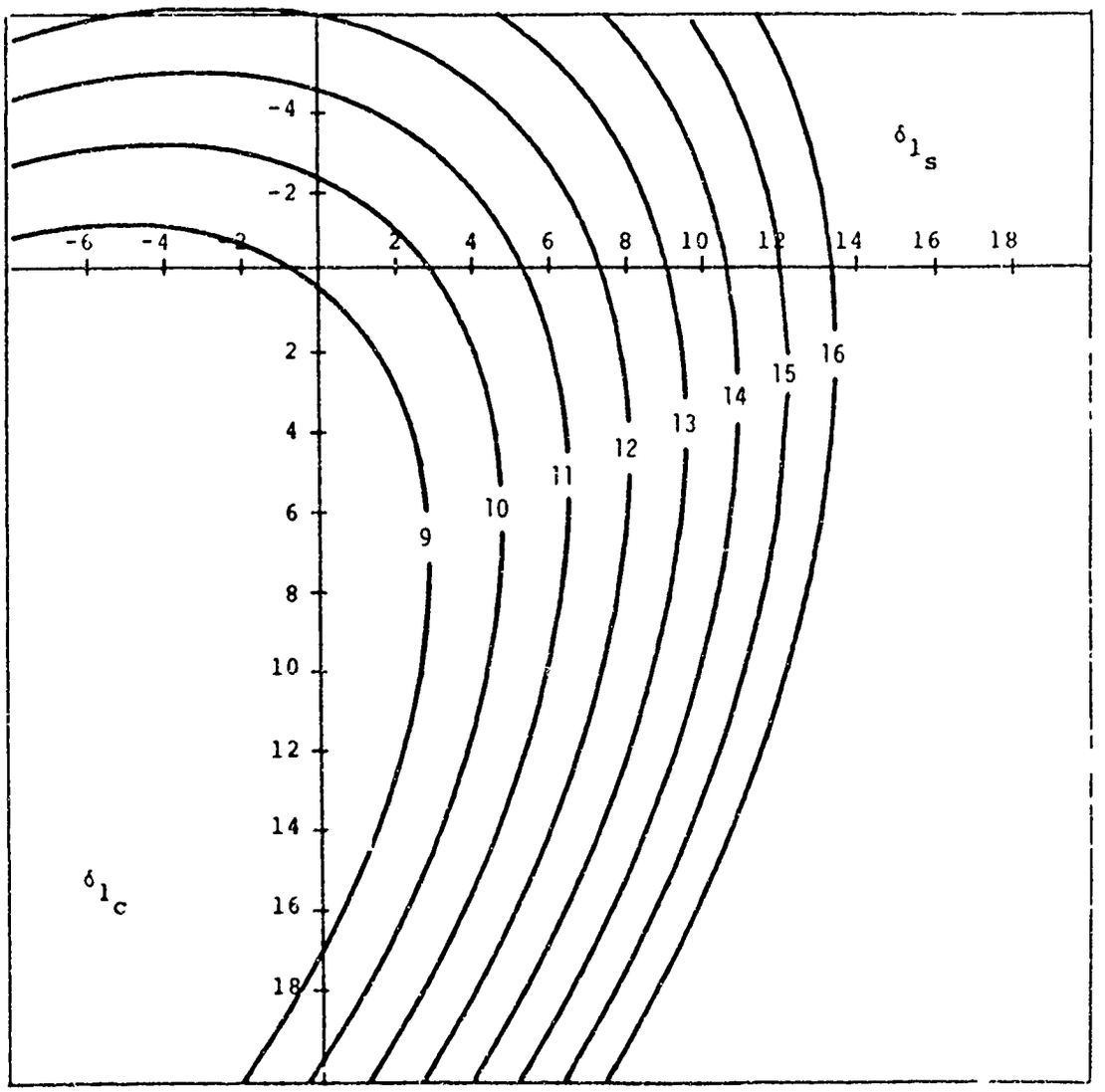

Figure 13. CTR Control Optimization - Bending Moment - Kip-Inches

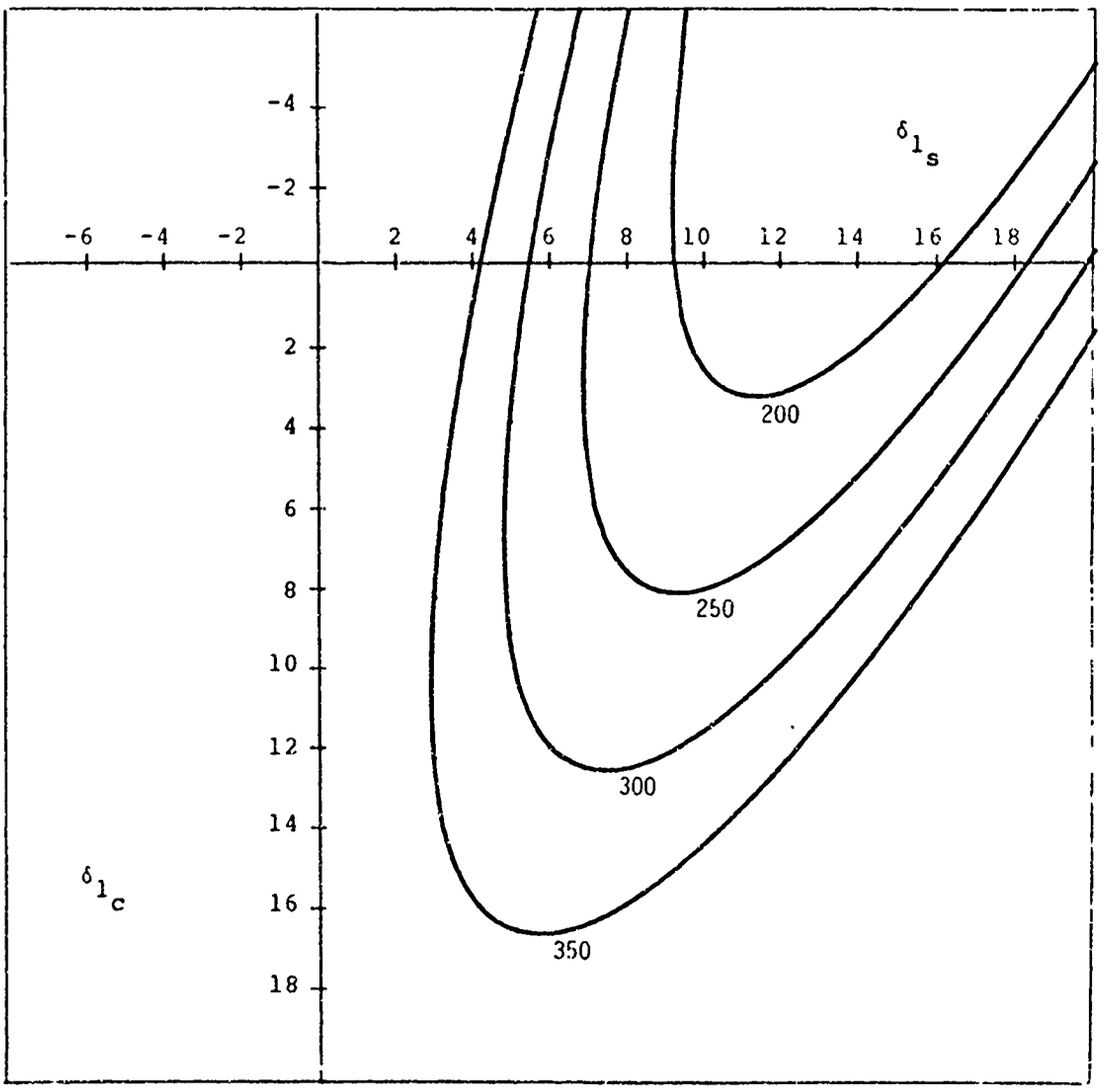

Figure A-14. CTR Control Optimization - 4Ω Pylon Shear - Lb

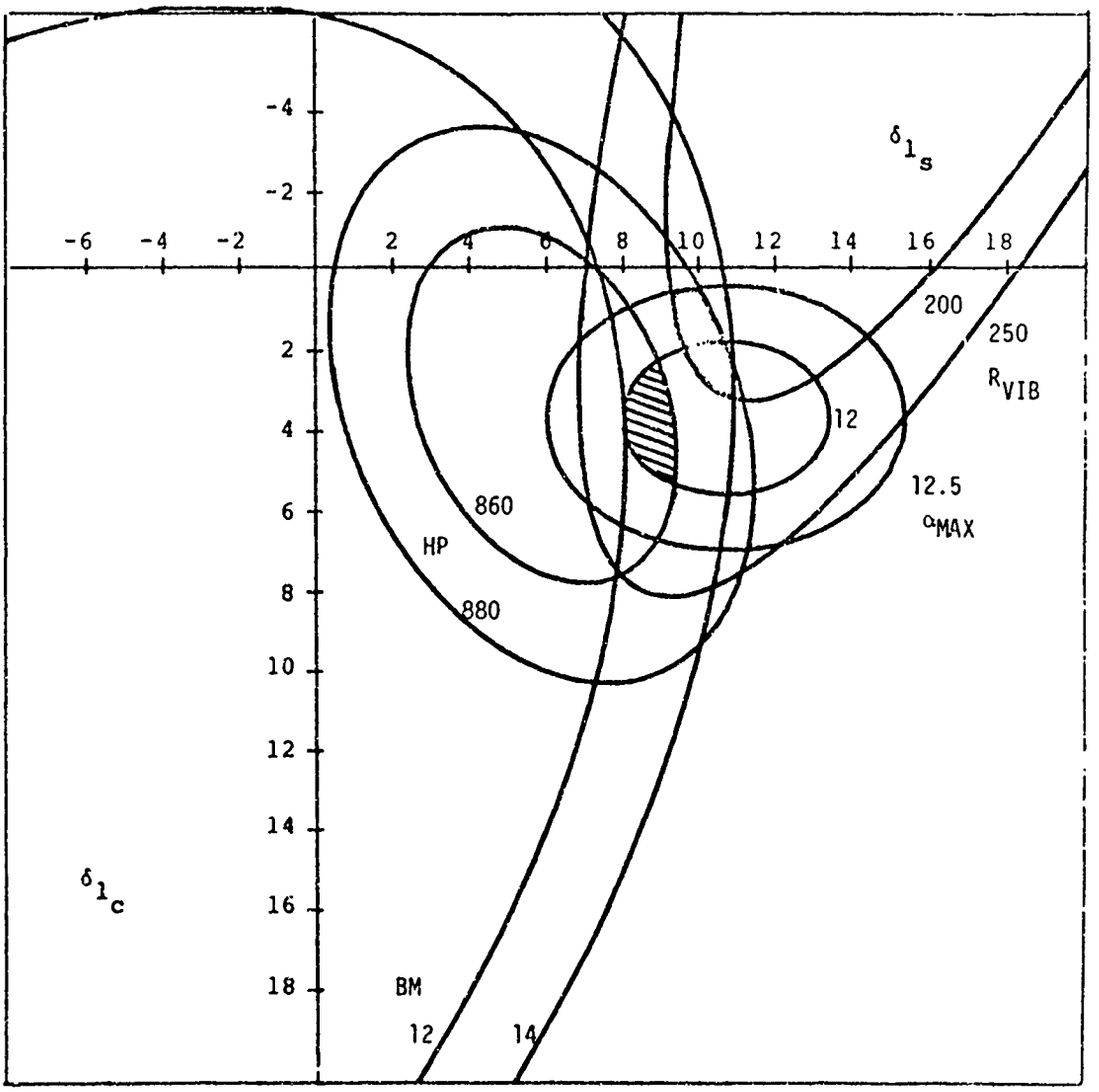

Figure A-15. CTR Control Optimization

Performance

The four performance parameters at a number of operating conditions are compared to the H-34 rotor in Figures A-16 and A-17. Each of the CTR points represents a consistent flap-control input chosen to strike a compromise between the four performance parameters. In general, any of the parameters could be further improved at the expense of the others. In a mission-oriented design, some optimization strategy, consistent with mission requirements, would be chosen, as discussed in Reference 14.

The CTR blades have a fatigue endurance limit vibratory stress consistent with a maximum peak-to-peak bending moment of 16 kip-in. Anything under that will give acceptable blade life with lower values providing extra margin for maneuvers and gusts. Stall limit is taken from a previous flight-test correlation on the SH-2 helicopter, at a maximum retreating blade angle-of-attack of 13°, occurring anywhere between the .5 and the .97 radius stations. For the H-34's 0012 airfoil, this may be optimistic.

It is seen that operating the CTR in this manner allows a 20%-higher gross weight or a thirty-knot higher airspeed at the stall limit, for a rotor of the same radius, solidity, and tip speed. Bending moments tend to lie below the H-34 blade. Vibratory shears are higher at the less extreme conditions and lower at the more extreme conditions, but are not very high in any case. CTR vibratory shear could be lowered further at the expense of another parameter.

Performance in this study was compared to a geometrically similar baseline rotor. For a mission-oriented design, the CTR's superior load-carrying capability would allow either higher disk loading or fewer blades at the maximum speed/maneuver condition. Either a smaller, more compact vehicle, or a hover-optimized rotor could then be chosen for maximum mission effectiveness, depending on requirements.

[14] See Robinson and Dunn

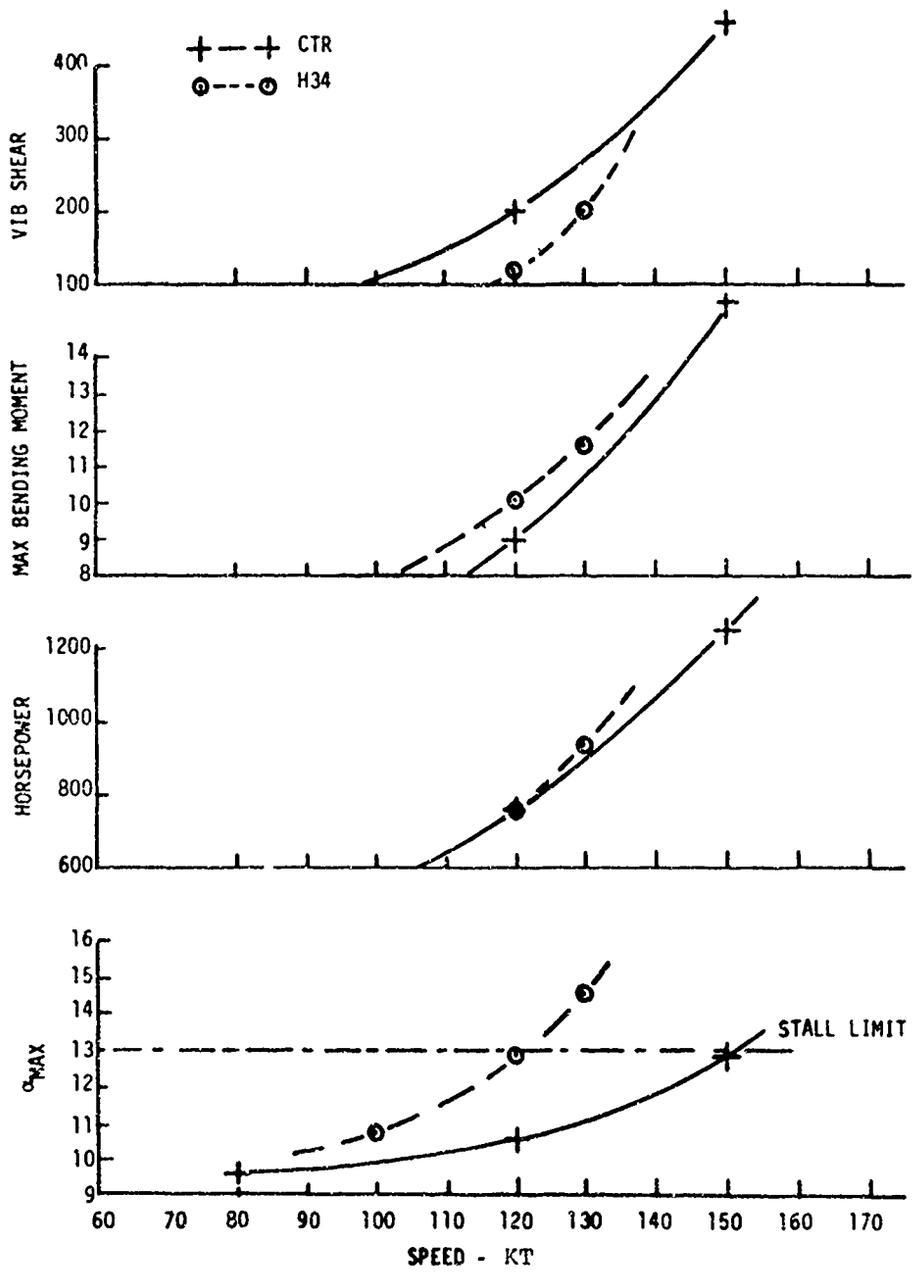

Figure A-16. CTR Performance - Effect of Speed

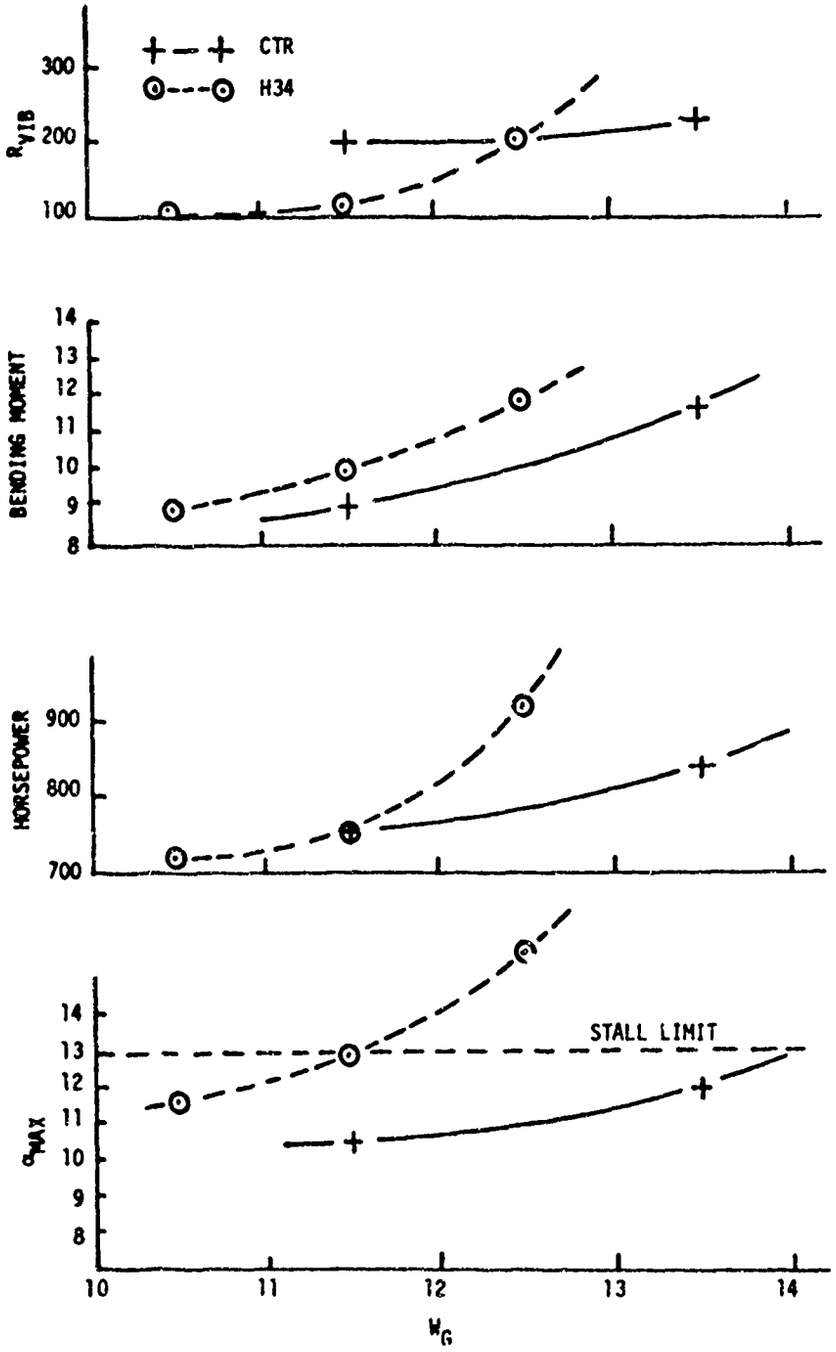

Figure A-17. CTR Performance - Effect of Gross Weight

STRUCTURAL SUBSTANTIATION

Static and fatigue stress analyses were performed using loadings calculated in the aeroelastic analyses. Table A-2 presents a summary of the components of the CTR system with predictions of the maximum anticipated loads and the life projection based on the maximum load. Components considered more critical than others were identified, and limits were established for monitoring during test operations.

Because so much of the CTR was based on existing production components, a major part of the substantiation was done by reference to published data. Detailed stress analysis was limited to new and modified areas.

TABLE A-2. CTR LOAD/LIFE PROJECTION.

COMPONENT & LOCATION	ANALYTICAL PREDICTED LOADS	ANALYTICAL PREDICTED LIFE
H34 Damper Trunnion Bolts (AN 177-34)	Vibratory Damper Piston Rod Load of ± 1500 lb.	200 Hrs.
H34 Damper Assembly	Vibratory Damper Piston Rod Load of ± 1500 lb.	> 1000 Hrs.
H34 Rotor Components Subjected to Hub Moments	Vibratory Flapping Angle of ± 3.84°	> 1000 Hrs.
H43/CTR Blade Root	Vibratory In-Plane Moment of ± 14.6 in kips. Vibratory Out-of-Plane moment of ± 8.37 in-kips.	> 1000 Hrs.
H43/CTR Blade Torsion Area	Vibratory Torsional Moment of ± 3.26 in-kips	> 1000 Hrs.
H43/CTR Blade Bending in Flap Area	Vibratory Flatwise Moment of ± 7.73 in-kips	> 1000 Hrs.
H43/CTR Servo-Flap Bending	Vibratory Flatwise Moment of ± .259 in-kips	1000 Hrs.
H43/CTR Servo-Flap Control System	Vibratory Chordwise Rod Load of ± .015 kips	> 1000 Hrs.
H34 Pitch-Link Control System	Vibratory Pitch-Link Load of ± .38 kips	> 1000 Hrs.

APPENDIX B

WHIRL TOWER TEST

CONTROLLABLE TWIST ROTOR

OBJECTIVE

The whirl tower test of the CTR, performed on the Contractor's rotor test tower, was the major qualifying test of the total rotor system prior to the wind tunnel test. Because all major rotor components were modifications of production articles, previous component qualification tests were directly related to the CTR. The whirl test then became a system qualification with the following objectives:

- Verification of rotor structural adequacy
- Establishment of rotor stability boundaries
- Definition of control linkage kinematics and freedom of mechanical interferences
- Verification of blade structural response
- Preliminary assessment of the effect of combined control inputs on blade twist
- Assessment of in-ground effect hover performance, recognizing expected turbulence due to wake interference effects

INTRODUCTION

The Contractor's 1300-horsepower electric-drive rotor-test tower was selected for the qualification tests of the CTR. Other test rigs available at the facility were better suited to production testing than experimental work. The 1300-horsepower tower was readily adaptable to the dual-control system. The H-34 rotor head was mounted with a shaft adapter that had provisions for mounting the H-34 swashplate. A primary consideration in the rig selection was the availability of both fine and coarse control of rotor rpm, allowing variations down to 1 rpm, a necessity for the required stability tests. Instrumentation provisions were also a consideration in the rig selection.

The basic test set-up featured the rotor head and CTR blades in both two- and four-blade configurations, mounted by means of the shaft adapter to the rotor drive shaft at the top of the tower. Pitch-horn control was available through the standard H-34 swashplate at the base of the tower.

Electric actuators for collective and cyclic controls were operated from the control block house. Meters for monitoring all controls were installed in the control room. Other parameters monitored visually were: rotor rpm, horsepower and thrust.

Rotating instrumentation was wired to the control room through two slip rings. One ring was mounted to the top of the rotor head, and the other was below the hub. Instrumentation parameters critical to the running of specific tests were recorded in the control room on a direct-writing oscillograph. Other parameters were telemetered to the data acquisition system located in the Contractor's main test facility.

System calibration included both preliminary and daily calibrations. All strain gage parameters were calibrated in advance to predicted load ranges. The control positions were initially calibrated in small increments through the total control range. In addition, the control coupling was calibrated by varying the servo flap while varying blade pitch, lag and flapping. Daily calibrations included recordings of null positions and equivalent calibration values along with full-range position calibrations.

Figure B-1 shows the CTR rotor installed on the whirl tower and Figure B-2 is a view of the whirl testing in progress.

AEROELASTIC STABILITY TESTS

Test Description

It has been Kaman's practice to whirl test torsionally soft servo flap rotors for aeroelastic stability by removing the flaps, which are aerodynamically stabilizing, and adding successive increments of weight at the flap hinge fitting, which is dynamically destabilizing. The decreasing tip dynamic pressure at which instability is encountered as the trailing-edge weight is increased defines a flaps-off stability boundary, as shown for the H-43 rotor in Figure B-3. The presence of the flap may be accounted for theoretically by adding an incremental, span-squared, weighted aerodynamic center shift or by analogy from the flight testing of previous rotors.

The CTR rotor was whirl tested in this manner, and the results are compared to those for the H-43 boundary on Figure B-3. Weight increments covering a range from 0.99 pound to 3 pounds, the maximum structurally allowable weight on the flap bracket, were installed between the flap brackets. For each weight increment installed, the rotor speed was increased to 210 rpm while blade strain-gage bridges were monitored for indications of abnormal buildups. No sign of instability was detected in the 0-to-5-knot wind conditions normally used as a restricted range for stability tests. The restricted wind-speed range was lifted, and tests were conducted in wind gusts up to 27 knots while trying to excite the rotor with large ramp pitch-horn control inputs. Through all of the tests conducted, the rotor was stable up to the maximum allowable tip speed. A safe flaps-off boundary was drawn through this point, which

Figure B-1. Whirl-Tower CTR Rotor

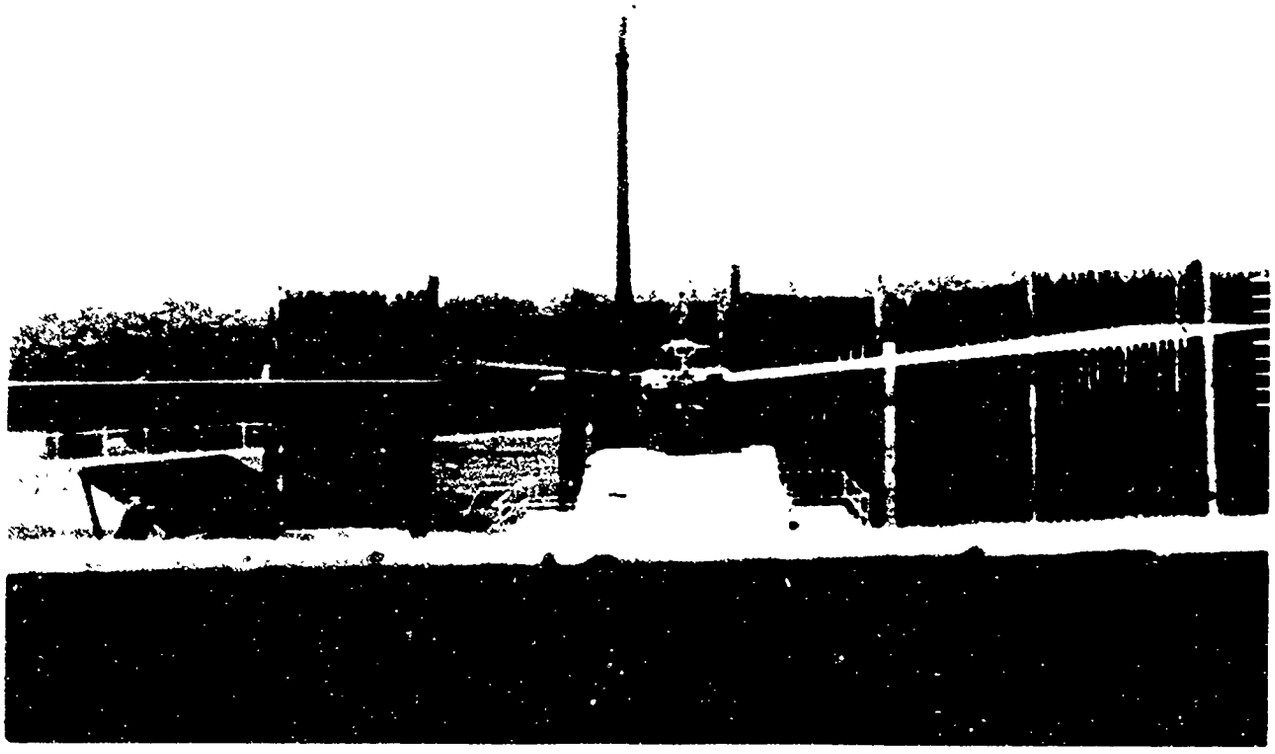

Figure B-2. CTR Whirl-Tower Testing

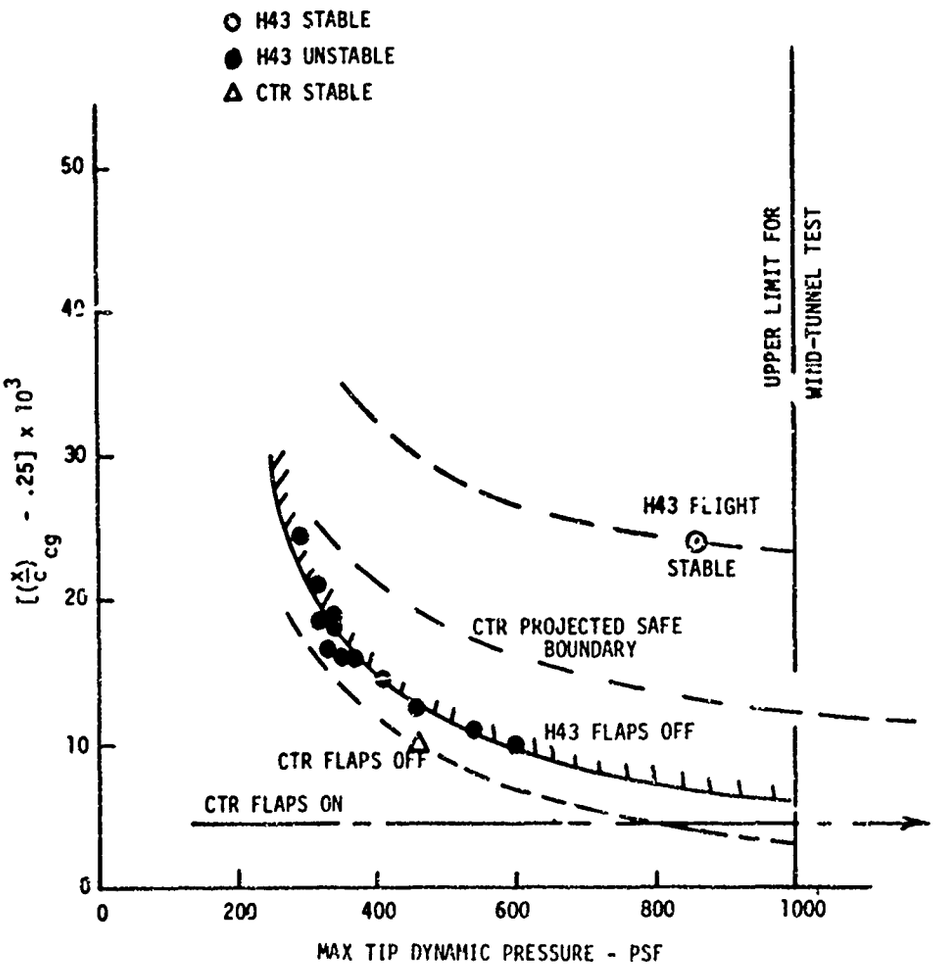

Figure B-3. Whirl-Test Stability Data

was at an increment below the H-43 flaps-off test boundary.

H-43 flight testing has established a flutter-free point at a large increment above the flaps-off whirl-test boundary, as shown in Figure B-3. The CTR span-squared weighted flap effectiveness is 54% of that of the H-43. This proportion of the H-43 stability increment which is due to flaps, was added to the safe flaps-off CTR boundary to form a projected safe boundary for flaps on. The actual CTR blade span-weighted cg locations are seen on Figure B-3 to lie below this boundary to tip dynamic pressures well beyond those to be investigated in the wind tunnel.

Rotor Configuration

The stability tests were run with two blades installed. The servo flaps were removed, and the control rods were tied down at the flap bracket. Pitch-horn control was connected in the normal manner.

Instrumentation

The following parameters were monitored and recorded on a direct-writing oscillograph:

Edgewise Bending - Blade Station 47.0
Flatwise Bending - Blade Station 47.0
Torsion - Blade Station 201.6
Rotor Speed

The following parameters were recorded via telemetry on magnetic tape:

Torsion - Blade Station 134.4
Pitch-Link Load (Rotating Star)
Rotor Shaft Torque
Blade Flapping Angle

OVERSPEED TEST

Test Description

The rotor overspeed test was the only qualifying structural test that was considered necessary prior to wind tunnel testing. Satisfactory fatigue characteristics were substantiated through analysis and the assessment of previous fatigue tests on the production components used in the CTR design.

The overspeed condition specified was 240 rpm, based on 115 percent of the intended operating speed of 210 rpm. Collective and cyclic controls were fixed to maintain 1000 pounds of thrust. The test duration was 30 minutes.

Flatwise, edgewise and torsional strains were monitored at several spanwise stations during all whirl tests. No unexpected load levels were

noted, except for the high vibratory amplification of edgewise bending at 215 rpm discussed in Appendix A. A detailed blade inspection following the whirl test revealed no structural discrepancies.

Rotor Configuration

The overspeed test was run with two blades installed, complete with servo flaps. Spare blades were used in the event any damage occurred.

Instrumentation

The following parameters were monitored and recorded on a direct-writer oscillograph:

Edgewise Bending - Blade Station 47.0
Flatwise Bending - Blade Station 47.0
Torsion - Blade Station 201.6
Lag - Damper Load
Rotor Shaft Torque
Rotor Speed
Pitch-Horn Collective

BLADE DYNAMICS AND PERFORMANCE TESTING

Test Description - Blade Dynamics

Most data runs during whirl testing were made in light wind conditions, but in ground effect and in considerable turbulence because of the partial down-wash containment by surrounding structure and protective fencing. Therefore, considerable random excitation was present, although integral harmonic excitation was predominant, and the blade response measurements provided a record of the natural frequencies of the less heavily damped normal modes. Typical spectral analyses for edgewise bending are presented on Figures B-4 and B-5. Figure B-4, taken at 195 rpm, shows the first elastic in-plane mode responding at its natural frequency at approximately 4.5 Ω. Figure B-5, taken at 215 rpm, shows a high response amplification as the natural frequency coincides with 4 Ω. Likewise, the second elastic flatwise bending mode was identified and tracked through the rpm range. Both modes correlated closely with the calculated frequencies shown in Appendix A, Figure A-7. Other modes were not excited sufficiently to identify them. All dynamic characteristics were considered satisfactory except for the in-plane elastic mode discussed previously.

The close correlation of the first elastic in-plane natural frequency as measured at 210 rpm (4.1 Ω) with that calculated as a pin-ended beam (4.0 Ω) shows a relatively small stiffening effect due to the H-34 lag dampers, contrary to previous experience with H-2 dampers. Additional calculations were therefore made to determine the degree of stiffening required to keep this mode above 4 Ω for the entire H-34 operating range.

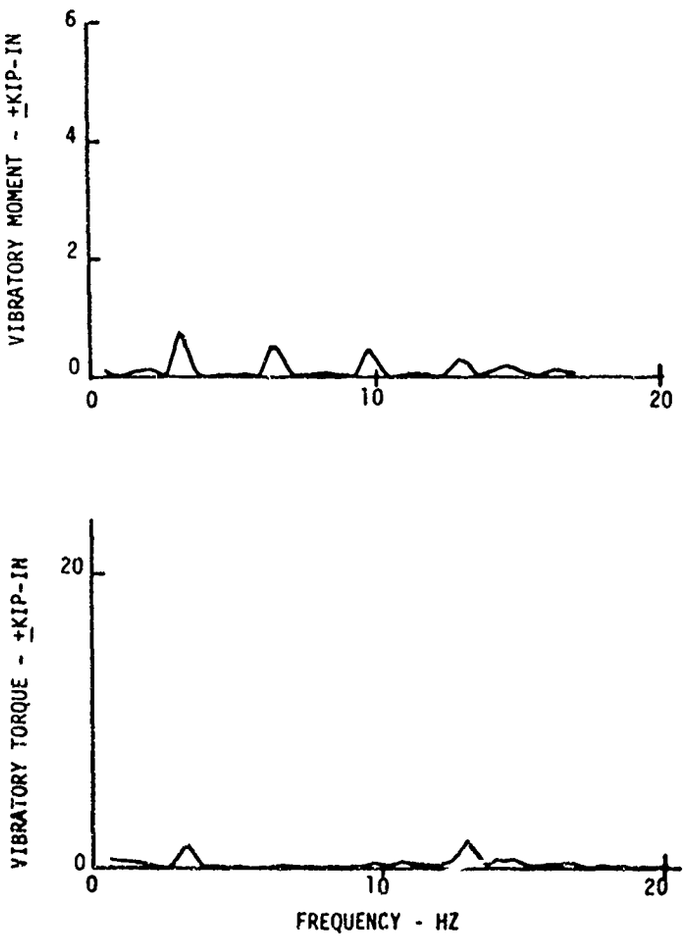

Figure B-4. Edgewise Response at 195 RPM (θ_o = 6°, δ_o = -4°)

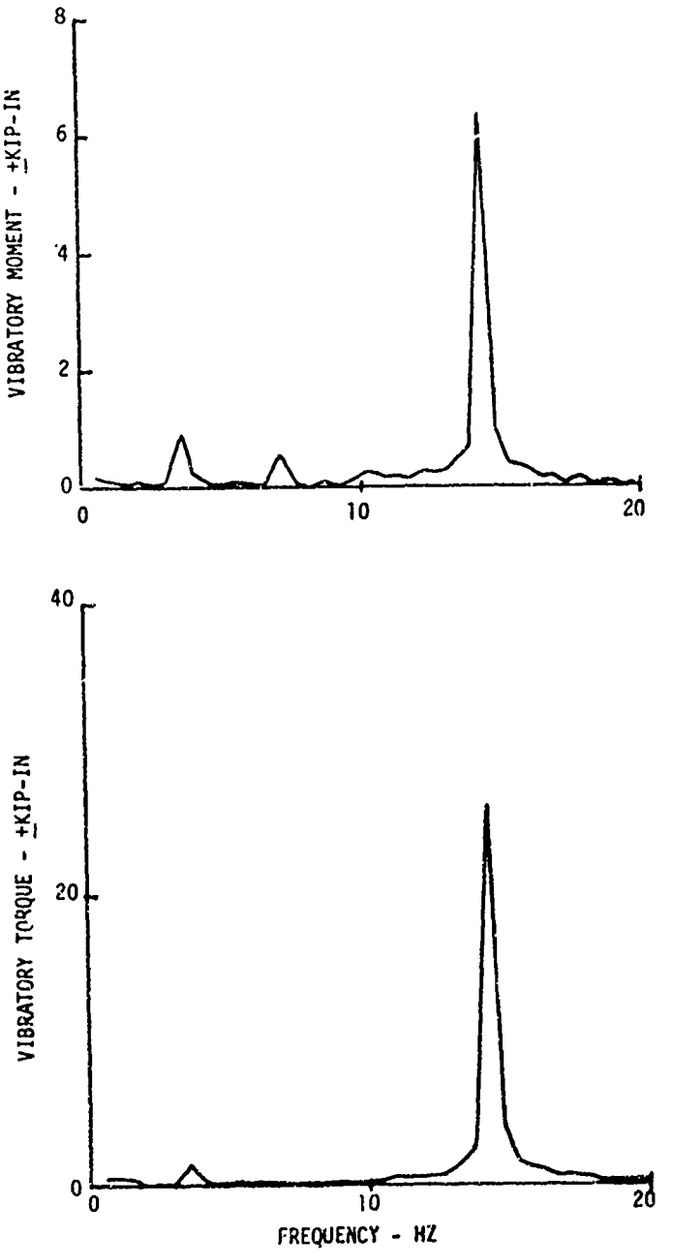

Figure B-5. Edgewise Response at 215 RPM (θ_o = 6°, δ_n = -4°)

It was found that this stiffness could be obtained practically by replacing a portion of the fiberglass-covered, wood, trailing-edge spline with a carbon-graphite composite. However, it was not considered necessary to incorporate this change for wind tunnel testing.

Wind tunnel testing was limited to 200 rpm to avoid excessive edgewise bending and shaft torsional stresses. This was close enough to design rpm to provide good data for validating the CTR principle and establishing its important characteristics.

Performance

As noted previously, whirl testing was in ground effect with substantial turbulence due to wake interference effects. Poor-quality hover performance data was therefore expected. Figure B-6 shows that such was indeed the case, with considerable scatter at the higher thrust levels. However, a clear trend of increasing efficiency with decreased negative flap deflection is seen. The peak Figure of Merit of .82 would correct to approximately .7 for out-of-ground effect.

Rotor Configuration

Both the blade dynamics and the performance tests were conducted with the four blades scheduled for testing in the wind tunnel. Collective and cyclic controls were provided for both the pitch horn and the servo flap.

Instrumentation

The following parameters were recorded via telemetry and processed through the Contractor's data acquisition system:

Edgewise Bending Moment - Blade Station 47.0
Flatwise Bending Moment - Blade Station 47.0
Flatwise Bending Moment - Blade Station 168.0
Flatwise Bending Moment - Blade Station 235.2
Flatwise Bending Moment - Blade Station 283.6
Torsion - Blade Station 134.4
Torsion - Blade Station 201.6
Torsion - Blade Station 252.2
Torsion - Blade Station 280.0
Servo Flap Bending Moment
Servo Flap Control Load
Pitch-Link Load
Lag-Damper Load
Rotor Shaft Torque
Blade Flapping Angle
Blade Lead-Lag Angle
Pitch-Horn Collective
Servo Flap Collective
Rotor Speed
Rotor Thrust

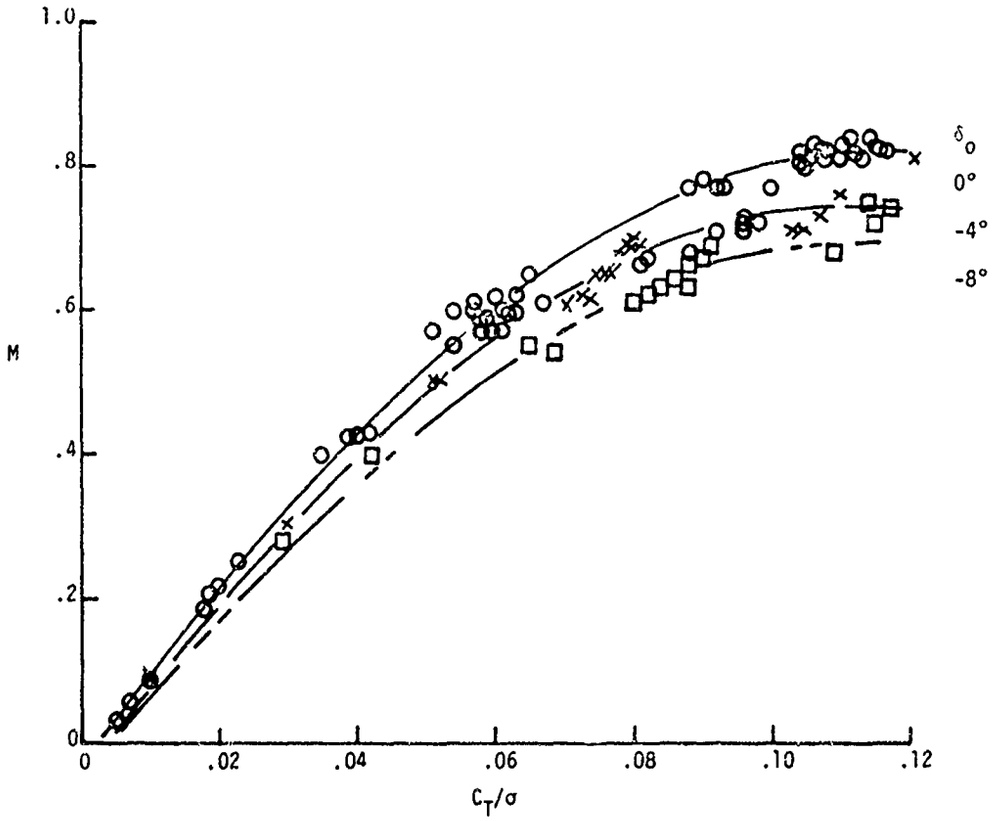

Figure B-6. Hovering Performance

Servo Flap Effectiveness

Figure B-7 shows blade response to collective servo flap input at normal rpm, two collective pitch angles, and two cyclic servo flap settings. Measured thrust and coning angle increase with negative collective-flap deflection at an average of two-thirds as much as the collective-pitch change. Collective servo flap effectiveness decreases somewhat with blade pitch setting but is unaffected by cyclic input. Cyclic servo flap effectiveness in producing blade flapping is shown on Figure B-8, for two values of blade cyclic pitch input. Cyclic servo flap effectiveness is substantially linear over the range tested and is independent of blade cyclic pitch.

Rotor Configuration

The rotor configuration for the servo flap effectiveness test was the same as for the performance test.

Instrumentation

The servo flap effectiveness data was recorded via telemetry. The following parameters were recorded:

Edgewise Bending Moment - Blade Station 47.0
Flatwise Bending Moment - Blade Station 168.0
Torsion - Blade Station 134.4
Torsion - Blade Station 252.2
Torsion - Blade Station 280.0
Servo Flap Bending Moment
Rotor Shaft Torque
Servo Flap Control Position - Measured at two places
Blade Pitch Angle
Blade Flapping Angle
Blade Lead-Lag Angle
Rotor Speed
Pitch-Horn Collective
Pitch-Horn Cyclic
Servo Flap Collective
Servo Flap Cyclic
Rotor Thrust

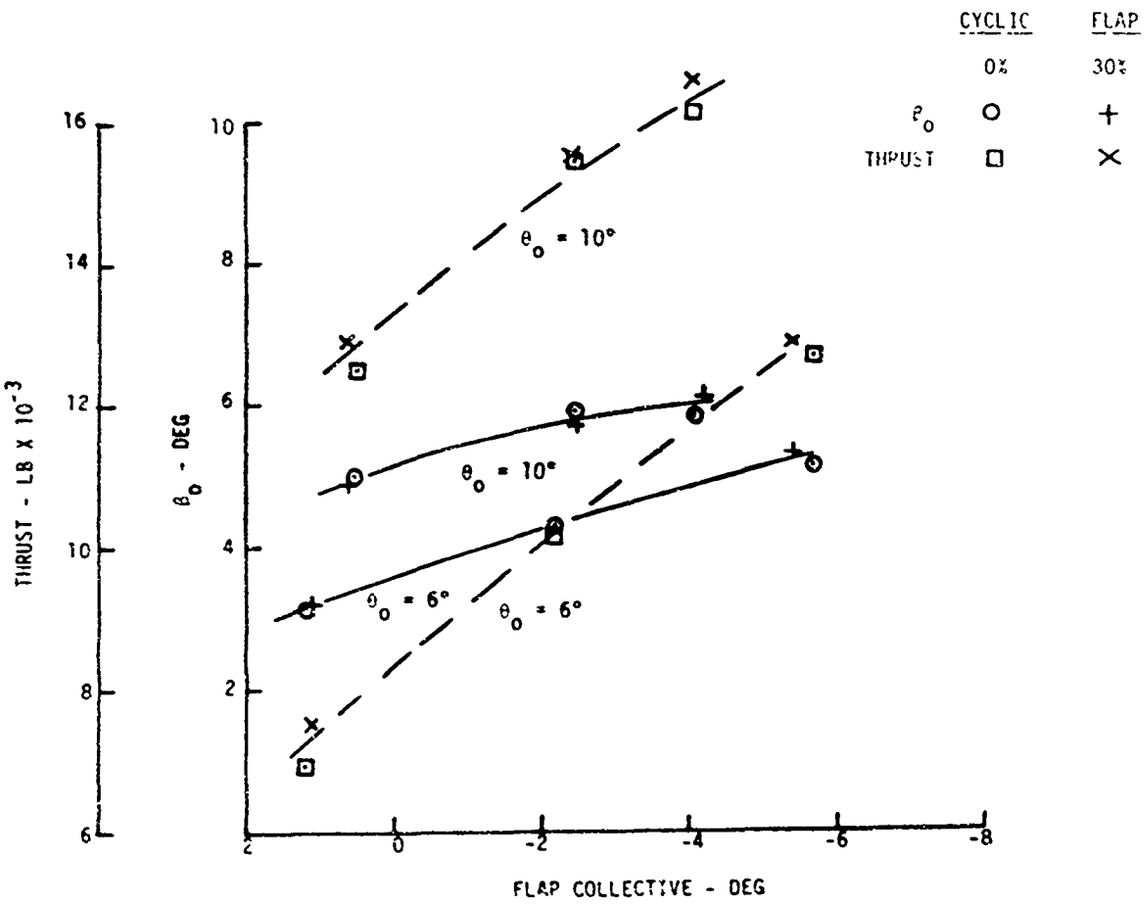

Figure B-7. Collective Flap Effectiveness

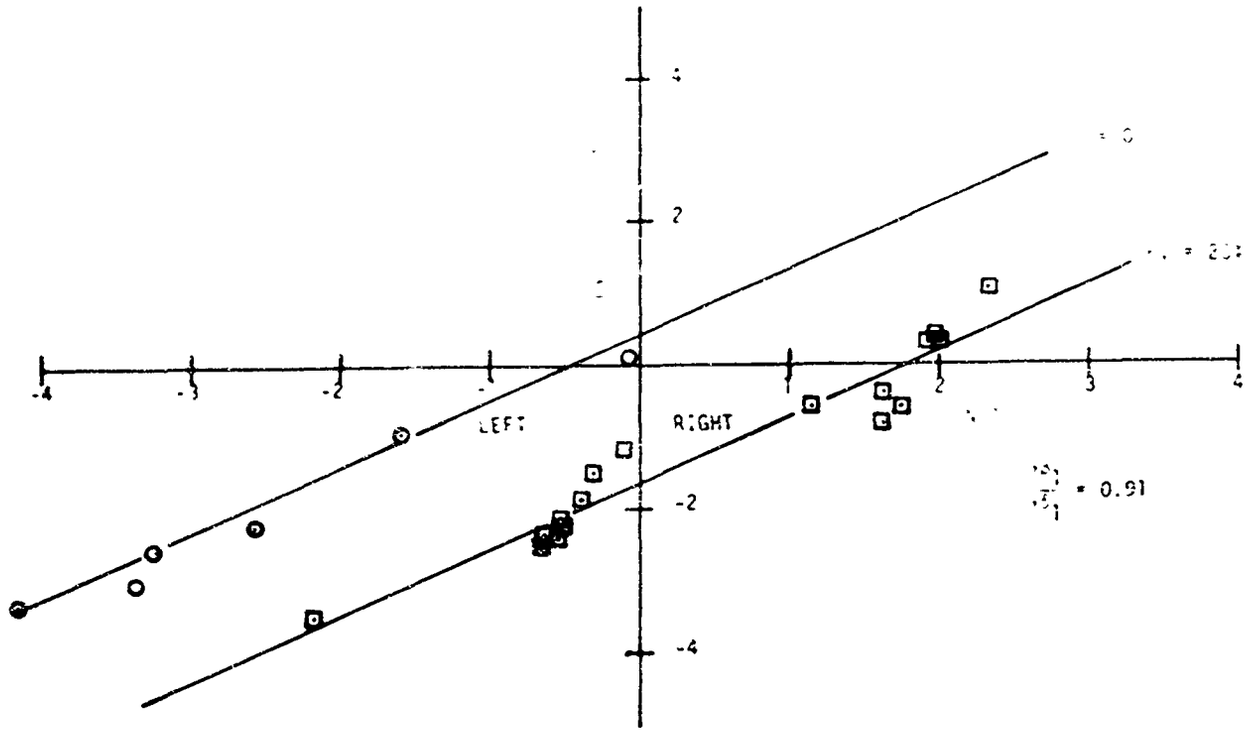

Figure B-8. Cyclic Flap Effectiveness

APPENDIX C

WIND TUNNEL TEST - OPERATIONS DESCRIPTION

CONTROLLABLE TWIST ROTOR

INTRODUCTION

The objectives of the wind tunnel tests were to demonstrate the accuracy of CTR predictions, validate the computer techniques used in the analysis and gather data for the design of an advanced CTR. Coordination for the wind tunnel phase started at the beginning of the present work and continued throughout the program. The interface was complicated by the plan to use new data acquisition systems at the 40- by 80-foot tunnel and a test module that was still under development.

A detailed discussion of data results, interpretation, analysis methods, and conclusions is presented in the body of this report. This Appendix presents a description of the wind tunnel interface regarding planning and system integration.

QUALIFICATION PLAN

Qualification planning for any wind tunnel test in the NASA-Ames 40- by 80-foot tunnel requires the preparation of detailed test plans, a system safety analysis, and documentation of the instrumentation design including a description of the control system. The required documentation presented a very complex task for the CTR system. The CTR rotor head and controls were comprised of both Kaman and Sikorsky, standard and experimental components. The test module was developed by Sikorsky under an independent contract, and the design was undergoing changes and testing at the start of the program. The wind tunnel data acquisition system was still in the planning stages at program go-ahead.

Close coordination was maintained throughout the program between the Eustis Directorate, NASA-Ames, Kaman and Sikorsky, resulting in the availability of all required systems and data at the start of model build-up.

Test Plan

The Contractor's test plan served a dual purpose. A detailed listing of test runs and test points was presented covering wind speeds from 0-170 knots and a range of control points intended to cover the desirable operating areas predicted by analysis. In addition, material was presented that partially fulfilled the system safety analysis requirement. The structural substantiation report completed the safety analysis documentation.

Contained in the test plan were detail system descriptions, normal test running procedures, emergency procedures, a definition of the test-crew interface, and instrumentation lists. Background material supplied included the load boundaries, gross hazard data, weight data, the dynamic analysis, aeroelastic analysis, and a listing of drawings and reports.

Instrumentation Design

An instrumentation manual was prepared giving detail data for all Kaman installed instrumentation and control systems. This book was used in conjunction with a similar manual supplied by Sikorsky covering test module systems and with detail instrumentation forms prepared by NASA-Ames.

Complete data covering calibrations, set up data, and the data system interface were included.

SYSTEM INTEGRATION - BUILD-UP

CTR System

The build-up of the wind tunnel CTR configuration required the marriage of systems and components supplied by Kaman, Sikorsky and NASA-Ames. First, the test module had to be dismantled to allow the removal of all systems not used for the CTR and the installation of CTR components. Existing instrumentation and control cabling was modified or replaced. Finally, system rigging and interference checks were made, and the documentation of individual systems was integrated to describe the newly assembled CTR system. The following is a brief description of some of the considerations in assembling the various systems.

Rotor

The rotor head required several parts from the standard test module head. The rotor head supplied by Kaman was a standard H-34 head, modified to incorporate control cranks for the servo flap and built-up with turret assemblies for the routing of control rods. Because of strength considerations, the pitch horns and the rotating scissors from the module's pitch-horn swashplate were transferred to the CTR head. Also, instrumentation for the measurement of blade motions was transferred. The head was then installed on the rotor shaft of the test module. The CTR blades were already equipped with blade retentions that would mate with the standard pitch barrel, making the blade installation a fairly simple procedure.

Test Module

Test module modifications centered around the removal of the module instrumentation slip ring and the fitting and installation of a framework to mount the servo flap rotating swashplate, the control actuators, and

the instrumentation slip ring. This assembly required precise alignment to avoid any adverse loading of controls. Fairings to house the control assembly were designed and fabricated by NASA-Ames. Two 1500-horsepower electric motors were installed. The power available with this installation at a rotor speed of 200 rpm was approximately 1300 horsepower.

Controls

Final control rigging involved independent set-up of the pitch-horn and servo flap controls. Conventional procedures were used for each system, and control limits were set in accordance with the anticipated control ranges. Extensive interference and control coupling checks were then made for both control systems.

Instrumentation

Instrumentation tasks in the build-up period consisted of: the final installation of transducers, the hook-up of rotor-head wiring for blade and other rotating parameters, the replacement of test module cabling with CTR cables, and a final checkout of all instrumentation. The instrumentation task required close coordination with NASA-Ames personnel because of the joint responsibility for cabling, control-panel wiring and checkout. All required systems were checked and calibrated successfully prior to tunnel entry.

SYSTEM INTEGRATION - TUNNEL TEST

CTR System/Tunnel Systems - General

System integration following tunnel entry included model installation and final instrumentation hook-up, followed by checkout and calibration of all data and monitoring systems. A view of the complete model as installed is shown earlier in the report in Figure 2.

The complete tunnel system for the CTR included: the model, the tunnel fans and windspeed controls, the model control systems, the balance and force measuring system, the data acquisition and processing system, and the test monitoring systems. Following instrumentation hook up, all parameters were calibrated through the total data system.

Measured Parameters

Transducer measurements that were recorded during the test were:

- Blade Torsion - Stations 134, 201, 252 and 280
- Blade Edgewise Moment - Stations 47, 168, and 235
- Blade Flatwise Moment - Stations 47, 168, 235, 283, and 309
- Blade Flapping Motion
- Blade Pitch Motion
- Blade Lag Motion
- Servo Flap Control Load - Measured in 3 places
- Servo Flap Bending - Measured at the flap centerline
- Lag Damper Load
- Pitch-Link Load - Rotating Star
- Pitch-Horn Actuator Load - 3 Actuators
- Rotating and Stationary Scissors Load
- Rotor Torque
- Servo Flap Control Position - Measured at the flap
- Servo Flap Command Position - Collective, longitudinal and lateral cyclic
- Accelerometers - Measurements in 3 planes
  - Nose
  - Crossbeam
  - Tail

All of the above parameters were fed to the primary data systems, and selected parameters were fed to monitoring systems.

CTR System/Tunnel Systems - Detail

Figure C-1 is a block diagram illustrating, in simplified form, the relationships of CTR systems to the overall tunnel systems. Within the test module, rotating transducers are fed from the blades, the rotor shaft, and upper controls through the slip ring and then via cabling to the tunnel control room. Stationary transducers below the slip ring provide data for control positions and the condition of critical drive system components for fault-detecting circuitry. Power is also supplied for the 1500-horsepower electric motors and the hydraulic power supplies.

The module is supported on struts that mount to the tunnel balance system. The balance system connects to a scale system that is the force system measuring aerodynamic forces exerted on the model.

Control Room Systems/Functions

The tunnel control room is the focal point for the control of the module and the flow and treatment of all data. Referring again to Figure C-1, the following descriptions are given for the various functional groups and their individual subsystems:

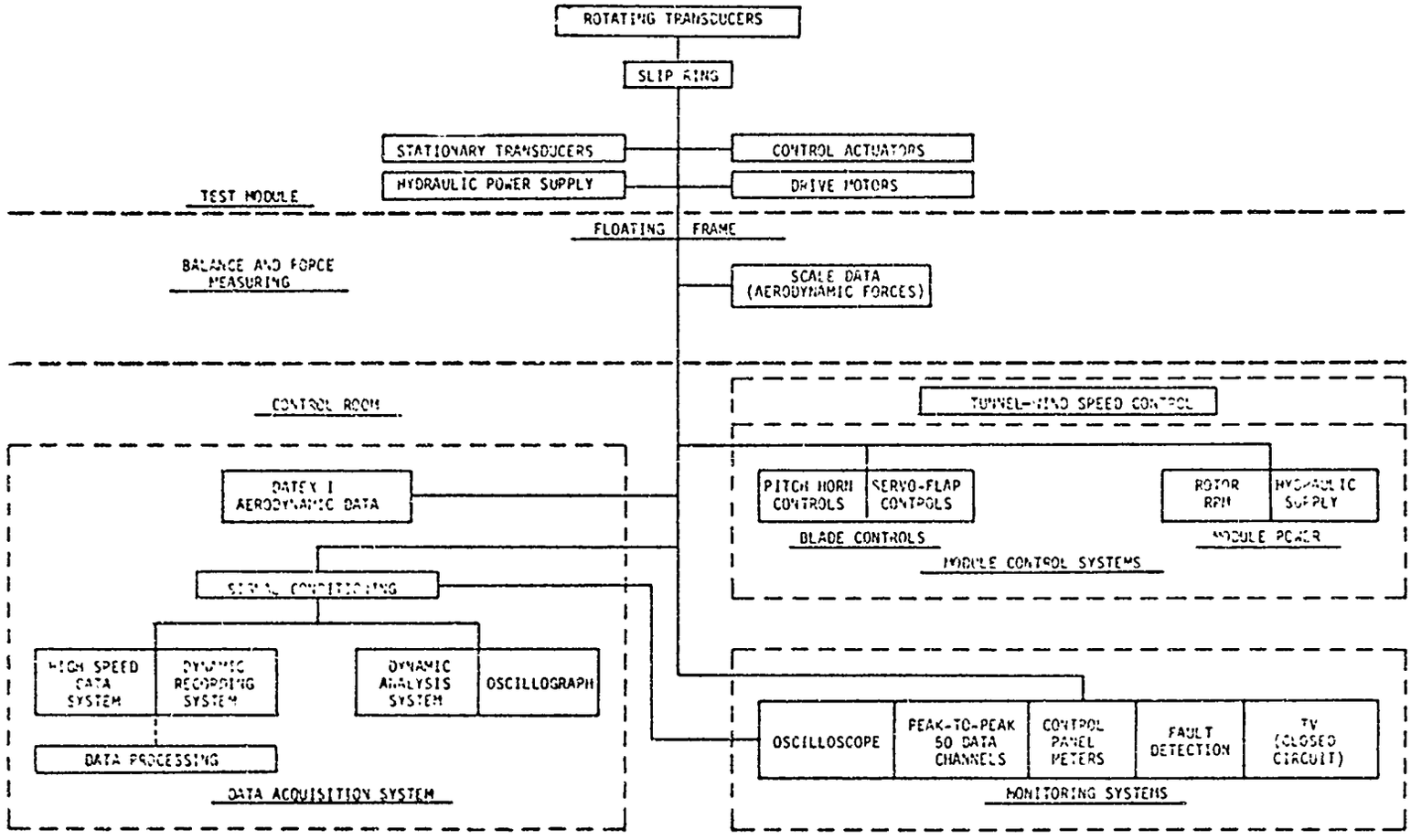

Figure C-1. CTR Module and Tunnel Systems

Control Systems

Module-Blade Controls

The module blade controls involved two consoles, located side by side, and operated by a NASA-Ames rotor operator. Each console had similar displays and switching functions. The pitch-horn console was used to input root pitch collective and cyclic commands, with readouts of the commanded angle, the resulting measured angle at the blade root, and the resulting blade flapping, which is resolved into blade coning, and longitudinal and lateral flapping. The servo flap console performed the same functions and gave similar readouts for angles measured at the servo flap.

Control technique involved commanded inputs to either the pitch horn or the servo flap. Blade flapping meters on the pitch-horn console were observed, and the longitudinal and lateral pitch-horn controls were used by the operator to achieve a zero-cyclic-flapping condition. When zero-cyclic blade flapping was achieved, readings were taken.

Module - Power

Module power controls consisted of speed controls for the 1500-horsepower rotor-drive motors and for the activating switches for electric motors used to drive the hydraulic power supply for the pitch-horn servo controls. Rotor speed was monitored with frequency counters.

Tunnel-Wind Speed Control

Tunnel-wind speed was controlled from a room below the main control room. Continuous voice communication was maintained between the two control rooms.

Tunnel air was driven by six 40-foot-diameter fans, powered by six 6000-horsepower electric motors.

Monitoring Systems

Various monitoring systems were used to control the test conditions. The critical nature of particular parameter determined the type of monitoring system used.

Control Panel Meters

As stated previously, meter displays on the control consoles gave readings for collective and cyclic conditions. The flapping meters were used as a primary test control since zero cyclic flapping had to be maintained to prevent adverse loading conditions.

Oscilloscope

A panel-mounted oscilloscope gave a continuous monitor of a few selected parameters that were known to be critical from either a stability or a loading standpoint.

Peak-to-Peak Display System

The peak-to-peak display system allowed continuous monitoring of all critical channels. The system consisted of 50 peak-to-peak detector circuits, a display in bar-chart format, and a digital printer with controller. Each of the 50 channels had a preset alarm capability, which permitted test operations to continue with only a visual scan to assure that no alarms had been activated without the need for noting specific levels of critical parameters.

For each test point, the digital printer was activated, giving an instantaneous record of peak-to-peak levels for each critical channel.

Fault Detection

Fault detection indicators were located in the module control consoles. These indicators gave warning lights for failures in the lubrication system, the hydraulic system, the controls, and the drive system, and for short circuits in the electrically isolated tunnel balance frame.

Television (Closed Circuit)

Television monitors viewed the module at all times from three stations. Each station had a limited scanning and zoom capability. Each station was recorded on video-tape.

Data Acquisition System

The NASA-Ames data acquisition system used for the CTR tests was made up of several subsystems. Some of the systems had been used in previous tests. However, two of the systems, in addition to the 50-channel peak-to-peak monitoring system, were new, and because they involved a major portion of the instrumentation set-up, problems were experienced with them. Following is a brief description of each of the various systems. Detailed system descriptions can be found in Reference 15.

Data Acquisition System I (Datex I)

This system takes data from the tunnel scale system. In addition, other data can be input through a special instrumentation system, which interfaces digital panel meters and various switching functions at an operator's console to the master computer. Primary output data is in the form of aerodynamic coefficients, which are both displayed on lamp banks at the operator's console and printed on a teleprinter for each test point. Each test point is established at the operator's console, which energizes other primary data acquisition systems.

High Speed Data System

The High Speed Data Acquisition System (HSDAS) is a data-gathering computer front end. Sixty channels of dynamic data can be input to the system. The HSDAS simultaneously conditions, samples and holds voltages from each source. The samples are multiplexed onto an analog-to-digital converter. Digital values are then transmitted to the master computer for recording on magnetic tape. The HSDAS is considered the primary data acquisition subsystem. It also conditions all signals for other data acquisition systems.

Dynamic Recording System

The Dynamic Recording System (DRS) stores raw-data. It receives its signals from the HSDAS and records on analog magnetic tape. The DRS records 56 analog signals and is running continuously during all testing in which the rotor is turning. This system provides a backup to all other systems.

---

[15] Joseph M. Cambra and Geno P. Tolari, REAL TIME COMPUTER DATA SYSTEMS FOR THE 40- BY 80-FOOT WIND TUNNEL FACILITY AT AMES RESEARCH CENTER, NASA Technical Note TN D-7970, Ames Research Center, Moffett Field, California, May 1975.

Dynamic Analysis System

The Dynamic Analysis System (DAS) can operate either on-line or off-line as a stand-alone data gathering and analysis system. In the on-line mode, the DAS performs as a quick-look system while the master computer gathers data from the other subsystems. While operating on-line, the system can gather data from all or any two of 32 signal sources and perform a number of time-series analyses in real time. In particular, it can perform histograms, autocorrelation, crosscorrelation, impulse responses, characteristic functions, Fourier transforms, autospectrums, cross-spectrums, and transfer functions. It can perform linear, continuous, or exponential averaging of up to 51,200 samples. Results can be displayed on command on a cathode-ray tube, an X-Y plotter, or a printer.

The DAS was most useful during the initial testing to determine rig resonance, and later the evaluation of control operation ranges.

Oscillograph

A 36-channel, 12-inch, direct-writing oscillograph was used during all test operations. The initial purpose of the oscillograph was for limited immediate review of critical parameters. It was also intended as a check on all parameters to insure that the data being recorded on tape was reliable data. Because of difficulties with primary data systems, it became necessary at the conclusion of the test to base all analysis on the Datex I data and the oscillograph data.

Figure C-2 is a close-up view of consoles used for collective and cyclic control of the pitch horn and servo flap. Figure C-3 is an overall view of panels used for both control and monitoring of the test operations. Looking from right to left, the components are: the rotor speed control station, the module electronic console, the pitch-horn control console, the servo flap control console, the peak-to-peak detector system, the oscillograph, the oscilloscope and panel meters, and the Datex I operator's control console. Located above the panels are the television monitors. All other data acquisition systems are located at the rear of the control room.

Details of the data analysis for all testing are found in the main body of this report.

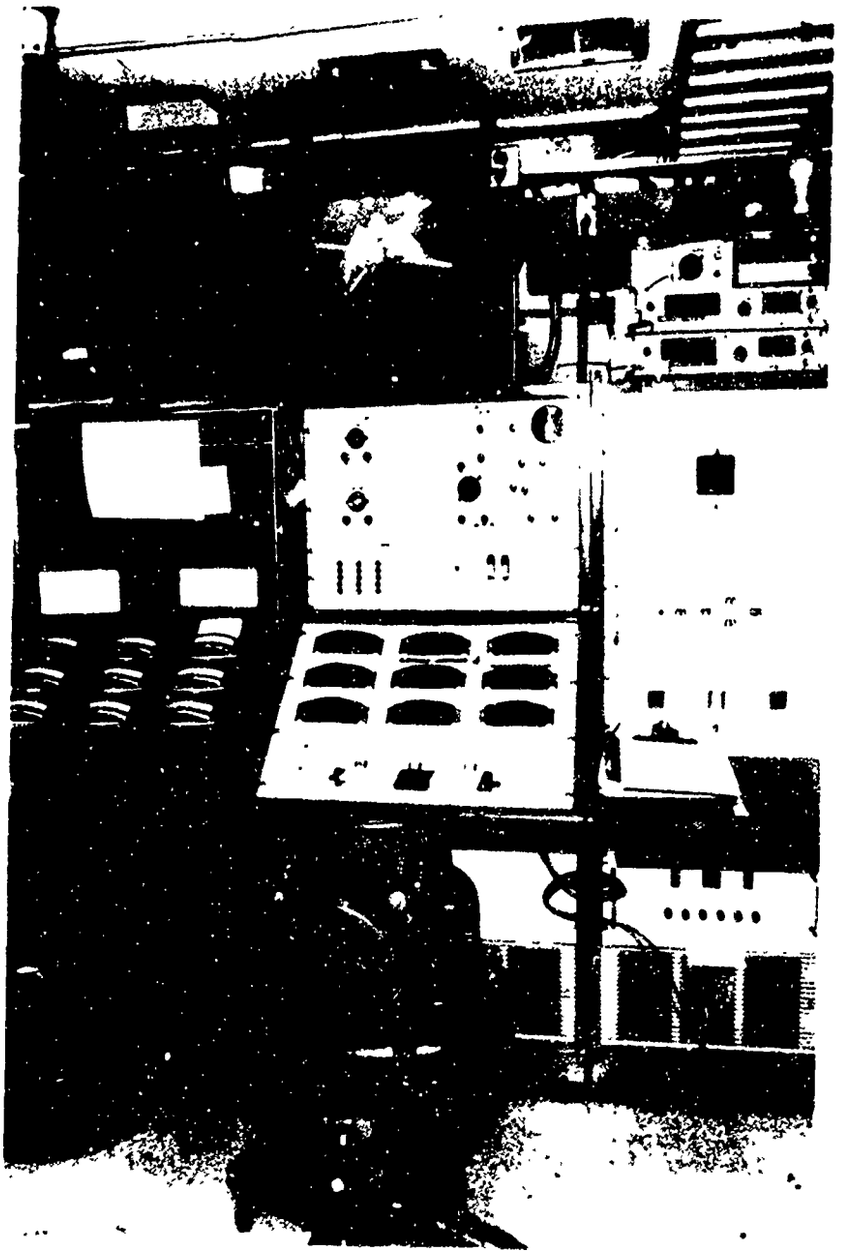

Figure C-2. CTR Module Control Consoles

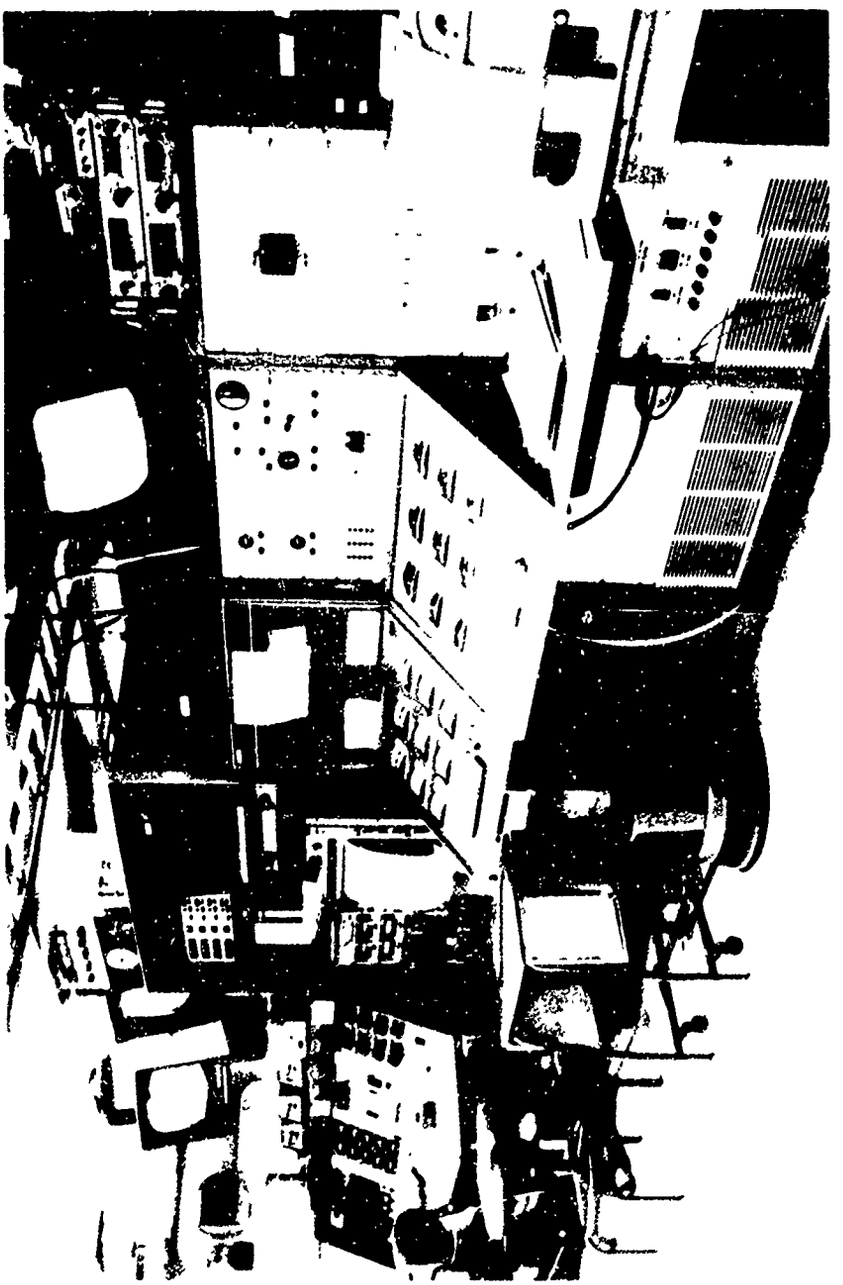

Figure C-3. Wind Tunnel Control Center-CTR Test

LIST OF SYMBOLS

a_{oj}, a_{ij},...a_{nj}	coefficient in a mathematical regression model
C_{L_R}	rotor lift coefficient
C_{Q_o}	blade profile power coefficient
C_{X_R}	propulsive force coefficient
E1, E2	edgewise modes
F1, F2, F3, F4	flapwise modes
M	Mach number ratio
R	radius of blade - ft
T1	torsion modes
V	wind tunnel speed - knots
x_i,...x_n	independent variables in a mathematical regression model
y_j	dependent variable in a mathematical regression model
α	blade section angle of attack - deg
α_s	shaft tilt - deg
β_o	rigid body coning - deg
δ_o	servo flap collective pitch - deg
δ_{1s}	servo flap longitudinal cyclic pitch - deg
δ_{1c}	servo flap lateral cyclic pitch - deg
θ_o	collective inboard control - deg

LIST OF SYMBOLS (Continued)

λ tip speed ratio - $V/\Omega R$

σ rotor solidity

ψ rotor azimuth position - deg

Ω rotor rotational speed - R/S

7482-77